THE HETEROGENEOUS INTERACTION OF TRACE GASES ON MINERAL DUST AND SOOT:KINETICS AND MECHANISM

THÈSE N° 3422 (2006)

PRÉSENTÉE À LA FACULTÉ ENVIRONNEMENT NATUREL, ARCHITECTURAL ET CONSTRUIT
Institut des sciences et technologies de l'environnement
SECTION DES SCIENCES ET INGÉNIERIE DE L'ENVIRONNEMENT

ÉCOLE POLYTECHNIQUE FÉDÉRALE DE LAUSANNE

POUR L'OBTENTION DU GRADE DE DOCTEUR ÈS SCIENCES

PAR

Federico KARAGULIAN

laurea in fisica, Università degli Studi di Milano, Italie

et de nationalité italienne

Lausanne, EPFL
2006

TABLE OF CONTENTS

4

Abstract

The present thesis work deals with the investigation of the heterogeneous reactions involving nitrate radical (NO_3), dinitrogen pentoxide (N_2O_5) and ozone (O_3) on surrogates of atmospheric mineral dust particles characteristic of the troposphere. An additional investigation of heterogeneous reaction of NO_3 on flame soot was carried out. The goal is to characterize the kinetics (the uptake coefficient γ) as well as the reaction products. The obtained results are intended to provide reliable data for numerical modelling studies. The experiments were performed in a very low pressure flow reactor (Knudsen cell reactor), coupled to mass spectrometry (MS) and optical probing (Resonance Enhanced Multiphoton Ionization (REMPI)).

The used mineral dust powder samples were: Kaolinite, $CaCO_3$, natural limestone, Saharan Dust and Arizona Test Dust. Two different types of soot were produced: soot originating from a rich decane flame at a high fuel/oxygen ratio ('grey' soot) and soot generated from a lean flame at a low fuel/oxygen ratio ('black' soot).

Uptake experiments of NO_3 on mineral dust were carried out under continuous molecular flow conditions (*steady state*) at 298 ± 2 K using the thermal decomposition of N_2O_5 as a NO_3 source. *In situ* laser detection (REMPI) was employed in addition to beam-sampling electron-impact mass spectrometry in order to specifically detect NO_2 and NO in the presence of N_2O_5, NO_3 and HNO_3. We found a steady state uptake coefficient γ_{ss} ranging from $(3.4 \pm 1.6) \times 10^{-2}$ for natural limestone to 0.12 ± 0.08 for Saharan Dust with γ_{ss} decreasing as $[NO_3]$ increased. NO_3 adsorbed on mineral dust led to uptake of NO_2 in an Eley-Rideal mechanism where usually no uptake is observed in the absence of NO_3. The disappearance of NO_3 was in part accompanied by the formation of N_2O_5 and HNO_3 in the presence of NO_2. NO_3 uptake performed on small amounts of Kaolinite and $CaCO_3$ led to formation of some N_2O_5 according to $NO_{3(ads)} + NO_{2(g)} \rightarrow N_2O_{5(ads)} \rightarrow N_2O_{5(g)}$. Slow formation of gas phase HNO_3 on Kaolinite, $CaCO_3$, Arizona Test Dust and natural

limestone has also been observed and is clearly related to the presence of adsorbed water involved in the heterogeneous hydrolysis of $N_2O_{5(ads)}$.

Uptake of N_2O_5 on mineral dust samples led to γ_{ss} values ranging from $(3.5 \pm 1.1) \times 10^{-2}$ for $CaCO_3$ to 0.20 ± 0.05 for Saharan Dust with γ_{ss} decreasing as $[N_2O_5]_0$ increased. We have observed delayed production of HNO_3 upon uptake of N_2O_5 for every investigated sample owing to hydrolysis of N_2O_5 with surface-adsorbed H_2O. At high and low $[N_2O_5]$ Arizona Test Dust and Kaolinite turned out to be the samples to produce the largest amount of gas phase HNO_3 with respect to N_2O_5 taken up. In contrast, the yield of HNO_3 for Saharan Dust and $CaCO_3$ is lower. On $CaCO_3$ the disappearance of N_2O_5 was also accompanied by the formation of CO_2. For $CaCO_3$ sample masses ranging from 0.33 to 2.0 g, the yield of CO_2 was approximately 42 - 50% with respect to the total number of N_2O_5 molecules taken up. The reaction of N_2O_5 with mineral dust and the subsequent production of gas phase HNO_3 leads to a decrease in $[NO_x]$ which may have a significant effect on global ozone decrease.

The rate of uptake of ozone on various mineral dust substrates was very similar for all the examined substrates. Both initial and steady state uptake coefficients γ_0 and γ_{ss} were found to be similar for all examined substrates. Uptake experiments on cut marble samples have shown that γ_0 and γ_{ss} based on the geometric and total internal (BET) surface area may be over and underestimated between a factor of 50 to 100, respectively. Based on these considerations we proposed initial and steady state uptake coefficients of the order of 10^{-4} and 10^{-5}, respectively. For all uptake experiments on mineral dust surrogates, the disappearance of O_3 was accompanied by formation of O_2. The different mineral dust surrogates may be more accurately distinguished by their time-dependent relative O_2 yield rather than the magnitude of γ. The heterogeneous reaction of O_3 on mineral dust has been found to be non-catalytic and of limited importance in the atmosphere.

Uptake experiments of NO_3 on decane flame soot led to a large steady state uptake coefficient γ_{ss} of 0.2 ± 0.02 for grey and black soot with γ_{ss} decreasing as $[NO_3]$ increased. Adsorbed NO_3 led to an uptake of NO_2 admitted from the hot NO_3 source. On large quantities of grey soot we observed production of HONO (nitrous acid) corresponding to almost 100% of NO_2 taken up, whereas no HONO was formed on black soot. The disappearance of NO_3 was in part accompanied by the formation of N_2O_5 according to reaction: $NO_{3(ads)} + NO_{2(ads)} \rightarrow N_2O_{5(ads)} \rightarrow N_2O_{5(g)}$ probably due to the presence of

adsorbed NO_3 on the substrate. Subsequently, hydrolysis of $N_2O_{5(ads)}$ with adsorbed H_2O led to production of gas phase HNO_3. For both grey and black soot we observed production of NO which did not depend of the amount of soot and [NO_3]. Decomposition of NO_3 and HONO on the soot substrates has been proposed to be responsible of gas phase NO formation.

Versione breve

Il presente lavoro di tesi verte sullo studio di reazioni eterogenee di radicale nitrato (NO_3), pentossido d'azoto (N_2O_5) e ozono (O_3) su surrogati di particelle di polvere minerale atmosferica. Un ulteriore studio e' stato svolto sull'interazione eterogenea di NO_3 su fuligine generata da una fiamma. Lo scopo e' di caratterizzare la cinetica (tramite il coefficiente di cattura, γ) cosi' come i prodotti di reazione. I risultati ottenuti vogliono costituire una base reale di dati per gli studi di modellizzazione numerica.

Gli esperimenti sono stati eseguiti in un reattore a bassa pressione (il reattore di Knudsen) accoppiato a uno spettrometro di massa (MS) e ad un sistema di rilevamento ottico (Resonance Enhanced Multiphoton Ionization (REMPI)).

I campioni di polvere minerale impiegati sono stati i seguenti: Kaolinite, $CaCO_3$, natural limestone, Saharan Dust e Arizona Test Dust. Due differenti tipi di fuligine sono stati prodotti: fuligine prodotta da una ricca fiamma alimentata a decano e mantenuta con un elevato rapporto combustibile/ossigeno ('grey' soot, fuligine grigia) e fuligine prodotta da una debole fiamma e mantenuta con un basso rapporto combustibile/ossigeno ('black' soot, fuligine nera).

Esperimenti di cinetica di cattura di NO_3 su polveri minerali sono stati eseguiti sotto condizioni di regime molecolare stazionario (*steady state*) a 298 ± 2 K usando la decomposizione termica di N_2O_5 come sorgente di NO_3. Una rivelazione laser (REMPI) *in situ* e' stata impiegata in aggiunta alla spettrometria di massa al fine di rivelare specificatamente NO_2 e NO in presenza di N_2O_5, NO_3 e HNO_3.

Abbiamo trovato coefficienti di cattura stazionaria γ_{ss} che vanno da $(3.4 ± 1.6) \times 10^{-2}$ per natural limestone a $0.12 ± 0.08$ per Saharan dust con γ_{ss} decrescente all'aumentare della concentrazione di NO_3. NO_3 adsorbito sulle polveri minerali porta alla cattura di molecole di NO_2 seguendo un meccanismo Eley-Rideal dove usualmente alcuna cattura e' osservata nell'assenza di NO_3. La disparizione di NO_3 e' stata in parte accompagnata dalla formazione di N_2O_5 e HNO_3 in presenza di NO_2. Esperimenti di

cinetica di cattura di NO_3 eseguiti su piccole quantita' di Kaolinite e $CaCO_3$ hanno portano alla formazione di N_2O_5 in accordo con la reazione $NO_{3(ads)} + NO_{2(g)} \rightarrow N_2O_{5(ads)} \rightarrow N_2O_{5(g)}$. Una lenta formazione di HNO_3 in fase gassosa su Kaolinite, $CaCO_3$, Arizona Test Dust e natural limestone e' stata anche osservata ed e' chiaramente legata alla presenza di acqua adsorbita che a sua volta ha portato all'idrolisi eterogenea di $N_2O_{5(ads)}$.

Esperimenti di cinetica di cattura di N_2O_5 su campioni di polvere minerale hanno portato a valori di γ_{ss} che vanno da $(3.5 \pm 1.1) \times 10^{-2}$ per $CaCO_3$ a 0.20 ± 0.05 per Saharan Dust con γ_{ss} decrescente all'aumentare della concentrazione di N_2O_5. Abbiamo osservato una ritardata produzione di HNO_3 in seguito a alla cattura di N_2O_5 per ogni campione analizzato dovuto all'idrolisi di N_2O_5 con H_2O adsorbita sulla superficie. Ad alta e bassa concentrazione di N_2O_5 Arizona Test Dust e Kaolnite si sono rivelati essere i campioni che producono il piu' grande ammontare di HNO_3 in fase gassosa in rapporto a N_2O_5 catturato. In contrasto, la quantita' di HNO_3 per Saharan Dust e $CaCO_3$ e' risultata essere piu' bassa. Su $CaCO_3$ la disparizione di N_2O_5 e' stata anche accompagnata dalla formazione di CO_2. Per campioni di $CaCO_3$ aventi massa tra 0.33 e 2.0 g, la produzione di CO_2 e' stata all'incirca del $42 - 50$ % rispetto al numero totale di molecole di N_2O_5 catturate. La reazione di N_2O_5 con polvere minerale e la conseguente produzione di HNO_3 in fase gassosa porta a una diminuzione nella concentrazione di NO_x che puo' avere un effetto significante sulla decrescita globale d'ozono.

Il coefficiente di cattura dell'ozono sui vari substrati di polvere minerale e' stato misurato molto simile per tutti i campioni esaminati. Sia il coefficiente di cattura iniziale γ_0 che quello a condizioni stazionarie γ_{ss} sono risultati simili per tutti i substrati esaminati. Esperimenti di cinetica di cattura su un campione di marmo hanno mostrato che γ_0 e γ_{ss} calcolati sulla base della superfice geometrica e sulla superficie interna (BET) possono essere sopra e sottostimati di un fattore tra 50 e 100, rispettivamente. Basandosi su queste considerazioni abbiamo proposto un coefficiente di cattura iniziale γ_0 e stazionario γ_{ss} dell'ordine di 10^{-4} a 10^{-5}, rispettivamente. Per tutti gli esperimenti di cinetica di cattura su surrogati di polveri minerali, la disparizione di O_3 e' stata accompagnata dalla formazione di O_2. I differenti surrogati di polveri minerali possono essere piu' accuratamente distinti dalla loro produzione di O_2 piuttosto che dalla grandezza del coefficiente di cattura γ. La reazione eterogenea di O_3 su polveri minerali e' stata trovata non catalitica e di importanza limitata nell'atmosfera.

Esperimenti di cinetica di cattura di NO_3 su fuligine prodotta da una fiamma di decano hanno riportato un grande coefficiente di cattura stazionario γ_{ss} di 0.20 ± 0.05 per fuligine grigia e nera con γ_{ss} decrescente all'aumentare della concentrazione di NO_3. NO_3 adsorbito ha portato a una cattura di NO_2 ammessa dalla sorgente di NO_3. Su grandi quantita' di fuligine grigia abbiamo osservato una produzione di HONO (acido nitroso) corrispondente ad almeno 100 % di NO_2 catturato, mentre alcuna quantita' di HONO si e' formata sulla fuligine nera. La disparizione di NO_3 e' stata in parte accompagnata dalla formazione di N_2O_5 in accordo con la reazione: $NO_{3(ads)} + NO_{2(ads)} \rightarrow N_2O_{5(ads)} \rightarrow N_2O_{5(g)}$ probabilmente dovuta alla presenza di NO_3 assorbito sul substrato. Successivamente, idrolisi di $N_2O_{5(ads)}$ con acqua adsorbita $H_2O_{(ads)}$ ha portato alla produzione di acido nitrico HNO_3 in fase gassosa. Per fuligine grigia e nera abbiamo osservato una produzione di NO che non dipende dalla quantita' di fuligine e dalla concentrazione di NO_3. La decomposizione di NO_3 e HONO su substrati di fuligine e' stata proposta essere responsabile della formazione di NO in fase gassosa.

CHAPTER 1

INTRODUCTION

1.1 The Atmosphere of the Earth

The main constituents of the atmosphere are N_2, O_2, $H_2O_{(g)}$ (water vapor), CO_2, O_3 and suspended particles. In Table 1.1 we report the main constituents of the atmosphere and their lifetimes τ defined as $\tau = M/F$ where M is the amount of chemical species and F the rate of destruction or generation.

Based on its vertical temperature profile the atmosphere is divided into different regions as displayed in Figure 1.1. The two lowest regions are the troposphere and the stratosphere. The troposphere is the atmospheric layer closest to the Earth's surface. Its thickness is variable: 7 km below the poles, 18 km below the equator and 13 km in the temperate areas. The troposphere extends from the surface of the Earth up to the tropopause and contains almost all of the atmosphere's water vapor. Although the troposphere accounts for only a small fraction of the atmosphere's total height, it contains about 80 % of its total mass estimated to be 5.2×10^{18} kg. In the troposphere, the temperature decreases almost linearly with height with a rate of 9.7 K km^{-1}. The reason for this progressive decline is the increasing distance from the sun-warmed earth[1]. At the tropopause, the temperature has fallen to an average of about 217 K (-56°C). As air moves vertically, its temperature changes in response to the local pressure. An air parcel that is transported from the surface to 1 km can decrease in temperature from 5 to 10 K depending on its water content. Because of the strong dependence of the saturation vapor pressure on temperature, this decrease of temperature of a rising parcel can be accompanied by an increase in relative humidity (RH) in the parcel. As a result, upward air motions of a few hundreds of meters can cause the air to reach saturation (RH = 100%) accompanied by the formation of clouds[1].

The troposphere can be divided into the *planetary boundary layer*, extending from the Earth's surface up to about 1 km, and the *free troposphere*, extending from about 1 km to the tropopause.

An important aspect of the atmosphere is the presence of ozone (O_3) in the stratosphere. This plays an important role in the protection of life against solar radiation, particularly, against high energy ultraviolet radiation (UVR) in the region from 290 to 320 nm.
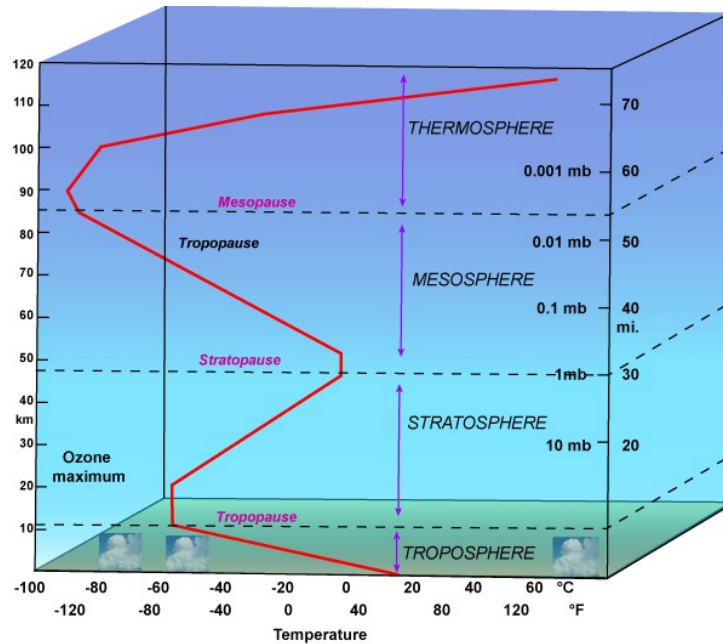
Figure 1.1. Temperature-altitude profile of the atmosphere of the Earth.

Gas	%$_v$	lifetime τ
N_2 (Nitrogen)	78	1.6×10^7 y
O_2 (Oxygen)	21	$3\text{-}10 \times 10^3$ y
Ar (Argon)	0.93	
H_2O (Water)	$0 - 4$	10 d
CO_2 (Carbon Dioxide)	3.3×10^{-2}	3-4 y
Ne (Neon)	1.8×10^{-3}	
He (Helium)	5.2×10^{-4}	10^6 y
CH_4 (Methane)	1.7×10^{-4}	9 y
Kr (Krypton)	1.1×10^4	
N_2O	5.0×10^{-5}	
Xe	8.7×10^{-6}	
O_3	1.0×10^{-6}	100 d

Table 1.1. Main constituents of the atmosphere of the Earth and lifetimes τ of the main components[2].

1.2 Atmospheric pollution

Tropospheric air pollution with examples displayed in Tables 1.2 and 1.3 has an impact on scales ranging from local to global. Reactive intermediates in the oxidation of mixtures of volatile organic compounds (VOCs) and oxides of nitrogen (NO_x) leading to tropospheric O_3 formation play a central role: the hydroxyl radical (OH) during the day; the nitrate radical (NO_3), at night; and ozone (O_3), which reacts both during day and night. Halogen atoms may also play a role during the day in the marine boundary layer.

Gas	Concentration	Lifetime τ
CO_2	350 ppm	3 – 4 y
CH_4	1.7 ppm	9 – 15 y
N_2O	310 ppb	120 y
CFC	100 ppt – 1ppb	> 100 y
O_3	1.0×10^{12} cm^{-3} (40 ppb)	100 d
H_2O		10 d

Table 1.2. Typical concentrations and lifetimes of the most important greenhouse gases[3].

Tropospheric O_3 formation highlights the essential role of solar radiation in atmospheric chemistry. At the Earth's surface, radiation of wavelength $\lambda \geq 290$ nm (actinic region) is available for inducing photochemical reactions. The complex chemistry involving volatile organic compounds (VOCs) and NO_x ($NO_x = NO + NO_2$) leads to the formation of NO_3 among many other species and a large variety of additional oxidizing species such as tropospheric O_3 and PAN ($CH_3C(O)OONO_2$). These oxidizing species are referred to as photochemical oxidants.

Gas	Concentration	Lifetime τ
NO_2	2.4×10^{12} cm^{-3} (100 ppb)	125 s
N_2O_5	5.0×10^9 cm^{-3} (200 ppt)	20 s
NO_3	2.0×10^9 cm^{-3} (100 ppt)	5 s
HNO_3	5.0×10^{10} cm^{-3} (2 ppb) polluted	6.3 d
	2.4×10^9 (100 ppt) background	
$NO_x = NO + NO_2$	10 – 1000 ppb Urban-suburban	1 d^4
	0.2 – 10 ppb Rural	
	0.02 – 0.08 ppb Tropical forest	
	0.02 – 0.04 ppb Remote marine	

Table 1.3. Typical concentrations and lifetimes of the most important nitrogen-containing pollutants[5].

An increase in tropospheric O_3 has been observed globally over the past century[6,7]. The surface concentrations of O_3 found in remote areas of the world are of the order of approximately 30 to 40 ppb as compared to 10 -15 ppb in pre-industrial times since 1850. This increase has been attributed to an increase in NO_x emissions associated with the switch to fossil fuels during the industrial period[8].

The influx of air containing O_3 from the stratosphere contributes to tropospheric ozone. However, the major source of O_3 is represented by the photolysis of NO_2 ($J_{NO_2} = 8.0 \times 10^{-3} s^{-1}$):

$$NO_2 + h\nu \rightarrow NO + O(^3P) \qquad (\lambda < 420 \text{ nm}) \qquad (1.1)$$

followed by

$$O(^3P) + O_2 \xrightarrow{\text{M}} O_3 \qquad (1.2)$$
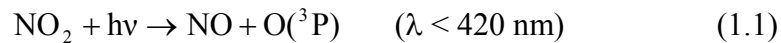
Increased concentrations of O_3 are expected to increase OH concentrations and decreased lifetimes of methane (CH_4). Because both O_3 and CH_4 are greenhouse gases, this chemistry has obvious implications for global climate change.

Nitrogen oxides ($NO + NO_2 = NO_x$) play a major role in ozone production, aerosol formation, and acid deposition. Nearly 50% of NO_x emissions come from motor vehicles. Although some NO_2 is emitted directly into the atmosphere by combustion processes, most is formed by oxidation of NO with ozone:

$$NO + O_3 \rightarrow NO_2 + O_2 \qquad (1.3)$$
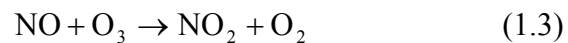
Reaction (1.3) proceeds with a rate constant that depends on temperature, while the photolytic rate constant for reaction (1.1) is a function of the actinic flux. Reaction (1.2) is assumed to proceed very fast at atmospheric pressure.

Once NO is converted to NO_2, a variety of potential reaction paths are available. These include photolysis to form ground-state oxygen atoms, $O(^3P)$, which generate O_3 according to equation (1.2) as well as reaction with OH to form nitric acid (HNO_3) according to:

$$NO_2 + OH \xrightarrow{\text{M}} HNO_3 \qquad (1.4)$$
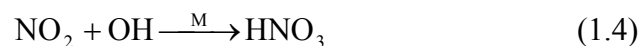
At a sufficiently high concentration of both NO_2 and O_3, the nitrate radical (NO_3) and dinitrogen pentoxide (N_2O_5) are formed as follows:

$$NO_2 + O_3 \rightarrow NO_3 + O_2 \qquad (1.5)$$

$$NO_3 + NO_2 + M \rightarrow N_2O_5 + M \qquad (1.6)$$
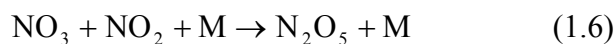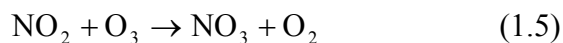
Like OH, NO_3 reacts with organics to initiate their oxidation. NO_3 chemistry is important only at night because it photolyzes rapidly during the day at $\lambda = 662$ nm (lifetime = 5 s). NO_3 has been detected in both polluted and remote regions and can be considered the driving force in the chemistry at night when the photolytic production of OH shuts down[9,10].

As discussed by Andreae and Crutzen[11] and Ravishankara[12], the formation and subsequent hydrolysis of N_2O_5 on wet surfaces, including those of aerosol particles out whose surface water has been adsorbed, is believed to be a significant contributor to the formation of nitric acid in the atmosphere on both local and global scales according to:

$$N_2O_5 + H_2O_{(ads)} \rightarrow 2HNO_3 \qquad (1.7)$$

The rate constant of reaction (1.4) is 4.1 x 10^{-11} cm^3/molecule s, whereas that one for reaction (1.7) is 1.4 x 10^{-14} cm^3/molecule s. Therefore, HNO_3 formation mainly occurs by way of reaction (1.4)[13]. HNO_3 is renoxified by the following two reactions:

$$HNO_3 + OH \rightarrow H_2O + NO_3 \qquad (1.8)$$

$$HNO_3 + h\nu \rightarrow OH + NO_2 \qquad (1.9)$$
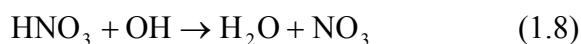
Reaction (1.9) produces NO_2 that may be photolysed producing $O(^3P)$ ultimately leading to O_3 in the atmosphere. However, reaction (1.9) is slow even at noontime in the mid-troposphere corresponding to a J_{HNO_3} value of 7.3 x 10^{-7} s^{-1} and the major removal processes for nitric acid in the troposphere are by dry and wet deposition[14].

Ozone is a source of hydroxyl radical (OH) according to the following equations:

$$O_3 + h\nu \rightarrow O(^1D) + O_2 \quad (\lambda < 320 \text{ nm}) \qquad (1.10)$$

$$O(^1D) + H_2O \rightarrow 2OH \qquad (1.11)$$

$$O(^1D) \xrightarrow{\quad M \quad} O(^3P) \tag{1.12}$$
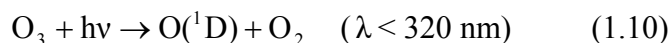
Another important source of OH in polluted atmospheres comes from reaction of O_3 with terpenes and photolysis of nitrous acid (HONO):

$$HONO + h\nu \rightarrow OH + NO \quad (\lambda < 400 \text{ nm}) \tag{1.13}$$
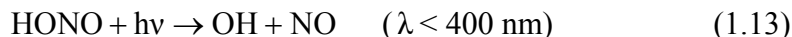
OH reacts rapidly with most air pollutants and trace species found in the atmosphere. However, sources of HONO are not well known. It has been measured in very small concentrations in the exhaust of automobiles that do not have emission catalysts[15,16], inside automobiles during operation[17], and indoors from the emissions of gas stoves[18,19]. There are also heterogeneous sources of HONO [20,21], in particular the following reaction:

$$2NO_2 + H_2O \xrightarrow{\quad surface \quad} HONO + HNO_3 \tag{1.14}$$

However, reaction (1.14) is very slow (6.0×10^{-6} m s^{-1})[19] and so it is of secondary importance for HONO formation.

1.3 Heterogeneous chemistry

The planetary atmosphere contains gases together with liquid and solid particles that all affect the terrestrial radiation field and atmospheric chemical composition. One of the most intense areas of current research in atmospheric sciences is the effect of these particles, natural and anthropogenic, on the radiative balance of Earth[12]. Recently, the importance of heterogeneous chemistry was boosted by the recognition of the crucial role played by the heterogeneous reactions in the dramatic Antarctic ozone hole and the global stratospheric ozone depletion[22]. However, the analysis of tropospheric heterogeneous chemistry is complicated by two factors: (a) rapid mixing in the troposphere which makes it difficult to attribute a change to a specific process, and (b) the variety of condensed matter and gaseous species that can participate in the reactions.

To calculate a heterogeneous reaction rate in the atmosphere we need to know:

- The surface area.
- The phase of the condensed matter.
- The composition of the bulk (for liquids) and the surface (for solids).

- The identity and concentrations of the gas-phase species that can undergo heterogeneous reactions, provided it is a first order process.

- The reactive uptake coefficient γ on the specific substrate under atmospheric conditions for the reaction.

The simplest way to include heterogeneous reactions in atmospheric models is to represent the loss of a reactant M from the gas phase as a result of reaction to generate a product Y as a first-order process:

$$M \xrightarrow{\text{heterogenous}, k_{het}} Y \qquad\qquad (1.15)$$

where k_{het} is the rate constant (s^{-1}). Such a rate law is often found as the rate of temporal change of the gas-phase concentration of reactant M in the presence of the condensed phase substrate will be first order in many, but not all cases:

$$-\frac{d[M]}{dt} = \frac{d[Y]}{dt} = k_{het}[M] \qquad\qquad (1.16)$$

where t is the reaction time and the square brackets indicate concentration. The first-order rate constant for removal of M from the gas phase, k_{het}, contains all the information on the heterogeneous reaction and is given by equation (1.17):

$$k_{het} = \frac{\bar{c}A\gamma}{4} \qquad\qquad (1.17)$$

where A is the surface to volume ratio or surface concentration ($cm^2 \ cm^{-3}$) for reactions in air, $\bar{c}$ is the mean molecular speed of species M, and γ is the reactive uptake coefficient. The determination of γ based on the measurement of k_{het} for any given atmospheric condition is one of the most important efforts in current atmospheric heterogeneous research[12]. Among the suspended material in the troposphere, *condensed water* is likely to be predominant. However, *sulphuric acid droplets, sea salt particles, soot, silicates, and organic aerosols* also provide media for important transformations via heterogeneous processes.

1.4 Total Aerosol Load and Mineral Dust Aerosols

	Estimated Flux (Tg yr^{-1})	Particle Size Category[a]
Source		
Primary		
Natural		
Soil dust (mineral aerosol)	1500	Mainly coarse
Sea salt	1300	Coarse
Volcanic dust	30	Coarse
Biological debris	50	Coarse
Secondary		
Sulfates from biogenic gases	130	Fine
Sulfates from volcanic SO_2	20	Fine
Organic matter from biogenic VOC	60	Fine
Nitrates from NO_x	30	Fine and coarse
Total natural	3100	
Anthropogenic		
Primary		
Industrial dust, etc. (except soot)	100	Fine and coarse
Soot	10	Mainly fine
Secondary		
Sulfates from SO_2	190	Fine
Biomass burning	90	Fine
Nitrates from NO_x	50	Mainly coarse
Organics from anthropogenic (VOC)	10	Fine
Total anthropogenic	450	
Total	3600	

[a]Coarse and fine size categories refer to mean particle diameter above and below 1 μm, respectively.
Note: Sulfates and nitrates are assumed to occur as ammonium salts. Flux unit: Tg yr^{-1} (dry mass).
1 Tg = 10^{12} g.

Table 1.4. Main sources of aerosol in the atmosphere.

Aerosols are small (sub-micron to several microns) particles in suspension in the atmosphere. They can be in the solid phase or in the liquid phase and originate both from natural and man-made (anthropogenic) sources[23]. Aerosols can be directly emitted as particles (primary aerosols) into the atmosphere by volcanoes, through the effect of wind

lifting dust particles in arid regions, from combustion during biomass burning, from sea spray and from oxidative processes of vegetation. They can also be the result of chemical reactions (secondary aerosols). Table 1.4 summarizes the main sources of aerosols expressed in Tg yr^{-1}. The global atmospheric lifetime (yr) characterizes the time required to turn over the global atmospheric burden. It is defined as the burden (Tg) divided by the mean global sink (Tg/yr) for a gas in steady state (i.e., with unchanging burden).

On a global scale, it is estimated that 10 to 20% of the aerosols can be characterized as anthropogenic. Aerosols represent a reactive surface in the atmosphere for heterogeneous chemical reactions[4]. In the atmosphere particles above > 2.5 μm diameter are mainly natural aerosols such as mineral dust and sea salt. It is estimated that 3.4×10^3 – 1.4×10^4 Tg of aerosols are emitted annually into the atmosphere. These aerosols come from such different sources as sea-salt, wind-blown soils, fossil fuel combustion, biomass burning, and volcanic-eruptions.

Recent modeling studies estimate yearly emission fluxes of mineral dust between 800 and 1500 Tg yr^{-1} [24] whipped up from approximately 33% of the global land surface that is arid and therefore may be a potential source region for atmospheric mineral dust aerosol[25]. Bauer et al.[26] estimated that the effective area of mineral aerosol is equivalent to 30% of the Earth's surface of which 10% may be attributed to Africa. Sea salt aerosols are present in the marine boundary layer[27], while desert dust can be transported by storms from Africa across the Atlantic all the way to the east coast of the United States[28].
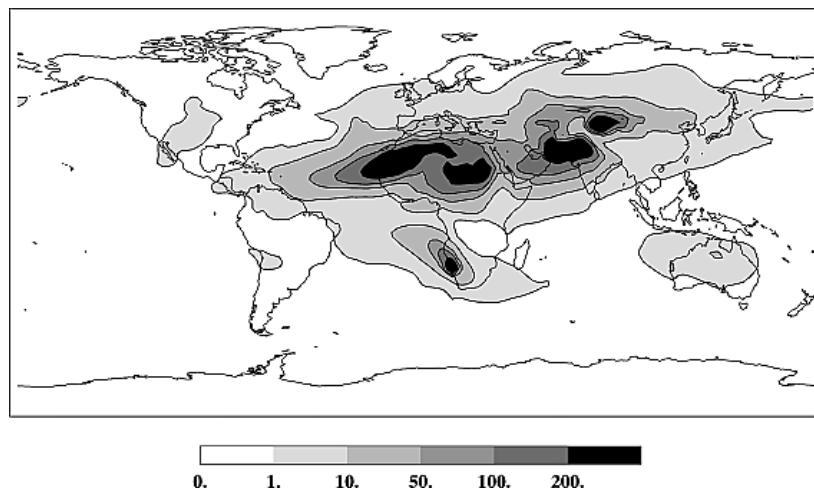
Figure 1.2. Annual mean average column dust (mg m^{-2})[29].

Figure 1.2 shows the horizontal distribution of the annual load of mineral dust[29]. The North African dust cloud covers the whole North African continent, travels over the tropical Atlantic and dust loads of approximately 10 mg m^{-2} are found over the coast of the South American continent. High dust loads are predicted over Pakistan, India and east China and downwind of those regions.

Although dust sources are unevenly distributed across the earth, evidence that they have global effects comes from satellite data that deliver optical depth images of dust blowing for instance from the Saharan desert all the way to the south-eastern US [30] during spring and summer as displayed in Figure 1.3.
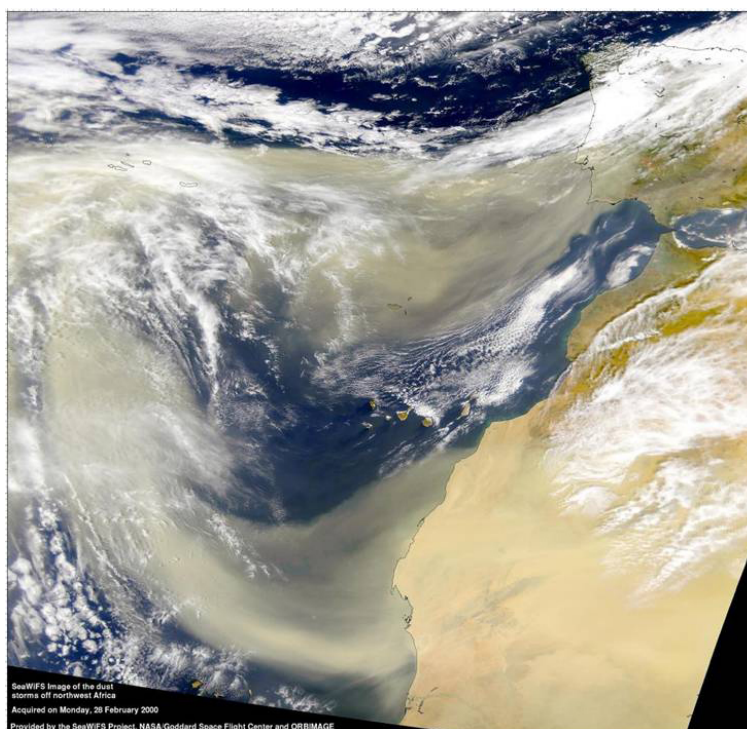
Figure 1.3. Dust plume from northwest Africa extending out over the Atlantic Ocean. Images courtesy Jeffrey Schmaltz and Jacques Descloitres, MODIS Rapid Response Team, NASA GSFC. An intense African dust storm sent a massive dust plume westward over the Atlantic Ocean March 2, 2003.

Atmospheric aerosols can cool or warm the atmosphere directly by absorption and scattering of solar and terrestrial radiation and they can change the optical properties of clouds through modification of the distribution of cloud condensation nuclei (CCN) [31]. The presence of mineral dust aerosols may also affect the photochemical reaction rates as well[32-35]. Mineral dust aerosols are recognized to have an important influence on atmospheric composition[12,36] because they provide reactive surfaces in the atmosphere

where heterogeneous chemical reactions may take place. Trace gases such as HNO_3 and N_2O_5 contribute to the formation of particulate nitrate on the dust particles by surface processes in the troposphere[14,37]. These processes represent an important sink for nitrogen oxide species, with decreases of daytime NO_y levels reaching up to 60 % in the presence of dust at a loading of about 1.8-11.5 $\mu g\ m^{-3}$ corresponding to a particle surface area of (0.11-0.7) x $10^{-6}\ cm^2\ cm^{-3}$.

Field observations[38,39], laboratory[40-44] and modeling studies[14,29,45-47] have established the interaction of trace gases with mineral dust aerosol, as schematically represented in Figure 1.4, as well as the quantitative impact of the latter on the composition of the atmosphere. Box, regional and global scale models have shown the importance of dust on both the photochemical rates of oxidant formation as well as the loss of trace gases regarding atmospheric composition.
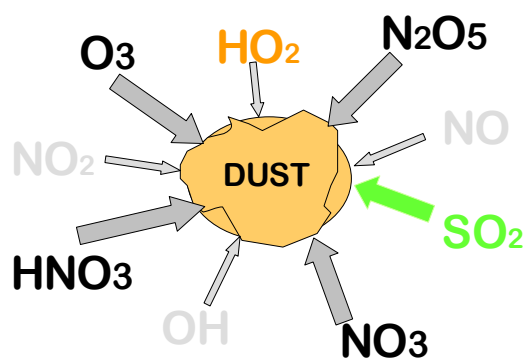
Figure 1.4. Simultaneous uptake of trace atmospheric gases on mineral dust.

Mineral dust has been found up to a height of 8 km [27]. The atmospheric residence time of mineral dust depends on the meteorological conditions and on the aerosol size. For example particles with a diameter of 100 μm are only found close to the source regions, whereas small particles of 2 μm diameter can stay in the atmosphere for several days and may travel for long distances[47].

Aerosols can also influence gas phase chemical cycles by absorbing and scattering of sun light and thus influencing the photochemical reaction rates (J values)[32]. Bian and Zender[46] showed the change of $J_{O(^1D)}$ and J_{NO_2} for $O(^1D)$ and NO_2, respectively, in a recent model.

The maximum photolytic rate forcing by dust on O_3 and OH, the key tropospheric oxidants, has been found in dust source regions in the boundary layer. Photolysis rate forcing has been shown to produce more O_3 with a global annual perturbation of 0.23 %. Dust absorption reduces photochemistry and hence this leads to an increase or decrease of $[O_3]$

depending on the availability of NO_x [33]. The radiative effect of aerosols is currently one of the most active areas in climate research. Aerosols influence the Earth's radiative balance directly by scattering incoming shortwave radiation back to space, or indirectly through their influence on cloud properties. The indirect effect is considered to be one of the largest uncertainties in current global climate models. There are several indirect ways in which aerosols influence the radiative balance of the Earth:

- The reflectivity of clouds through the cloud albedo.

- Perturbation of precipitation processes.

- Change of the initial droplet size distributions produced close to cloud base, and subsequent change of the effectiveness of coalescence of atmospheric aerosol particles at a later stage of cloud development through changing of the spread in drop sizes.

- Modification of freezing processes in mixed-phase clouds. Both of these two latter mechanisms (coalescence and freezing) influence precipitation development.

Precipitation is a key component in determining the lifetime and extent of clouds. It also is a key component in the atmospheric energy balance through the redistribution of latent heat. These phenomena are illustrated in Figure 1.5. The left panel represents a clean (background) case with a given cloud albedo, extent, precipitation intensity and dynamic structure.
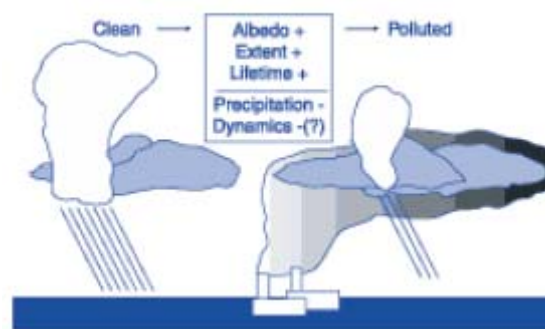
Figure 1.5. Schematic representation of the indirect effects of aerosols.

The right panel depicts the case where all of the indirect effects of aerosols act at the same time. In the polluted case, cloud albedo has increased. Precipitation has decreased due to changes in cloud microphysics as well as a weakening in the overall dynamic driving force

for convection. The rectangle in the middle of Figure 1.5 indicates the expected sign of the indirect effect (increase or decrease) in going from clean to polluted conditions. The first to be recognized was the albedo or "Twomey" effect which is the increase in cloud albedo due to an increase in aerosol concentration. On average, mineral dust contributes more than 60% of total optical depth in dusty regions, 15% in urban regions, and up to 10% in the remote Southern Hemisphere[48]. For a dynamic forcing that creates a cloud with a given vertical extent and liquid water content, an increase in aerosol concentration going into the cloud can result in the formation of a larger number of smaller droplets and therefore in cloud condensation nuclei (CCN). The end result is in an increase in cloud albedo[49]. On the whole, however, increasing aerosol concentrations are expected to increase cloud albedo[50]. The same processes that increase cloud albedo in low-level clouds, and subsequently lead to production of more and smaller droplets, tends to decrease the efficiency with which precipitation is formed. If precipitation is suppressed, water that would have been removed from the atmosphere remains aloft and can be transported to other locations before it is deposited to the surface.

1.5 Mineral dust: field measurements

Suitable locations to study the heterogeneous depletion of gaseous species in the presence of mineral dust are the Mount Cimone research Station (Italy) and Izana observatory (Spain). These stations perform measurements on several significant dust episodes each year and most episodes occur during spring and summer. The Monte Cimone station is located in the Mediterranean region in northern Italy south of the Alps and the Po valley and north of the Mediterranean Sea at 44°12'N and 10°22'E. Owing to its altitude, 2165 m above sea level, air masses reflect European continental background conditions in the free troposphere. This measurement site is located at about 1600 km from the Saharan desert. The Izana observatory is part of the World Meteorological Organization (WMO) Global Atmosphere Watch (GAW) network, and is operated by the Spanish Meteorological Institute. This station is located on a mountain ridge on the island of Tenerife at 2360 m above sea level (a.s.l., 28° 18' N, 16° 29' W).

In 2000 a study was initiated on Mineral Dust and Tropospheric Chemistry (MINATROC) in the framework of an EU program on Environment and Climate. This project combines a

study on the molecular level details, field observations and mineral modeling in order to estimate the global significance of heterogeneous reactions on dust. It combines laboratory investigations field measurements and atmospheric chemistry models. In this context the laboratory studies provided mechanistic information on absorption and reaction of atmospheric gases on aerosol surfaces, and the identification of the saturating effect of adsorbed species. The measurement campaign MINATROC took place during 5 weeks in June and July 2000, at Mount Cimone[39] and between 15 July and 15 August 2002 at the Izana observatory[51]. Intensive measurements were carried out between 1 June and 5 July 2000 at Monte Cimone[39]. Aerosols were observed by means of particle sizing instruments, differential mobility analyzer and optical particle counter[52], LIDAR systems[53], and impactor measurements. In addition atmospheric trace gases were measured by Hanke[58], Bonasoni[39] and other personal participating in the MINATROC campaign. Subsequently to this extensive field campaign observations of ozone concentration and PM_{10} (particulate matter less than 10 μm, known as PM_{10}) particle size and mass distribution were carried out until December 2000 by Bonasoni et al.[39]. The long term measurements of coarse aerosol particles, in the size range of 1-2 μm in diameter, are shown in Figure 1.6.
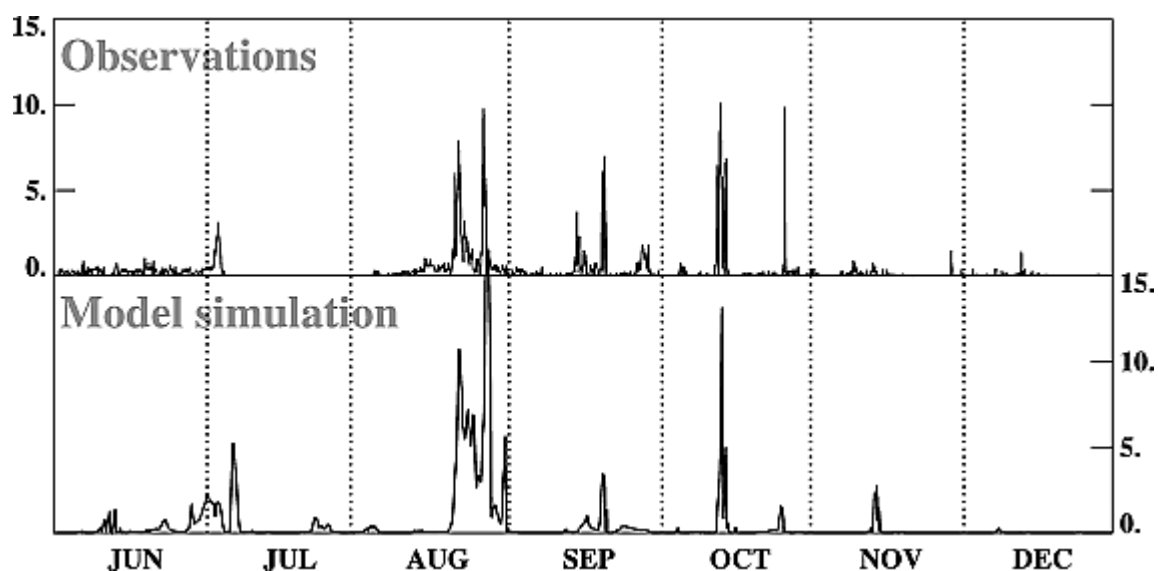
Figure 1.6. Time series of aerosol volume concentrations (size bin 1–2 μm diameter) at Mount Cimone in $\mu m^3\ cm^{-3}$. (top) Observations by Bonasoni et al.[39] (bottom) Model results.

During the MINATROC field campaign airborne Saharan dust reached Mount Cimone at the beginning of July. During this event the volume concentration of particles of 1-2 μm diameters was 3 μm^3 cm^{-3}. Trajectory analysis by Bonasoni et al.[39] showed that all the measured peaks in the coarse aerosol concentrations originate from North Africa. Figure 1.6 compares the observed aerosol concentrations to the model results. Generally, there is good agreement between the observed most prominent dust events and the model simulation, indicating that the model captures dust uplift in the Saharan desert and transport to the Mediterranean region.

As displayed in Figure 1.7, during 3 and 4 July, enhanced coarse aerosol concentrations were observed. The first panel compares measured and model aerosol volume concentrations. The analysis of the aerosol chemical composition[52] showed that the largest contribution of nitrate was observed in air masses originating from Western Europe, whereas the most dominant submicron aerosol mass was made of soot in air masses originating from Eastern Europe. During the Saharan dust outbreak, Saharan dust and anthropogenic particles seemed to be externally mixed.
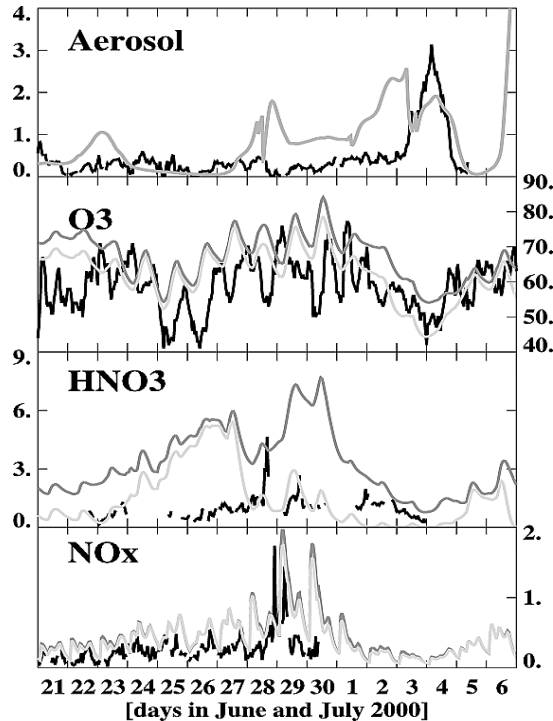
Figure 1.7. (top) Time series of aerosol volume concentrations (size bin 1–2 μm) at Mount Cimone in μm^3 cm^{-3}. The black line shows observations [39], and the grey line shows model results. (bottom) Time series of ozone, HNO$_3$, and NO$_x$ concentrations in ppb$_v$ [39], [54], [55], respectively. The black line is observations, the dark grey line is the model CTR simulation, and the light grey line is the HET simulation.

The episode shown in Figure 1.7, 21 June to 6 July, was influenced during the first days until 23 June, by Eastern European air masses. In the following day the air masses came from Western Europe. Polluted air reached the measurement site at the end of June. This event can clearly be seen in the NO_x measurement time series[55]. As displayed in Figure 1.7 (third panel), HNO_3 concentrations are lower, that is between 0.2 to 1.2 ppbv, and increase to 2 ppbv before the pollution event. Around 2 July, before the dust event, about 1 ppbv of HNO_3 is measured. During the dust event, HNO_3 is strongly reduced and very low concentrations are measured. The ozone measurements (Figure 1.7, second panel) show that the low concentrations at 25 and 26 June are related to the arrival of Mediterranean air. The highest pollution levels are observed for air masses spending most of their time in the continental boundary layer over NW Europe and arriving between 27 and 30 June. Ozone decreases by about 20 ppbv and increases immediately after the dust event. Following the models, 80 % of ozone reduction occurring during the dust event can be explained by transport of ozone poor air from desert and 20 % by heterogeneous chemical reactions.

1.6 Mineral dust characterization

In order to make a link between the mineral dust samples used in the present work and the real composition of the mineral dust collected during dust episodes, we want to refer to a recent field campaign[56]. A strong African dust episode affected the Canary Islands from 28 to 31/07/02 and has been characterised at the Izana Observatory (IZO) in the free troposphere (FT), and Sta. Cruz de Tenerife (SCO), in the Marine Boundary Layer (MBL). The IZO station is normally unaffected by local and regional pollution sources in contrast to the SCO station located in the MBL that is most often under the direct influence of local anthropogenic emissions related to traffic and harbour activities. Therefore, using data from IZO it has been possible to characterize the Saharan dust with minor or no interference of other pollutants. Levels of TSP, and PM10, PM 2.5 and PM1 were monitored at IZO by means of an optical particle counter. The mineralogic characterisation of TSP (total suspended particles) was carried out by X-ray diffraction (XRD) analysis using a powder diffractometer[56].

Semiquantitative concentrations of major mineral phases identified by XRD in TSP samples collected at IZO (top) and at SCO (bottom) are shown in Table 1.5. Quartz is the major mineral phase identified at both sites (23%). As regards clay minerals, the presence of Illite, Paligorskite, Kaolinite and Clinochlore was identified at both sites in similar proportions. The clay minerals accounted for 47 % of TSP mass at IZO and 42 % at SCO. Calcite was estimated to be present to the extent of 9 % of TSP at IZO, and only of 6 % at SCO. By contrast, gypsum contents were lower at IZO (3.5 %) than at SCO (10%). The presence of Halite (NaCl, related to the marine aerosol) has only been detected at SCO (2%)[56].

		Izana	Sta. Cruz
		%	%
Clay minerals			
Paligorskite	$Mg_5(Si,Al)_8O_{20}(OH)_2.8H_2O$	10	9
Illite	$(KH_3O)Al_2Si_3AlO_{10}(OH)_2$	15	13
Kaolinite	$Al_2Si_2O_5(OH)_4$	14	10
Cinochlore	$(Mg,Fe)_6(Si,Al)_4O_{10}(OH)_8$	8	9
Feldspars			
Albite	$NaAlSi_3O_8$	5	5
Microcline	$KAlSi_3O_8$	4	5
Quartz	SiO_2	23	23
Calcite	$CaCO_3$	9	6
Halite	NaCl	0	2
Gypsum	$CaSO_4.2H_2O$	3.5	10
Mascagnite	$(NH_4)_2SO_4$	6	5

Table 1.5. Semiquantitative concentrations of major mineral phases identified in TSP in samples collected at Izana and Sta. Cruz. (2002).

SEM images of TSP sampled at IZO and SCO during 29 July 2002 (Figure 1.8) confirmed the results obtained by XRD.

The majority of African dust collected at IZO are made up of clay minerals and quartz (Figure 1.8, a). The clay particles may be grouped into two sub-groups: (a) typical large

(usually > 10μm) and flat clay mineral crystals (Figure 1.8, c), and (b) small aggregates of micro-crystals (approximately 1μm) of clay minerals (Figure 1.8, c).
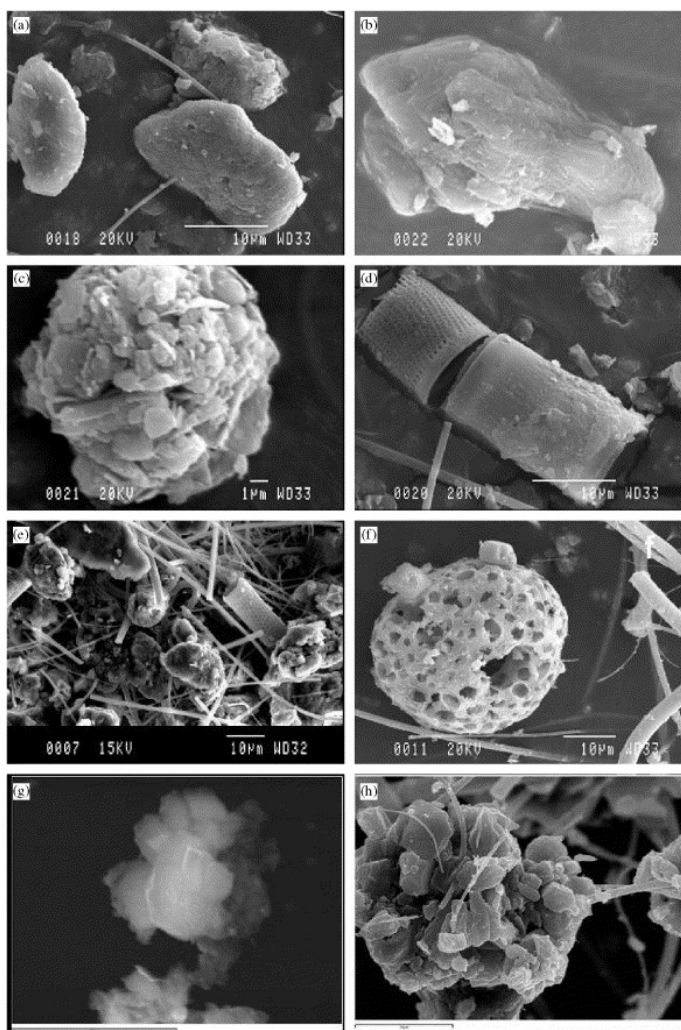
Figure 1.8. SEM microphotographs of TSP collected on 29th July 2002 at IZO (a–d) and at SCO (e–h). IZO: (a) rounded quartz; (b) large (>10 μm) plate clay particles; (c) aggregates of micro-crystals of clay minerals; (d) silica skeletons of fresh water diatom from the *Melosira* genus, present in lakes or ponds from Northern Africa. SCO: (e) general aspect showing the presence of mineral dust, marine aerosol and *Melosira* genus diatoms, coated with sulphate; (f) spongy carbonaceous particles with sodium chloride crystals from marine aerosol; (g) K/Ca sulphate coating clay aggregates and (h) <5 μm Ca sulphate particles with crystalline habit[56].

The EDAX analysis did not show any compositional difference between these two types of clay particles, both containing Si and Al with minor proportions of Fe, K and Mg. The presence of quartz (SiO_2) and other silicate particles was also very frequent[56].

Similar findings were made in TSP at SCO (Figure 1.8, e) although a high proportion of natural marine aerosols and spongy carbonaceous anthropogenic particles were also present (Figure 1.8, f). Sulphate submicron particles associated with other particles (carbonate, clays) forming aggregates of total diameter 10µm were also observed (Figure1.8, g, h).

1.6 Soot particles

Soot consists of partially burned carbon produced under fuel rich conditions. 90% of soot particles come from the consumption of fossil fuels, particularly Diesel fuel, coal, jet fuel, natural gas and kerosene, as well as the burning of wood and other biomass. Under ideal conditions the combustion of hydrocarbons exclusively leads to carbon dioxide CO_2 and H_2O. Ideal conditions means that the oxygen content of the mixture everywhere is sufficient to oxidize the fuel completely according to equation (1.17):

$$C_xH_y + (x + y/4)O_2 \rightarrow xCO_2 + y/2H_2O \qquad (1.17)$$
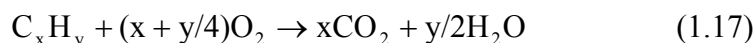
Under these conditions the maximum of heat is released and a minimum of chemical energy is available for mechanical work. Practical combustion deviate from ideal conditions; if the local oxygen concentration is not sufficient to oxide the fuel according to equation (1.17) other products of incomplete combustion such as carbon monoxide (CO), hydrocarbons and soot appear. The terms "soot" and black carbon "BC" are often referred to designate carbonaceous particles. Soot is related to primary combustion generated carbonaceous aerosols, whereas BC is used to point out the light-absorbing property of carbonaceous particles[57]. Its reactive surface is likely to be irreversibly affected by O_2 and other species. Therefore, soot may play a special role only if its surface remains active[12].

Soot is formed through different chemical and physics processes such as the formation and growth of large hydrocarbons and their aggregation to particles[58]. In addition, it may serve as cloud nucleation nuclei (CCN) for aerosols, for example, in the wake of aircraft engines[59].

Soot particles are mainly composed of amorphous carbon or black carbon but may contain a significant quantity (up to 50% of the soot particle mass) of hydrocarbons as a bulk phase or adsorbed on the particle surface[60]. This organic fraction may play a significant role in the reactivity of soot and may take an active part in the formation of secondary reaction products such as HONO according to equation (1.18):

$$NO_2 + \{C-H\}_{red} \rightarrow HONO + \{C\}_{ox} \qquad (1.18)$$
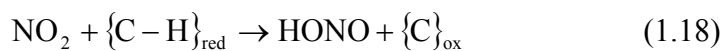
Soot aerosols present in polluted atmospheres may have typical sizes of 10 to 50 nm and a lifetime of several days up to tens of days before being precipitated to the ground by rain. Meanwhile, they are strongly suspected to partake actively in physico-chemical reactions with gaseous pollutants such as HNO_3, NO_2 and O_3 [61-64] and therefore reduce oxidized species in the atmosphere.

Novakov T. et al.[65] presented estimates of black carbon emissions from the United States, United Kingdom, Germany, Soviet Union, India and China for the period from 1875 to the present. These countries are the major producers of coal and diesel fuel, which are the principal black carbon-producing fuels. The concentration of black carbon is variable: 800 ng/m^3 in continental rural regions[66], 40 ng/m^3 in the Arctic[67] and 20 ng/m^3 in the remote oceanic regions[68,69]. Black carbon is of special interest because it absorbs sunlight, heats the Earth's atmosphere, and contributes to global warming that might accelerate the greenhouse effect, unlike most aerosols, which reflect sunlight to space and have a global cooling effect.

Because soot particles are the principal light-absorbing atmospheric aerosol, any analysis or prediction of climate variability must include an accurate inventory of this species. Because both absorbing BC aerosols and reflective aerosols reduce the amount of sunlight reaching the ground it should tend to cause local cooling on the earth's surface, in contrast to greenhouses gases which trap heat in earth's atmosphere.

As a very recent example of soot emission a study on the characterization of different types of carbonaceous particles in smoke and its aging behaviour was reported[70,71]. In that study individual aerosol particles in smoke plumes from biomass fires and in regional hazes in southern Africa were studied using analytical transmission electron microscopy (TEM). Based on these analyses, three distinct types of carbonaceous particles were present in the smoke: organic particles with inorganic (K-salt) intrusion, "tar ball" particles, and soot

(Figures 1.9 and 1.10)[70,71]. The relative concentrations of organic particles were largest in young smoke, whereas tar balls were dominant a slightly aged (~1 hour) smoke from a smoldering fire. Further aging caused the accumulation of sulphate on organic soot particles. In addition, large aggregates of calcium-bearing particles were present in the aged smoke samples, and the length of the aggregates ranged from 2 to 15 μm. The calcium-bearing particles were very fine grained, with diameter ranging from 50 to 300 nm, although some were up to 500 nm large (Figure 1.10)[71]. These particles included the carbonaceous minerals aragonite and calcite, sulphate (gypsum) and phosphate in the form of apatite.
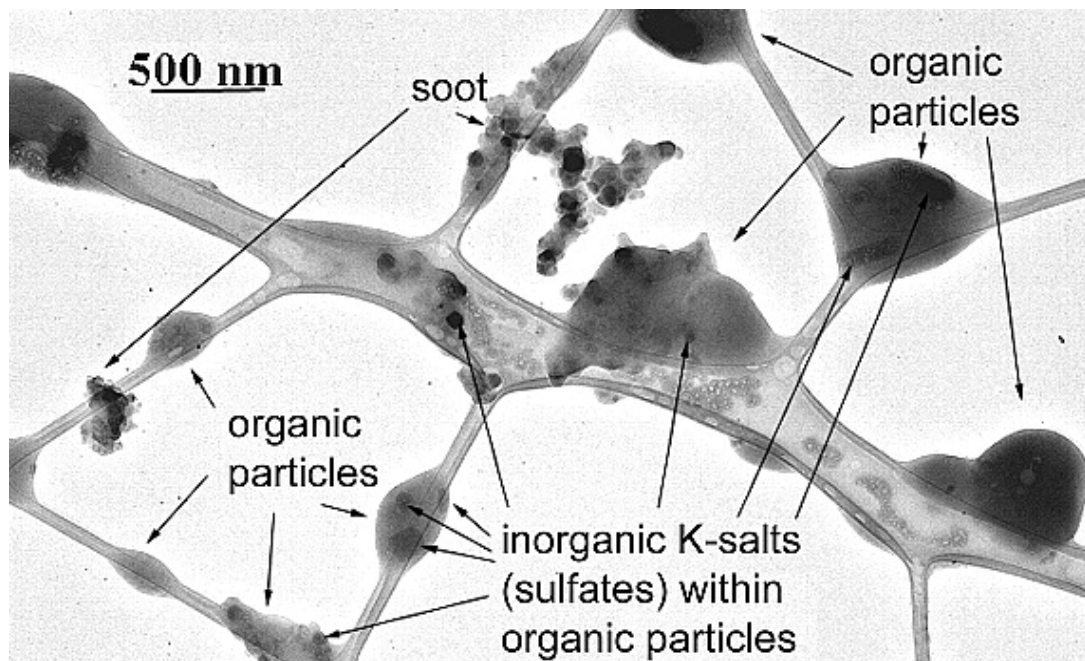
Figure 1.9. TEM image of a typical portion of a sample of young smoke from a flaming fire. Particles are attached to the lacy support film; most particles are carbonaceous (organic) with inorganic K-sulphate inclusions[70].
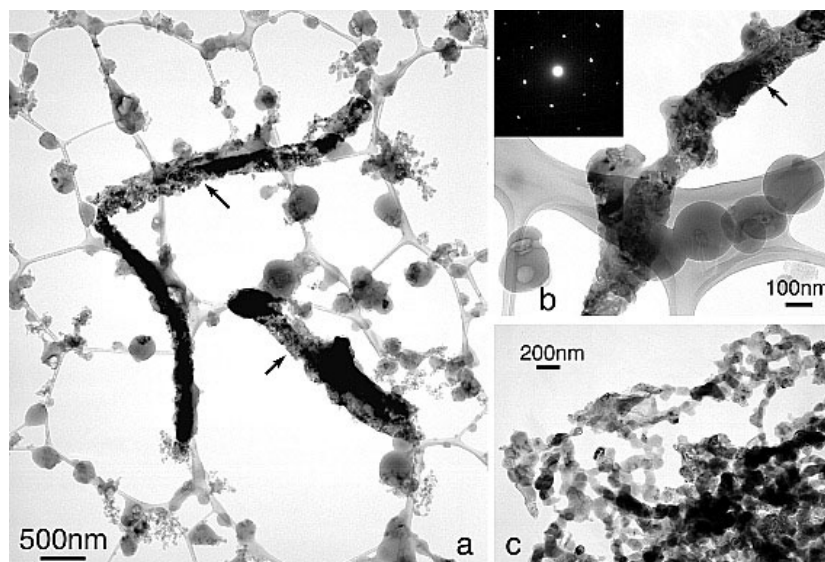
Figure 1.10. TEM images of aggregates of calcium-rich particles. (a) Large aggregates of fine calcium sulfate from a fire from Zambia. (b) Calcium carbonate particles aggregated with tar balls in aged smoke 8 to 38 km downwind of the fire. (c) $CaCO_3$ particles and aragonite crystals[71].

1.7 Motivation for the present work

Despite the published results of field observations and modeling studies[38,39,46,47], there are only few reports on laboratory experiments that deal with the heterogeneous reactivity of NO_3 and N_2O_5 on mineral dust aerosol surrogates and soot substrates. Only a very recent laboratory study has been performed with N_2O_5 on Saharan Dust using a combination of Knudsen flow reactors and DRIFTS[72]. We have therefore embarked on a laboratory program to measure some of the heterogeneous reactions involving N_2O_5 and NO_3 [73] as relevant trace atmospheric gases. In the present work, we have used a Knudsen flow reactor in order to investigate the uptake and reaction of O_3, NO_3 and N_2O_5 on selected authentic mineral dust samples such as Kaolinite, Saharan Dust from Cape Verde Islands, Arizona test dust and natural limestone as well as on samples of pure $CaCO_3$. Additional work has been carried out on soot samples regarding its heterogeneous interaction with NO_3.

The present thesis work also reports a kinetic study of the heterogeneous reaction of O_3 on mineral dust surrogates presented as powders. Its specific objective was the investigation of the mechanism of adsorption of ozone on surrogates of mineral dust as well as the kinetics of the heterogeneous reaction including reaction products that are released into the gas phase.

1.8 References

(1)   Seinfeld, J. H.; Pandis, S. P.: Atmospheric Chemistry and Physics, John Wiley & Sons, Inc., pp.6-8, (1998).

(2)   Hobbs, P. V.: Introduction to Atmospheric chemistry, Cambridde University Press, pp. 262, (2000).

(3)   WMO: IPCC Second Assessment Climate Change 1995, pp. 63, (1995).

(4)   Dentener, F. J.; Crutzen, P. J.: Reaction of N_2O_5 on Tropospheric Aerosols - Impact on the Global Distributions of NO_x, O_3, and OH, Journal of Geophysical Research-Atmospheres, 98, 7149-7163, (1993).

(5)   Seinfeld, J. H.; Pandis, S. P.: Atmopheric Chemistry and Physics, John Wiley & Sons, Inc., pp. 72-74, (1998).

(6)   Anfossi, D.; Sandroni, S.; Viarengo, S.: Tropospheric Ozone in the 19th-Century - the Moncalieri Series, Journal of Geophysical Research-Atmospheres, 96, 17349-17352, (1991).

(7)   Fishman, J.; Crutzen, P. J.: Origin of Ozone in Troposphere, Nature, 274, 855-858, (1978).

(8)   Finlayson-Pitts, B. J.; Pitts, J. N.: Tropospheric Air Pollution: Ozone, Airborne Toxics, Polycyclic Aromatic Hydrocarbons, and Particles, Science, 276, 1045-1052, (1997).

(9)   Finlayson-Pitts, B. J.; Pitts, J. N.: Atmospheric Chemistry: Fundamentals and Experimental Techniques, Wiley, New York, (1986).

(10)   Atkinson, R.; Winer, A. M.; Pitts, J. N.: Estimation of Nighttime N2o5 Concentrations from Ambient No2 and No3 Radical Concentrations and the Role of N2o5 in Nighttime Chemistry, Atmospheric Environment, 20, 331-339, (1986).

(11)   Andreae, M. O.; Crutzen, P. J.: Atmospheric aerosols: Biogeochemical sources and role in atmospheric chemistry, Science, 276, 1052-1058, (1997).

(12)   Ravishankara, A. R.: Heterogeneous and multiphase chemistry in the troposphere, Science, 276, 1058-1065, (1997).

(13)   Atkinson, R.; Baulch, D. L.; Cox, R. A.; Crowley, J. N.; Hampson, R. F.; Hynes, R. G.; Jenkin, M. E.; Rossi, M. J.; Troe, J.: Evaluated kinetic and photochemical data for atmospheric chemistry: Volume I - gas phase reactions of O-x, HO_x, NO_x and SO_x species, Atmospheric Chemistry and Physics, 4, 1461-1738, (2004).

(14)   Zhang, Y.; Sunwoo, Y.; Kotamarthi, V.; Carmichael, R.: Photochemical Oxidant Processes in the Presence of Dust: An Evaluation of the Impact of Dust on Particulate Nitrate and Ozone Formation., Journal of Applied Meteorology, 33, 813-824, (1994).

(15)   Pitts, J. N.; Biermann, H. W.; Winer, A. M.; Tuazon, E. C.: Spectroscopic Identification and Measurement of Gaseous Nitrous-Acid in Dilute Auto Exhaust, Atmospheric Environment, 18, 847-854, (1984).

(16)   Kirchstetter, T. W.; Harley, R. A.; Littlejohn, D.: Measurement of nitrous acid in motor vehicle exhaust, Environmental Science & Technology, 30, 2843-2849, (1996).

(17)   Febo, A.; Perrino, C.: Measurement of High-Concentration of Nitrous-Acid inside Automobiles, Atmospheric Environment, 29, 345-351, (1995).

(18)   Pitts, J. N.; Biermann, H. W.; Tuazon, E. C.; Green, M.; Long, W. D.; Winer, A. M.: Time-Resolved Identification and Measurement of Indoor Air-Pollutants by Spectroscopic Techniques - Gaseous Nitrous-Acid, Methanol, Formaldehyde and Formic-Acid, Japca-the Journal of the Air & Waste Management Association, 39, 1344-1347, (1989).

(19)   Febo, A.; Perrino, C.: Prediction and Experimental-Evidence for High Air Concentration of Nitrous-Acid in Indoor Environments, Atmospheric Environment Part a-General Topics, 25, 1055-1061, (1991).

(20)   Sakamaki, F.; Hatakeyama, S.; Akimoto, H.: Formation of Nitrous-Acid and Nitric-Oxide in the Heterogeneous Dark Reaction of Nitrogen-Dioxide and Water-Vapor in a Smog Chamber, International Journal of Chemical Kinetics, 15, 1013-1029, (1983).

(21)   Bambauer, A.; Brantner, B.; Paige, M.; Novakov, T.: Laboratory Study of No2 Reaction with Dispersed and Bulk Liquid Water, Atmospheric Environment, 28, 3225-3232, (1994).

(22)   World Meteorological Organization, G., Switzeralnd, 1994.: Scientific assessment of ozone depletio: 1994, world meteorological organization, " *Global Ozone Res. Monit. Proj. Rep. No. 37* (World Meterological Organization, Geneva, Switzeralnd, 1994).

(23)   Seinfeld, J. H.; Pandis, S. P.: Atmospheric Chemistry and Physics, John Wiley &
        Sons, Inc., p. 97, (1998).

(24)   Tegen, I.; Miller, R.: A general circulation model study on the interannual
        variability of soil dust aerosol, Journal of Geophysical Research-Atmospheres, 103,
        25975-25995, 10.1029/98JD02345., (1998).

(25)   Tegen, I.; Fung, I.: Modeling of Mineral Dust in the Atmosphere - Sources,
        Transport, and Optical-Thickness, Journal of Geophysical Research-Atmospheres,
        99, 22897-22914, 10.1029/94JD01928., (1994).

(26)   Bauer, S. E.; Balkanski, Y.; Schulz, M.; Hauglustaine, D. A.; Dentener, F.: Global
        modeling of heterogeneous chemistry on mineral aerosol surfaces: Influence on
        tropospheric ozone chemistry and comparison to observations, Journal of
        Geophysical Research-Atmospheres, 109, art. no.-D02304, (2004).

(27)   Jaenicke, R.: Troposheric aerosols, in *Aerosol-Cloud- Climate Interactions.*, P.V.
        Hobbs. Academic, San Diego, Calif., pp. 1-31, (1993).

(28)   Prospero, J. M.: The atmospheric transport of particles to the ocean, in *Particle Flux
        in the Ocean, Scope Rep. 57.*, John Wiley & Sons, Inc., pp. 19-52, (1995).

(29)   Dentener, F. J.; Carmichael, G. R.; Zhang, Y.; Lelieveld, J.; Crutzen, P. J.: Role of
        mineral aerosol as a reactive surface in the global troposphere, Journal of
        Geophysical Research-Atmospheres, 101, 22869-22889, 10.1029/96JD01818.,
        (1996).

(30)   Schulz, M.; Balkanski, Y. J.; Guelle, W.; Dulac, F.: Role of aerosol size distribution
        and source location in a three-dimensional simulation of a Saharan dust episode
        tested against satellite-derived optical thickness, Journal of Geophysical Research-
        Atmospheres, 103, 10579-10592, (1998).

(31)   Charlson, R. J.; Schwartz, S. E.; Hales, J. M.; Cess, R. D.; Coakley, J. A.; Hansen,
        J. E.; Hofmann, D. J.: Climate Forcing by Anthropogenic Aerosols, Science, 255,
        423-430, (1992).

(32)   Dickerson, R. R.; Kondragunta, S.; Stenchikov, G.; Civerolo, K. L.; Doddridge, B.
        G.; Holben, B. N.: The impact of aerosols on solar ultraviolet radiation and
        photochemical smog, Science, 278, 827-830, (1997).

(33)   He, S.; Carmichael, G. R.: Sensitivity of photolysis rates and ozone production in
        the troposphere to aerosol properties, Journal of Geophysical Research-
        Atmospheres, 104, 26307-26324, 10.1029/1999JD900789., (1999).

(34)   Martin, R. V.; Jacob, D. J.; Yantosca, R. M.; Chin, M.; Ginoux, P.: Global and
        regional decreases in tropospheric oxidants from photochemical effects of aerosols,
        Journal of Geophysical Research-Atmospheres, 108, art. no.-4097,
        doi:10.1029/2002JD002622., (2003).

(35)   Liao, H.; Adams, P. J.; Chung, S. H.; Seinfeld, J. H.; Mickley, L. J.; Jacob, D. J.:
Interactions between tropospheric chemistry and aerosols in a unified general
circulation model, Journal of Geophysical Research-Atmospheres, 108, art. no.-
4001, doi:10.1029/2001JD001260, (2003).

(36)   Jacob, D. J.: Heterogeneous chemistry and tropospheric ozone, Atmospheric
Environment, 34, 2131-2159, (2000).

(37)   Seisel, S.; Börensen, C.; Vogt, R.; Zellner, R.: The heterogeneous reaction of HNO_3
on mineral dust and gamma-alumina surfaces: a combined Knudsen cell and
DRIFTS study, Physical Chemistry Chemical Physics, 6, 5498-5508, (2004).

(38)   de Reus, M.; Dentener, F.; Thomas, A.; Borrmann, S.; Strom, J.; Lelieveld, J.:
Airborne observations of dust aerosol over the North Atlantic Ocean during ACE 2:
Indications for heterogeneous ozone destruction, Journal of Geophysical Research-
Atmospheres, 105, 15263-15275, (2000).

(39)   Bonasoni, P.; Cristofanelli, P.; Calzolari, F.; Bonafé, U.; Evangelisti, F.; Stohl, A.;
Sajani, S. Z.; van Dingenen, R.; Colombo, T.; Balkanski, Y.: Aerosol-ozone
correlations during dust transport episodes, Atmospheric Chemistry and Physics, 4,
1201-1215, (2004).

(40)   Usher, C. R.; Michel, A. E.; Grassian, V. H.: Reactions on mineral dust, Chemical
Reviews, 103, 4883-4939, (2003).

(41)   Hanisch, F.; Crowley, J. N.: The heterogeneous reactivity of gaseous nitric acid on
authentic mineral dust samples, and on individual mineral and clay mineral
components, Physical Chemistry Chemical Physics, 3, 2474-2482, (2001 b).

(42)   Hanisch, F.; Crowley, J. N.: Heterogeneous reactivity of gaseous nitric acid on
Al_2O_3, $CaCO_3$, and atmospheric dust samples: A Knudsen cell study, Journal of
Physical Chemistry A, 105, 3096-3106, (2001 a).

(43)   Hanisch, F.; Crowley, J. N.: Ozone decomposition on Saharan dust: an
experimental investigation, Atmospheric Chemistry and Physics, 3, 119-130, (2003
d).

(44)   Hanisch, F.; Crowley, J. N.: Heterogeneous reactivity of NO and HNO_3 on mineral
dust in the presence of ozone, Physical Chemistry Chemical Physics, 5, 883-887,
(2003 c).

(45)   Tabazadeh, A.; Jacobson, M. Z.; Singh, H. B.; Toon, O. B.; Lin, J. S.; Chatfield, R.
B.; Thakur, A. N.; Talbot, R. W.; Dibb, J. E.: Nitric acid scavenging by mineral and
biomass burning aerosols, Geophysical Research Letters, 25, 4185-4188,
10.1029/1998GL900062., (1998).

(46)   Bian, H. S.; Zender, C. S.: Mineral dust and global tropospheric chemistry: Relative
roles of photolysis and heterogeneous uptake, Journal of Geophysical Research-
Atmospheres, 108, 4672, doi:10.1029/2002JD003143., (2003).

(47)   Bauer, S. E.; Balkanski, Y.; Schulz, M.; Hauglustaine, D. A.; Dentener, F.: Global modeling of heterogeneous chemistry on mineral aerosol surfaces: Influence on tropospheric ozone chemistry and comparison to observations, Journal of Geophysical Research-Atmospheres, 109, art. no.-D02304, doi:10.1029/2003JD003868., (2004).

(48)   Kinne, S.; Lohmann, U.; Feichter, J.; Schulz, M.; Timmreck, C.; Ghan, S.; Easter, R.; Chin, M.; Ginoux, P.; Takemura, T.; Tegen, I.; Koch, D.; Herzog, M.; Penner, J.; Pitari, G.; Holben, B.; Eck, T.; Smirnov, A.; Dubovik, O.; Slutsker, I.; Tanre, D.; Torres, O.; Mishchenko, M.; Geogdzhayev, I.; Chu, D. A.; Kaufman, Y.: Monthly averages of aerosol properties: A global comparison among models, satellite data, and AERONET ground data, Journal of Geophysical Research-Atmospheres, 108, (2003).

(49)   Twomey, S.: Pollution and Planetary Albedo, Atmospheric Environment, 8, 1251-1256, (1974).

(50)   Twomey, S.: Influence of Pollution on Shortwave Albedo of Clouds, Journal of the Atmospheric Sciences, 34, 1149-1152, (1977).

(51)   de Reus, M.; Fischer, H.; Sander, R.; Gros, V.; Kormann, R.; Salisbury, G.; Van Dingenen, R.; Williams, J.; Zollner, M.; Lelieveld, J.: Observations and model calculations of trace gas scavenging in a dense Saharan dust plume during MINATROC, Atmospheric Chemistry and Physics, 5, 1787-1803, (2005).

(52)   Putaud, J. P.; Van Dingenen, R.; Dell'Acqua, A.; Raes, F.; Matta, E.; Decesari, S.; Facchini, M. C.; Fuzzi, S.: Size-segregated aerosol mass closure and chemical composition in Monte Cimone (I) during MINATROC, Atmospheric Chemistry and Physics, 4, 889-902, (2004).

(53)   Gobbi, G. P.; Barnaba, F.; Van Dingenen, R.; Putaud, J. P.; Mircea, M.; Facchini, M. C.: Lidar and in situ observations of continental and Saharan aerosol: closure analysis of particles optical and physical properties, Atmospheric Chemistry and Physics, 3, 2161-2172, (2003).

(54)   Hanke, M.; Umann, B.; Uecker, J.; Arnold, F.; Bunz, H.: Atmospheric measurements of gas-phase HNO3 and SO2 using chemical ionization mass spectrometry during the MINATROC field campaign 2000 on Monte Cimone, Atmospheric Chemistry and Physics, 3, 417-436, (2003).

(55)   Fischer, H.; Kormann, R.; Klupfel, T.; Gurk, C.; Konigstedt, R. K.; Parchatka, U.; Muhle, J.; Rhee, T. S.; Brenninkmeijer, C. A. M.; Bonasoni, P.; Stohl, A.: Ozone production and trace gas correlations during the June 2000 MINATROC intensive measurement campaign at Mt. Cimone, Atmospheric Chemistry and Physics, 3, 725-738, (2003).

(56)   Alastuey, A.; Querol, X.; Castillo, S.; Escudero, M.; Avila, A.; Cuevas, E.; Torres, C.; Romero, P. M.; Exposito, F.; Garcia, O.; Diaz, J. P.; Van Dingenen, R.; Putaud, J. P.: Characterisation of TSP and PM2.5 at Izana and Sta. Cruz de Tenerife

(Canary Islands, Spain) during a Saharan Dust Episode (July 2002), Atmospheric Environment, 39, 4715-4728, (2005).

(57)   Penner, J. E.; Novakov, T.: Carbonaceous particles in the atmosphere - Preface, Journal of Geophysical Research-Atmospheres, 101, 19371-19371, (1996).

(58)   Bockhorn, H.: Soot Formation in Combustion: Mechanisms and Models, Springer Verlag, (1994).

(59)   Hallett, J.; Hudson, J. G.; Rogers, C. F.: Characterization of Combustion Aerosols for Haze and Cloud Formation, Aerosol Science and Technology, 10, 70-83, (1989).

(60)   Akhter, M. S.; Chughtai, A. R.; Smith, D. M.: The Structure of Hexane Soot-I - Spectroscopic Studies, Applied Spectroscopy, 39, 143-153, (1985).

(61)   Schurath, U.; Naumann, K. H.: Heterogeneous processes involving atmospheric particulate matter, Pure and Applied Chemistry, 70, 1353-1361, (1998).

(62)   Salgado, M. S.; Rossi, M. J.: Flame soot generated under controlled combustion conditions: Heterogeneous reaction of NO_2 on hexane soot, International Journal of Chemical Kinetics, 34, 620-631, (2002).

(63)   Munoz, M. S. S.; Rossi, M. J.: Heterogeneous reactions of HNO_3 with flame soot generated under different combustion conditions. Reaction mechanism and kinetics, Physical Chemistry Chemical Physics, 4, 5110-5118, (2002).

(64)   Stadler, D.; Rossi, M. J.: The reactivity of NO_2 and HONO on flame soot at ambient temperature: The influence of combustion conditions, Physical Chemistry Chemical Physics, 2, 5420-5429, (2000).

(65)   Novakov, T.; Ramanathan, V.; Hansen, J. E.; Kirchstetter, T. W.; Sato, M.; Sinton, J. E.; Sathaye, J. A.: Large historical changes of fossil-fuel black carbon aerosols, Geophysical Research Letters, 30, (2003).

(66)   Penner, J. E.; Eddleman, H.; Novakov, T.: Towards the Development of a Global Inventory for Black Carbon Emissions, Atmospheric Environment Part a-General Topics, 27, 1277-1295, (1993).

(67)   Bodhaine, B. A.: Aerosol Absorption-Measurements at Barrow, Mauna-Loa and the South-Pole, Journal of Geophysical Research-Atmospheres, 100, 8967-8975, (1995).

(68)   Clarke, A. D.: Aerosol Light-Absorption by Soot in Remote Environments, Aerosol Science and Technology, 10, 161-171, (1989).

(69)   Rau, J. A.; Khalil, M. A. K.: Anthropogenic Contributions to the Carbonaceous Content of Aerosols over the Pacific-Ocean, Atmospheric Environment Part a-General Topics, 27, 1297-1307, (1993).

(70)   Posfai, M.; Simonics, R.; Li, J.; Hobbs, P. V.; Buseck, P. R.: Individual aerosol
       particles from biomass burning in southern Africa: 1. Compositions and size
       distributions of carbonaceous particles, Journal of Geophysical Research-
       Atmospheres, 108, (D13): Art. No. 8483 MAR 8 (2003).

(71)   Li, J.; Posfai, M.; Hobbs, P. V.; Buseck, P. R.: Individual aerosol particles from
       biomass burning in southern Africa: 2, Compositions and aging of inorganic
       particles, Journal of Geophysical Research-Atmospheres, 108, (D13): Art. No. 8484
       MAR 8 (2003).

(72)   Seisel, S.; Börensen, C.; Zellner, R.: Kinetics and mechanism of the uptake of N_2O_5
       on mineral dust at 298 K, Atmospheric Chemistry and Physics Discussions, 5,
       5645-5667, (2005).

(73)   Karagulian, F.; Rossi, M. J.: The heterogeneous chemical kinetics of NO_3 on
       atmospheric mineral dust surrogates, Physical Chemistry Chemical Physics, 7,
   3150, (2005).

CHAPTER 2

EXPERIMENTAL SETUP

The Knudsen flow reactor has been specifically designed for the study of heterogeneous reactions with detection using mass spectrometry (MS) and *in situ* Resonance Enhanced Multiphoton Ionization (REMPI). The Knudsen reactor has been developed more than thirty five years ago for kinetics measurements. It is a low pressure flow reactor that operates under the molecular flow regime. This technique has been applied to the study of chemical kinetic over a wide variety of systems. In the pressure regime of $P_{tot} < 10^{-3}$ Torr, gas wall-collisions are strongly favoured over gas phase collisions; the technique is thus ideally suited for the study of heterogeneous chemistry. The gases under study react with the substrate in the absence of limiting gas phase diffusion, and the collision frequency between the gas and the substrate may be determined using gas kinetics[1].

2.1 The Knudsen flow reactor

The apparatus is displayed schematically in Figure 2.1 [2]. It consists of a vacuum line (4) from which the gases are admitted into the reactor (1). The Knudsen Cell (1) is the reactor where the gas-surface interaction takes place. The vacuum line is used to store gases and is evacuated by an oil-sealed pump (6). Gas is injected into the reactor either in pulses of milliseconds duration via a solenoid valve (24) (General Valve Corporation, model series 9, IOTA ONE system) or continuously via a capillary backed by a calibrated volume V_c (25) and a needle valve (26). The pressure in the calibrated volume is measured by a Baratron pressure gauge. The molecules that escape from the reactor form an effusive molecular beam that is collected by an electron impact quadrupole mass spectrometer QMS (Balzers QMA 421) (10) placed in the lower part of a differentially pumped vacuum chamber. The Phase

Sensitive Detection (PSD) enables the separation of the MS signal of the sample molecular beam from the background signal owing to secondary interaction of the reactants with the walls of the detection chamber. Therefore, the beam effusing from the reactor is modulated using a tunable chopping wheel (20 – 350 Hz) (9) located just above the ionization zone of the mass spectrometer in the lower differentially pumped chamber. The PDS is then processed by a lock-in amplifier (SRS 830) (11).
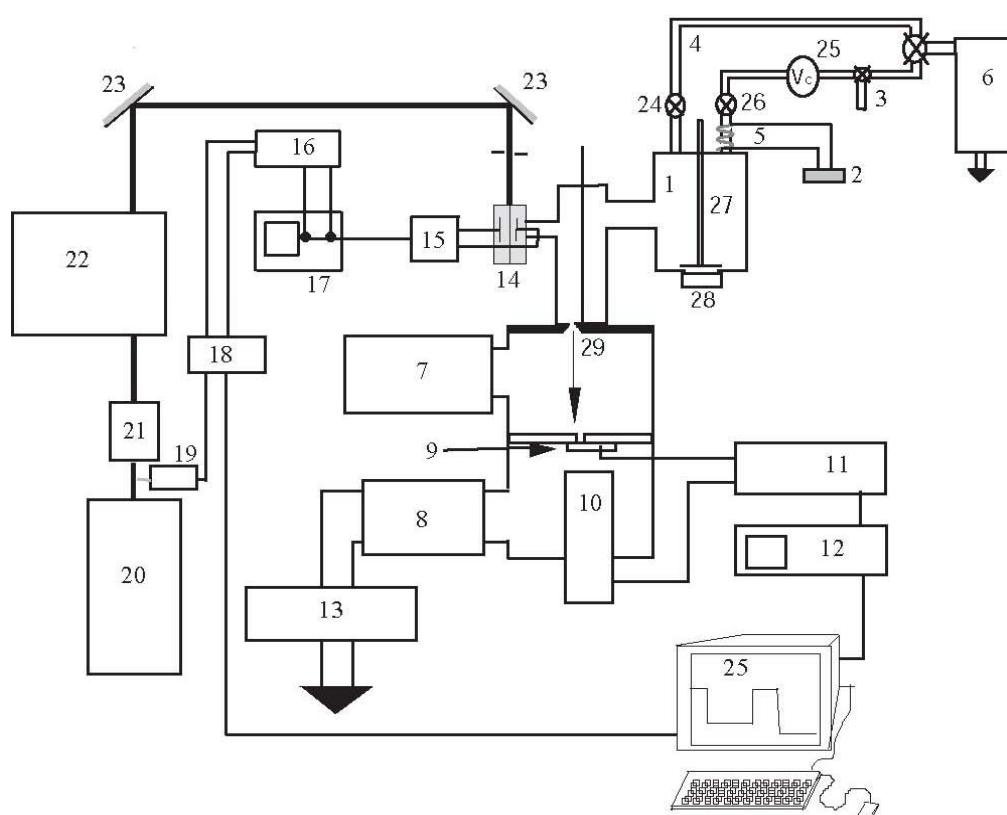
Figure 2.1. Schematic drawing of the Knudsen cell reactor and view of the REMPI excitation and detection parts, including triggering and signal processing electronics.

1, Knudsen cell reactor; 2, variable potentiometer; 3, sample (N_2O_5, NO_3, O_3); 4, gas inlet lines; 5, 6 cm hot glass tube of 0.6 cm diameter externally heated to 530 K using NiCr wire for the gas sample inlet (V = 1.7 cm^3); 6, mechanical pump; 7, cryogenic pump; 8, turbo pump; 9, mechanical chopper; 10, quadrupole mass spectrometer; 11, lock-in amplifier; 12, oscilloscope; 13, dry pump; 14, Pyrex cell for REMPI detection; 15, preamplifier; 16, boxcar integrator; 17, oscilloscope; 18, delayed beam triggering; 19, photodiode (FND 100); 20, pulsed Nd:YAG laser; 21, dichroic harmonic separator; 22, PDL (Pulsed Dye laser)-3; 23, mirror; 24, inlet valves; 25, calibrated volume (V_c); 26, needle valve; 27, isolation plunger; 28, sample holder; 29, escape orifice.

The main characteristic of the Knudsen flow reactor is that molecules entering into the reactor interact with the whole reactive surface area of the substrate at any given time. The kinetic measurements are performed under dynamic conditions, controlled by the rate of effusion through the escape orifice (29). The change in the orifice size is related to changes in the gas concentration [M] in the reactor as well the first order rate constant of effusion. The molecular flow leaving the reactor during an experiment is controlled by the escape rate constant k_{esc}. In addition, the experimental rate of a given reaction or its corresponding rate constant is always assessed by comparison to a reference experiment.

Definition	Value
Reactor volume (V)	2000 cm^3
Reactor surface area (A_R)	1830 cm^2
Sample geometric surface area (A_s)	19.6 cm^2 (TEFLON holder), 4.9 cm^2 (DELRIN holder)
Orifice diameter (nominal)	1, 4 , 8 and 14 mm

Table 2.1 Characteristic parameters of the Knudsen cell reactor.

An O-ring sealed movable plunger (27) allows the separation of the reactive surface area located in the sample holder (28) from the reactor volume. The change of the MS signal levels upon opening and closing the sample chamber obtains a value of the net uptake coefficient γ which represents the probability that molecules have, within their lifetime in the reactor, to disappear from the gas phase by uptake on the reactive surface. The escape aperture may be varied by fitting a plunger-mounted plate with different orifice sizes. The internal surface of the reactor (made of Pyrex glass and stainless steel) are fully TEFLON$^{®}$ (FEP) coated in order to limit potential interactions between gas phase species and the walls. Under the molecular flow conditions, each molecule that enters the volume of the reactor collides with the walls until it is lost by reaction with a probability γ, or leaves the cell through the escape orifice. From gas kinetic theory, the gas-wall collision frequency of the average molecule (per molecule per cm^2), referred to as Z_1, is calculated from the mean velocity $\bar{c}$ of the gas-phase molecule and the reactor volume V:

$$Z_1 = \frac{\bar{c}}{4V} = \sqrt{\frac{8RT}{\pi M}} \cdot \frac{1}{4V} \qquad (2.1)$$

where R is the gas ideal gas constant, T the temperature in Kelvin, $\bar{c}$ the mean molecular speed and M the molecular mass in kg/mol.

The geometry of the escape orifice limits the probability of back-diffusion of molecules that collide with the walls of the orifice hole (Clausing factor). Thus, after Clausing correction every molecule which crosses the orifice of surface area A_H leaves the reactor with a probability equal to 1. The condition for N molecules in the reactor can then be expressed according to:

$$\frac{-\dfrac{d}{dt}N(t)}{N(t)Z_1A_H} = 1 \qquad (2.2)$$

Thus the flow F_0^M of molecules M leaving the reactor via the orifice with area A_H is expressed as:

$$F_0^M - \frac{dN(t)}{dt} = Z_1A_HN(t) \qquad (2.3)$$

where N(t) is the time dependent total number of molecules inside the reactor. In the absence of any reactive surface the escape rate constant, k_{esc} [s^{-1}] which characterizes the kinetics of molecular effusion out of the Knudsen reactor, is defined as:

$$k_{esc} = Z_1A_H \qquad (2.4)$$

The molecular residence time in the gas phase is $\tau_g = 1/k_{esc}$. It depends on the molecular weight of the gas molecules as well on the area of the escape orifice. The MS signal I_0^M [Volt] is directly proportional to F_0^M [molecule s^{-1}] via a calibration factor following equation (2.5):

$$F_0^M = I_0^M \cdot C_{cal(M)} \qquad (2.5)$$

where $C_{cal(M)}$ is a calibration factor for the species M of interest whose value depends on the MS instrumental parameters.

The experimental value of k_{esc} is assessed by fitting the single exponential decay of the MS signal during a reference experiment either after the source of the molecules entering the reactor has been halted at time t_0 or after pulsed injection (Figure 2.3); the rate law of the effusion is first order based on the solution of the differential equation (2.3):

$$N(t) = N(t_0) \cdot e^{-(k_{esc})t} \qquad\qquad (2.6)$$

Table 2.2 reports the characteristic parameter of the Knudsen reactor. We performed experiments according to two protocols characterized by their different procedure. In continuous flow (or *steady state*) experiments, reactants were introduced at a constant flow. In *pulsed valve* experiments, we observe the exponential decrease of the gas concentration in the reactor upon injection of a known dose of gas. Both techniques are complementary and provide information on the kinetics and the mass balance of a given reaction.

Definition	Theoretical Value
k_{esc} (experimentally determined values for nominal orifice diameters)[a]	$0.02(T/M)^{1/2}$ s^{-1} for 1 mm orifice
	$0.25(T/M)^{1/2}$ s^{-1} for 4 mm orifice
	$0.8(T/M)^{1/2}$ s^{-1} for 8 mm orifice
	$1.9(T/M)^{1/2}$ s^{-1} for 14 mm orifice
Collision frequency ω (nominal) with A_s	$\omega = Z_1 A_s = 1.81(T/M)^{1/2} A_s$ [s^{-1}]

[a] T given in K, M in g, A_s in cm^2

Table 2.2. Kinetic parameters of the Knudsen cell. The theoretical value of k_{esc} is calculated according to equation (2.4).

2.2 Steady State Experiment

When a continuous flow F_{in}^M of molecules is admitted into the reactor through a capillary inlet, we obtain a constant molecular flow. Once the equilibrium is established in the reactor and in the absence of any reaction, the steady state flow of molecules effusing out of the reactor F_0^M is equal to the flow F_{in}^M (Figure 2.2). When a reactive surface is exposed, the new

steady state molecular flow F_r^M is reduced with respect to F_0^M because of the rate of loss to the substrate. If we exclude the saturation of surface sites during the uptake, F_r^M may be expressed as:

$$F_r^M = F_0^M - \frac{dN_r(t)}{dt} = F_{in}^M - (\gamma_{ss} \cdot Z_1 A_S) \cdot N_r(t) \qquad (2.7)$$

$Z_1 A_S$ is the collision frequency ω over the total reactive geometric surface with area A_S and γ_{ss} is the probability that molecules have, within their lifetime in the reactor, to disappear from the gas phase by uptake on the reactive surface. By multiplying equation (2.7) by k_{esc} the observed pseudo first order rate constant k_{obs} for reaction is derived according to equation (2.8):

$$k_{obs} = (\frac{F_0^M}{F_r^M} - 1) \cdot k_{esc} = \gamma_{obs} \cdot \omega \qquad (2.8)$$

Usually, at steady state conditions, γ_{obs} is named steady state uptake γ_{ss} coefficient.

The MS signal is directly proportional to the flow of molecules leaving the reactor. It drops from I_0^M to I_r^M after exposing a reactive surface. The gases leave the Knudsen reactor through the escape orifice whose diameters (1, 4, 8, 14 mm) determine the residence time ($\tau_g = 1/k_{esc}$) and molecular concentration at a given flow rate according to:

$$F_0^M = I_0^M \cdot C_{(M)} \qquad (2.9)$$

where I_0^M is the mass spectrometric signal amplitude (MS) flow of molecules effusing from the reactor and $C_{(M)}$ is the calibration factor for species M of interest that depends on instrumental parameters. Based on the ideal gas law ($PV = nRT$) the MS signal is calibrated in the following manner:

$$\frac{dN}{dt} = \frac{dP}{dt} \underbrace{\frac{V_C}{RT}}_{X} N_A = F_{in}^M \qquad (2.10)$$

where R is the ideal gas constant, T the temperature in Kelvin, V_c a calibrated volume, N_A the Avogadro's number and F_{in}^M the inlet gas flow. Under the assumption that $F_o^M = F_{in}^M$, that is at steady state, the calibration factor $C_{cal(M)}$ results:

$$C_{cal(M)} = \frac{\frac{dP}{dt} \cdot x}{I_0^M} \qquad (2.11)$$

where I_0^M is the MS signal. The concentration $[M]_{MS} = N/V$ in the reactor is related to the flow of molecules leaving the reactor F_0^M according to equation (2.12):

$$[M]_{MS} = \frac{F_0^M}{k_{esc} \cdot V_{cell}} \qquad (2.12)$$
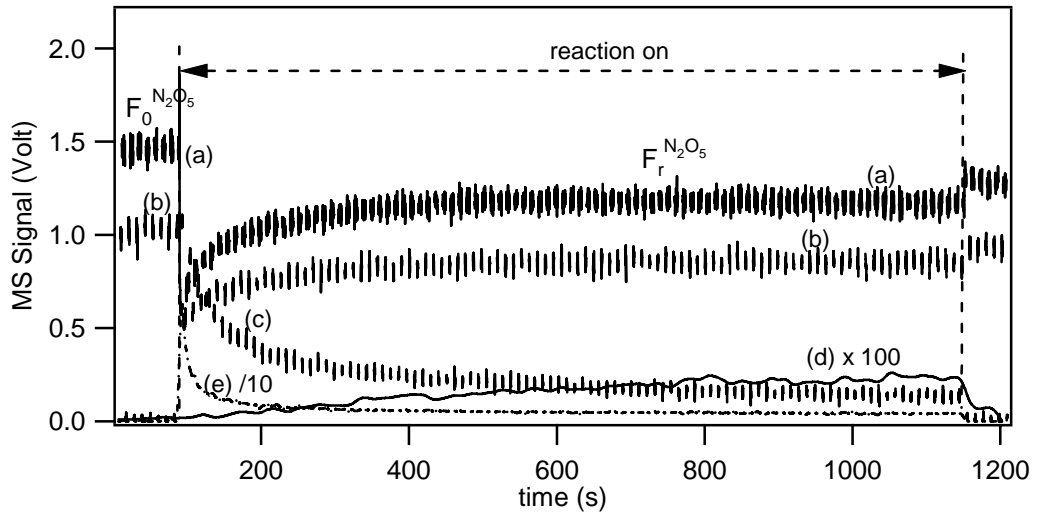
Figure 2.2. N_2O_5 steady state uptake experiment on a sample of 510 mg of $CaCO_3$. Curves (a), (b), (c) and (e) correspond to the raw MS signals monitored at m/e 46, m/e 30, m/e 44 and m/e 18, respectively. The MS signal monitored at m/e 63 (curve (d) corresponds to HNO_3 production. Orifice diameter of 14 mm, $A_s = 19.6$ cm^2 and $[N_2O_5]_0 = (4.0 \pm 1.0) \times 10^{11}$ cm^{-3}.

The concentration in the reactor may be chosen within the range $(1-1000) \times 10^{10}$ cm^{-3} either by adjusting the inlet flow $F_0^M = F_i^M$ or at a given flow rate changing the orifice size and thus the residence time τ_g.

2.3 Pulsed Valve Experiment

Pulses of reactive gas are admitted into the reactor during the short-opening period of the solenoid valve on the millisecond time scale. In the reactive case, the plunger is lifted and allows the heterogeneous interaction between the gas phase and the surface of interest. The MS probes molecules which have, within their lifetime in the reactor, the possibility to disappear from the gas phase by uptake on the reactive surface with an effective probability γ_{eff}. Equation (2.3) may be written for this case as follow:

$$-\frac{dN_r(t)}{dt} = (Z_1 A_H + \gamma_{eff} Z_1 A_s) \cdot N_r(t) \qquad (2.13)$$

where $N_r(t)$ is the time dependent number of molecules in the reactor. The solution of equation (2.13) is given by:

$$N_r(t) = N_0 e^{-(Z_1 A_H + \gamma_{eff} Z_1 A_s)t} \qquad (2.14)$$

N_0 is the number of molecules injected into the reactor and is experimentally determined by integration of the reference pulse (see Figure 2.3). Typically, pulses have a duration of 5 ms at a dose of 5.0×10^{15} molecules per pulse[2]. The "reference pulse" is fired when the sample is still isolated from the gas. We determine the total number of injected molecules per pulse and the value of k_{esc}, which is obtained by simply fitting the decaying MS signal to a single exponential decay in the absence of reaction. The "reactive pulse" is obtained by repeating the same operation with the plunger lifted. The total observed exponential decay in the presence of a reactive substrate is thus characterized by a new rate constant, k_{dec}, given by

$k_{dec} = \gamma_{eff} Z_1 A_S + k_{esc}$. By identification of $\gamma_{eff} Z_1 A_S$ with the first order reactive rate constant k_{eff}, the uptake coefficient may de derived according to equation (2.15):

$$\gamma_{eff} = \frac{k_{eff}}{Z_1 A_S} = \frac{k_{eff}}{\omega} \tag{2.15}$$

k_{eff} is obtained by comparing k_{dec} with k_{esc} measured in a reactive and a reference experiment, respectively. The number of collision per surface area at a given gas concentration [M] expressed in cm^{-3} is $Z_{11} = \frac{\bar{c}}{4}[M]$ following the kinetic theory of gases. At a given γ_{eff} the total number n of collisions per surface area is given by the following equation (2.16):

$$n = Z_{11} \cdot \gamma_{eff} = \frac{\bar{c}}{4} \cdot [M] \cdot \gamma_{eff} \tag{2.16}$$

Figure 2.3 shows a pulsed valve measurement performed with ozone (O_3) on 400 mg of Kaolinite. The two curves represent the reference pulse and the reactive pulse of O_3 on the substrate, respectively. For each reactive pulse we defined the "cumulative dose of O_3 taken up" as the difference of the area between the two curves.
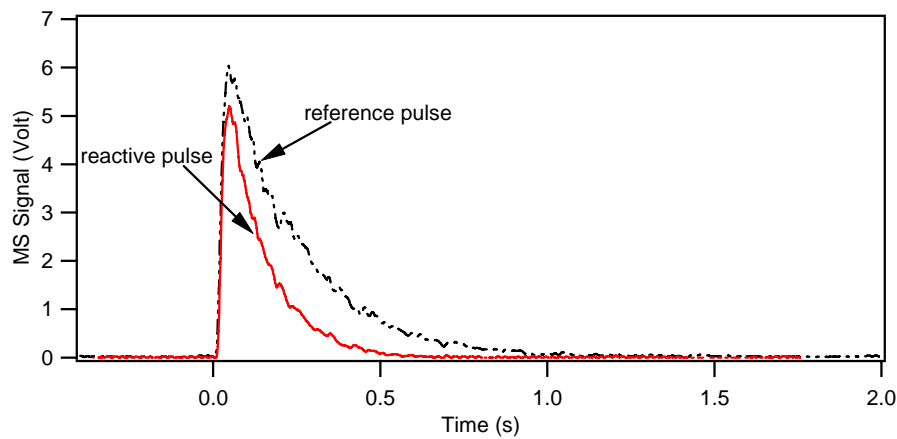
Figure 2.3. Pulsed valve experiment performed in the Knudsen reactor: the reference pulse corresponds to 5.0 x 10^{15} molecules of O_3 entering in the reactor, without interacting with the substrate, the reactive pulse corresponds to 5 x10^{15} molecules of O_3 interacting with 400 mg of Kaolinite ($A_s = 19.5$ cm^2; 14 mm orifice).

2.4 Optical detection: Resonance Enhanced Multiphoton Ionization (REMPI) of NO$_2$ and NO in the Knudsen flow reactor

As displayed in Figure 2.1, a Pyrex cell (14) has been added to the main body of the reactor in order to enable *in situ* REMPI detection. Inside this REMPI cell two electrodes were mounted, each on an electrical feedthrough. The electrodes consist of two polished Cu plates mounted in a cell that is equipped with two quartz windows for the entry and exit of a focused visible laser beam. The dye laser beam is focused by means of a 70 mm (focal length) plano-convex lens in the center of the two plate electrodes which are biased at ± 65 V against ground. REMPI was performed using a Quanta Ray$^{®}$ PDL-3 dye laser (22) pumped by the third harmonic of a Quanta Ray$^{®}$ Nd:YaG (GCR-3) laser (20) at 355 nm which generates visible light in the wavelength range 420 to 520 nm. Two different dyes were used to study REMPI of NO and NO$_2$: Coumarin 120 (absorption $\lambda_{max} = 354$ nm) and Coumarin 307 (absorption $\lambda_{max} = 395$ nm) for NO and NO$_2$, respectively[3]. Ions and electrons created in the focal volume of the dye laser are collected by the plate electrodes, amplified (15) and, after inversion of one of the signals, added before averaging by a box-car (SRS 250) integrator (16) in order to yield the REMPI signal.

The signal area A_{REMPI} resulting from the integration for 300 µs under the REMPI signal is proportional to the number of charge carriers initially generated by REMPI and so is directly proportional to the gas concentration $[M]_{REMPI}$ following equation (2.17):

$$[M]_{REMPI} = A_{REMPI} \cdot C_{(M)REMPI} \qquad (2.17)$$

where $C_{(M)REMPI}$ is a calibration factor that is directly determined from an absolute determination of [M] using a suitably calibrated MS signal for species M. In order to determine this calibration factor we monitored $[M]_{MS}$ against the integrated REMPI signal A_{REMPI} following equation (2.18):

$$C_{(M)REMPI} = \frac{[M]_{MS}}{A_{REMPI}} \qquad (2.18)$$

Previous studies have already examined the complexity of the REMPI spectrum of NO at ambient temperature. Nitric oxide can be ionized by four photons including both two and three-photon resonances. The two-photon resonances are found to be much more intense than the three-photon ones. Absorption of two more photon promotes the excited state molecule above its ionization potential and the molecule spontaneously ionizes[4]. The excitation process is depicted in Figure 2.4 and corresponds to a [2 + 2] process: two photons at $\lambda_{NO} = 452.6$ nm resonantly excite NO in the $X^2\Pi \rightarrow A^2\Sigma^+$ band[5,6].
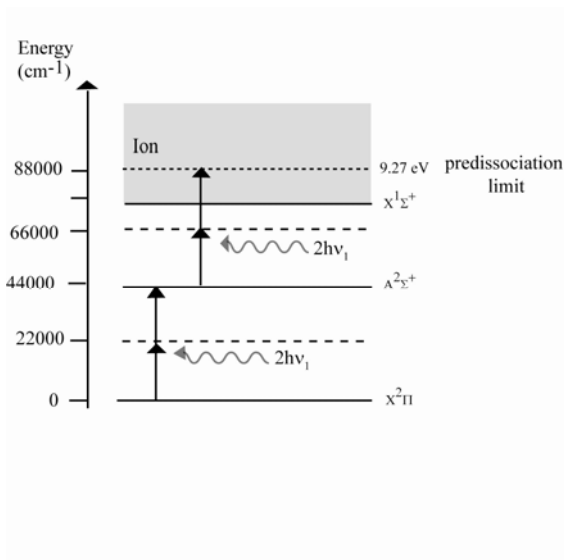

Figure 2.4. Energy level diagram showing the two-photon resonant, four-photon ionization of nitric oxide via vibrations of the $A^2\Sigma^+$ state. The final four-photon energy in the continuum (shaded region) and the ionization energy (dashed line) are indicated.

Two additional photons at $\lambda_{NO} = 452.6$ nm are absorbed between the $A^2\Sigma^+$ states and the vibrational Rydberg levels resulting in the ionization of the molecule. The overall process is described by the following reactions:

$$NO(X^2\Pi) + 2h\nu_1 \rightarrow NO(A^2\Sigma^+) \qquad\qquad (2.E1)$$

$$NO(A^2\Sigma^+) + 2h\nu_1 \rightarrow NO^+ + e^- \qquad\qquad (2.E2)$$
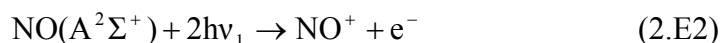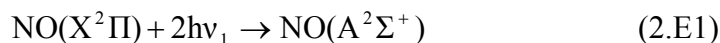
The REMPI spectrum of NO and the energy of the dye laser (Coumarin 120) near 452 nm is shown in Figure 2.5. The region of major intensity of the REMPI spectrum ranges between 451.2 and 452.4 nm, the most intense narrow peak is at $\lambda_{NO} = 452.6$ nm.
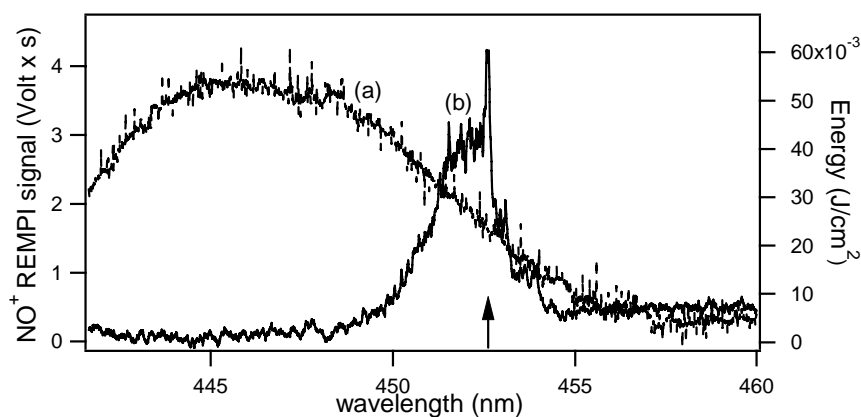
Figure 2.5. REMPI spectrum of NO between 442 and 460 nm (trace (b)) compared with the corresponding gain curve of the laser dye (Coumarin 120, absorption $\lambda_{max} = 354$ nm used for the ionization process (curve (a)). The sharp peak located at $\lambda_{NO} = 452.6$ nm has been used to monitor NO (arrow).

In order to ionize NO_2 we have used a one color excitation scheme requiring four photons. The nature of the process is revealed by a resonance involving a three-photon transition from the ground state to a vibrational level of a 3s Rydberg state originating near 50000 cm^{-1} [7,8]. The complete excitation process presented in the diagram displayed in Figure 2.6 corresponds to a [3 + 1] mechanism: one photon at $\lambda_{NO_2} = 511$ nm resonantly excites NO_2 in the band connecting the ground state X^2A_1 to a virtual intermediate state. At our chosen excitation wavelength of 511 nm, the two-photon energy for wavelengths longer than 498.2 nm falls just short of the origin of the 249.1 nm B^2B_2 state in NO_2. Both excited state levels, namely A^2B_2 and A^2B_1 of NO_2 are not involved in the electronic transition at $\lambda_{NO_2} = 511$ nm. Therefore, it has to take place via a virtual intermediate level located above A^2B_1. Two additional photons at $\lambda_{NO_2} = 511$ nm are resonantly absorbed from this virtual state to the four photon excited state via the $E^2\Sigma_u^+$ Rydberg levels[8].

The complete excitation process may be viewed as a [3 + 1] ionization process, with the spectral structure reflecting the resonance at the three-photon level:

$$NO_2(X^2A_1) + 3hv_2 \rightarrow NO_2(E^2\Sigma_u^+) \qquad (2.E3)$$

$$NO_2(E^2\Sigma_u^+) + hv_2 \rightarrow NO_2^+ + e^- \qquad (2.E4)$$
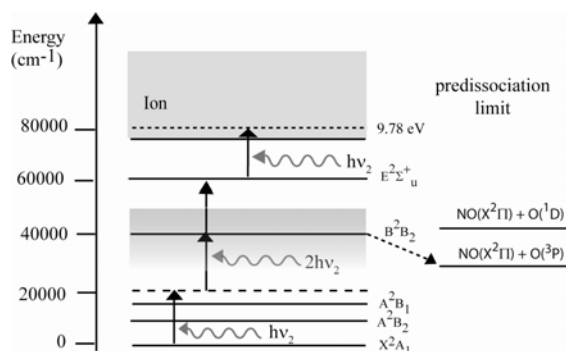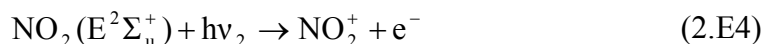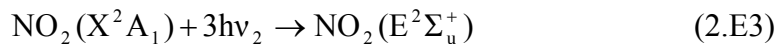
Figure 2.6. Energy level diagram showing the three-photon resonant, four-photon ionization of NO_2 via vibrations of the B^2B_2 state. The NO_2 dissociation to yield neutral $NO(X^2\Pi)$ and $O(^3P)$ is indicated (dashed arrow). The final four-photon energy in the continuum (shaded region) and the ionization energy (dashed line) are indicated.

The REMPI spectrum of NO_2 and the energy of the dye laser (Coumarin 307) near 511 nm is shown in Figure 2.7. The high level background below the REMPI signal is due to vibrationally excited NO produced from NO_2 dissociation during the excitation/photoionization process. The resulting spectrum is thus the sum of an ionization spectrum for NO_2 overlaid on a continuous ionization spectrum for NO generated by photodissociation of NO_2 [8]. In this case molecular NO_2 undergoes a transition to the electronically excited B^2B_2 dissociative state, producing vibrationally excited $NO(X^2\Pi)$ which then interacts with the laser beam as displayed in Figure 2.7. The fact that we observe a REMPI signal presumably due to NO^+ above 500 nm shows that two-photon dissociation of NO_2 must occur below the origin of the B^2B_2 state. Energetically speaking, the only possible pathway is to $NO(X^2\Pi) + O(^3P)$, and as anticipated, the NO^+ spectrum is

continuous and unassignable in this region[8]. An ancillary REMPI experiment has been performed by exciting a flow of pure NO at $\lambda_{NO_2} = 511$ nm. As expected, we did not observe any NO^+ REMPI signal which must mean that NO was formed with significant excess energy during NO_2 excitation enabling REMPI detection of NO_2 at $\lambda_{NO_2} = 511$ nm [8].
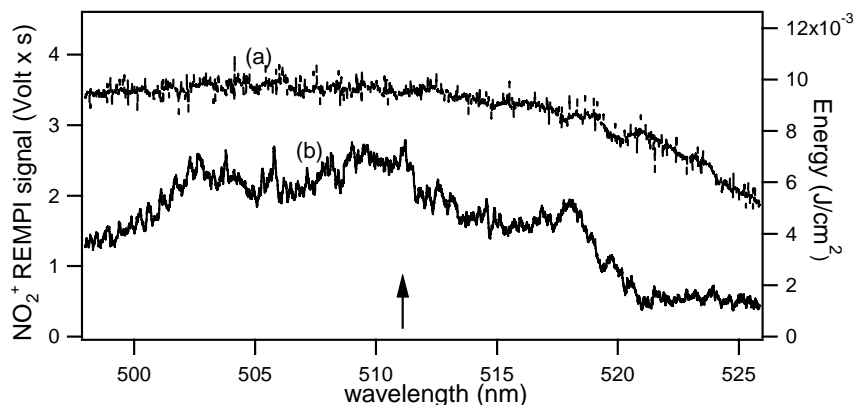
Figure 2.7. REMPI spectrum of NO_2 between 500 and 525 nm (trace (b)) compared to the corresponding gain curve of the laser dye (Coumarin 307, absorption $\lambda_{max} = 395$ nm) used for the ionization process (curve (a)). $\lambda_{NO_2} = 511$ nm was used for detection of NO_2 (arrow).

In order to examine the kinetics of the rate-limiting step of the REMPI process for NO_2 and NO we have studied the dependence of the NO_2^+ ion yield as a function of laser intensity. At the limit of low intensities or small cross sections, that is in the absence of significant saturation, the overall ionization is simply given by the following expression of absorption[9]:

$$N = \sigma_I \sigma_{II} I^{n+m} \qquad\qquad (2.E5)$$

In this equation I represents the laser intensity, $\sigma_I I^n$ the transition probability for the n-resonant transitions and $\sigma_{II} I^m$ the transition probability for the m ionization photons. σ_I and σ_{II} are the cross-sections for the n-photon transition and m-photon-ionization, respectively. Typical values for NO cross-sections are:

σ_I (two photon; NO) = 4.8 x 10^{-51} cm^4 s and σ_{II} (two-photon; NO) = 2.0 x 10^{-49} cm^4 s, obtained from the theoretical calculation of the two-photon resonant excitation of NO and of

the two-photon ionization of NO [10]. For NO_2, typical values for NO_2 cross-sections are: σ_I (three-photon; NO_2) = 2.6 x 10^{-82} cm^6 s^2 and σ_{II} (one-photon; NO_2) = 2.0 x 10^{-20} cm^2, obtained for the theoretical calculation of the three-photon resonant excitation of NO_2 and the one-photon ionization of NO_2 [10].

At moderate laser intensities, the ionization rate is saturated and the overall ionization probability is proportional to:

$$N = \sigma_I I^n \qquad (2.E6)$$

As displayed in Figure 2.8 the measurement of the yield of NO^+ ($\lambda_{NO} = 452.6$ nm) versus laser intensity showed an I^2 and $I^{1.7}$ dependence at low and high laser intensities, respectively, whereas NO_2^+ ($\lambda_{NO_2} = 511$ nm) showed an $I^{2.9}$ and $I^{1.9}$ dependence at low and high laser intensities, respectively. Therefore, the NO^+ and NO_2^+ REMPI spectra are controlled by the $X^2\Pi \xrightarrow{2h\nu} A^2\Sigma^+$ and $X^2A_1 \xrightarrow{3h\nu} E^2\Sigma_u^+$ transitions in NO and NO_2, respectively.
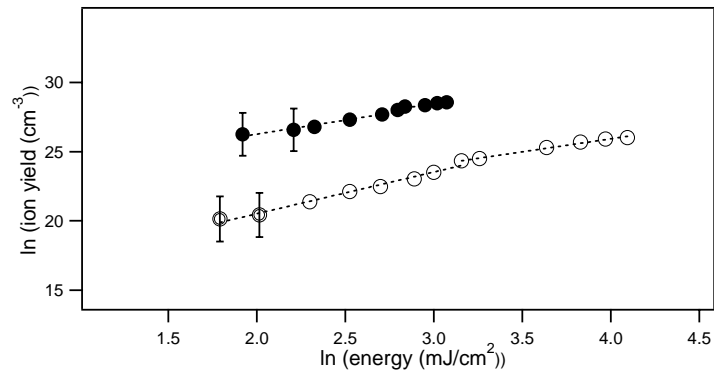
Figure 2.8. REMPI signal for NO and NO_2 excitation at 452.6 nm and 511 nm, respectively. The full and open circles represent experimental data for NO and NO_2, respectively. The fit of the data to a power law is shown as the dashed lines.

The conditions chosen for REMPI detection of NO_2 and NO did not show a measurable contribution from the photodissociation of NO_3 which otherwise would have complicated the interpretation of the present results owing to secondary photolysis at $\lambda_{NO_2} = 511$ nm and

λ_{NO} = 452.6 nm. Figure 2.9 displays an auxiliary experiment of NO_3 interacting with the DELRIN® support that has been carried out in order to show that the uptake of NO_3 on DELRIN® (γ_{DELRIN} = 8.2 x 10^{-3}) and the subsequent decrease of the m/e 62 (NO_3^+) signal does not affect the REMPI signal for NO_2 present as an impurity from the NO_3 source. Moreover, NO_2 did not show any uptake on DELRIN® under all conditions.

On the other hand, REMPI detection of NO at λ_{NO} = 452.6 nm leads to some two-photon photodissociation of NO_2, if present. In order to prove the photodissociation of NO_2 and subsequent ionization of the product NO under NO REMPI detection conditions, we photoionized a flow of pure NO at λ_{NO} = 452.6 nm. Subsequently, we introduced an additional flow of pure NO_2 identical to [NO] and observed an increase in the NO REMPI signal of approximately (20±5) % of that of the original NO (at 20 mJ/cm^2 power energy). This means that the REMPI detection of NO at λ_{NO} = 452.6 nm will lead to an additional REMPI signal if NO_2 is present at the same time as NO. This secondary photoexcitation/ionization process in NO_2 has been fully accounted for in the present data evaluation.
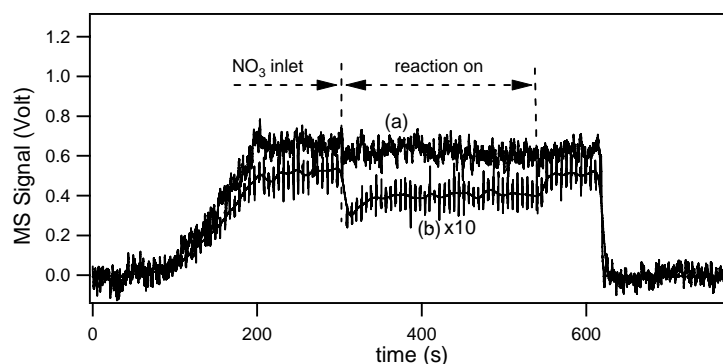
Figure 2.9. Simultaneous measurement of the NO_3 uptake on a DELRIN sample holder using MS at m/e 62 (curve (b)) and the REMPI signal for NO_2 at λ_{NO_2} = 511 nm converted to a MS signal at m/e 46 (curve (a)). [NO_3] = (7.0 ± 1.0) x 10^{11} cm^{-3} at orifice diameter 8 mm. The constant REMPI NO_2 signal that is equivalent to the displayed MS signal in the presence of the changing NO_3 MS signal, upon NO_3 uptake indicates that NO_3 secondary photolysis at λ_{NO_2} = 511 nm does not contribute to the NO_2 REMPI signal according to $NO_3 + h\nu \rightarrow NO_2 + O(^3P)$ under the present experimental conditions.

2.5 Reactants preparations used in the present work

The studies presented in this work required the synthesis of some products which are not commercially available. Therefore, they were synthesised in the laboratory before performing each series of experiments. The purity of the gas samples was checked in the Knudsen reactor by mass spectrometry before their reaction with the substrates.

NO$_2$ and **NO** were obtained from Carbagas SA and Matheson Inc., respectively.

HONO was generated in situ by flowing gaseous HNO$_3$ through a reaction vessel filled with humid KNO$_2$ (FLUKA puriss. p.a $\geq$ 98.8%).

Pure **HNO$_3$** was prepared from a mixture of liquid HNO$_3$ (90%, Fluka AG) and H$_2$SO$_4$ (98%, Fluka AG) in a ratio of 1:3 v/v. Subsequently, N$_2$ was bubbled through the solution under reduced pressure for about 10 minutes in order to rid the solution of trace amounts of NO$_2$.

N$_2$O$_5$ was synthesized by the oxidation of NO$_2$ with excess ozone. The O$_3$/O$_2$ mixture at the outlet of the ozonator (Fisher 502) is passed through a P$_2$O$_5$ trap in order to eliminate residual moisture before being mixed with equally dried NO$_2$. The N$_2$O$_5$ is collected in a methanol/dry-ice bath at 195 K and is subsequently analyzed for purity by MS.

NO$_3$ was generated by thermal decomposition of N$_2$O$_5$. This will be described in detail in Chapter 3.

O$_3$ was prepared in an ozone generator (Fischer 502) in which O$_3$ is generated by a corona discharge using a flow of pure oxygen at a pressure of 400 mbar. Subsequently O$_3$ was condensed in a Pyrex trap containing silica gel cooled to 185 K in a methanol bath. Subsequently we let O$_3$ desorb from silica gel into a darkened storage vessel in order to stock it for some time. Since the absorption spectrum of ozone is well known, it was used to quantitatively determine the concentration of ozone in the sample[11]. A glass absorption cell of 7 cm optical path length and equipped with quartz windows was used for the measurement

of ozone absorption at 256.3 nm using a cross section $\sigma = 1.15 \times 10^{-17}$ cm^2 for the calculation of the concentration at the measured total pressure in the absorption cell[12].

2.6 References

(1)   Addison, C. C.: Liquid Dinitrogen-Tetroxide as a Solvent, Angewandte Chemie-International Edition, 72, 193-197, (1960).

(2)   Caloz, F.; Fenter, F. F.; Tabor, K. D.; Rossi, M. J.: Paper I: Design and construction of a Knudsen-cell reactor for the study of heterogeneous reactions over the temperature range 130-750 K: Performances and limitations, Review of Scientific Instruments, 68, 3172-3179, (1997).

(3)   Brackmann, U., Lamdachrome Laser Dyes (data sheets): Lambda Physik, Lasertecnik, (1986).

(4)   Miller, J. C.; Compton, R. N.: Multi-Photon Ionization Photoelectron-Spectroscopy of Nitric-Oxide, Journal of Chemical Physics, 75, 22-29, (1981).

(5)   Garnica, R. M.; Appel, M. F.; Eagan, L.; McKeachie, J. R.; Benter, T.: A REMPI method for the ultrasensitive detection of NO and NO_2 using atmospheric pressure laser ionization mass spectrometry, Analytical Chemistry, 72, 5639-5646, (2000).

(6)   Johnson, P. M.; Berman, M. R.; Zakheim, D.: Nonresonant Multiphoton Ionization Spectroscopy- 4-Photon Ionization Spectrum of Nitric-Oxide, Journal of Chemical Physics, 62, 2500-2502, (1975).

(7)   Rockney, B. H.; Grant, E. R.: Resonant Multi-Photon Ionization Detection of the NO_2 Fragment from Infrared Multi-Photon Dissociation of CH_3NO_2, Chemical Physics Letters, 79, 15-18, (1981).

(8)   Morrison, R. J. S.; Rockney, B. H.; Grant, E. R.: Multi-Photon Ionization of NO_2 - Spectroscopy and Dynamics, Journal of Chemical Physics, 75, 2643-2651, (1981).

(9)   Johnson, P. M.: Molecular Multi-Photon Ionization Spectroscopy, Applied Optics, 19, 3920-3925, (1980).

(10)   Cremaschi, P.; Johnson, P. M.; Whitten, J. L.: Multi-Photon Ionization Spectroscopy - Theoretical-Analysis of NO Spectrum, Journal of Chemical Physics, 69, 4341-4348, (1978).

(11)   Horvarth, M.; Bilitzky, L.; Huttner, J.: Ozone, Elsevier, New York, 26-29, (1985).

(12)   Atkinson, R.; Baulch, D. L.; Cox, R. A.; Hampson, R. F.; Kerr, J. A.; Rossi, M. J.; Troe, J.: Evaluated kinetic, photochemical and heterogeneous data for atmospheric chemistry .5. IUPAC Subcommittee on Gas Kinetic Data Evaluation for Atmospheric Chemistry, Journal of Physical and Chemical Reference Data, 26, 521-1011, (1997).

CHAPTER 3

THE HETEROGENEOUS CHEMICAL KINETICS OF NO$_3$ ON ATMOSPHERIC MINERAL DUST SURROGATES

3.1 Introduction

Atmospheric chemistry is driven by reactions of free radicals owing to their reactivity with many trace gases. In addition to OH, HO$_2$ and O$_3$ that exert their oxidizing potential in the atmosphere under photolytic conditions, the nitrate free radical, NO$_3$ [1], is an important atmospheric oxidizing agent in the nighttime atmosphere whose reactivity with unsaturated biogenic hydrocarbons as well as with aldehydes and ketones[2] is comparable to the reactivity of the hydroxyl free radical in the daytime atmosphere. Together with O$_3$, nitrate radical represents a significant part of the oxidation potential of the atmosphere at night. Under conditions of the simultaneous presence of NO$_x$, O$_3$ and reactive organic gases in the same air mass, NO$_3$ is responsible for the nighttime formation of organic peroxy free radicals that are precursors to tropospheric O$_3$. NO$_3$ is thereby involved in the rate-limiting step of either H abstraction from or addition to an olefinic double bond.

Specifically, the presence of NO$_3$ that rapidly undergoes photolysis during the day has several important consequences for tropospheric chemistry. It controls reactive nitrogen, NO$_y$, at night by forming N$_2$O$_5$ which undergoes heterogeneous hydrolysis to HNO$_3$, an important daytime reservoir compound for NO$_2$. The fast radical recombination reaction

between NO_3 and NO_2 leading to N_2O_5 is the only known source for HNO_3 at nighttime. NO_3 also acts as an initiator for the formation of non-photolytic OH free radicals at night through reaction of HO_2 with NO, thereby starting oxidation chain reactions of reactive organic gases. Lastly, NO_3 may form peroxyacetyl and other organic nitrates that may also act as temporary NO_x reservoirs[2,3].

Atmospheric nigthttime concentrations of NO_3 reach values of up to 4.0×10^7 molecule cm^{-3} in the stratosphere[4] and 2.0×10^9 molecule cm^{-3} in the troposphere[5]. Despite these significant concentrations only a few studies of the heterogeneous reactions of the nitrate radical have been performed[6-10], none so far on mineral dust. The present work intends to fill this gap by studying the NO_3 uptake on mineral dust and some of its surrogates in order to obtain a value for the uptake coefficient γ for NO_3 that may be included in global modeling of heterogeneous chemistry on mineral dust aerosols. Together with HNO_3 and N_2O_5, NO_3 contributes to the formation of particulate nitrate on the dust particles by surface processes in the troposphere[11].

There is no study at this time that directly proposes the uptake of NO_3 on mineral dust surfaces from measurements of the nitrate radical in the lower troposphere despite field measurements that report NO_3 concentrations[12] and mixing ratios[13] as a function of meteorological data. Box, regional and global scale models have gauged the importance of dust on both the photochemical rates of oxidant formation as well as the loss of trace gases regarding atmospheric composition[11,14-17]. The comparison of the global scale models of Bian and Zender[16] with the one presented by Bauer et al[17] reveals significant quantitative differences of the effect of mineral dust on O_3 and several important trace gases such as HNO_3, N_2O_5 and H_2O_2. However, both studies agree that the direct interaction of O_3 with mineral dust is of minor importance, whereas the uptake of its precursor HNO_3 is responsible for most of the ozone decrease in the areas affected by dust. It is difficult to quantitatively compare the results of Bian and Zender with Bauer et al. because the uptake coefficient γ for HNO_3 on global mineral dust is a factor of 100 lower whereas γ for NO_3 is a factor of 33 larger in the former. The estimated uptake coefficients (guesses) used in the simulations performed by Bauer et al. where $\gamma_{HNO_3} = 0.1$, $\gamma_{N_2O_5} = 3.0x10^{-3}$ (rH = 70%) and $\gamma_{NO_3} = 3.0x10^{-3}$. On the other hand, Bian and Zender used different estimated values: $\gamma_{HNO_3} = 1.1x10^{-3}$, $\gamma_{N_2O_5} = 1.0x10^{-3}$ and $\gamma_{NO_3} = 0.1$. This reflects both the uncertainty of past measurements as well as the absence of experimental information that is replaced by

guesswork such as in the case of NO$_3$. We have therefore embarked on a laboratory program to measure some of the heterogeneous reactions involving NO$_3$ and N$_2$O$_5$ (chapter 4) likely to be important in global mineral dust studies.

3.2.1 Experimental Aspects

Experiments have been performed at 298 ± 2K using the Knudsen flow reactor, described in detail in Chapter 2. In order to unambiguously monitor the concentration of NO, NO$_2$, NO$_3$, HNO$_3$ and N$_2$O$_5$, Resonance Enhanced Multiphoton Ionization (REMPI) was employed in situ as part of a multi-diagnostic experimental technique in addition to molecular beam-sampling electron-impact mass spectrometry (MS) coupled to phase-sensitive detection.

The rate constant for the effusive loss k_{esc} is given by the kinetic theory of gases and was routinely measured for each compound. However, owing to the fact that the loss of the NO$_3$ free radical includes both physical, that is effusion, and chemical wall-loss processes, the usual algebra for the retrieval of γ is slightly more complex as explained below. The characteristic parameters and relevant kinetic expressions used in this work are given in Table 2.2.

3.2.2 Sample preparation

The used samples are the following: Kaolinite, poorly ordered (KGa-2, Warren County, Georgia, USA), CaCO$_3$ (Fluka), natural limestone (Transmat SA, La Sarraz, Switzerland), Arizona Medium Test Dust (Powder Technology Incorporated, Burnsville MN, USA), Saharan Dust collected from deposits on the Cape Verde Islands and Molecular sieve (Fluka). Table 3.1 reports the composition of the main components of the analysed mineral dust. The true density ρ_t of all the examined powder samples was taken from the literature while the bulk density ρ_b was determined from the weight and the volume of the sample. The average particle diameter was determined using SEM, and the Brunauer-Emmett-

Teller (BET) surface area of every sample displayed in Table 3.1 was measured using a Sorptomatic 1900 Carlo Erba (Fisous Instruments).

Two kinds of sample holders were used: one consisted of a TEFLON® coated Pyrex holder having an available sample surface of 19.6 cm^2, the other consisted of an internal reduction piece made out of DELRIN®, an acetal resin, leading to a sample surface of 4.9 cm^2. DELRIN® showed a modest reactivity towards uptake of NO_3 resulting in $\gamma_{DELRIN} = 8.2 \times 10^{-3}$. We discovered during the study that DELRIN® is less porous for small molecules such as H_2O and less sticky for HNO_3 with respect to TEFLON®. As a consequence, we applied the appropriate corrections to all uptake measurements.

Kaolinite[1]	CaCO$_3$[2]	Natural limestone[3]	Saharan Dust[4]	Arizona Test Dust[5]
$Al_2Si_2O_5(OH)_4$	$CaCO_3$ 99.9%	$CaCO_3$ 97%	SiO_2 47%	SiO_2 68-76%
SiO_2 44.2%		SiO_2 1.9%		Al_2O_3 10-15%
TiO_2 2.17%		Al_2O_3 0.5%	FeO 14.7%	Fe_2O_3 2-5%
Al_2O_3 37.2%		Fe_2O_3 0.3%	Al_2O_3 17.6%	Na_2O 2-4%
Fe_2O_3 1.14%		MgO 0.2%	MgO 5.1%	CaO 2-5%
FeO 0.05%		Other elements 0.1%	Na_2O 2.1%	MgO 1-2%
MgO 0.04%			K_2O 2.5%	TiO_2 0.5-1.0%
CaO 0.04%			CaO 5.0%	K_2O 2-5%
Na_2O 0.02%			TiO_2 4.5%	
K_2O 0.02%			P_2O_5 0.6%	
P_2O_5 0.06%			SO_3 0.3%	
F 0.02%			MnO 0.3%	
ρ_t = 2.1-2.6 g/cm^3	ρ_t = 2.93 g/cm^3	ρ_t = 2.7 g/cm^3	ρ_t = 2.7 g/cm^3	ρ_t = 2.65 g/cm^3
ρ_b = 0.528 g/cm^3	ρ_b = 0.96 g/cm^3	ρ_b = 1.13 g/cm^3	ρ_b = 1.2 g/cm^3	ρ_b = 0.6 g/cm^3
d = 1.0 μm	d = 3.5 μm	-	d = 0.9 μm	-
S_{BET} = 22.57 m^2/g	S_{BET} = 5.06 m^2/g	-	S_{BET} = 39.6 m^2/g	-

Table 3.1. Composition of mineral dust samples used in this work.

[1] C.V. Clemency, Dept. of Geological Sciences, SUNY at Buffalo, Buffalo N.Y.(USA), for the Clay Minerals Society.
[2] Fluka AG, CH-9471 Buchs (Switzerland).
[3] Transmat SA, Route de Ferreyres, CH-1315 La Sarraz (Switzerland).
[4] F. Hanisch and J.N. Crowley, *Atmos.* Chem. Phys. 2003, 3, 119.
[5] Powder Technology Inc., 1433 Ewing Avenue S. Burnsville, MN 55306, USA.

In order to probe diffusion effects of NO$_3$ inside bulk powders, several additional reference experiments were carried out. Glass optical flats of 19.6 cm^2 were sprayed with a mineral dust suspension in methanol or water in order to obtain a sample whose total exposed surface is equal to the sample holder. Typically, 5 – 20 mg of powder can be deposited onto the glass support to full coverage judged by eye and resulting in an average thickness of less than 4 μm. The purpose of these experiments was to obtain samples consisting of a few monolayers ever so poorly characterized in order to probe the mass dependence of NO$_3$ uptake. Most of the experiments have been carried out with gram quantities rather than mg. Uptake experiments have been carried out using mineral dust samples that were pumped for half an hour to less than 10^{-7} Torr at T = 294 K after which no H$_2$O desorption has been observed.

3.2.3 NO$_3$ source

NO$_3$ was generated by thermal decomposition of N$_2$O$_5$ inside a 6 cm hot glass tube of 0.6 cm diameter ((5), Figure 2.1, Chapter 2) that was externally heated to 530 K using NiCr wire thereby approaching 100% decomposition of N$_2$O$_5$ under the chosen experimental conditions according to reaction (3.1):

$$N_2O_5 \rightarrow NO_2 + NO_3 \qquad\qquad (3.1)$$
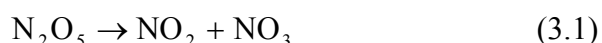
The gas phase residence time at ambient temperature of N$_2$O$_5$ in the gas injection line upstream of the NO$_3$ hot source has been calculated to be 5.7 s.

N$_2$O$_5$ flow rates were on the order of 10^{16} molecule s^{-1}. NO$_3$ was monitored using mass spectrometry at m/e = 62 (NO$_3^+$), HNO$_3$ at m/e = 63 (HNO$_3^+$), NO and NO$_2$ by REMPI detection at λ_{NO} = 452.6 nm and λ_{NO_2} = 511 nm, respectively. N$_2$O$_5$ did not have a measurable parent peak under our experimental conditions; the most intense peak was its fragment NO$_2^+$ at m/e 46. Both N$_2$O$_5$ and HNO$_3$ did not show any measurable contribution at m/e 62 in reference experiments such that these two species did not interfere with the MS detection of NO$_3$. In reference experiments of pure N$_2$O$_5$ m/e 62 was 0.01% of m/e 46.

Hydrolysis of N$_2$O$_5$ may occur on internal surfaces of the inlet line before admission into the hot glass 0.6 cm tube generating HNO$_3$ as an impurity on the order of 10 to 15%. HNO$_3$ does not thermally decompose inside the hot glass tube of the NO$_3$ source because we did not observe any change in the MS signal amplitude at m/e 63 when increasing the source temperature to 530 K. In addition, using pure NO$_2$-free HNO$_3$ flowing through the hot NO$_3$ source and using REMPI detection at $\lambda_{NO_2} = 511$ nm no REMPI signal of NO$_2$ from potential heterogeneous decomposition of HNO$_3$ on the hot walls of the source vessel was detected. We attribute this apparent resistance to decomposition to the small HNO$_3$ residence time of approximately 400 μs in the hot glass tube.

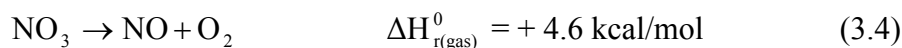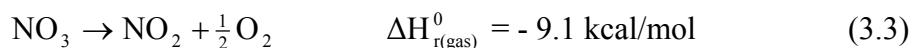### 3.2.4 Calibration of NO$_3$ and secondary reactions in the NO$_3$ source

The NO$_3$ concentration has been determined by titration with NO according to reaction (3.2) where the end point has been detected by monitoring the additional NO$_2$ at excess NO:

$$NO_3 + NO \rightarrow 2NO_2 \qquad\qquad (3.2)$$

With a NO concentration of approximately 1.0 x 10^{12} molecule cm^{-3} the reaction is fast enough to convert more than 90% of the NO$_3$ inside the reactor using $k_{(298K)} = 2.6$ x 10^{-11} cm^3 molecule^{-1} s^{-1}. The titration experiment at T = 298 K resulted in a yield of 143 $\pm$ 29% NO$_2$ and 54 $\pm$ 18% NO$_3$ (error represents one standard deviation) with respect to N$_2$O$_5$ decomposed. The deviation from the expected 100% yield for both NO$_2$ and NO$_3$ indicates a fast secondary decomposition reaction of NO$_3$ into NO$_2$ or NO within the hot glass tube of the source[18].

Both REMPI detection at λ_{NO_2} = 511 nm (NO$_2$) and MS detection at m/e 62 (NO$_3$) allowed us to verify the mass balance of NO$_3$ with N$_2$O$_5$ and to conclude that the thermal decomposition of N$_2$O$_5$ is complete and that therefore no N$_2$O$_5$ is present in the mixture of NO$_3$ and NO$_2$ coming from the NO$_3$ source.

Possible candidates for products resulting from wall decomposition of NO_3 are NO_2 and NO according to reactions (3.3) and (3.4):

$$NO_3 \rightarrow NO_2 + \tfrac{1}{2}O_2 \qquad \Delta H^0_{r(gas)} = -9.1 \text{ kcal/mol} \qquad (3.3)$$

$$NO_3 \rightarrow NO + O_2 \qquad \Delta H^0_{r(gas)} = +4.6 \text{ kcal/mol} \qquad (3.4)$$

In order to find the products of the wall decomposition of NO_3 without ambiguity we performed an ancillary experiment taking advantage of simultaneous REMPI detection of NO and NO_2 at $\lambda_{NO} = 452.6$ nm, the primary wavelength for NO detection (Chapter 2). In addition to NO, NO_2 is also detected at this wavelength owing to concomitant photolysis of NO_2 to NO and subsequent REMPI detection of NO as discussed at the end of chapter 2. As displayed in Figure 3.1, the ion yield for REMPI detection at $\lambda_{NO} = 452.6$ nm has been plotted as a function of $[NO_2]$ originating from a pure NO_2 flow (open triangles) together with the ion yield of $[NO_2]$ from a mixture of NO_2 and NO_3 originating from the hot NO_2 source (filled circles).
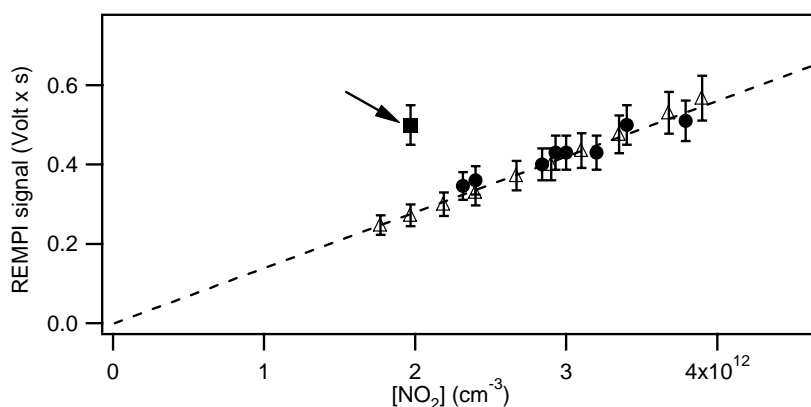
Figure 3.1. REMPI signal at $\lambda_{NO} = 452.6$ nm as a function of $[NO_2]$ for a pure NO_2 flow (open triangles) plotted together with the signal resulting from a mixture of NO_2 and NO_3 flowing out of the hot NO_3 source (filled circles). The point marked with the arrow represents the hypothetical REMPI signal at $\lambda_{NO} = 452.6$ nm if we have 10% of NO in a mixture of NO_2 and NO_3 at $[NO_3] = 2.0 \times 10^{12}$ cm^{-3}. The absolute concentrations of NO_2 and NO_3 have been separately determined using REMPI detection at $\lambda_{NO_2} = 511$ nm and MS at m/e 62, respectively, (orifice diameter = 8 mm).

Both [NO$_2$] and [NO$_3$] in the mixture have previously been independently determined by using REMPI detection at λ_{NO_2} = 511 nm for [NO$_2$] and the MS signal I^{62} at m/e 62 for [NO$_3$], respectively. Based on Figure 3.1, we conclude that reaction (3.3) is the reason for the excess of NO$_2$ over NO$_3$ (see above) because it shows the complete absence of NO detected at λ_{NO} = 452.6 nm. The fact that the REMPI signal of the pure NO$_2$ reference gas coincides with the mixture flowing out of the NO$_3$ source leads to the conclusion that NO must be absent from the mixture which excludes reaction (3.4) as a candidate for wall decomposition of NO$_3$. Figure 3.1 shows the expected REMPI signal of NO$_2$ containing 10% NO which is 50% larger compared to pure NO$_2$ owing to the four-fold higher sensitivity of NO vs. NO$_2$ at λ_{NO} = 452.6 nm as explained in Chapter 2. Figure 3.1 also shows that a 5% impurity of NO in NO$_2$ may be detected using REMPI. Potential NO that is formed heterogeneously following reaction (3.4) can only be partially titrated via reaction (3.2) because the titration rate is too slow in the absence of an excess of [NO$_3$]. Based on this slow titration rate NO should therefore be detectable if formed in reaction (3.4). We therefore exclude the heterogeneous decomposition of NO$_3$ according to reaction (3.4) with high confidence.

We were unable to measure any change in the O$_2$ signal following reaction (3.3) because molecular oxygen is present as a background gas in the Knudsen flow reactor owing to small leaks (o-ring seals). It was therefore impossible to separate the small expected O$_2$ contribution due to the NO$_3$ decomposition from the O$_2$ background. Molecular oxygen is the expected stable NO$_3$ decomposition product from both reaction pathways, reactions (3.3) and (3.4).

3.2.5   Wall loss of NO$_3$ in the Knudsen flow reactor

NO$_3$ itself was also subject to unspecified wall-loss in the Knudsen reactor as the measured rate of loss was consistently higher than the expected or calculated value (see Table 3.2). This indicated that a competing NO$_3$ loss process with a rate constant k$_{dec}$ adds to the expected, that is calculated, rate constant for effusion k$_{esc}$ based on the measured effusion rate of non-reactive gases such as N$_2$, Ar, CO$_2$ and SF$_6$. The relative concentration of NO$_3$

decreases with decreasing orifice size because it undergoes wall loss with increasing residence time in the Knudsen reactor. Lower signals at smaller orifices, that is, at longer residence time in the reactor, indicate a loss process for NO$_3$ [19]. The measured first-order rate of loss given by k' of NO$_3$ at a given escape orifice size of the reactor is based on the observed single-exponential decay of NO$_3$. It may actually be expressed as the sum of two components, namely k_{esc} and k_{dec}, representing escape, that is physical, and chemical loss, respectively:

$$k' = k_{esc} + k_{dec} \qquad (3.E1)$$

The measurement of k' at three different aperture sizes (Table 3.2) enabled the determination of $k_{dec} = 0.6 \pm 0.27$ s^{-1}. The additional loss process of NO$_3$ was found to be first order with respect to NO$_3$ and constant over the course of all performed experiments. In this work every measurement of k_{obs} has been performed using k' instead of k_{esc}. We determined the observed rate constant k_{obs} by taking k' = k_{esc} (theoretical value) + k_{dec}, where $k_{dec} = 0.6 \pm 0.27$ s^{-1}, as an effective loss process instead of k_{esc} by itself resulting in the following equation:

$$k_{obs} = \left(\frac{I_0^{62(NO_3)}}{I_r^{62(NO_3)}} - 1 \right) \cdot (k_{esc} + k_{dec}) \qquad (3.E2)$$

where $I_0^{62(NO_3)}$ and $I_r^{62(NO_3)}$ are MS signal at m/e 62 before and during reaction, respectively.

Ø escape orifice (mm)	Calculated k_{esc}(s^{-1})	Measured k$'$(s^{-1})	k_{dec} (s^{-1})
14	4.15	5.0	0.85
8	1.74	2.3	0.56
4	0.54	0.9	0.36

Table 3.2. Comparison of calculated rate constant for effusion, k_{esc}, and measured loss rate constant of NO$_3$, $k' = k_{esc} + k_{dec}$, in Knudsen flow reactor of differing orifice diameters.

3.2.6 Determination of the uptake coefficient

The net observed uptake coefficient for NO$_3$ is $\gamma_{obs} = \dfrac{k_{obs}}{\omega}$ and is only valid if the rate law

for uptake is first order in NO$_3$. In our data analysis, γ_{obs} was calculated using the geometric surface area of the sample holder which will be justified below based on additional reference experiments. In the present work the observed uptake coefficient γ_{obs}

became γ_{ss}, when the uptake of NO$_3$ monitored at m/e 62 clearly reached steady state at 400 s of exposure time whereas γ_0 equals γ_{obs} at t = 0 s, i.e. immediately after lifting the plunger. Upon increasing the exposure time by a factor of two, γ_{ss} did not change significantly.

Continuous flow uptake experiments were carried out at ambient temperature (298 ± 2 K) under molecular flow conditions. The concentration of NO$_3$ inside the Knudsen reactor was kept constant at (7.0 ±1.0) x 10^{11} and (4.0 ±1.0) x 10^{12} cm^{-3} for low and high [NO$_3$] experiments, respectively. The associated [NO$_2$] determined by REMPI was (1.7 ±1.0) x 10^{12} cm^{-3} for [NO$_3$] = (7.0 ±1.0) x 10^{11} and (7.3 ±2.0) x 10^{12} cm^{-3} for [NO$_3$] = (4.0 ±1.0) x 10^{12}. In ancillary experiments, it was found that NO$_2$ only interacted with Saharan Dust whereas all other examined surrogate dust samples did not show any reactivity towards NO$_2$ under the selected experimental conditions.

3.2.7 Product study

The mass spectra of the species involved in the NO$_3$ source share common fragment peaks when using MS detection. The main common fragment and molecular ion peaks for NO$_3$, N$_2$O$_5$, NO$_2$, NO and HNO$_3$ are m/e 46 and 30. The REMPI detection of NO$_2$ allowed us to subtract with great accuracy the contribution of NO$_2$ to the total MS signal I_0^{46} at m/e 46 originating from the source.

As indicated above, we observed that the NO$_3$ source contains HNO$_3$ as an impurity that contributes to the total MS signal at m/e 46. Fortunately, at the present experimental conditions HNO$_3$ has a measurable, albeit low intensity, parent peak at m/e 63. In order to evaluate the contribution of HNO$_3$ at m/e 63 and m/e 46, we have analyzed the MS

spectrum of pure HNO_3. The base and parent peak of HNO_3 are at m/e 46 (NO_2^+) and m/e 63 (HNO_3^+), respectively. In addition we did not observe any NO_2 impurity in HNO_3 following REMPI detection at $\lambda_{NO_2} = 511$ nm that is specific for NO_2.

In the following, the subscript 0 and r will refer to continuous gas uptake experiments in the absence and presence, respectively, of the solid sample.

Using the detailed mass spectrum of pure HNO_3 we have accurately determined the effective contribution of HNO_3 at m/e 46 by using the measured fragmentation pattern $f = \dfrac{I_0^{46(HNO_3)}}{I_o^{63(HNO_3)}} = 52 \pm 8$. The absolute NO_2 concentration $[NO_2]_{0(REMPI)}$ originating from the NO_3 source has been determined by means of REMPI detection according to equation (2.17). In order to calculate its corresponding MS signal contribution $I_{0(REMPI)}^{46(NO_2)}$ at m/e 46, we used the following equation:

$$I_{0(REMPI)}^{46(NO_2)} = \frac{F_0^{NO_2}}{C_{cal(NO_2)}} = \frac{[NO_2]_{0(REMPI)} \cdot k_{esc(NO_2)} \cdot V_{cell}}{C_{cal(NO_2)}} \qquad (3.E3)$$

where $C_{cal(NO_2)}$ is the NO_2 calibration factor obtained from equation (2.11) for pure NO_2 and $k_{esc(NO_2)}$ is its effusive loss rate constant. Equation (3.E3) allows one to calculate the fraction of the MS signal at m/e 46 owing to the presence of NO_2 using the measured REMPI signal for NO_2 to establish its absolute concentration. No molecular species including NO_3 other than NO_2 gives rise to a REMPI signal at $\lambda_{NO_2} = 511$ nm.

In the absence of any substrate, $I_{0(REMPI)}^{46(NO_2)}$ and $f \cdot I_0^{63(HNO_3)}$ have been subtracted from the total MS signal I_0^{46} at m/e 46 in order to attribute the remaining signal to the NO_2^+ fragment of the electron-impact ionization of NO_3 once the absence of undissociated N_2O_5 from the NO_3 source was established:

$$I_0^{46(NO_3)} = I_0^{46} - I_{0(REMPI)}^{46(NO_2)} - f \cdot I_0^{63(HNO_3)} \qquad (3.E4)$$

When the sample is exposed to the gases from the NO_3 source, NO_3 is taken up and reacts on the mineral dust surface resulting in a decrease of $[NO_3]$ which leads to a concomitant

decrease of the MS signal I_r^{46} at m/e 46. As shown in previous studies on mineral dust[20], HNO_3, present as an impurity, reacts on the dust surface without formation of volatile products that may contribute to the total MS signal I_r^{46}.

We have determined $r = \dfrac{I_0^{46(NO_3)}}{I_0^{62(NO_3)}} = 9.5 \pm 2.0$ as the ratio of the MS signal $I_0^{46(NO_3)}$ at m/e 46 (NO_2^+) and $I_0^{62(NO_3)}$ at m/e 62 (NO_3^+) for NO_3 free radical in the absence of a reactive substrate. As a result of the exposure of the sample to NO_3 we expect two possible reaction products: HNO_3 and/or N_2O_5. Under our experimental conditions HNO_3 may possibly be formed at high densities by heterogeneous recombination of NO_2 and NO_3 to N_2O_5 and subsequent heterogeneous hydrolysis. HNO_3 has in fact been observed at m/e 63 resulting from the interaction of NO_3 with excess NO_2 under the present experimental conditions. In order to find other possible reaction products contributing to an excess I_{exc}^{46} at MS signal intensity at m/e = 46 not due to HNO_3, we have subtracted the following known contributions from the total MS signal I_r^{46} : a) $I_{r(REMPI)}^{46(NO_2)}$ for NO_2, b) $r \cdot I_r^{62(NO_3)}$ for NO_3, c) $f \cdot I_r^{63(HNO_3)}$ for the possible HNO_3 formation during the reaction. The final expression for the residual amplitude I_{exc}^{46} resulted from the following equation:

$$I_{exc}^{46} = I_r^{46} - I_{r(REMPI)}^{46(NO_2)} - r \cdot I_r^{62(NO_3)} - f \cdot I_r^{63(HNO_3)} \qquad (3.E5)$$

The resulting residual MS signal from equation (3.E5) is related to reaction products owing to the heterogeneous interaction of NO_3 with the exposed surface of the sample. It is reasonable to expect that N_2O_5 may be the only reaction product contributing to m/e 46 as will be discussed below.

It was not possible to quantify the possible formation of NO by REMPI detection at $\lambda_{NO} = 452.6$ nm because its concentration dropped below our detection limit at the chosen detection conditions. Therefore, in order to estimate a possible excess at m/e 30 (I_{exc}^{30}) due to NO formation during the exposure of mineral dust substrates to NO_3, we have corrected the total MS at m/e 30 for the contribution of NO_3, HNO_3, NO_2 and N_2O_5. In all uptake experiments of NO_3 with mineral dust substrates $I_{exc}^{30} = 0$. The detailed procedure utilized to determine I_{exc}^{30} has been reported in Chapter 5 for reaction of NO_3 on soot.

3.2.8 Experimental uncertainties

The uncertainties for NO$_3$ and HNO$_3$ were determined from the signal to noise ratio of the MS signal at m/e 62 and m/e 63 and were estimated at $\pm$ 15 % and $\pm$ 20 %. The uncertainties for [NO] and [NO$_2$] were estimated at $\pm$ 15 % and $\pm$ 10 %, respectively. They have been determined from the signal to noise ratio of the REMPI signal at $\lambda_{NO} = 452.6$ nm and $\lambda_{NO_2} = 511$ nm, respectively.

Based on the uncertainty of f ($\pm$ 8 %) and on a typical uncertainty of $\pm$ 10 % of the REMPI signal the resulting overall uncertainty for $I_0^{46(NO_3)}$ is estimated at $\pm$ 18 %. On the other hand, the composite uncertainty of I_{exc}^{46} is evaluated at $\pm$ 45 % based on the relative uncertainties of 10, 15 and 20 % for the REMPI signal of NO$_2$ as well as the MS signal contributions of NO$_3$ and HNO$_3$ to m/e 46, respectively. Therefore, N$_2$O$_5$ will be the only species that will be measured at an appreciable uncertainty of $\pm$ 45 % owing to the numerous subtracted contributions at m/e 46.

3.3 Uptake of NO$_3$: Results and Discussion

Typical raw data of an uptake experiment of NO$_3$ on 2g of CaCO$_3$ are shown in Figure 3.2a. After a steady flow of NO$_3$ had been established, the isolation plunger is lifted at t = 400 s and the substrate is exposed to the NO$_3$ flow. Because of the uptake of NO$_3$ on CaCO$_3$, the number of molecules effusing through the escape orifice into the MS decreases immediately. In all the performed experiments, NO$_3$ adsorbed on available surface sites gave rise to uptake of NO$_2$ that stems from the thermal decomposition of N$_2$O$_5$ and NO$_3$ (reactions (3.1) and (3.3)). This leads to a net decrease of the REMPI signal for NO$_2$ at $\lambda_{NO_2} = 511$ nm.
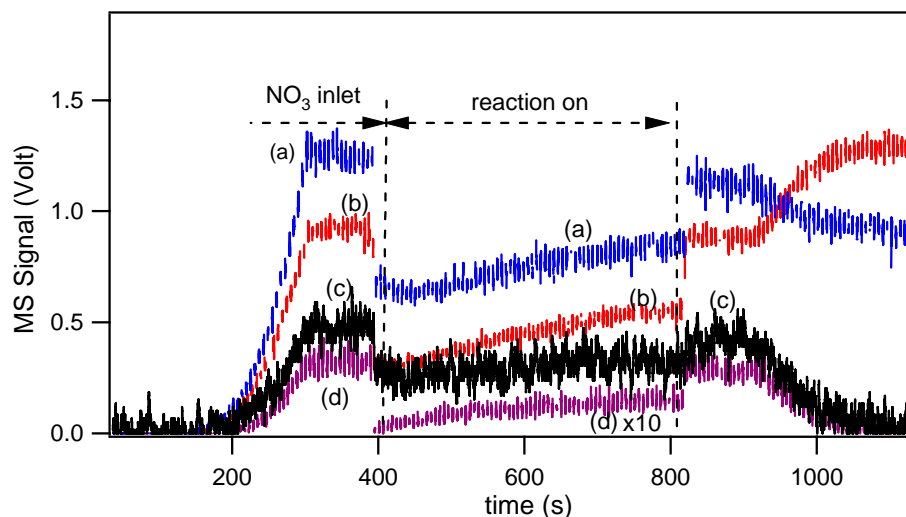
Figure 3.2a. Typical Knudsen reactor experiment for NO_3 uptake on a sample of 2g of $CaCO_3$ at $[NO_3] = (7.0 \pm 1.0)$ x 10^{11} cm^{-3} (orifice diameter = 8 mm, A_s = 19.6 cm^2). Curves (a), (b) and (d) correspond to the raw MS signals monitored at m/e 30, m/e 46 and m/e 62, respectively. Curve (c) corresponds to the raw REMPI signal for NO_2 detection at $\lambda_{NO_2} = 511$ nm converted to a MS signal at m/e 46.
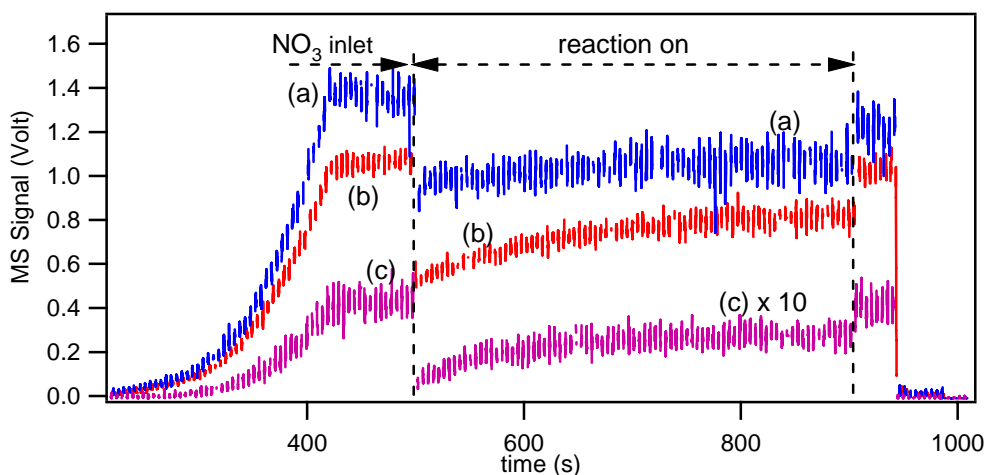

Figure 3.2b. Typical Knudsen reactor experiment for NO_3 uptake on a sample of 2g of $CaCO_3$ at $[NO_3] = (7.0 \pm 1.0)$ x 10^{11} cm^{-3} (orifice diameter = 14 mm, A_s = 19.6 cm^2). Curves (a), (b) and (c) correspond to the raw MS signals monitored at m/e 30, m/e 46 and m/e 62, respectively.

As the exposure time increases, the MS signal at m/e 62 (curve (d), Figure 3.2a) partially recovers, indicating a decrease in the rate of uptake of NO$_3$ presumably owing to a decrease of the number of available surface sites for reaction. This results in an apparent reduction of the uptake coefficient. At t = 820 s the sample compartment is sealed by lowering the plunger and the MS signal at m/e 62 returns to its initial value. Figure 3.2b shows analogous results for the largest escape orifice leading to a larger rate of NO$_3$ uptake on solid CaCO$_3$. The lower concentration and the concomitant lower residence time τ_g of NO$_3$ in the reactor results in a lower degree of saturation and thus enhanced uptake.

In order to unravel whether or not the effective available surface area is influenced by the internal surface area formed by interstitial voids between individual dust particles, the mass dependence of the NO$_3$ uptake on Kaolinite was measured in the Knudsen flow reactor at ambient temperature and at [NO$_3$] = (7.0 $\pm$ 1.0) x 10^{11} cm^{-3}. The mass of Kaolinite ranged from 5 mg to 1 g and the results are shown in Figure 3.3.

For the experiments performed at masses between 5 and 30 mg we used sprayed samples, whereas for masses between 110 mg and 1g Kaolinite powder samples were used.
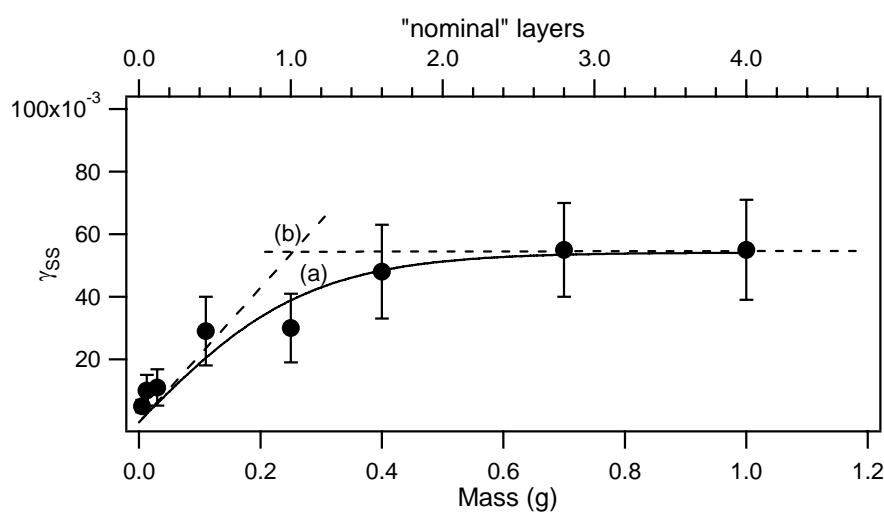
Figure 3.3. Uptake of NO$_3$ on Kaolinite: dependence of the steady state uptake coefficient γ_{ss} on sample mass at [NO$_3$] = (7.0 $\pm$ 1.0) x 10^{11} cm^{-3} (orifice diameter = 8 mm, A$_s$ = 19.6 cm^2). The number of nominal layers is reported on the upper abscissa. Full circles: experimental values. Curve (a): fit of the data using the pore diffusion model. Point (b): intersection of the linear and horizontal part of the curve which corresponds to the mass of one nominal layer of Kaolinite (see text).

Table 3.3 reports values of γ_{ss} using the geometric surface area of the sample holder that increase linearly with mass at low masses as displayed in Figure 3.3. Samples of mass below 250 mg were considered part of this linear mass-dependent regime beyond which γ_{ss} converged to a limiting value of $\gamma_{ss} = 5.5 \times 10^{-2}$ corresponding to 4.5×10^{17} molecules of NO_3 taken up during a reaction time of 400 s. The significance of this number will be discussed below. Increasing the sample mass beyond 250 mg at the intersection of the linear mass dependence (point (b)) of γ_{ss} in Figure 3.3 with the horizontal line, γ_{ss} had no effect on γ_{ss} as well as the amount of adsorbed NO_3 because apparently not the entire internal sample surface area is available for NO_3 adsorption. The limiting γ_{ss} value represents the maximum amount of NO_3 able to interact with Kaolinite powder within the NO_3 residence time owing to the inability of NO_3 to penetrate into the sample.

Mass (g)	γ_{ss}	Number of nominal layers[c]	Number of formal layers[d]
0.005[a]	$(5.0 \pm 2.0) \times 10^{-3}$	0.02	1
0.013[a]	$(1.0 \pm 0.5) \times 10^{-2}$	0.05	3
0.03[a]	$(1.1 \pm 0.6) \times 10^{-2}$	0.12	6
0.11[a]	$(2.9 \pm 1.1) \times 10^{-2}$	0.44	22
0.25[b]	$(3.0 \pm 1.1) \times 10^{-2}$	1	50
0.4[b]	$(4.8 \pm 1.5) \times 10^{-2}$	1.6	82
0.7[b]	$(5.5 \pm 1.5) \times 10^{-2}$	2.8	143
1.0[b]	$(5.5 \pm 1.6) \times 10^{-2}$	4	204

[a] Sprayed sample. [b] Powder sample. [c] Calculated for average grain size of 50 μm. [d] Calculated for an average grain size of 1 μm disclosed by the manufacturer albeit without documentation.

Table 3.3. Summary of uptake experiments with NO_3 on Kaolinite as a function of sample mass at $[NO_3] = (7.0 \pm 1.0) \times 10^{11}$ cm^{-3}, orifice diameter = 8 mm, A_s = 19.6 cm^2.

In order to determine the number of layers, N_L, the total volume of Kaolinite powder was calculated from its true density $\rho_t = 2.3$ g/cm^3 and the mass of the sample spread out across the geometric area of the sample holder ($V_{tot} = m/\rho_t$). From the average particle size d and

the measured thickness of the sample h_{tot} we calculated the number of layers. Therefore, the number of layers has been expressed as $N_L = \dfrac{h_{tot}}{d} = \dfrac{V_{tot}}{A_S d} = \dfrac{m}{\rho_t A_S d}$.

The number of formal layers calculated for an average sample grain diameter of 1.0 μm is reported in Table 3.3. The typical grain diameter of 1.0 μm has been obtained from the manufacturer's undocumented specifications of the used Kaolinite powder. However, most mineral dust powders are porous materials and the microstructure of the dust substrate is composed of clusters of random distribution with interstitial voids between them. Therefore it is more reasonable to take into account a grain size diameter that is much larger than 1.0 μm as suggested by electron microscopy (SEM) (Figure 3.4) of similar material where characteristic grain diameters are in the tens of μm (© OMNI Laboratories, Inc, http://www.omnilabs.com/).

Figure 3.3 shows that a mass of 250 mg corresponds to one nominal layer of 50 μm diameter Kaolinite spread out over the geometric surface of the sample holder (19.6 cm^2). Thus, one nominal layer of Kaolinite will contain closely packed spheres of "effective" grain diameter of 50 μm knowing full well that the sample in reality is multidisperse and structurally heterogeneous. Therefore, the linear mass-dependent portion of γ_{ss} vs. mass corresponds to a sample holder partially covered with 50 μm diameter Kaolinite particles which is the structural model we adopt in this work.
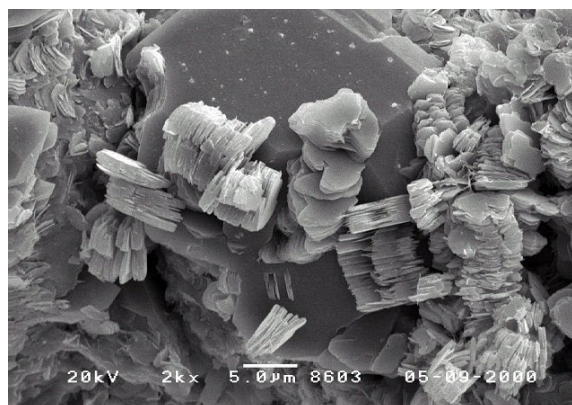
Figure 3.4. SEM-image of a Kaolinite powder sample: Authigenic kaolinite plates covering a quartz grain overgrown with authigenic quartz. SEM image of a core sample (© OMNI Laboratories, Inc, http://www.omnilabs.com/).

The use of the BET (Brunauer-Emmett-Teller) surface area and the Pore Diffusion Theory (KLM)[21] (see appendix) would substantially underestimate the true uptake coefficient based approximately on A_s, the geometric surface area, between a factor of 10^2 to 10^3. The application of the pore diffusion theory results in $\gamma_{pd} = 1.7 \times 10^{-5}$, using a tortuosity factor $\tau = 2$ for a grain size of 1 μm (curve (a), Figure 3.3). The assumption that NO_3 interacts with the BET internal surface leads to $\gamma_{BET} = 2.0 \times 10^{-4}$ in contrast to $\gamma_{geom} = (5.5 \pm 1.5) \times 10^{-2}$ calculated on the basis of the geometrical surface area of the sample and displayed in Table 3.3. In order to show that this underestimation of γ resulting from the application of the KLM model or the BET surface is excessive we have performed NO_3 and NO_2 uptake experiments on activated molecular sieve particles that consist of macroscopic rods with a certified pore diameter of 3, 5 and 10 Å.

The strategy of this experiment is to compare γ_{ss} of NO_3 between a microporous material whose average pore diameter enables penetration of the NO_3 probe, and one that does not allow for pore diffusion because of geometrical constraints. In case no large increase of γ_{ss} is observed in going from small to large pore size one must conclude that pore diffusion will not occur to a significant extent during the lifetime of NO_3 in the reactor.

We chose the following molecular sieve particles having micropores of different diameters: $K_{12}[(AlO_2)_{12}(SiO_2)_{12}] \cdot XH_2O$, with pore diameter of 3 Å, $Ca_{12}[(AlO_2)_{12}(SiO_2)_{12}] \cdot XH_2O$, with pore diameter of 5 Å and $Na_{86}[(AlO_2)_{86}(SiO_2)_{106}] \cdot XH_2O$ (Fluka) with pore diameter of 10 Å, and where X represents the equilibrium H_2O content exclusive of water remaining adsorbed in the molecular pores. In order to rid the sample of adsorbed water, molecular sieves have been activated by pumping and heating to 200°C. For 9 g of molecular sieve which resulted in the complete coverage of the 19.6 cm^2 sample support we estimated an external surface area of 1.6×10^2 cm^2 leading to 1.8×10^{-3} $m^2 g^{-1}$. The internal surface area for molecular sieves of different diameter has been reported in Table 3.4 and is consistent with a ratio r of internal to external surface area of 2.5×10^5, 1.95×10^5 and 1.4×10^5, respectively, for the molecular sieve materials listed in Table 3.4. We estimate that NO_3 has a characteristic size of approximately 4.5 Å which would lead to a surface density of approximately 5.0×10^{14} molecule cm^{-2}. Therefore, uptake of NO_3 on molecular sieve of 3 Å pore size should not take place on the internal surface of the pores in contrast to 5 and 10 Å molecular sieve where extensive pore diffusion of NO_3 is expected, at a given sufficient interaction time.

Molecular sieve (nominal pore diameter Å)	γ_{ss} [NO$_3$] = 7.0 x 10^{11} cm^{-3}	γ_{ss} [NO$_2$] = 3.0 x 10^{11} cm^{-3}	BET Surface area (m^2 g^{-1})[22]	r[a]
10	(1.0 ± 0.3) x 10^{-2}	(1.2 ± 0.2) x 10^{-3}	455	2.5 x 10^5
5	(7.8 ± 3.1) x 10^{-3}	(7.4 ± 1.3) x 10^{-4}	333	1.9 x 10^5
3	(5.7 ± 2.2) x 10^{-3}	(7.1 ± 1.9) x 10^{-4}	243	1.4 x 10^5

[a] ratio of internal to external surface area.

Table 3.4. Summary of the uptake experiments of NO$_3$ and NO$_2$ on 9 g of activated molecular sieve particles of different pore size: steady state (γ_{ss}) uptake coefficients at an orifice diameter = 8 mm and A$_s$ = 19.6 cm^2.

As displayed in Figure 3.5 and reported in Table 3.4, γ_{ss} for the 3 and 5 Å pore size molecular sieve samples were found to be identical within experimental uncertainty. In addition, for molecular sieve particles of nominal 10 Å pore diameter we observed γ_{ss} value larger by a factor 1.7 at a residence time of 0.58 s (8 mm orifice) for NO$_3$. The spread in γ_{ss} between the different molecular sieves is only a factor of 1.7, whereas we expected NO$_3$ to explore the internal microporous structure of the 5 and certainly of the 10 Å molecular alumosilicate sieve material, both of which are expected to lead to a marked increase in γ_{ss}.
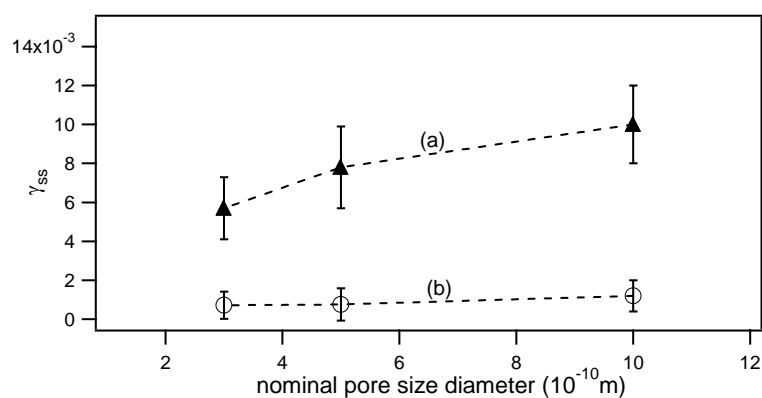
Figure 3.5. Uptake experiment performed on activated molecular sieve samples: γ_{ss} as a function of the certified pore diameter. Triangles: [NO$_3$] = (7.0 ± 1.0) x 10^{11} molecule cm^{-3} (k$_{esc}$ = 1.75 s^{-1}),

Circles: [NO$_2$] = (6.0 ± 1.0) x 10^{11} molecule cm^{-3} (k$_{esc}$ = 2.0 s^{-1}). All experiments have been performed at an orifice diameter of 8 mm and a surface sample area A$_s$ of 19.6 cm^2

We emphasize that the three microporous materials had identical interstitial voids because ceramic particles of identical dimension have been used in experiments using the same mass for all three types of molecular sieve. Therefore the packing of the molecular sieve was identical for all experiments. We conclude that on the time scale of our experiment NO$_3$ does not explore the internal surface of the pores where pore diffusion is expected on geometrical grounds, namely on the 5 and 10 Å molecular sieves. The same result has been obtained employing the less reactive radical NO$_2$ (Table 3.4) whose extent of pore diffusion is expected to be larger in view of its smaller γ value as displayed in Figure 3.5.

Mineral dust sample	Mass (g)	γ$_0$ [NO$_3$]$_0$ = (7.0 ±1.0) x 10^{11} cm^{-3}	γ$_0$ [NO$_3$]$_0$ = (4.0 ±1.0) x 10^{12} cm^{-3}
CaCO$_3$	2	0.13 ± 0.1	0.14 ± 0.05
Natural limestone	2	0.12 ± 0.08	0.20 ± 0.07
Kaolinite	1	0.11 ± 0.08	0.12 ± 0.04
Saharan Dust	1	0.23 ± 0.2	0.16 ± 0.05
Arizona Test Dust	2	0.20 ± 0.10	0.14 ± 0.04
	Mass (g)	γ$_{ss}$ [NO$_3$]$_0$ = (7.0 ±1.0) x 10^{11} cm^{-3}	γ$_{ss}$ [NO$_3$]$_0$ = (4.0 ±1.0) x 10^{12} cm^{-3}
CaCO$_3$	2	(6.7 ± 4.0) x 10^{-2}	(1.4 ± 0.4) x 10^{-2}
Natural limestone	2	(3.4 ± 1.6) x 10^{-2}	(2.2 ± 0.5) x 10^{-2}
Kaolinite	1	0.14 ± 0.02	(5.0 ± 1.4) x 10^{-2}
Saharan Dust	1	0.12 ± 0.08	(6.5 ± 1.2) x 10^{-2}
Arizona Test Dust	2	0.10 ± 0.06	(2.5 ± 0.7) x 10^{-2}

Table 3.5. Summary of Uptake Experiments of NO$_3$ on mineral dust samples: initial (γ$_0$) and steady state (γ$_{ss}$) uptake coefficients at an orifice diameter = 8 mm, A$_s$ = 19.6 cm^2.

We take this result as convincing justification to use the geometric surface area in evaluating the gas-surface collision frequency ω under the constraint of the present experimental condition of low gas-phase residence times. We think that the present conclusion may overestimate the true γ value by up to a factor of two if we approximate the

shape of the ceramic material by a half sphere and assume a closely-packed arrangement. According to Table 3.5 we use Kaolinite as a typical example to extrapolate the kinetics to the other samples because its γ_0 is smallest compared to the other examined substrates. However, we also note that γ_0 is almost identical for all investigated samples within experimental uncertainty. Table 3.5 reports all results concerning experiments performed on $1 - 2$ g of surrogate mineral dust powder at the high concentration of $[NO_3] = (4.0 \pm 1.0) \times 10^{12}$ cm^{-3}. The steady-state uptake coefficients γ_{ss} of NO$_3$ range from $(1.4 \pm 0.4) \times 10^{-2}$ for CaCO$_3$ to $(6.5 \pm 1.1) \times 10^{-2}$ for Saharan Dust using the geometric surface area. At the lower concentration of $[NO_3] = (7.0 \pm 1.0) \times 10^{11}$ cm^{-3} we found larger γ_{ss} values ranging from $(3.4 \pm 1.6) \times 10^{-2}$ for natural limestone to (0.12 ± 0.08) for Saharan Dust compared to the experiments at higher $[NO_3]$. In Table 3.5 we also report the measured γ_0 values for NO$_3$ on all the samples of mineral dust at low and high values of $[NO_3]$. For the low value of $[NO_3] = (7.0 \pm 1.0) \times 10^{11}$ cm^{-3} the γ_0 values range from 0.12 ± 0.08 for Kaolinite to 0.23 ± 0.2 for Saharan Dust. At the high value of $[NO_3] = (4.0 \pm 1.0) \times 10^{12}$ cm^{-3} the γ_0 values range from 0.12 ± 0.04 for Kaolinite to 0.2 ± 0.07 for natural limestone. In comparison, γ_{ss} is lower only by a factor of two relative to γ_0 obtained at the same experimental conditions of low $[NO_3]$. Table 3.5 shows in general that the values of γ_{ss} and γ_0 are larger for low compared to high values of $[NO_3]$ which we attribute to partial inhibition of adsorption sites for NO$_3$. We take the small difference between γ_0 and γ_{ss} at both values of $[NO_3]$ as an additional confirmation for the absence of pore diffusion because γ_0 should only be minimally affected by pore diffusion and is expected to come close to the true value of the initial uptake coefficient. From Table 3.5 we may conclude that the uptake of NO$_3$ on mineral dust measured at low $[NO_3]$ is rapid. We propose to take the evidence of the high reactivity of NO$_3$ and the fact that diffusion of NO$_3$ into a porous material, such as molecular sieves, is immeasurably slow at our experimental conditions as an argument to convince the reader of the non-applicability of pore diffusion in the present case[21].
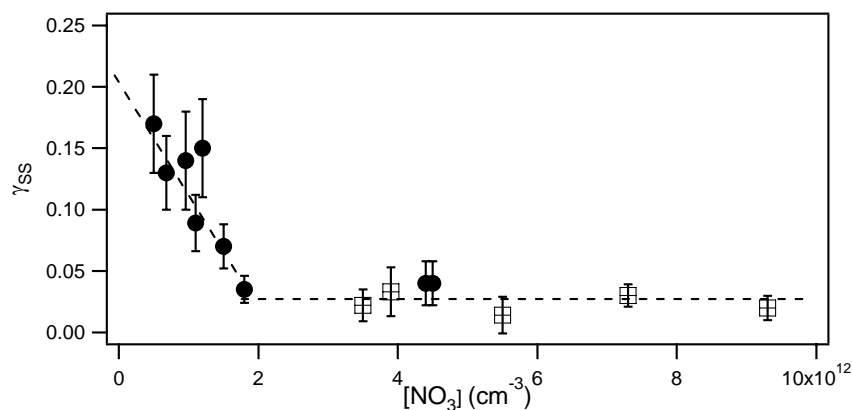
Figure 3.6. NO_3 on Kaolinite: uptake coefficient γ_{ss} of NO_3 as a function of $[NO_3]$ ($A_s = 19.6$ cm^2). Full circles and squares represent the experimental uptake values obtained at 4 and 8 mm orifice diameter, respectively.

$[NO_3]$ cm^{-3}	γ_{ss}
[a] 5.0×10^{11}	$(1.7 \pm 0.4) \times 10^{-1}$
[a] 6.8×10^{11}	$(1.3 \pm 0.3) \times 10^{-1}$
[a] 9.6×10^{11}	$(1.4 \pm 0.4) \times 10^{-1}$
[a] 1.1×10^{12}	$(8.9 \pm 2.3) \times 10^{-2}$
[a] 1.2×10^{12}	$(1.5 \pm 0.4) \times 10^{-1}$
[a] 1.5×10^{12}	$(7.0 \pm 1.8) \times 10^{-2}$
[a] 1.8×10^{12}	$(3.5 \pm 1.1) \times 10^{-2}$
[b] 3.5×10^{12}	$(2.2 \pm 1.3) \times 10^{-2}$
[b] 3.9×10^{12}	$(3.3 \pm 2.0) \times 10^{-2}$
[a] 4.4×10^{12}	$(5.0 \pm 1.6) \times 10^{-2}$
[a] 4.5×10^{12}	$(5.0 \pm 1.6) \times 10^{-2}$
[b] 5.5×10^{12}	$(1.4 \pm 1.5) \times 10^{-2}$
[b] 7.3×10^{12}	$(3.0 \pm 0.9) \times 10^{-3}$
[b] 9.3×10^{12}	$(2.0 \pm 1.0) \times 10^{-2}$

Experiments performed using an escape orifice diameter of: [a)] 8 mm, [b)] 4 mm.

Table 3.6. Uptake experiments of NO_3 on 1g of Kaolinite: steady state (γ_{ss}) uptake coefficients ($A_s = 19.6$ cm^2).

As already pointed out above, γ_0 is similar for all samples. However, this is not the case for γ_{ss} which reflects the different saturation behavior of the mineral dust samples which is also the reason for the increasing difference between γ_0 and γ_{ss} with increasing $[NO_3]$.

Several uptake experiments of NO_3 on 1g of Kaolinite powder were carried out at different $[NO_3]$ (Table 3.6).

Figure 3.6 displays data for the 8 and 4 mm escape orifice corresponding to a residence time τ_g of 0.57 s and 2.1 s, respectively, for a variation of $[NO_3]$ between 5.5×10^{11} and 9.3×10^{12} cm^{-3}. We observe two limiting values of γ_{ss}: a) for $[NO_3]$ increasing from 5.5×10^{11} cm^{-3} to 1.8×10^{12} cm^{-3} γ_{ss} decreases from $(1.7 \pm 0.4) \times 10^{-1}$ to $(3.5 \pm 1.1) \times 10^{-2}$, b) for $[NO_3]$ between 1.8×10^{12} cm^{-3} and 9.3×10^{12} cm^{-3} γ_{ss} is constant at $(3.2 \pm 1.4) \times 10^{-2}$ within experimental uncertainty and independent of $[NO_3]$. From this series of measurements it is evident that γ_{ss} follows a rate law pseudo first order in NO_3 at $[NO_3] > 1.8 \times 10^{12}$ cm^{-3}. Conversely, at $[NO_3] < 1.8 \times 10^{12}$ cm^{-3} the inverse dependence of γ_{ss} on $[NO_3]$ suggests that the mechanism of NO_3 uptake is complex and does not correspond to simple first-order uptake.

A similar dependence has been observed before by Hanisch and Crowley[23] in their work on ozone decomposition on Saharan dust and by Sullivan and coworkers[24] in their study of ozone decomposition on fresh alumina films. The reason for this behaviour may be related to the finite number of available surface sites of the substrate that are not completely saturated at low $[NO_3]$ resulting therefore in a larger uptake coefficient compared to high $[NO_3]$. It is the interplay between the finite number of adsorption sites and the competitive rates of desorption and surface reaction of NO_3 that leads to this typical inhibition behaviour that was also observed for other free radicals interacting with a solid substrate, so for example for NO_2 interacting with soot[25].

Further experiments performed on natural limestone and $CaCO_3$ showed a strong dependence of γ_{ss} on the gas residence time at $[NO_3] = 2.3 \times 10^{12}$ cm^{-3} suggesting that the mechanism of NO_3 uptake is complex and does not correspond to a simple first order uptake reaction as already pointed out for Kaolinite. The γ_{ss} value decreased from $(5.1 \pm 2.0) \times 10^{-2}$ to $(2.7 \pm 1.1) \times 10^{-2}$ in going from $\tau_g = (1/k_{esc}) = 0.24$ s ($k_{esc} = 4.15$ s^{-1}) to $\tau_g = 1.85$ s ($k_{esc} = 0.54$ s^{-1}). These observations indicate that the reactivity of NO_3 on natural limestone and $CaCO_3$ decreases for long gas residence times τ_g as the heterogeneous reaction rate not only depends on the gas phase concentration but apparently

also on intermediates whose surface concentration depend on the extent of reaction that scales with τ_g.

3.4 Reaction products

In all experiments adsorbed NO$_3$ gave rise to uptake of NO$_2$ that is associated with the NO$_3$ source. It is important to note that NO$_2$ itself did not show any uptake on the mineral dust surrogates, except for Saharan Dust, where $\gamma_{ss} = (3.1 \pm 0.5)$ x 10^{-3} has been observed for pure NO$_2$ uptake. For 250 mg of Kaolinite we have observed the formation of small amounts of gas phase reaction products such as N$_2$O$_5$ and HNO$_3$. Using equation (3.E5) we have calculated the rate of formation of N$_2$O$_5$ from the increase of the MS signal at m/e 46, I_{exc}^{46}, displayed in Figure 3.7 (curve (c)). From the experiment displayed in Figure 3.7 we conclude that for an initial value of [NO$_3$] = (6.5 $\pm$ 1.0) x 10^{11} cm^{-3} and in the presence of [NO$_2$] = (1.2 $\pm$ 1.0) x 10^{12} cm^{-3} (8.8 $\pm$ 2.0) x 10^{11} molecule cm^{-3} of N$_2$O$_5$ are produced at steady state conditions. The yield of N$_2$O$_5$ following the uptake of NO$_3$ decreased with increasing saturation of Kaolinite which may be explained by the slow deactivation of reactive surface sites and by the complete saturation of the NO$_3$ uptake at the end of the exposure time after the adsorption of 9.5 x 10^{17} NO$_3$ molecules (Figure 3.7 (curve b)). For the NO$_3$ uptake on 250 mg of Kaolinite we also observed a small contribution of m/e 63, $I_r^{63(HNO_3)}$, related to the production of gas phase HNO$_3$ as displayed in Figure 3.7 (curve (d)). At these experimental conditions this corresponds to the production of (1.2 $\pm$ 1.5) x 10^{10} molecule cm^{-3} of HNO$_3$ at steady state.

As pointed out above, NO$_3$ may be represented by a 4.5 Å diameter sphere with a projected surface area of 1.59 x 10^{-15} cm^2/molecule which leads to a full surface coverage of 6.3 x 10^{14} molecules cm^{-2}. The 250 mg sample has a total surface area of 5.5 x 10^4 cm^2 based on a BET surface area of 22 m^2/g for Kaolinite. This leads to 1.3x10^{16} and 3.5 x 10^{19} NO$_3$ forming a monolayer on 250 mg Kaolinite based on the geometric and BET surface area, respectively.
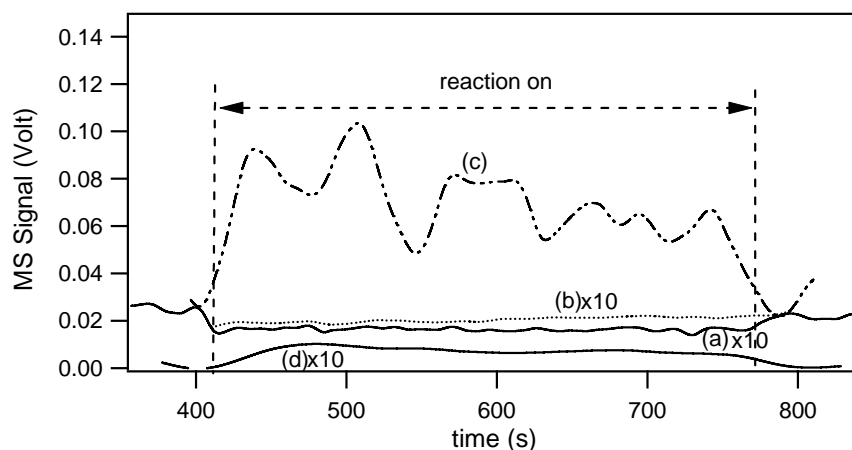
Figure 3.7. Uptake of NO$_3$ on 250 mg of Kaolinite and resulting reaction products at [NO$_3$] = (6.5 ± 1.0) x 10^{11} molecule cm^{-3}. Curve (a) represents the raw MS signal at m/e 62 for the NO$_3$ uptake on the DELRIN$^{®}$ sample holder with Kaolinite, the dashed line (curve (b)) indicates $I_r^{62(NO_3)}$ of the NO$_3$ uptake corrected for the DELRIN$^{®}$ contribution. Curve (c) is the calculated MS signal at m/e 46, I_{exc}^{46}, corresponding to N$_2$O$_5$ formation. The variable amplitude of curve (c) is the consequence of the large experimental uncertainty. Curve (d) represents the raw MS signal at m/e 63, $I_r^{63(HNO_3)}$, related to the production of gas phase HNO$_3$ (orifice diameter = 8 mm, A$_s$ = 4.9 cm^2).

The total number of 9.5 x 10^{17} molecules of NO$_3$ taken up on 250 mg of Kaolinite leads to a surface concentration of $\frac{9.5x10^{17}}{5.5x10^{4}} = 1.72x10^{13}$ molecule cm^{-2} which corresponds to a coverage (θ) of approximately 2.7 % based on the BET surface area.

Next to Kaolinite, samples of 250 mg of CaCO$_3$ have been the only samples to show formation of N$_2$O$_5$ and HNO$_3$ upon uptake of NO$_3$ (see Table 3.7). When the samples begin to saturate, the observed amounts of N$_2$O$_5$ and HNO$_3$ both decrease. In order to understand the reason for the gas phase production of N$_2$O$_5$ and HNO$_3$ we have to remind the reader that all the investigated samples have a non negligible amount of adsorbed water available on the substrate surface. The significant quantity of adsorbed H$_2$O$_{(ads)}$ that still remains on the different mineral dust substrates at our experimental conditions is reported in Table 3.7 and was measured by gravimetric measurements. Adsorbed water may therefore play an important role for the uptake of NO$_3$ on all samples examined in the Knudsen reactor.

Under our experimental conditions the formation of N$_2$O$_5$ may be related to the presence of NO$_2$ effusing from the NO$_3$ source via its reaction with adsorbed NO$_3$ on the mineral dust

substrate. The observed simultaneous uptake for both NO_3 and NO_2 suggests the formation of $N_2O_{5(ads)}$ through the heterogeneous recombination reaction (3.5a):

$$NO_{3(ads)} + NO_2 \rightarrow N_2O_{5(ads)} \qquad (3.5a)$$
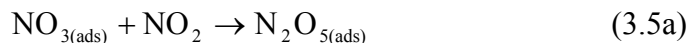
The conversion of NO_3 to N_2O_5 occurs via an Eley-Rideal mechanism where NO_3 first adsorbs onto the dust surface as $NO_{3(ads)}$ and subsequently reacts with gas phase NO_2. This reaction is the interfacial analogue of the well known gas-phase equilibrium:

$$NO_2 + NO_3 + M \quad \leftrightarrows \quad N_2O_5 + M \qquad (3.5b)$$
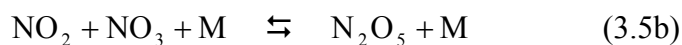
whose equilibrium constant is known from recent work[26].

Once N_2O_5 has been adsorbed, it may desorb into the gas phase:

$$N_2O_{5(ads)} \rightarrow N_2O_{5(g)} \qquad (3.5c)$$

Mineral Dust Sample	[a]γ_0	Reaction Products (250 mg)		[b]γ_{ss}	Reaction Products (1g)		Adsorbed water	BET surface area (m^2 g^{-1})
		[c]N$_2$O$_5$	[c]HNO$_3$		[d]N$_2$O$_5$	[d]HNO$_3$	H$_2$O$_{(ads)}$ [mg g^{-1}]	
CaCO$_3$	$(7.9 \pm 2.0) \times 10^{-2}$	12%	15%	$(1.4 \pm 0.8) \times 10^{-2}$	-	17%	4	5.06
Kaolinite	$(2.1 \pm 0.5) \times 10^{-2}$	23%	16%	$(5.0 \pm 1.5) \times 10^{-2}$	-	15%	23	22.57
Arizona Test Dust		-	-	$(2.5 \pm 1.0) \times 10^{-2}$	-	20%	22	
Saharan Dust		-	-	$(6.5 \pm 2.0) \times 10^{-2}$	-	-	20	39.6
Natural Limestone		-	-	$(1.2 \pm 0.4) \times 10^{-2}$	-	35%	7	

[a] Uptake experiment performed at $[NO_3]_0 = (7.0 \pm 1.0) \times 10^{11}$ cm^{-3} on 250 mg of sample. [b] Uptake experiment performed at $[NO_3]_0 = (2.3 \pm 1.0) \times 10^{12}$ cm^{-3} on 1 g of sample. [c] Saturated sample (250 mg, $A_s = 4.9$ cm^2). [d] Non-saturated sample (1 g, $A_s = 19.6$ cm^2). The yield of N$_2$O$_5$ and HNO$_3$ is given as a percentage with respect to the total number of molecules of NO$_3$ taken up during the same reaction time. Dash (-) indicates a negative result of the experiment.

Table 3.7 Summary of reaction products during the heterogeneous reaction of NO$_3$ on 250 mg and 1g of mineral dust surrogate samples at an orifice diameter of 8mm.

On the other hand, $N_2O_{5(ads)}$ may react with adsorbed water $H_2O_{(ads)}$ and form gas phase HNO_3, part of which may desorb into the gas phase, according to reaction (3.5d):

$$N_2O_{5(ads)} + H_2O_{(ads)} \rightarrow 2HNO_{3(g)} \qquad (3.5d)$$
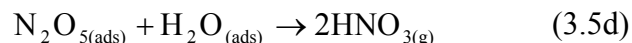
Additional NO$_3$ uptake experiments have been performed on all mineral dust samples at $[NO_3] = 2.3 \times 10^{12}$ cm^{-3} on 1.0 g of powder (see Table 3.7). Under these conditions we did not succeed in saturating the substrates at practical reaction times as they are apparently able to adsorb large amounts of NO$_3$. NO$_3$ uptake gave rise to gas phase HNO$_3$ formation for CaCO$_3$, Kaolinite, Arizona Test Dust and natural limestone without any visible trace of desorbing N$_2$O$_5$ from the surface. Figure 3.8 displays raw data of an uptake experiment of NO$_3$ on 2 g of natural limestone showing the production of gas phase HNO$_3$ at a yield of 35% with respect to NO$_3$ taken up on the substrate.
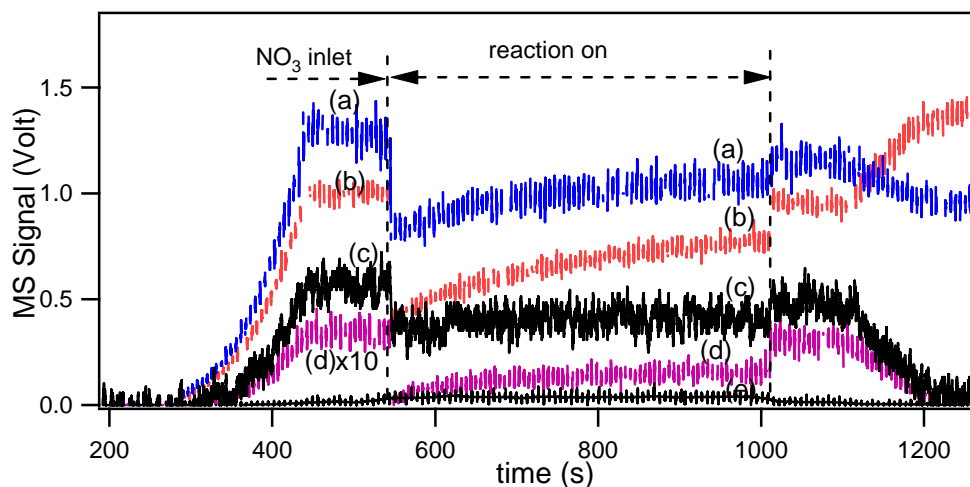
Figure 3.8. NO$_3$ uptake on a sample of 2g of natural limestone at $[NO_3] = (7.0 \pm 1.0) \times 10^{11}$ cm^{-3}. Curves (a), (b), (d) and (e) correspond to the raw MS signals monitored at m/e 30, 46, 62 and 63 respectively. Curve (c) corresponds to the raw REMPI signal for NO$_2$ detection at $\lambda_{NO_2} = 511$ nm converted to a MS signal at m/e 46 (orifice diameter = 8 mm, A$_s$ = 19.6 cm^2).

Of note is the fact that a small impurity of 0.5 % and 0.3 % of Al$_2$O$_3$ and Fe$_2$O$_3$, respectively, in natural limestone of 97 % (by weight) CaCO$_3$ has a significant effect on

the formation of HNO$_3$ as displayed in Table 3.7. The fact that we did not observe gas phase formation of N$_2$O$_5$ upon uptake of NO$_3$ on samples of 1g, where large quantities of adsorbed water are present as displayed in Table 3.7, suggests that reaction (3.5d) may be faster than reaction (3.5c).

In order to probe for the presence of an adsorbed reactive species on the substrate during NO$_3$ uptake, experiments using NO and NO$_2$ were performed on all the examined substrates immediately after the uptake of known quantities of NO$_3$. The goal has been to determine whether or not the adsorbed NO$_3$ is able to react with NO or NO$_2$. On 1g of Arizona Test Dust, uptake of NO on adsorbed NO$_3$ produced a small amount of NO$_2$ which has been observed using REMPI at λ_{NO_2} = 511 nm (Figure 3.9). On the time scale of this experiment of approximately 300 s, 1.3 x 10^{18} molecules of NO$_3$ have been adsorbed on the substrate. The reaction with an excess of NO in the absence of gas phase NO$_3$ during 230 s resulted in a production of 3.2 x 10^{17} molecules of NO$_2$ which corresponds to a 12.3 % retrieval of adsorbed NO$_3$. The observed reaction may be viewed as a titration reaction at the surface of the substrate according to reaction (3.6)[27,28]:

$$NO + NO_{3(ads)} \rightarrow 2NO_2 \qquad (3.6)$$
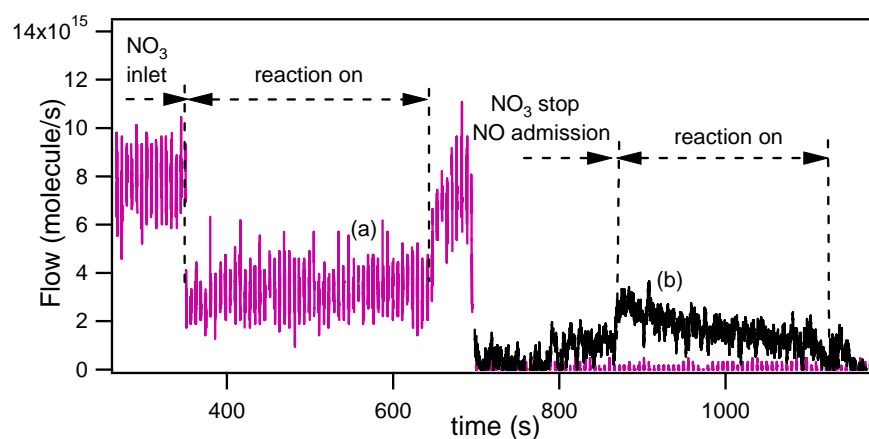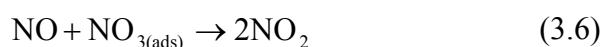
Figure 3.9. Uptake of NO$_3$ on Arizona Test Dust (F_{NO_3} = 8.0 x 10^{15} cm^{-3}, escape orifice of 8 mm, A$_s$ = 19.6 cm^2), curve (a). Curve (b) corresponds to the flow of generated NO$_2$ following the reaction with excess NO on the substrate in the absence of gas phase NO$_3$. The flow of NO$_2$ has been monitored by the REMPI signal at λ_{NO_2} = 511 nm.

On Saharan Dust that has previously been exposed to NO$_3$ and NO$_2$ we have observed uptake of NO but no visible trace of gas phase NO$_2$. As discussed above, NO$_2$ shows an uptake on virgin Saharan Dust samples. On exposed CaCO$_3$ and natural limestone samples, however, no NO uptake has been observed, and as a consequence no NO$_2$ gas phase formation. An additional experiment was carried out on 1g of Saharan Dust where NO$_2$ was used as a probe for adsorbed NO$_3$. On 1g of Saharan Dust, uptake of NO$_2$ on adsorbed NO$_3$ produced a small amount of excess NO$_2$ which has been observed using REMPI at λ_{NO_2} = 511 nm (Figure 3.10). On the time scale of this experiment of approximately 400 s, 8.0 x 10^{17} molecules of NO$_3$ have been adsorbed on 1g of Saharan Dust. The reaction with an excess of NO$_2$ in the absence of gas phase NO$_3$ during 100 s resulted in a production of 1.8 x 10^{17} molecules of NO$_2$ as displayed by the increase in the NO$_2$ signal in Figure 3.10. The observed reaction may be represented by the following reaction (3.7):

$$NO_2 + NO_{3(ads)} \rightarrow 2NO_2 + \tfrac{1}{2}O_2 \qquad \Delta H^0_{r(gas)} = -9.1 \text{ kcal/mol} \qquad (3.7)$$
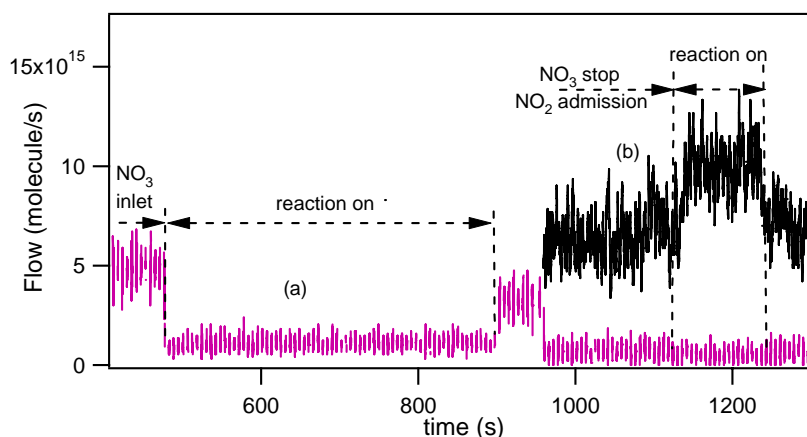
Figure 3.10. Uptake of NO$_3$ on Saharan Dust (F_{NO_3} = 1.7 x 10^{16} cm^{-3}, escape orifice of 8 mm, A$_s$ = 19.6 cm^2), curve (a). Curve (b) corresponds to the flow of generated NO$_2$ following the reaction with excess NO$_2$ on the substrate in the absence of gas phase NO$_3$. The flow of NO$_2$ has been monitored by the REMPI signal at λ_{NO_2} = 511 nm.

The observed NO_2 production corresponds to 22.5 % of adsorbed NO_3. In this case we did not observe any NO production using REMPI detection at $\lambda_{NO} = 452.6$ nm which is probably related to the fact that NO, if formed, may rapidly react with adsorbed NO_3 as discussed above.

For all the mineral dust substrates studied, the uptake of NO_3 on mineral dust was irreversible, at least on timescales used in this work. This was checked in experiments such as NO_3 uptake on Kaolinite where after approximately 7 minutes of exposure, the sample was isolated and the NO_3 flow subsequently turned off. When the isolation plunger was lifted again, no release of NO_3 was observed at m/e 62. Free radical adsorption on solid polar surfaces are known from the literature. For example, recent work has shown the adsorption of CH_3O_2 free radical on KCl surfaces and effective bimolecular reactions with NO_2 and organic molecules whose kinetic parameters revealed a heterogeneous mechanism[29].

In summary, we must clearly point out that the uptake of NO_3 on mineral dust is not in any way catalytic in nature. This conclusion is supported by the formation of volatile reaction products such as N_2O_5 and HNO_3 (Table 3.7) as well as by the complete eventual saturation of the NO_3 uptake on small mass samples of mineral dust as displayed in Figure 3.7. The chemical turnover or reaction rate of NO_3 is accompanied by the slow irreversible build-up of non-volatile reaction products leading to the final inhibition or saturation of NO_3 uptake.

3.5 Conclusions and atmospheric implications

We have shown in this work that NO_3 undergoes fast heterogeneous reactions with surrogate substrates of mineral dust aerosol at T = 298 ± 2 K. Ancillary uptake experiments performed with NO_3 on molecular sieve alumosilicate particles of different nominal pore diameter have led to the conclusion that the pore diffusion correction is not appropriate for the present experimental conditions of relativity short contact times. Therefore, the geometric surface area of the dust sample has been used for the calculation of γ_0 and γ_{ss}. The measured uptake coefficient showed different values for high and low $[NO_3]$. At $[NO_3] = (4.0 \pm 1.0) \times 10^{12}$ cm^{-3} γ_{ss} ranged from $(1.4 \pm 0.4) \times 10^{-2}$ for $CaCO_3$ to

(6.5 ± 1.1) x 10^{-2} for Saharan Dust. At $[NO_3] = (7.0 \pm 1.0)$ x 10^{11} cm^{-3} γ_{ss} ranged from (3.4 ± 1.6) x 10^{-2} for natural limestone to (0.12 ± 0.08) for Saharan Dust.

These values are significantly larger than the ones used in a recent global modeling simulation of heterogeneous chemistry on mineral dust aerosol[17], where a γ value of 3.0 x 10^{-3} for NO_3 has been used. However, the modeling study performed by Bian and Zender[16] used a γ value of 0.1 for NO_3. This value is in agreement with the one we obtained by extrapolation of γ to vanishing NO_3 concentration from our uptake experiments performed on Kaolinite as displayed in Figure 3.6. We therefore have extrapolated the value of γ_{ss} for $[NO_3] < 5.0$ x 10^{11} molecule cm^{-3}. With trophospheric $[NO_3]$ at a typical value of 2.0 x 10^{9} molecule cm^{-3}, γ_{ss} tends towards values larger than 0.2 ± 0.03 according to the results displayed in Figure 3.6.

The present experimental results of γ for NO_3 seem to be more in agreement with the guess of Bian and Zender[16] compared to Bauer et al.[17] and suggests a significant removal of NO_3 in areas affected by mineral dust close to ground. This leads to a decrease of the oxidation potential of the atmosphere at night by virtue of the removal of NO_3 and the decrease of O_3 observed in all model results, albeit to a variable extent. However, the NO_3 removal also affects the abundance of HNO_3 because the nighttime sources are the heterogeneous hydrolysis of N_2O_5 and to a minor extent, the reaction of NO_3 with HO_2, both of which directly depend on NO_3 [17]. It is therefore of some importance to obtain reliable values for the kinetics of key free radicals that control in part important precursors such as HNO_3 and N_2O_5.

The specific comparison of the results of Bauer et al.[17] and Bian and Zender[16] highlights the importance of key free radicals such as NO_3. The latter attribute a large reactivity to NO_3 and a small one to HNO_3, and vice versa for the former. However, the resulting trend in both models is the same, namely the decrease of O_3 through the reactive process of the ozone precursor NO_3 or HNO_3. The conclusion is that the resulting effect on the traces gas composition is insensitive to the detailed allocation of heterogeneous reactivity, provided the species in question are chemically coupled as for NO_3 and HNO_3.

In summary, this work delivers several messages of potential importance to atmospheric chemistry: a) The uptake coefficient of NO_3 on mineral dust aerosol under tropospheric conditions is larger than 0.1 for a selection of surrogate mineral dust materials and does not seem to be affected by the presence of NO_2; b) in contrast to the uptake kinetics the observed reaction products HNO_3 and N_2O_5 seem to depend on the presence of NO_2 and on the quantity of the available adsorbed H_2O; c) a significant part of NO_3 that is

disappearing from the gas phase seems to retain its reactivity in the adsorbed state as shown in experiments with NO$_2$ and NO; d) the uptake of NO$_3$ on mineral dust is non-catalytic. Despite the open nitrogen mass balance a significant fraction of adsorbed NO$_3$ is expected to be released as volatile HNO$_3$ and N$_2$O$_5$ on mineral dust aerosol which is in fact observed in laboratory experiments.

Water is expected to play an important role because of the hydrolysis of N$_2$O$_5$, even under the present experimental (dry) conditions. Despite our inability to perform experiments at elevated humidity using the Knudsen flow reactor, we believe that H$_2$O cannot substantially alter the uptake kinetics of NO$_3$. Our laboratory observations also indicate that the reactivity of NO$_3$ on mineral dust aerosols decreases for long gas residence times τ_g as the heterogeneous reaction rate not only depends on the gas phase concentration but also on intermediates whose concentration depend on the extent of reaction. Despite the presence of NO$_2$ this work indicates that interaction with mineral dust may be an important loss process for tropospheric NO$_3$ whose quantitative consequences will have to be assessed by modeling studies. Therefore, the uptake of NO$_3$ on mineral dust aerosols may have a much greater influence on the reduction of O$_3$ as compared to the estimated value of 0.4% of global ozone reduction[17] for γ_{NO_3} = 3.0 x 10^{-3}. The NO$_3$ loss rate constant (k_{het}) due to heterogeneous uptake onto aerosol is given by $k_{het} = \tau^{-1}(NO_3) = \gamma A \bar{c}/4$ where γ is the uptake coefficient of NO$_3$ and is a function of the mineral dust aerosol composition; A is the surface area density of the dust and $\bar{c}$ is the mean molecular speed of NO$_3$. Assuming a surface area density of A = 1.5 x 10^{-6} cm^2 cm^{-3} for a dust plume[30] and γ = 0.2 from our extrapolated value for NO$_3$ we evaluated a lifetime of 7 min for NO$_3$. This value has to be compared to the diurnal photolysis of NO$_3$. During the day, NO$_3$ has a very short lifetime (about 5s) due to its strong absorption in the visible region (662 nm) and its rapid photodissociation, mainly to NO$_2$ according to $NO_3 + h\nu \rightarrow NO_2 + O(^3P)$. Since this photochemical gas-phase loss process takes place only during the day, NO$_3$ loss by reaction on dust is important only during the night. Heterogeneous nighttime removal of NO$_3$ by mineral dust and formation of gas-phase HNO$_3$ after reacting with gas-phase NO$_2$ could change the NO$_x$/NO$_y$ ratio during the night and in the presence of dust plumes[4].

3.6 References

(1)   Wayne, R. P.; Barnes, I.; Biggs, P.; Burrows, J. P.; Canosamas, C. E.; Hjorth, J.; Lebras, G.; Moortgat, G. K.; Perner, D.; Poulet, G.; Restelli, G.; Sidebottom, H.: The Nitrate Radical - Physics, Chemistry, and the Atmosphere, Atmospheric Environment Part a-General Topics, 25, 1-203, (1991).

(2)   Platt, U.; Lebras, G.; Poulet, G.; Burrows, J. P.; Moortgat, G.: Peroxy-Radicals from Nighttime Reaction of NO$_3$ with Organic-Compounds, Nature, 348, 147-149, (1990).

(3)   Mihelcic, D.; Klemp, D.; Musgen, P.; Patz, H. W.; Volz-Thomas, A.: Simultaneous Measurements of Peroxy and Nitrate Radicals at Schauinsland, Journal of Atmospheric Chemistry, 16, 313-335, (1993).

(4)   Naudet, J. P.; Rigaud, P.; Pirre, M.: Altitude Distribution of Stratospheric NO$_3$ .1. Observations of NO$_3$ and Related Species, Journal of Geophysical Research-Atmospheres, 94, 6374-6382, 10.1029/88JD03856., (1989).

(5)   Platt, U.; Perner, D.; Harris, G. W.; Winer, A. M.; Pitts, J. N.: Observations of Nitrous-Acid in an Urban Atmosphere by Differential Optical-Absorption, Nature, 285, 312-314, (1980).

(6)   Thomas, K.; Volz-Thomas, A.; Mihelcic, D.; Smit, H. G. J.; Kley, D.: On the exchange of NO$_3$ radicals with aqueous solutions: Solubility and sticking coefficient, Journal of Atmospheric Chemistry, 29, 17-43, (1998).

(7)   Gratpanche, F.; Sawerysyn, J. P.: Uptake coefficients of NO$_3$ radicals on solid surfaces of sea- salts, Journal De Chimie Physique Et De Physico-Chimie Biologique, 96, 213-231, (1999).

(8)   Gershenzon, M. Y.; Il'in, S.; Fedotov, N. G.; Gershenzon, Y. M.; Aparina, E. V.; Zelenov, V. V.: The mechanism of reactive NO$_3$ uptake on dry NaX (X=Cl, Br), Journal of Atmospheric Chemistry, 34, 119-135, (1999).

(9)   Rudich, Y.; Talukdar, R. K.; Ravishankara, A. R.: Multiphase chemistry of NO$_3$ in the remote troposphere, Journal of Geophysical Research-Atmospheres, 103, 16133-16143, 10.1029/98JD01280., (1998).

(10)   Seisel, S.; Caloz, F.; Fenter, F. F.; Van den Bergh, H.; Rossi, M. J.: The heterogeneous reaction of NO$_3$ with NaCl and KBr: A nonphotolytic source of halogen atoms, Geophysical Research Letters, 24, 2757-2760, 10.1029/97GL02857., (1997).

(11)   Zhang, Y.; Sunwoo, Y.; Kotamarthi, V.; Carmichael, R.: Photochemical Oxidant Processes in the Presence of Dust: An Evaluation of the Impact of Dust on Particulate Nitrate and Ozone Formation., Journal of Applied Meteorology, 33, 813-824, (1994).

(12)   Carslaw, N.; Plane, J. M. C.; Coe, H.; Cuevas, E.: Observations of the nitrate radical in the free troposphere at Izana de Tenerife, Journal of Geophysical Research-Atmospheres, 102, 10613-10622, (1997).

(13)   Vrekoussis, M.; Kanakidou, M.; Mihalopoulos, N.; Crutzen, P. J.; Lelieveld, J.; Perner, D.; Berresheim, H.; Baboukas, E.: Role of the NO$_3$ radicals in oxidation processes in the eastern Mediterranean troposphere during the MINOS campaign, Atmospheric Chemistry and Physics, 4, 169-182, (2004).

(14)   Dentener, F. J.; Carmichael, G. R.; Zhang, Y.; Lelieveld, J.; Crutzen, P. J.: Role of mineral aerosol as a reactive surface in the global troposphere, Journal of Geophysical Research-Atmospheres, 101, 22869-22889, 10.1029/96JD01818., (1996).

(15)   Tabazadeh, A.; Jacobson, M. Z.; Singh, H. B.; Toon, O. B.; Lin, J. S.; Chatfield, R. B.; Thakur, A. N.; Talbot, R. W.; Dibb, J. E.: Nitric acid scavenging by mineral and biomass burning aerosols, Geophysical Research Letters, 25, 4185-4188, 10.1029/1998GL900062., (1998).

(16)   Bian, H. S.; Zender, C. S.: Mineral dust and global tropospheric chemistry: Relative roles of photolysis and heterogeneous uptake, Journal of Geophysical Research-Atmospheres, 108, 4672, doi:10.1029/2002JD003143., (2003).

(17)   Bauer, S. E.; Balkanski, Y.; Schulz, M.; Hauglustaine, D. A.; Dentener, F.: Global modeling of heterogeneous chemistry on mineral aerosol surfaces: Influence on tropospheric ozone chemistry and comparison to observations, Journal of Geophysical Research-Atmospheres, 109, art. no.-D02304, doi:10.1029/2003JD003868., (2004).

(18)   Seisel, S.; Fluckiger, B.; Caloz, F.; Rossi, M. J.: Heterogeneous reactivity of the nitrate radical: reactions on halogen salt at ambient temperature and on ice in the presence of HX (X = Cl, Br, I) at 190 K, Physical Chemistry Chemical Physics, 1, 2257-2266, (1999).

(19)   Fenter, F. F.; Rossi, M. J.: Heterogeneous reaction of NO$_3$ with ice and sulfuric acid solutions: Upper limits for the uptake coefficients, Journal of Physical Chemistry A, 101, 4110-4113, (1997).

(20)   Hanisch, F.; Crowley, J. N.: Heterogeneous reactivity of gaseous nitric acid on Al$_2$O$_3$, CaCO$_3$, and atmospheric dust samples: A Knudsen cell study, Journal of Physical Chemistry A, 105, 3096-3106, (2001 a).

(21)   Keyser, L. F.; Moore, S. B.; Leu, M. T.: Surface-Reaction and Pore Diffusion in Flow-Tube Reactors, Journal of Physical Chemistry, 95, 5496-5502, (1991).

(22)   Breck, D. W., Zeolite Molecular Sieves,: Zeolite Molecular Sieves, Krieger Publishing Company, 593-724, (1984).

(23)   Hanisch, F.; Crowley, J. N.: Ozone decomposition on Saharan dust: an experimental investigation, Atmospheric Chemistry and Physics, 3, 119-130, (2003 d).

(24)   Sullivan, R. C.; Thornberry, T.; Abbatt, J. P. D.: Ozone decomposition kinetics on alumina: effects of ozone partial pressure, relative humidity and repeated oxidation cycles, Atmospheric Chemistry and Physics, 4, 1301-1310, (2004).

(25)   Tabor, K.; Gutzwiller, L.; Rossi, M. J.: Heterogeneous Chemical-Kinetics of NO_2 on Amorphous-Carbon at Ambient-Temperature, Journal of Physical Chemistry, 98, 6172-6186, (1994).

(26)   Wangberg, I.; Etzkorn, T.; Barnes, I.; Platt, U.; Becker, K. H.: Absolute determination of the temperature behavior of the $NO_2+NO_3+(M)<-->N_2O_5+(M)$ equilibrium, Journal of Physical Chemistry A, 101, 9694-9698, (1997).

(27)   Sander, S. P.; Kircher, C. C.: Temperature-Dependence of the Reaction $NO+NO_3 ---> 2NO_2$, Chemical Physics Letters, 126, 149-152, (1986).

(28)   Hammer, P. D.; Dlugokencky, E. J.; Howard, C. J.: Kinetics of the Gas-Phase Reaction $NO + NO_3 ---> 2NO_2$, Journal of Physical Chemistry, 90, 2491-2496, (1986).

(29)   Manucharova, L. A.; Tsarukyan, S. V.; Vardanyan, I. A.: Reactions of CH_3O_2 radicals on solid surface, International Journal of Chemical Kinetics, 36, 591-595, (2004).

(30)   de Reus, M.; Dentener, F.; Thomas, A.; Borrmann, S.; Strom, J.; Lelieveld, J.: Airborne observations of dust aerosol over the North Atlantic Ocean during ACE 2: Indications for heterogeneous ozone destruction, Journal of Geophysical Research-Atmospheres, 105, 15263-15275, (2000).

CHAPTER 4

THE HETEROGENEOUS CHEMICAL KINETICS OF N_2O_5 ON $CaCO_3$ AND OTHER ATMOSPHERIC MINERAL DUST SURROGATES

4.1 Introduction

Dinitrogen pentoxide, N_2O_5, is part of the family of active nitrogen, NO_y, owing to its equilibrium with NO_2 and NO_3 according to reaction (4.1), which releases photochemically active NO_3 and NO_2 free radicals.

$$N_2O_5 \leftrightarrows NO_2 + NO_3 \qquad (4.1)$$
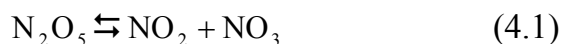
Under atmospheric pressure and 298 K the thermal lifetime of N_2O_5 is approximately 20 s and is a strong function of temperature[1,2]. The observation of the build up of the concentration of nitric acid, HNO_3, in the polluted urban PBL during the night could only be explained by the heterogeneous conversion of N_2O_5 to HNO_3 according to reaction (4.2) [3,4]

$$N_2O_5 + H_2O_{(ads)} \rightarrow 2HNO_3 \qquad (4.2)$$

The substrate for the heterogeneous reaction (4.2) has not been unambiguously identified but is thought to be urban H_2O-containing aerosols or humid surfaces on the ground whose purpose is to make available adsorbed H_2O in order to enable reaction (4.2).

Together with HNO_3 and NO_3, N_2O_5 contributes to the formation of particulate nitrate on the dust particles by surface processes in the troposphere[5]. These processes represent an important sink for nitrogen oxide species, with decreases of daytime NO_y levels reaching up to 60 % in the presence of dust at a loading of about 1.8-11.5 µg m^{-3} corresponding to a particle surface area of (0.11-0.7) x 10^{-6} cm^2 cm^{-3}. During the nighttime, the gas-to-particle conversions of NO_3 and N_2O_5 dominates the overall nitrate formation accounting for 80 % of total particulate nitrate formation, while the heterogeneous hydrolysis of N_2O_5 leading to HNO_3 accounts for only about 20 % [5].

Dentener showed how the interaction of N_2O_5, O_3 and HO_2 radicals with mineral dust affects the photochemical oxidant cycle, with ozone concentrations decreasing by up to 10% in and nearby the dust source areas[6]. In the modelling simulation performed by Bauer et al. the uptake of N_2O_5 resulted in a reduction of 11% of its mass in the gas phase whereas the simulations of Bian and Zender indicate a global reduction of 2% of N_2O_5 using an uptake coefficient $\gamma_{N_2O_5} = 10^{-3}$ at a relatively humidity (rh) of 30 %.

Despite the published results of field observations and modeling studies[7-10], there is only a single laboratory study that deals with the heterogeneous reactivity of N_2O_5 on mineral dust aerosol surrogates, namely the interaction of N_2O_5 on Saharan Dust using a combination of Knudsen reactor and DRIFTS (Diffuse Reflectance Infrared Transmission Spectroscopy)[11].

4.2 Experimental setup and detection

All experiments were performed in the TEFLON$^®$ coated Knudsen flow reactor operating in the molecular flow regime. The characteristic parameters and relevant kinetic expressions for steady state and pulsed experiments are reported in Chapter 2 as well as the synthesis of N_2O_5. The mineral dust composition used in this study is reported in Table 3.1. The two kinds of sample holders, TEFLON$^®$ coated Pyrex of 19.6 cm^2 of available sample surface and the internal reduction piece made out of DELRIN$^®$ of available surface area of 4.9 cm^2, did not show any reactivity with N_2O_5 under the present experimental conditions.

Hydrolysis of N_2O_5 may occur on surfaces of the traps and of the inlet line before admission into the Knudsen flow reactor generating HNO_3 as an impurity ranging from 10 to 15% as studied by MS at m/e 63, its molecular ion peak. N_2O_5 does not have a measurable parent and fragment peak at m/e 108 and 62, respectively, under the present experimental conditions; the most intense peaks are its fragment NO_2^+ at m/e 46 followed by the less intense fragment NO^+ at m/e 30. However, the HNO_3 impurity also contributes to the MS signal at m/e 46 and 30. Under the experimental conditions used HNO_3 has a detectable parent peak at m/e 63.

In the following, the subscript 0 and r will refer to continuous gas uptake experiments in the absence and presence, respectively, of the solid sample.

Through a calibrated mass spectrum of pure HNO_3 we have accurately determined the effective contribution of HNO_3 at m/e 46 and 30 by using the fragmentation pattern expressed as the ratios $f_{46} = \dfrac{I_0^{46(HNO_3)}}{I_0^{63(HNO_3)}} = 52 \pm 8$ and $f_{30} = \dfrac{I_0^{30(HNO_3)}}{I_0^{63(HNO_3)}} = 33 \pm 4$. In the absence of a substrate, $f_{46} \cdot I_0^{63(HNO_3)}$ and $f_{30} \cdot I_0^{63(HNO_3)}$ have been subtracted from the total MS signals I_0^{46} and I_0^{30} at m/e 46 and 30, respectively, in order to assign the remaining MS amplitude to the NO_2^+ and NO^+ fragments to N_2O_5: $I_0^{46(N_2O_5)} = I_0^{46} - f_{46} \cdot I_0^{63(HNO_3)}$ and $I_0^{30(N_2O_5)} = I_0^{30} - f_{30} \cdot I_0^{63(HNO_3)}$.

The ratio between the two most intense peaks of N_2O_5 therefore was $r = \dfrac{I_0^{46(N_2O_5)}}{I_0^{30(N_2O_5)}} = 1.4 \pm 0.2$. Mixtures of N_2O_5 and HNO_3 may thus be monitored using MS signal intensities at m/e 46, 30 and 63. However, in order to quantify N_2O_5 we chose its most intense peak corresponding to its fragment NO_2^+ at m/e 46.

4.3 Uptake coefficient of N_2O_5 and identity of reaction products

When N_2O_5 is exposed to the sample, it is taken up and undergoes a heterogeneous reaction on the mineral dust surface which results in a decrease of the N_2O_5 concentration that is monitored using the MS signal $I_r^{46(N_2O_5)}$. As shown in previous studies on mineral dust, HNO_3 that is always present as an impurity, is taken up on the mineral dust surface

without releasing any product that may contribute to the total MS signal I_r^{46} at m/e 46 [12]. We have therefore determined the rate constant k_{obs} for the disappearance of N_2O_5 following equation (4.E1), assuming that the rate law is first order in N_2O_5:

$$k_{obs} = \left(\frac{I_0^{46(N_2O_5)}}{I_r^{46(N_2O_5)}} - 1\right) \cdot k_{esc} \qquad (4.E1)$$

where $I_0^{46(N_2O_5)}$ and $I_r^{46(N_2O_5)}$ are the intensities of the NO_2^+ fragment of N_2O_5 before and during heterogeneous reaction, respectively, and k_{esc} is the measured rate constant of effusion for N_2O_5 out of the flow reactor. In order to determine $I_r^{46(N_2O_5)}$, the raw MS signal at m/e 46 was corrected for HNO_3 generated through hydrolysis of N_2O_5 with water adsorbed on the substrate surface. Production of HNO_3 has in fact been observed at m/e 63 in every uptake experiment of N_2O_5. Figure 4.1 shows the raw MS signal at m/e 63 for a typical uptake experiment of N_2O_5 on $CaCO_3$. Therefore, we have corrected the MS signal of N_2O_5 at m/e 46 for the presence of HNO_3 according to equation (4.E2) when the sample is exposed to N_2O_5:

$$I_r^{46(N_2O_5)} = I_r^{46} - f \cdot I_r^{63(HNO_3)} \qquad (4.E2)$$

The ratio r, reported above, turned out to be the same before and during the exposure of the mineral dust sample to N_2O_5. Therefore, $I_r^{46(N_2O_5)}$ exclusively corresponds to N_2O_5 for this experiment after correction of the MS signal at m/e 46 for the contribution of HNO_3 desorbing from the mineral dust substrate.

The net observed uptake coefficient for N_2O_5, γ_{obs}, is given by expression (2.8). In our data analysis, γ_{obs} was calculated using the geometric surface area of the sample holder as will be justified below. In the following, we evaluate γ_{obs} at the initial and steady state values of the uptake rate leading to γ_0 and γ_{ss}, respectively.

4.4 Uptake of N_2O_5 on $CaCO_3$: Results and Discussion

Typical raw data from an uptake experiment of N_2O_5 on 510 mg of $CaCO_3$ are shown in Figure 4.1 using the 14 mm diameter-orifice. After a steady state flow of N_2O_5 has been established, the isolation plunger is lifted at $t = 92$ s and the substrate is thus exposed to the N_2O_5 flow. MS signals of 18 (H_2O^+), 30 (NO^+), 44 (CO_2^+), 46 (NO_2^+), and 63 (HNO_3^+) were simultaneously monitored during the uptake. Because of the uptake of N_2O_5 on $CaCO_3$, the number of molecules exiting through the escape orifice into the MS immediately decreases which leads to a decrease of the MS signal $I_r^{46(N_2O_5)}$ at m/e 46. During the exposure of the sample to N_2O_5 both HNO_3 and CO_2 monitored at m/e 63 and 44, respectively, have been observed in the gas phase. As the exposure time increases, the MS signal at m/e 46 partially recovers, indicating a decrease in the rate of uptake that ultimately leads to steady state towards the end of the displayed uptake experiment. At $t = 1150$ s the sample compartment is sealed by lowering the plunger and the MS signal at m/e 46 approximately returns to its initial steady-state value. The slight decrease of $I_0^{46(N_2O_5)}$ over extended periods of time such as displayed if Figure 4.1 can be explained by a slight decrease of the corresponding flow rate into the reactor.
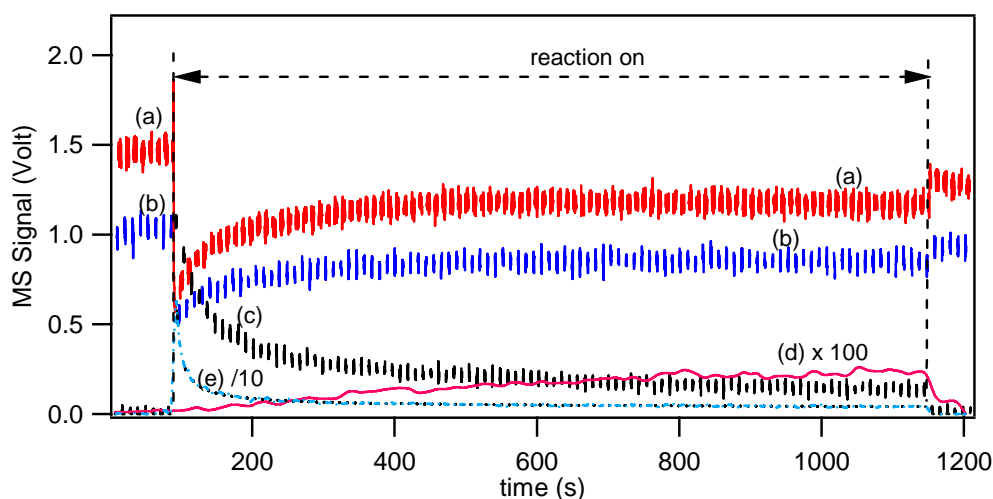
Figure 4.1. Typical N_2O_5 uptake experiment on a sample of 510 mg of $CaCO_3$. Curves (a), (b), (c), (d) and (e) correspond to the raw MS signals monitored at m/e 46, m/e 30, m/e 44, m/e 63 and m/e 18, respectively, using an orifice diameter of 14 mm, $A_s = 19.6$ cm^2 and $[N_2O_5]_0 = (4.0 \pm 1.0) \times 10^{11}$ cm^{-3}.

An ancillary experiment was performed in order to estimate the amount of water $H_2O_{(ads)}$ adsorbed on the $CaCO_3$ substrate surface after a given pumping time. In order to limit H_2O desorbing from the Pyrex sample holder it was replaced by a gold-coated all-metal sample holder. In this way most desorbing H_2O may be attributed to the mineral dust sample. Typically, a fresh sample of 1g of $CaCO_3$ was pumped for 30 minutes at $T = 298 \pm 2$ K in the 14 mm-orifice reactor until the MS signal of H_2O at m/e 18 dropped to the background level. Subsequently, the $CaCO_3$ sample was heated up to 470 K and the MS signal at m/e 18 recorded until it reached background as well indicating that no additional water desorbed at that temperature. The MS signal at m/e 18 was integrated in order to calculate the number of adsorbed water molecules $H_2O_{(ads)}$ using the measured BET surface area of 5.06 m^2 g^{-1} for $CaCO_3$. A value of approximately 3.0 x 10^{13} molecule cm^{-2} has been found for the surface density of strongly adsorbed $H_2O_{(ads)}$[13].

When the $CaCO_3$ substrate is exposed to N_2O_5 at 92 s, we observed rapid formation of $CO_{2(g)}$ and $H_2O_{(g)}$ as displayed in Figure 4.1 which were either generated in a chemical reaction or desorbing from a precursor state. In order to better understand the uptake of N_2O_5 on solid $CaCO_3$ powder, we will briefly digress to the description of the chemical nature of a carbonate surface. From experimental and theoretical surface science studies, [14-16] there is clear evidence that under ambient conditions of pressure, temperature, and relative humidity, the surface of $CaCO_3$ is terminated by OH groups that persist even under ultrahigh vacuum conditions. The OH-terminated surface may be a result of the dissociative adsorption of water according to reaction (4.3):

$$CaCO_3 + H_2O \rightarrow Ca(OH)(HCO_3) \qquad (4.3)$$

In a recent study[17], the surface chemistry of $CaCO_3$ with trace atmospheric gases such as HNO_3, SO_2, HCOOH, and CH_3COOH was investigated using FTIR absorption spectrometry. This study has pinpointed adsorbed carbonic acid H_2CO_3 to be involved in the surface chemistry of $CaCO_3$ and was identified as a stable intermediate species on the $CaCO_3$ surface in the presence of H_2O vapor. The vibrational spectrum of carbonic acid is thought to be characterized by its C=O stretching frequency at 1685 and 1705 cm^{-1}

corresponding to the adsorbed and condensed phase, respectively. In the following, adsorbed H_2CO_3 will occur as a proposed intermediate in several instances.

Dissolution of $CaCO_3$ in the system $H_2O - CO_2 - CaCO_3$ is controlled by three rate-determining processes: the kinetics of dissolution at the mineral surface, mass transport by diffusion, and the slow kinetics of formation of H_2CO_3 in reaction (4.4):

$$CO_{2(g)} + H_2O_{(ads)} \leftrightarrows H_2CO_{3(ads)} \leftrightarrows H^+_{(aq)} + HCO^-_{3(aq)} \tag{4.4}$$

A theoretical model by Buhmann and Dreybrodt[18] taking these processes into account predicts that, due to the slow kinetics of formation of H_2CO_3 in reaction (4.4), precipitation rates on the surface of $CaCO_3$ minerals critically depend on the ratio V/A of the volume V of the solution to the surface area A of the mineral in contact with it. They concluded that H_2CO_3 formation in reaction (4.4) is rate limiting[19].

Bicarbonate ion, HCO_3^-, may react with $CaCO_3$ to yield a surface intermediate that is proposed to be the active surface reactant for the heterogeneous reactions discussed below according to the well – known "Karst dissolution" mechanism of $CaCO_3$ by bicarbonate ion[20]:

$$CaCO_{3(s)} + H^+_{(ads)} + HCO^-_{3(ads)} \rightarrow Ca(OH)(HCO_3) + CO_{2(g)} \tag{4.5}$$
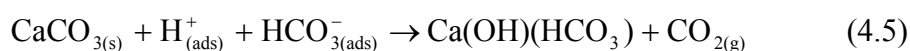
When the $CaCO_3$ sample is exposed to N_2O_5 the surface intermediate may react as follows:

$$N_2O_{5(g)} + Ca(OH)(HCO_3) \rightarrow Ca(NO_3)_2 + H_2O_{(s)} + CO_{2(g)} \tag{4.6}$$

and the net reaction resulting from reaction (4.4), (4.5) and (4.6) will be:

$$N_2O_5 + CaCO_3 \rightarrow Ca(NO_3)_2 + CO_{2(g)} \tag{4.7}$$
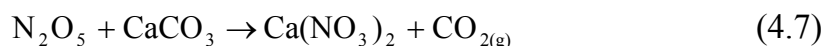
It is evident that $H_2O_{(g)}$ and CO_2 resulting from reaction (4.6) could be used again to generate additional $Ca(OH)(HCO_3)$ according to reactions (4.4) and (4.5) provided

reaction (4.5) is fast enough under flow reaction conditions. In this way H_2O is neither consumed nor generated and may therefore be viewed as a catalytic species. However, we leave evidence that equations (4.4) and (4.5) do not take place under flow reactor conditions.

On the time scale of the uptake experiments reported in Figure 4.1 the calculated ratio CO_2/N_2O_5 of the product yields was 0.42 which is significantly smaller than 1.0 that is stoichiometrically expected according to reaction (4.7) (see Table 4.1). The mass balance between the adsorbed N_2O_5 and the reaction product CO_2 is therefore not closed. If reactions (4.4) and (4.5) were fast and not rate limiting, the CO_2 yield could be 100%. We therefore have to consider another possible pathway for reaction (4.6) that does not result in release of CO_2:

$$N_2O_5 + Ca(OH)(HCO_3) \rightarrow Ca(NO_3)(HCO_3) + HNO_{3(g)} \qquad (4.8)$$

In this case N_2O_5 may directly be converted into gas phase HNO_3 which is also observed at longer exposure times as displayed in Figure 4.1. Reaction (4.8) may also help explain why the ratio CO_2/N_2O_5 differs from 1.0 as no CO_2 is released from reaction (4.8). In addition, HNO_3 may also react with $CaCO_3$ as already observed by Hanisch and Crowley, 2001. We routinely measure a yield of 51 % of gas phase H_2O with respect to N_2O_5 consumed which is comparable to the CO_2 yield according to equation (4.6) and results from the uptake of N_2O_5 on samples of different mass of powdered $CaCO_3$.

$CaCO_3$ Mass in g	γ_0	γ_{ss}	Yield of HNO_3[c]	Yield of CO_2[c]
0.33[a]	0.16 ± 0.03	(2.0 ± 0.6) x 10^{-2}	5.2 %	47.8 %
0.51[a, b]	0.2 ± 0.05	(2.2 ± 0.5) x 10^{-2}	5.4 %	42.4 %
0.58[a]	0.18 ± 0.05	(2.3 ± 0.5) x 10^{-2}	-	-
0.73[a]	0.22 ± 0.04	(2.4 ± 0.4) x 10^{-2}	5.4 %	50 %
2[a]	0.18 ± 0.025	(1.6 ± 1.6) x 10^{-2}	5.4 %	50 %

[a] Uptake measurements performed with a surface sample area $A_s = 19.6$ cm^2.
[b] Uptake experiment displayed in Figure 4.1.
[c] The yield is given as a percentage with respect to the total number of molecules of N_2O_5 taken up during a reaction time of 550 s.

Table 4.1. Uptake experiments with N_2O_5 on $CaCO_3$ as a function of sample mass at $[N_2O_5]_0 = (4.0 ± 1.0)$ x 10^{11} cm^{-3}.

In the wake of the observation of H_2O, CO_2 and HNO_3 we propose that reactions (4.6) and (4.8) compete with each other. H_2O is formed in reaction (4.6) on $CaCO_3$ that is in part preexisting as a surface intermediate $Ca(OH)(HCO_3)$ from prior exposure to atmospheric CO_2 and H_2O following reactions (4.4) and (4.5).

Owing to the fact that $CaCO_3$ has a specific surface area (BET) of 5.06 m^2/g, the 510 mg sample from the experiment displayed in Figure 4.1 has a total surface area of 2.6×10^4 cm^2. N_2O_5 may be represented as a sphere with a projected surface area of 6.4×10^{-15} cm^2/molecule or 1.56×10^{14} molecules cm^{-2}, assuming that N_2O_5 has a molecular diameter of approximately 9 Å and a density of 2.93 g/cm^3. After an exposure time of 1060 s 2.2×10^{18} molecules of N_2O_5 are taken up on 510 mg of $CaCO_3$ leading to

a surface concentration of $\dfrac{2.2 \times 10^{18}}{2.6 \times 10^4} = 8.4 \times 10^{13}$ N_2O_5 molecule cm^{-2} which corresponds

to a coverage (θ) of approximately 54 % based on the BET surface area after a reaction time of 1060 s. After N_2O_5 reacted on $CaCO_3$ powder for 1060 s the substrate is apparently at steady state as displayed in Figure 4.1. This means that there is a sufficient number of intermediate species $Ca(OH)(HCO_3)$ to allow reactions (4.6) and (4.8) to occur. However, once reacted with N_2O_5, the intermediate species cannot regenerate because reactions (4.4) and (4.5) are too slow under flow reactor conditions. Therefore, we observe an amount of $CO_{2(g)}$ smaller than the maximum yield of 100 % at steady state conditions. On the other hand, N_2O_5 may react with adsorbed water $H_2O_{(ads)}$ that still remains on the $CaCO_3$ substrate, thereby forming two molecules of nitric acid as follows:

$$N_2O_{5(g)} + H_2O_{(ads)} \rightarrow 2HNO_{3(g)} \qquad (4.9)$$

In this case solid $CaCO_3$ is just the support for the reactive adsorbed water $H_2O_{(ads)}$ and is not consumed in the chemical reaction. Initially, $HNO_{3(g)}$ is physically adsorbed on the surface to result in adsorbed HNO_3 which reacts with a surface OH-group and slowly forms surface nitrates and H_2O according to reaction (4.10):

$$SS - OH + HNO_{3(ads)} \rightarrow S - NO_3 + H_2O_{(ads,g)} \qquad (4.10)$$

where SS represents a surface site for physical adsorption. This mechanism has been proposed by Seisel and co-workers[21] in a DRIFTS study of the heterogeneous reaction of HNO_3 on mineral dust where they observed the presence of free OH-groups located on the surface of mineral dust and the formation of surface nitrates.

The fact that CO_2 is formed immediately after lifting the plunger (Figure 4.1) whereas HNO_3 is formed later on after a time delay clearly indicates that there are two competitive processes occurring during the reaction of N_2O_5 with $CaCO_3$. Immediately after the exposure of the substrate, N_2O_5 reacts with the intermediate species $Ca(OH)(HCO_3)$ on the $CaCO_3$ sample according to reactions (4.6) and (4.8). At the same time heterogeneous hydrolysis of N_2O_5 may occur due to the presence of $H_2O_{(ads)}$ on the substrate reaction (4.9)). However, the presence of a sufficient quantity of the intermediate formed in reaction (4.5) may make reactions (4.7) and (4.8) predominant at first with respect to reaction (4.9). This explains the initial rapid formation of $CO_{2(g)}$ and the absence of any measurable trace of gas phase HNO_3 at t = 92 s in Figure 4.1. Once the surface intermediate starts to be consumed owing to the initial fast reaction with N_2O_5 the sample starts saturating and reaction (4.9) becomes predominant compared to reactions (4.7) and (4.8) which would explain the delayed formation of HNO_3 displayed in Figure 4.1.
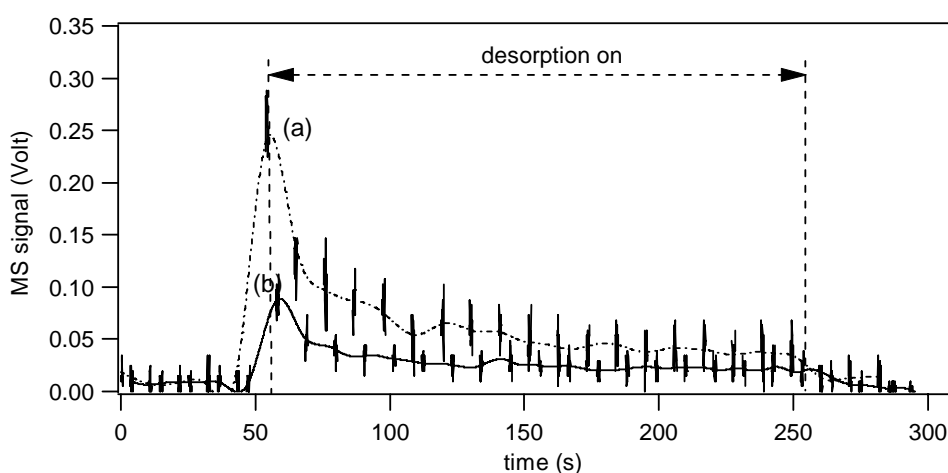

Figure 4.2. Desorption after N_2O_5 uptake on a sample of 510 mg $CaCO_3$. Curves (a) and (b) correspond to the raw MS signals monitored at m/e 44 and m/e 30, respectively, at an orifice diameter of 14 mm and $A_s = 19.6$ cm^2.

After having performed the uptake experiment shown in Figure 4.1 on a substrate of
$CaCO_3$, we sealed the sample and halted the inlet flow of N_2O_5 for approximately 10
minutes. Subsequently, we lifted the plunger again and observed small amounts of
desorbing CO_2 (curve (a), Figure 4.2) as well as a MS signal at m/e 30 without any
measurable MS signal at m/e 46 (curve (b), Figure 4.2). The total yield of desorbed CO_2
only represented 5% of N_2O_5 taken up on the substrate of $CaCO_3$ during the reaction time
of 1058 s. (Figure 4.1). The small intensity of the MS signal at m/e 30 strongly suggests
formation of NO as a decomposition product of N_2O_5.

Uptake experiments of N_2O_5 on 0.58 g of $CaCO_3$ powder were carried out at smaller
orifice size, thus increased residence time τ_g at constant flow of N_2O_5 of 2.3 x 10^{15}
molecule s^{-1}. The values of γ_0 and γ_{ss} decrease with increasing values of the residence time
as displayed in Figure 4.3 and Table 4.2. The strong dependence of γ_{ss} on τ_g suggests that
the mechanism of N_2O_5 uptake is complex and does not correspond to a simple first order
uptake reaction. These observations indicate that the reactivity of N_2O_5 on $CaCO_3$
decreases for long residence times as the heterogeneous reaction rate not only depends on
the gas phase concentration but apparently also on intermediates whose surface
concentration depend on the extent of reaction that scales with τ_g akin to an effective
second order reaction.

Orifice (mm)	γ_0	γ_{ss}	τ_g (s)
14	(1.6 ± 0.13) x 10^{-1}	(6.0 ± 1.2) x 10^{-2}	0.34
8	(8.5 ± 0.8) x 10^{-2}	(3.0 ± 0.7) x 10^{-2}	0.81
4	(3.4 ± 1.0) x 10^{-2}	(1.8 ± 1.1) x 10^{-2}	2.72
1	(1.1 ± 1.0) x 10^{-2}	(1.0 ± 1.0) x 10^{-2}	30

Table 4.2. Relationship between γ_0 and γ_{ss} at different residence times τ_g (s) of N_2O_5 interacting
with 580 mg of $CaCO_3$ powder for data plotted in Figure 2, surface sample area A_s = 19.6 cm^2;
$F_0^{N_2O_5}$ = 2.3 x 10^{15} molecule s^{-1}
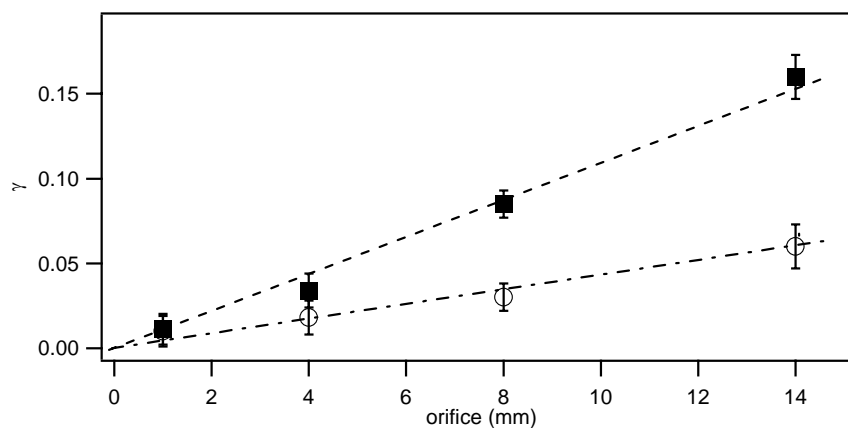
Figure 4.3. Dependence of γ_0 (full squares) and γ_{ss} (open circles) for the uptake of N_2O_5 on 580 mg $CaCO_3$ powder on orifice size: A_s is 4.9 cm^2, $F_0^{N_2O_5} = 2.3$ x 10^{15} molecule s^{-1}.

Apparently, the active surface intermediate $Ca(OH)(HCO_3)$ cannot regenerate sufficiently fast according to reaction (4.5) so as to maintain the rate limiting reaction (4.6) at higher partial pressure, that is at longer residence time τ_g.

In order to unravel whether or not the effective available surface area for uptake is influenced by the internal surface area formed by interstitial voids between individual dust particles, the mass dependence of the N_2O_5 uptake on $CaCO_3$ was investigated in the Knudsen flow reactor at ambient temperature and at $[N_2O_5] = (4.0 \pm 1.0)$ x 10^{11} cm^{-3}. The mass of $CaCO_3$ which is a non-porous material ranged from 0.11 g to 1.8 g and the results are shown in Figure 4.4. Table 4.3 reports values of γ_{ss} and γ_0 using the geometric surface area $A_s = 19.6$ cm^2. The steady state and initial uptake coefficient γ_{ss} and γ_0, respectively, of N_2O_5 were found to increase linearly at low masses of $CaCO_3$. Samples below 0.33 g were considered to be part of this linear mass-dependent regime. Increasing the sample mass further had a negligible effect on the amount of adsorbed N_2O_5 because not the entire sample surface is apparently available for N_2O_5 adsorption. This maximum value is attributed to the inability of N_2O_5 to penetrate through all layers of the sample within the residence time of N_2O_5 in the gas phase, thus resulting in a constant number of molecules taken up despite the increasing sample mass. The limiting γ_{ss} value therefore represents the maximum amount of N_2O_5 able to interact with $CaCO_3$ powder within the N_2O_5 residence time.

Mass (g)	γ_{ss}	γ_0	$\gamma_{0(pulsed\ valve)}$	[a]Number of formal layers	[b]Number of nominal layers
0.11	$(8.0 \pm 5.0) \times 10^{-3}$	$(5.5 \pm 2.0) \times 10^{-2}$	$(4.7 \pm 1.5) \times 10^{-2}$	5	0.3
0.15	$(1.5 \pm 0.5) \times 10^{-2}$	$(6.4 \pm 3.0) \times 10^{-2}$		7	0.5
0.33	$(2.0 \pm 0.6) \times 10^{-2}$	0.16 ± 0.03	0.13 ± 0.018	16	1
0.51	$(2.2 \pm 0.5) \times 10^{-2}$	0.2 ± 0.02		25	1.5
0.58	$(2.3 \pm 0.5) \times 10^{-2}$	0.18 ± 0.02		30	1.8
0.73	$(2.4 \pm 0.5) \times 10^{-2}$	0.22 ± 0.02	0.21 ± 0.016	36	2.2
1.0	$(2.7 \pm 0.4) \times 10^{-2}$	0.15 ± 0.025		50	3
1.3	$(2.8 \pm 0.5) \times 10^{-2}$	0.16 ± 0.024		64	4
1.6	$(2.8 \pm 0.5) \times 10^{-2}$	0.15 ± 0.024	0.15 ± 0.015	80	5
1.8	$(2.8 \pm 0.5) \times 10^{-2}$	0.17 ± 0.03		90	5.5

Effective diameter of [a]3.5 μm and [b]57 μm.

Table 4.3. Summary of uptake experiments with N_2O_5 on $CaCO_3$ as a function of sample mass ($[N_2O_5] = (4.0 \pm 1.0) \times 10^{11}$ cm^{-3}, orifice diameter = 14 mm, A_s = 19.6 cm^2).
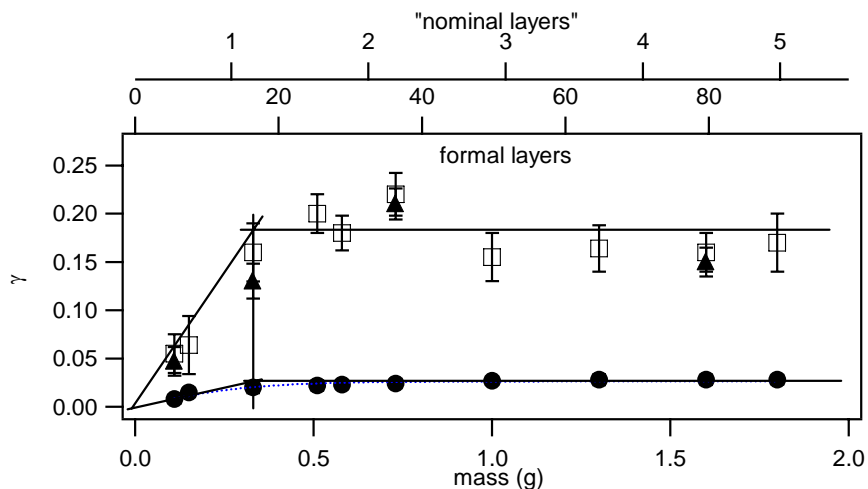
Figure 4.4. Dependence of the uptake coefficient γ_0 (open squares) and γ_{ss} (full circles) on sample mass at $[N_2O_5]_0 = (4.0 \pm 1.0) \times 10^{11}$ cm^{-3} at an orifice diameter of 14 mm for the uptake of N_2O_5 on $CaCO_3$ powder ($A_s = 19.6$ cm^2). Full triangles represent pulsed valve experiments carried out at the same experimental conditions. The average particle diameter on the two scales of the abscissa, namely formal and nominal layers, are 57 and 3.5 μm, respectively.

In order to better define the saturation behaviour of N_2O_5 on the substrate further uptake experiments were performed on $CaCO_3$ employing a pulsed valve to admit N_2O_5 into the reactor. The pulsed-valve experiments were carried out by using a solenoid valve, through which the gas was introduced in pulses with a duration of 5 ms and at a dose of 2.5×10^{15} molecules per pulse[22] corresponding to $[N_2O_5]_0 = 1.3 \times 10^{12}$ cm^{-3}. The pulsed valve uptake experiments on $CaCO_3$ showed that there is a modest mass-dependence of the measured uptake γ_{obs} by approximately a factor of three to four. For a dose of about 2.5×10^{15} molecules per pulse we observed an unexpected increase of the uptake γ_{obs} with increasing mass of $CaCO_3$ as reported for steady state experiments in Table 4.3 and displayed in Figure 4.4. The increase of γ_{obs} saturates at large sample mass because the number of layers exceeds the depth of diffusion of gas into the internal voids. For all series of pulses the measurements are identical, within the uncertainty, to those for steady state experiments. In order to convince the reader that the geometric surface area is appropriate, we want to point out that the results obtained from the pulsed valve experiments are virtually identical to the steady state experiments at "zero" time after the

start of the uptake experiment reaction (Figure 4.4). It is improbable for the gas to explore the BET surface area of the sample during typical pulse decay.

Similar behavior has been observed in a recent study carried out by Seisel et al[11]. In that study uptake experiments of N_2O_5 on Saharan Dust obtained from pulsed and steady state experiments were in good agreement, indicating that the steady state uptake coefficients are not influenced by saturation effects under their experimental conditions.
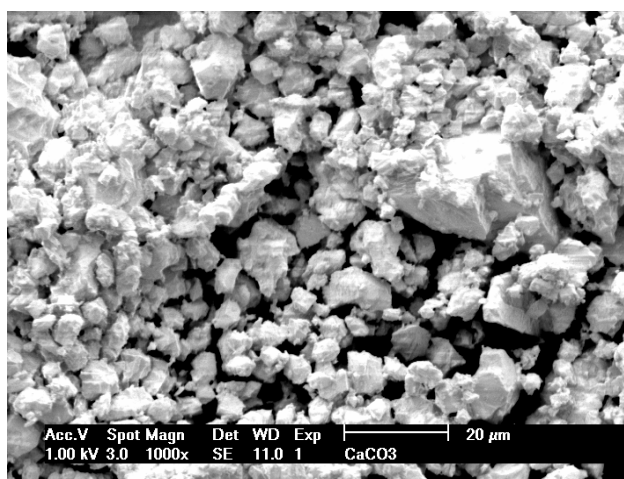
Figure 4.5. SEM-image of $CaCO_3$ powder sample used in this work.

In order to determine the number of layers, the total volume of the powder was calculated from its true density ($\rho_t = 2.93$ g/cm^3) and the mass of the sample spread out across the geometric area of the sample holder. The number of formal layers calculated for an average sample grain diameter of 3.5 μm from the average particle size and the height of the sample is reported in Table 4.3. The typical grain diameter of 3.5 μm has been obtained from the manufacturer's specifications of the used $CaCO_3$ powder.

Based on published microscopic images, it is reasonable to take into account a grain size diameter that is larger than 3.5 μm as suggested by electron microscopy (SEM) displayed in Figure 4.5. Figure 4.4 shows that a mass of 0.33 g corresponds to one nominal layer of 57 μm diameter $CaCO_3$ spread out over the geometric surface of the sample holder (19.6 cm^2). Thus, one nominal layer of $CaCO_3$ will contain 330 mg of closely packed spheres of "effective" grain diameter of 57 μm knowing full well that the sample in reality is multidisperse and structurally heterogeneous. Therefore, the linear mass-dependent

portion of γ_{ss} vs. mass for masses less that 330 mg corresponds to a sample holder that is partially covered with 57 μm diameter $CaCO_3$ particles.

The use of the BET surface area and the application of the pore diffusion theory[23] yields $\gamma_{pd,ss} = (7.4 \pm 1.7) \times 10^{-6}$ for steady state experiments using a grain diameter for $CaCO_3$ of 3.5 μm. This value is lower by a factor of 10^3 compared to $\gamma_{ss} = (2.8 \pm 0.5) \times 10^{-2}$ and $\gamma_0 = 0.16 \pm 0.02$ which were calculated on the basis of the geometrical surface area of the sample as displayed in Table 4.3. The use of the pore diffusion theory substantially underestimates the true uptake coefficient so that it may be interpreted as a lower limit for γ whereas γ_{ss} and γ_0 based on the geometrical surface area may be regarded as an upper limit to the true value of γ.

4.5 Uptake of N_2O_5 on mineral Dust Substrates: Results and Discussion

Table 4.4 reports results on experiments performed on 1g samples of surrogate mineral dust powder at a high initial concentration of $[N_2O_5]_0 = (3.8 \pm 1.0)$ x 10^{12} cm^{-3}. The steady-state uptake coefficients γ_{ss} of N_2O_5 range from (2.2 ± 0.6) x 10^{-3} for natural limestone to (5.9 ± 1.6) x 10^{-2} for Saharan Dust using the geometric surface area. At a lower initial concentration of $[N_2O_5]_0 = (4.0 \pm 1.0)$ x 10^{11} cm^{-3} uptake experiments performed on 0.3 g have revealed larger values of γ_{ss} ranging from (3.5 ± 1.1) x 10^{-2} for $CaCO_3$ to 0.2 ± 0.05 for Saharan Dust.

Mineral dust sample	$^a\gamma_0$	$^a\gamma_{ss}$	$^aHNO_3$	$H_2O_{(ads)}$ [mg g^{-1}]
Kaolinite	0.14 ± 0.04	(2.2 ± 0.6) x 10^{-2}	30 %	23
Natural Limestone	(1.1 ± 0.3) x 10^{-2}	(2.2 ± 0.6) x 10^{-3}	18 %	7
Arizona Test Dust	(6.4 ± 1.9) x 10^{-2}	(1.6 ± 0.4) x 10^{-2}	72 %	22
$CaCO_3$	(3.3 ± 1.0) x 10^{-2}	(6.2 ± 1.8) x 10^{-3}	5 %	4
Saharan Dust	(9.0 ± 2.6) x 10^{-2}	(5.9 ± 1.6) x 10^{-2}	6 %	20

	$^b\gamma_0$	$^b\gamma_{ss}$	$^bHNO_3$
Kaolinite	(0.16 ± 0.04)	(2.1 ± 0.6) x 10^{-2}	17 %
Natural Limestone	(0.43 ± 0.13)	(4.3 ± 1.3) x 10^{-2}	12%
Arizona Test Dust	(0.2 ± 0.06)	(0.11 ± 0.03)	20 %
$CaCO_3$	(0.12 ± 0.04)	(2.1 ± 0.6) x 10^{-2}	5 %
Saharan Dust	(0.3 ± 0.08)	0.2 ± 0.05	4 %

Uptake experiments were performed at $^a[N_2O_5]_0 = (3.8 \pm 0.5)$ x 10^{12} cm^{-3} using 1g of sample powder for $A_s = 19.6$ cm^2; $^b[N_2O_5]_0 = (4.0 \pm 1.0)$ x 10^{11} cm^{-3} using 300 mg of sample powder for $A_s = 4.9$ cm^2. The yield of HNO_3 is given as a percentage with respect to the total molecules of N_2O_5 taken up after a given reaction time of 200 s at an orifice diameter of 8 mm

Table 4.4. Summary of uptake experiments of N_2O_5 on mineral dust samples: initial (γ_0) and steady state (γ_{ss}) uptake coefficients.

We report the observed initial uptake coefficients γ_0 for N_2O_5 on all the samples of mineral dust at low and high values of $[N_2O_5]$. For a concentration of $[N_2O_5]_0 = (3.8 \pm 0.5)$ x 10^{12} cm^{-3} the γ_0 values range from (6.4 ± 1.9) x 10^{-3} for Arizona test dust to (9.0 ± 2.6) x 10^{-2} for Saharan Dust. At $[N_2O_5]_0 = (4.0 \pm 1.0)$ x 10^{11} cm^{-3} the γ_0 values range from 0.12 ± 0.04 for $CaCO_3$ to 0.43 ± 0.13 for natural limestone. For samples such as Saharan Dust, $CaCO_3$ and Arizona Test Dust values of γ_{ss} and γ_0 decrease

between a factor of 3 and 7 from low to high $[N_2O_5]_0$. As indicated in Table 4.4, both the values γ_{ss} and γ_0 for $CaCO_3$ decrease only by a factor 3.5 from low to high $[N_2O_5]$. On the other hand a particular case is represented by natural limestone which shows a decrease of γ_{ss} and γ_0 by a factor of 20 and 40, respectively, when increasing $[N_2O_5]_0$. $CaCO_3$ showed values of γ_{ss} and γ_0 higher by a factor of 3 with respect to natural limestone at high $[N_2O_5]_0$. This difference is reversed by the same amount for low $[N_2O_5]_0$ with γ of natural limestone being highly sensitive to saturation by $[N_2O_5]$. Natural limestone is a sedimentary rock containing 97 % $CaCO_3$ by weight and a small percentage of metal oxides (1.9% of SiO_2, 0.5% of Al_2O_3, 0.3% of Fe_2O_3, and 0.3% of MgO) that may be responsible for the difference in the kinetic properties of $CaCO_3$ and natural limestone in addition to morphological properties. In recent work Krueger and co-workers[24] showed that dust containing calcium is very reactive with respect to the uptake of nitric acid. However, because of differences in mineralogy of single dust-particles, not all of the calcium-containing particles react similarly. It is important to note that for Kaolinite γ_{ss} and γ_0 are independent of $[N_2O_5]_0$ over the investigated range. Typical raw data from an uptake experiment of N_2O_5 on 1 g of Kaolinite and Saharan Dust are shown in Figures 4.6 and 4.7. In this series of experiments we did not succeed to saturate the samples during the present observation period.
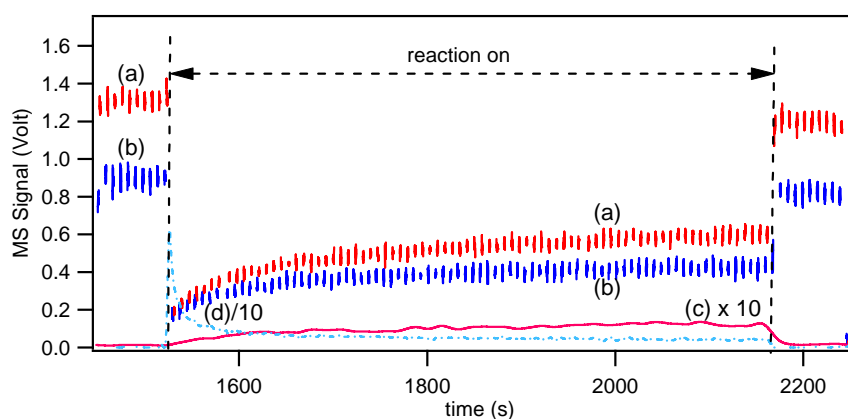
Figure 4.6. Typical N_2O_5 uptake experiment on a sample of 1 g of Kaolinite. Curves (a), (b), (c) and (d) correspond to the raw MS signals monitored at m/e 46, m/e 30, m/e 63 and m/e 18, respectively, using an orifice diameter of 8 mm and $[N_2O_5]_0 = (3.8 \pm 0.5) \times 10^{12}$ cm^{-3}.
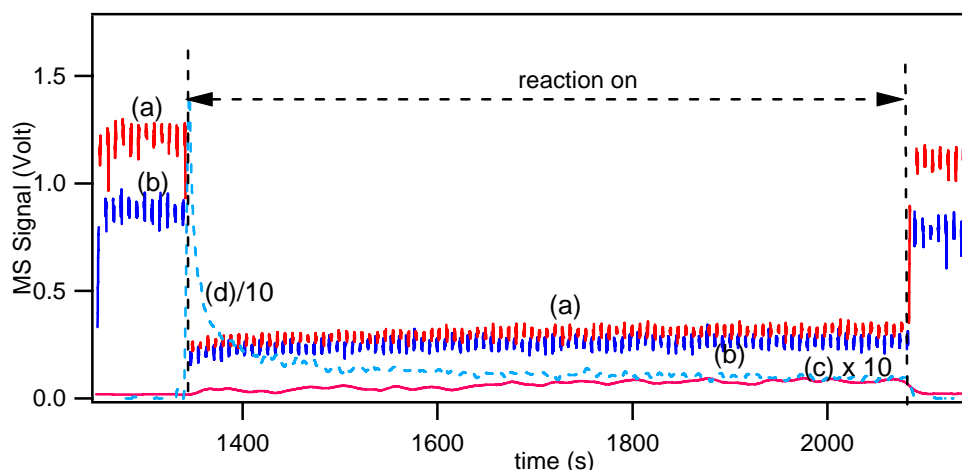
Figure 4.7. Typical N_2O_5 uptake experiment on a sample of 1 g of Saharan Dust. Curves (a), (b), (c) and (d) correspond to the raw MS signals monitored at m/e 46, m/e 30, m/e 63 and m/e 18, respectively, using an orifice diameter of 8 mm and $[N_2O_5]_0 = (3.8 \pm 0.5) \times 10^{12}$ cm^{-3}.

Uptake experiments of N_2O_5 on 0.2 g of Kaolinite powder were carried out by varying the initial flow of N_2O_5 into the reactor (Table 4.5). Figure 4.8 displays data for the 8 mm orifice corresponding to a residence time τ_g of 1.32 s for a variation of $[N_2O_5]_0$ by a factor 9.5 that is between $(4.0 \pm 1.0) \times 10^{11}$ cm^{-3} and $(3.8 \pm 0.5) \times 10^{12}$ cm^{-3}. Figure 4.8 shows that both γ_0 and γ_{ss} remain constant at 0.19 ± 0.05 and $(2.3 \pm 0.6) \times 10^{-2}$, respectively, independent of an increase in $[N_2O_5]$ and a change of the gas residence time τ_g. From this series of measurements it is evident that γ_{ss} follows a pseudo first order rate law in N_2O_5 in contrast to the other substrates which showed a decreasing trend from low to high $[N_2O_5]$ (see Figure 4.3 and Table 4.4).

$[N_2O_5]$ molecules cm^{-3}	γ_0	γ_{ss}
[a]$(4.0 \pm 1.0) \times 10^{11}$	0.16 ± 0.04	$(2.1 \pm 0.6) \times 10^{-2}$
[b]$(6.2 \pm 1.5) \times 10^{11}$	0.23 ± 0.06	$(2.6 \pm 0.5) \times 10^{-2}$
[a]$(9.0 \pm 0.5) \times 10^{11}$	0.22 ± 0.06	$(2.2 \pm 0.5) \times 10^{-2}$
[b]$(2.1 \pm 0.5) \times 10^{12}$	0.18 ± 0.05	$(2.4 \pm 0.7) \times 10^{-2}$
[a]$(3.8 \pm 0.5) \times 10^{12}$	0.16 ± 0.04	$(2.2 \pm 0.6) \times 10^{-2}$

[a] Orifice diameter = 8mm; [b]Orifice diameter = 4 mm.

Table 4.5. Summary of uptake experiments of N_2O_5 on 200 mg Kaolinite for data plotted in Figure 8: initial (γ_0) and steady state (γ_{ss}) uptake coefficients ($A_s = 4.9$ cm^2).

In recent work the uptake of N_2O_5 on Saharan Dust was found to be independent of $[N_2O_5]$ [11]. An initial uptake coefficient $\gamma_0 = (8.0 \pm 0.3)$ x 10^{-2} was found, whereas the steady state value $\gamma_{ss} = (1.3 \pm 0.3)$ x 10^{-2} was lower by a factor of five with respect to the present results at $[N_2O_5]_0 = (3.8 \pm 0.5)$ x 10^{12} cm^{-3}.
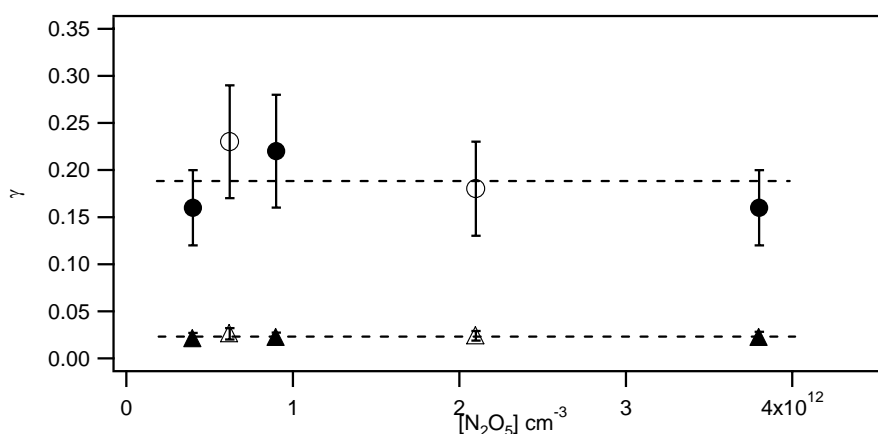
Figure 4.8. N_2O_5 on 200 mg Kaolinite: uptake coefficient γ of N_2O_5 as a function of $[N_2O_5]$: initial (γ_0, open circles) and steady state (γ_{ss}, full triangles) uptake coefficients for $A_s = 4.9$ cm^2. Full and empty symbols are referred to uptake experiments carried out with an orifice diameter of 4 and 8 mm orifice diameter, respectively.

We have observed delayed production of HNO_3 upon uptake of N_2O_5 for every sample investigated. Gas phase HNO_3 formation may be due to the heterogeneous hydrolysis of N_2O_5 according to reaction (4.9). In order to understand the gas phase production of HNO_3 we want to stress that all the investigated samples have a non negligible amount of adsorbed water available on the substrate surface. The quantities of $H_2O_{(ads)}$ that still remain on the different mineral dust substrates at our experimental conditions as reported in Table 4.4 and were measured by gravimetric measurements. The hygroscopic properties of mineral aerosol samples have been examined in recent work[25] which showed significant water adsorption on Arizona Test Dust compared to $CaCO_3$.

In Table 4.4 we also report the percentage of gas phase HNO$_3$ produced with respect to N$_2$O$_5$ taken up during a reaction time of 200 s. At [N$_2$O$_5$] = (3.8 ± 0.5) x 10^{12} cm^{-3}, Arizona Test Dust and Kaolinite turned out to be the samples to produce the largest amount of gas phase HNO$_3$, that is 72 % and 30 %, respectively, with respect to N$_2$O$_5$ taken up. On the other hand, Saharan Dust and CaCO$_3$ have been the samples with a lower yield of absolute HNO$_3$ produced, namely 5 % and 6 %, respectively. At [N$_2$O$_5$] = (4.0 ± 1.0) x 10^{11} cm^{-3} we obtained lower yields of gas phase HNO$_3$ compared to ten times higher [N$_2$O$_5$]. In this case we may correlate the low yield of HNO$_3$ to the large rate of uptake of N$_2$O$_5$ and of HNO$_3$ on mineral dust. Adsorbed HNO$_3$ may then form salts such as Ca(NO$_3$)$_2$, Fe(NO$_3$)$_3$ and surface nitrates as shown in other experimental studies[26-28]. A recent study on the reactivity of gaseous HNO$_3$ on atmospheric mineral dust samples reported values for the uptake of HNO$_3$ on CaCO$_3$, Saharan Dust and Arizona Test Dust[29]. In that work, a value of γ_0 = 0.11 was determined for Saharan Dust at [HNO$_3$] = (5.6 ± 0.4) x 10^{11} cm^{-3}, 0.14 for CaCO$_3$ and 6.6 x 10^{-2} for Arizona Test Dust. These results are consistent with the trend of the present yields of HNO$_3$ measured for nominally the same mineral dust samples. Whenever the uptake coefficient of HNO$_3$ on the mineral substrates was low such as for Arizona Test Dust and Kaolinite, we find increased amounts of HNO$_3$ in the gas phase. Conversely, the reverse is true for samples that rapidly take up HNO$_3$ as for CaCO$_3$ and Saharan Dust[28].

4.6 Atmospheric implications

We have shown in this work that N$_2$O$_5$ undergoes a heterogeneous reaction with surrogate substrates of mineral dust aerosol at T = 298 ± 2 K. The measured uptake coefficient showed different values for high and low N$_2$O$_5$ concentrations with the smallest differences for Saharan Dust. These γ values are generally larger than the ones used in a recent global modeling simulation of heterogeneous chemistry on mineral dust aerosol at dry conditions[9] where γ = 3.0 x 10^{-3} for N$_2$O$_5$ has been used. The γ values resulting from

the present measurements are larger by at least a factor of 10. Therefore, the uptake of N_2O_5 on mineral dust aerosols may potentially have a greater influence on the reduction of the global ozone concentration compared to the estimated value of 0.7 % [9].

The measured uptake coefficient γ of N_2O_5 on sulfuric acid aerosols was reported to lie within the range 0.06-0.12 at a temperature between 230 and 300 K [30]. Other measurements reported γ values of 0.05 on aqueous surfaces over a temperature range from 282 to 294 K [31]. To our knowledge no reaction probabilities of N_2O_5 on mineral aerosol have been determined to date. In a recent numerical modeling study the interaction of N_2O_5 ($\gamma = 0.1$), O_3 and HO_2 radicals with dust resulted in a decrease of tropospheric ozone of up to 10% near the dust source areas[6].

The photolytic rate of NO_3 ($J(NO_3) = 0.2$ s^{-1}) is too fast to allow its recombination with NO_2 to N_2O_5 during daylight. Therefore, the heterogeneous chemistry of N_2O_5 is important only at night-time. The heterogeneous reaction of N_2O_5 is most effective during the night when rh is at a maximum in the boundary layer. Thus, under these conditions, dust particles are likely to contain significant quantities of adsorbed water and the assumed high values of γ appear to be justified[32]. In a recent global modeling study $\gamma = 0.02$ (rh = 70%) and $\gamma = 3.0 \times 10^{-3}$ (rh = 30%) for humid and dry conditions have been used as upper and lower limits, respectively[9]. The modeling results show that when applying the high value for the uptake coefficient 0.8 % of the global ozone mass is removed by uptake of N_2O_5 on aerosols. The observed reaction products of the heterogeneous reaction of N_2O_5 with mineral dust, mainly HNO_3, may also have an influence on the oxidizing potential of the atmosphere as well as on the atmospheric ozone balance. Previous laboratory work[21,29,33] has shown the importance of the reactivity of HNO_3 on mineral dust substrates. In addition, modeling studies have quantitatively shown decreases in ozone concentration close to the area of HNO_3 destruction[9].

The Saharan dust sample, from Cape Verde (SDCV), that we have used is representative of atmospheric dust aerosol from a mineralogical standpoint. Its composition has been described in the literature[34] and closely simulates atmospheric particles of crustal origin[35]. The clay fraction (< 2 µm) of dust from Cape Verde shows a Kaolinite-Illite-Chlorite assemblage which is typical for central Saharan Dust. In the free troposphere mineral dust aerosol of a size less than 2 µm have a settling velocity of approximately 50 cm h^{-1} [36].

Therefore it can remain in the atmosphere for several days, travel long distances and undergoes heterogeneous reactions with trace gases.

The loss rate constant (k_{het}^{M}) due to heterogeneous uptake of a gas species M onto small aerosol particles is given by $k_{het}^{M} = \gamma A \bar{c}/4$ if the rate is not limited by diffusion, where γ is the uptake coefficient of M and is a function of the mineral dust aerosol composition, A is the surface area density of the dust aerosol and $\bar{c}$ is the mean molecular speed of M. Assuming a surface area density for Saharan Dust of about 1.5×10^{-6} cm^2 cm^{-3} [7], we estimate $k_{het}^{N_2O_5} = 1.76 \times 10^{-3}$ s^{-1} ($\tau_{het}^{N_2O_5} = 9.5$ min) for N_2O_5 based on $\gamma = 0.2$ for Saharan dust at $[N_2O_5] < (4.0 \pm 1.0) \times 10^{11}$ cm^{-3} (16 ppb). From the difference between the N_2O_5 formation and loss in the presence of the equilibrium with NO_3 we obtain the expression for the N_2O_5 steady state lifetime given in equation (4.11) [37]:

$$\tau_{ss}^{N_2O_5} = \left(k_{het}^{N_2O_5} + \frac{k_{het}^{NO_3} k_1(T)}{k_{-1}[NO_2]} \right)^{-1} \qquad (4.11)$$

$k_1(T)$ and k_{-1} are the rate constant for thermal decomposition of N_2O_5 and its inverse at atmospheric pressure according to equilibrium (4.1), respectively. From recent work on the NO_3 heterogeneous reaction on mineral dust we have obtained $\gamma = 0.2$ which leads to $k_{het}^{NO_3} = 2.4 \times 10^{-3}$ s^{-1} ($\tau_{het}^{NO_3} = 7$ min) for NO_3 [38] according to expression (4.11).

At T = 273 K $k_1(273K) = 3.1 \times 10^{-3}$ s^{-1} ($\tau = 5$ min) [2] and equilibrium (4.1) is shifted to the left. For $[NO_2]$ a typical value is 10 ppb in polluted air so that the pseudo first-order recombination rate $k_{-1}[NO_2]$ is 0.48 s^{-1} and is thus much larger than the rate constant for heterogeneous loss $k_{het}^{NO_3} = 2.4 \times 10^{-3}$ s^{-1}. Therefore, the second term of expression (4.11) will be negligible and the steady state lifetime $\tau_{ss}^{N_2O_5}$ of N_2O_5 will be determined by its heterogeneous loss rate constant $k_{het}^{N_2O_5}$.

At T = 293 K equilibrium (4.1) is shifted to the right with $k_1(293K) = 4.6 \times 10^{-2}$ s^{-1} ($\tau = 20$ s) which is an order of magnitude larger than at T = 273 K. Therefore, both terms in equation (4.11) will be of comparable magnitude which will decrease the steady state lifetime of N_2O_5 with respect to 273 K somewhat.

The calculated overall steady state lifetime for N_2O_5 at 293 K ($\tau_{ss}^{N_2O_5} = 8.5$ min) is significantly larger than the thermal dissociation lifetime ($\tau = 20$ s) of N_2O_5. At the same surface area concentration for dust aerosol of 1.5×10^{-6} cm^2 cm^{-3}, the heterogeneous loss rate k_{het}^{hydr} constant due to hydrolysis (reaction 4.9) is 2.25×10^{-4} s^{-1} corresponding to a lifetime of 74 min. This means that some N_2O_5 may be irreversibly converted to HNO_3 during the night by hydrolysis. During January 2004, Wood[39] performed in situ measurement of N_2O_5 in Contra Costa Country, California, and derived a steady state lifetime for N_2O_5 that ranged from 5 to 30 min at $[N_2O_5] = 200$ ppt (5.0×10^9 cm^{-3}) in the temperature range $275 - 285$ K which is comparable to $\tau_{ss}^{N_2O_5}$ calculated above. The measured lifetime for N_2O_5 from the field thus supports the heterogeneous loss rates of NO_3 and N_2O_5 measured in the present work.

4.7 References

(1)   Atkinson, R.; Baulch, D. L.; Cox, R. A.; Hampson, R. F.; Kerr, J. A.; Rossi, M. J.;
Troe, J.: Evaluated kinetic and photochemical data for atmospheric chemistry:
Supplement VI - IUPAC subcommittee on gas kinetic data evaluation for
atmospheric chemistry, Journal of Physical and Chemical Reference Data, 26,
1329-1499, (1997).

(2)   Wängberg, I.; Etzkorn, T.; Barnes, I.; Platt, U.; Becker, K. H.: Absolute
determination of the temperature behavior of the $NO_2+NO_3+(M)<-->N_2O_5+(M)$
equilibrium, Journal of Physical Chemistry A, 101, 9694-9698, (1997).

(3)   Tuazon, E. C.; Atkinson, R.; Plum, C. N.; Winer, A. M.; Pitts, J. N.: The Reaction
of Gas-Phase N_2O_5 with Water-Vapor, Geophysical Research Letters, 10, 953-
956, (1983).

(4)   Hjorth, J.; Ottobrini, G.; Cappellani, F.; Restelli, G.: A Fourier-Transform Infrared
Study of the Rate-Constant of the Homogeneous Gas-Phase Reaction $N_2O_5 + H_2O$
and Determination of Absolute Infrared Band Intensities of N_2O_5 and HNO_3,
Journal of Physical Chemistry, 91, 1565-1568, (1987).

(5)   Zhang, Y.; Sunwoo, Y.; Kotamarthi, V.; Carmichael, R.: Photochemical Oxidant
Processes in the Presence of Dust: An Evaluation of the Impact of Dust on
Particulate Nitrate and Ozone Formation., Journal of Applied Meteorology, 33,
813-824, (1994).

(6)   Dentener, F. J.; Carmichael, G. R.; Zhang, Y.; Lelieveld, J.; Crutzen, P. J.: Role of
mineral aerosol as a reactive surface in the global troposphere, Journal of
Geophysical Research-Atmospheres, 101, 22869-22889, (1996).

(7)   de Reus, M.; Dentener, F.; Thomas, A.; Borrmann, S.; Strom, J.; Lelieveld, J.:
Airborne observations of dust aerosol over the North Atlantic Ocean during ACE
2: Indications for heterogeneous ozone destruction, Journal of Geophysical
Research-Atmospheres, 105, 15263-15275, (2000).

(8)   Bonasoni, P.; Cristofanelli, P.; Calzolari, F.; Bonafé, U.; Evangelisti, F.; Stohl, A.;
Sajani, S. Z.; van Dingenen, R.; Colombo, T.; Balkanski, Y.: Aerosol-ozone
correlations during dust transport episodes, Atmospheric Chemistry and Physics,
4, 1201-1215, (2004).

(9)   Bauer, S. E.; Balkanski, Y.; Schulz, M.; Hauglustaine, D. A.; Dentener, F.: Global
modeling of heterogeneous chemistry on mineral aerosol surfaces: Influence on
tropospheric ozone chemistry and comparison to observations, Journal of
Geophysical Research-Atmospheres, 109, art. no.-D02304,
doi:10.1029/2003JD003868., (2004).

(10)   Bian, H. S.; Zender, C. S.: Mineral dust and global tropospheric chemistry: Relative roles of photolysis and heterogeneous uptake, Journal of Geophysical Research-Atmospheres, 108, 4672, doi:10.1029/2002JD003143., (2003).

(11)   Seisel, S.; Borensen, C.; Zellner, R.: Kinetics and mechanism of the uptake of N_2O_5 on mineral dust at 298 K, Atmospheric Chemistry and Physics Discussions, 5, 5645-5667, (2005).

(12)   Hanisch, F.; Crowley, J. N.: The heterogeneous reactivity of gaseous nitric acid on authentic mineral dust samples, and on individual mineral and clay mineral components, Physical Chemistry Chemical Physics, 3, 2474-2482, (2001 b).

(13)   Santschi, C.: Heterogeneous reactions of tropospheric trace-gases on solid model aerosol surface: a laboratory study, EPFL (Thesis work), p.254, (Thesis n. 2746 2003).

(14)   Stipp, S. L. S.; Eggleston, C. M.; Nielsen, B. S.: Calcite Surface-Structure Observed at Microtopographic and Molecular Scales with Atomic-Force Microscopy (AFM), Geochimica Et Cosmochimica Acta, 58, 3023-3033, (1994).

(15)   Kuriyavar, S. I.; Vetrivel, R.; Hegde, S. G.; Ramaswamy, A. V.; Chakrabarty, D.; Mahapatra, S.: Insights into the formation of hydroxyl ions in calcium carbonate: temperature dependent FTIR and molecular modelling studies, Journal of Materials Chemistry, 10, 1835-1840, (2000).

(16)   De Leeuw, N. H.; Parker, S. C.: Surface structure and morphology of calcium carbonate polymorphs calcite, aragonite, and vaterite: An atomistic approach, Journal of Physical Chemistry B, 102, 2914-2922, (1998).

(17)   Al-Hosney, H. A.; Grassian, V. H.: Carbonic acid: An important intermediate in the surface chemistry of calcium carbonate, Journal of the American Chemical Society, 126, 8068-8069, (2004).

(18)   Buhmann, D.; Dreybrodt, W.: The Kinetics of Calcite Dissolution and Precipitation in Geologically Relevant Situations of Karst Areas .1. Open System, Chemical Geology, 48, 189-211, (1985).

(19)   Dreybrodt, W.; Eisenlohr, L.; Madry, B.; Ringer, S.: Precipitation kinetics of calcite in the system $CaCO_3$-H_2O-CO_2: The conversion to CO_2 by the slow process H^++HCO_3-->CO_2+H_2O as a rate limiting step, Geochimica et Cosmochimica Acta, 61, 3897-3904, (1997).

(20)   Dreybrodt, W.; Lauckner, J.; Liu, Z. H.; Svensson, U.; Buhmann, D.: The kinetics of the reaction CO_2+H_2O^- --> H^++HCO_3^- as one of the rate limiting steps for the dissolution of calcite in the system H_2O-CO_2-$CaCO_3$, Geochimica et Cosmochimica Acta, 60, 3375-3381, (1996).

(21)   Seisel, S.; Börensen, C.; Vogt, R.; Zellner, R.: The heterogeneous reaction of HNO_3 on mineral dust and gamma-alumina surfaces: a combined Knudsen cell and DRIFTS study, Physical Chemistry Chemical Physics, 6, 5498-5508, (2004).

(22)   Caloz, F.; Fenter, F. F.; Tabor, K. D.; Rossi, M. J.: Paper I: Design and construction of a Knudsen-cell reactor for the study of heterogeneous reactions over the temperature range 130-750 K: Performances and limitations, Review of Scientific Instruments, 68, 3172-3179, (1997).

(23)   Keyser, L. F.; Moore, S. B.; Leu, M. T.: Surface-Reaction and Pore Diffusion in Flow-Tube Reactors, Journal of Physical Chemistry, 95, 5496-5502, (1991).

(24)   Krueger, B. J.; Grassian, V. H.; Cowin, J. P.; Laskin, A.: Heterogeneous chemistry of individual mineral dust particles from different dust source regions: the importance of particle mineralogy (vol 38, pg 6253, 2004), Atmospheric Environment, 39, 395-395, (2005).

(25)   Gustafsson, R. J.; Orlov, A.; Badger, C. L.; Griffiths, P. T.; Cox, R. A.; Lambert, R. M.: A comprehnsive evaluation of water uptake on atmospheric relevant mineral survaces: DRIFTS spectroscopy, thermogravinetric analysis and aerosol growth measurements, Atmospheric Chemistry and Physics Discussions, 5, 7191-7210, (2005).

(26)   Goodman, A. L.; Bernard, E. T.; Grassian, V. H.: Spectroscopic study of nitric acid and water adsorption on oxide particles: Enhanced nitric acid uptake kinetics in the presence of adsorbed water, Journal of Physical Chemistry A, 105, 6443-6457, (2001).

(27)   Vogt, R.; Finlayson-Pitts, B. J.: A Diffuse-Reflectance Infrared Fourier-Transform Spectroscopic (Drifts) Study of the Surface-Reaction of NaCl with Gaseous NO_2 and HNO_3, Journal of Physical Chemistry, 98, 3747-3755, (1994).

(28)   Börensen, C.; Kirchner, U.; Scheer, V.; Vogt, R.; Zellner, R.: Mechanism and kinetics of the reactions of NO_2 or HNO_3 with alumina as a mineral dust model compound, Journal of Physical Chemistry A, 104, 5036-5045, (2000).

(29)   Hanisch, F.; Crowley, J. N.: Heterogeneous reactivity of gaseous nitric acid on Al_2O_3, $CaCO_3$, and atmospheric dust samples: A Knudsen cell study, Journal of Physical Chemistry A, 105, 3096-3106, (2001 a).

(30)   Hanson, D. R.; Lovejoy, E. R.: The Uptake of N_2O_5 onto Small Sulfuric-Acid Particles, Geophysical Research Letters, 21, 2401-2404, (1994).

(31)   van Doren, J. M.; Watson, L. R.; Davidovits, P.; Worsnop, D. R.; Zahniser, M. S.; Kolb, C. E.: Temperature-Dependence of the Uptake Coefficients of HNO_3, HCl, and N_2O_5 by Water Droplets, Journal of Physical Chemistry, 94, 3265-3269, (1990).

(32)   Dentener, F. J.; Crutzen, P. J.: Reaction of N_2O_5 on Tropospheric Aerosols - Impact on the Global Distributions of NO_x, O_3, and OH, Journal of Geophysical Research-Atmospheres, 98, 7149-7163, (1993).

(33)   Goodman, A. L.; Underwood, G. M.; Grassian, V. H.: A laboratory study of the heterogeneous reaction of nitric acid on calcium carbonate particles, Journal of Geophysical Research-Atmospheres, 105, 29053-29064, (2000).

(34)   Coudé-gaussen, G.; Rognon, P.; Lecoustumer, M.: Gradual Input of Saharan Dust in the Silty Deposits of the Eastern Cape-Verde Islands, Comptes Rendus De L' Academie Des Sciences Serie Ii, 319, 1343-1349, (1994).

(35)   Desboeufs, K. V.; Losno, R.; Vimeux, F.; Cholbi, S.: The pH-dependent dissolution of wind-transported Saharan dust, Journal of Geophysical Research-Atmospheres, 104, 21287-21299, (1999).

(36)   Seinfeld, J. H.; Pandis, S. P.: Atmospheric Chemistry and Physics, John Wiley & Sons, Inc., pp.6-8, (1998).

(37)   Brown, S. S.; Stark, H.; Ravishankara, A. R.: Applicability of the steady state approximation to the interpretation of atmospheric observations of NO_2 and N_2O_5, Journal of Geophysical Research-Atmospheres, 108 (B3), 2162, DOI: 10.1029/2002JD002917, 2003, (2003).

(38)   Karagulian, F.; Rossi, M. J.: The heterogeneous chemical kinetics of NO_3 on atmospheric mineral dust surrogates, Physical Chemistry Chemical Physics, 7, 3150, (2005).

(39)   Wood, E. C.; Bertram, T. H.; Wooldridge, P. J.; Cohen, R. C.: Measurements of N_2O_5, NO_2, and O_3 east of the San Francisco Bay, Atmospheric Chemistry and Physics, 5, 483-491, (2005).

CHAPTER 5

HIGH REACTIVITY AND CHEMICAL KINETICS OF NO_3 ON LABORATORY FLAME SOOT

5.1 Introduction

Soot particles may allow heterogeneous chemical processes which are known to be important for the conversion of atmospheric trace gases like O_3 or NO_x[1,2]. Collision rates of radical species like HO_2 and NO_3 with soot particles may become comparable to the rates of their fastest homogeneous loss processes, indicating the potential oxidizing capacity of the atmosphere. However, in order to quantitatively estimate the importance of heterogeneous processes on soot surfaces we need to improve the experimental data base for a more intimate knowledge of the heterogeneous reaction mechanism.

Previous studies have examined the heterogeneous reaction of NO_2 with soot knowing that NO is un-reactive on this substrate[3-10]. One of the reaction products which results from the interaction of NO_2 with soot substrates is HONO. Nevertheless, there must be additional sources of HONO because soot is not sufficient to explain the [HONO] in the atmosphere. HONO is an important trace gas in the atmosphere because it is easily photolysed to produce OH + NO. In this manner, HONO photolysis increases the rate of photo-oxidation processes in the morning[11].

During daytime, HONO concentrations up to 200 ppt have been measured[12]. However, the HONO/NO_x ratio in the exhaust of modern vehicles is so much smaller that it cannot be resoponsible for the amounts measured during the night-time in the boundary layer[13]. Heterogeneous formation of HONO resulting from the reaction of NO_x with adsorbed H_2O

or reducing substrates has been studied extensively in the past but it does not explain the HONO concentrations observed in the atmosphere because this reaction is too slow[14]. This probably means that there is an important unknown source of HONO at daytime.

5.2 Experimental setup

A custom-designed co-flow system has been used in order to produce fresh flame soot from decane fuel in a reproducible way[8] (Figure 5.1). It consists of a diffusion flame maintained in a measurable flow of air. In order to regulate the fuel flow feeding the flame by capillary fores, two types of ceramics of different porosity were used. One type of soot has been generated in a lean flame (low fuel/oxygen ratio) and will be referred to as "black" soot, the second has been generated in a rich flame (high fuel/oxygen ratio) and will be referred to as "grey" soot. Table 5.1 displays the characteristic parameters we have used to produce the two types of flame soot. The samples were collected from the burnt gases at 1 cm above the visible flame on ambient temperature Pyrex glass plates of 19.6 cm^2 surface area. The soot substrates used in this work are meant to adequately represent the chemical and physical characteristics of fresh soot emitted into the atmosphere by combustion sources and suitable for a systematic laboratory study.
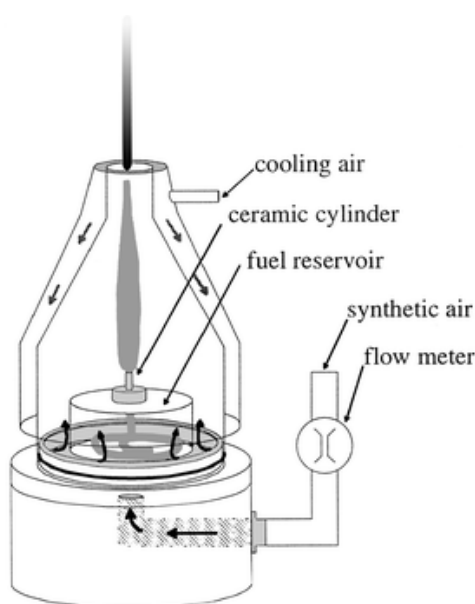
Figure 5.1. Schematic diagram of the co-flow system used to produce soot from liquid fuels.

Flame Type (Decane)	Air flow [L min^1]	Fuel duct (pore Ø) [μm]	Soot type	[8]BET surface Area [m^2 g^{-1}]	[3]Diameter of soot particle [nm]
Rich	1.2-1.4	17-40	"grey"	69	40
Lean	1.3-1.5	11-16	"black"	218	20

Table 5.1. Characteristic parameters of flame soot used to produce decane soot and general properties.

The mass of soot used in these experiments was varied between 1.5 and 20 mg spread out over 19.6 cm^2. Each sample was pumped for 10 min before performing an uptake experiment. The gas under study, NO$_3$, was generated by thermal decomposition of N$_2$O$_5$ at 530 K following the same procedure reported in Chapter 3. Hydrolysis of N$_2$O$_5$ may occur on internal surfaces of the inlet line before admission into the hot glass capillary generating HNO$_3$ as an impurity on the order of 10 to 15%. However, HNO$_3$ does not thermally decompose inside the hot glass tube of the NO$_3$ source because we did not observe any change in the MS signal amplitude at m/e 63 when increasing the source temperature from ambient to 530 K. In order to unambiguously monitor the concentration of NO and NO$_2$ in situ, Resonance Enhanced Multiphoton Ionization (REMPI) was employed as part of a multi-diagnostic experimental technique in addition to beam-sampling phase-sensitive mass spectrometry (MS). The experimental REMPI set up used is described in Chapter 2. The characterization of NO$_3$, its calibration and the secondary reactions in the hot NO$_3$ source are explained in Chapter 3.

We denoted $I_0^{62(NO_3)}$ and $I_r^{62(NO_3)}$ the MS signal at m/e 62 before and during reaction, respectively, and the observed rate constant k$_{obs}$ is given by equation (3.E2).

In the present data analysis, the observed uptake coefficient γ_{obs} (equation 2.8) was calculated using the geometric surface area A$_s$ of the sample holder which will be justified below based on suitable reference experiments. In the present chapter the observed uptake coefficient γ_{obs} became γ_{ss}, the steady state uptake coefficient, once steady state conditions were achieved after an exposure time of 500 s or so; γ_0 is γ_{obs} at t = 0 s, that is immediately after lifting the plunger.

Continuous flow uptake experiments were carried out at ambient temperature (298 ± 2 K) under molecular flow conditions. The concentration of NO$_3$ inside the Knudsen reactor

ranged between (2.7 ± 0.5) x 10^{11} cm^{-3} and (2.4 ± 0.5) x 10^{12} cm^{-3}. The associated [NO$_2$] determined by REMPI was (8.0 ± 1.0) x 10^{11} cm^{-3} for [NO$_3$] = (2.7 ± 0.5) x 10^{11} cm^{-3} and (6.2 ± 1.5) x 10^{12} cm^{-3} for [NO$_3$] = (2.4 ± 0.5) x 10^{12} cm^{-3}.

As shown in Figure 5.2, a large rate of disappearance of NO$_3$ was observed at m/e 62 (curve (d)). At the same time, initial formation of HONO as a reaction product was observed on grey soot and detected at m/e 47 (HONO$^+$) (curve (e)).
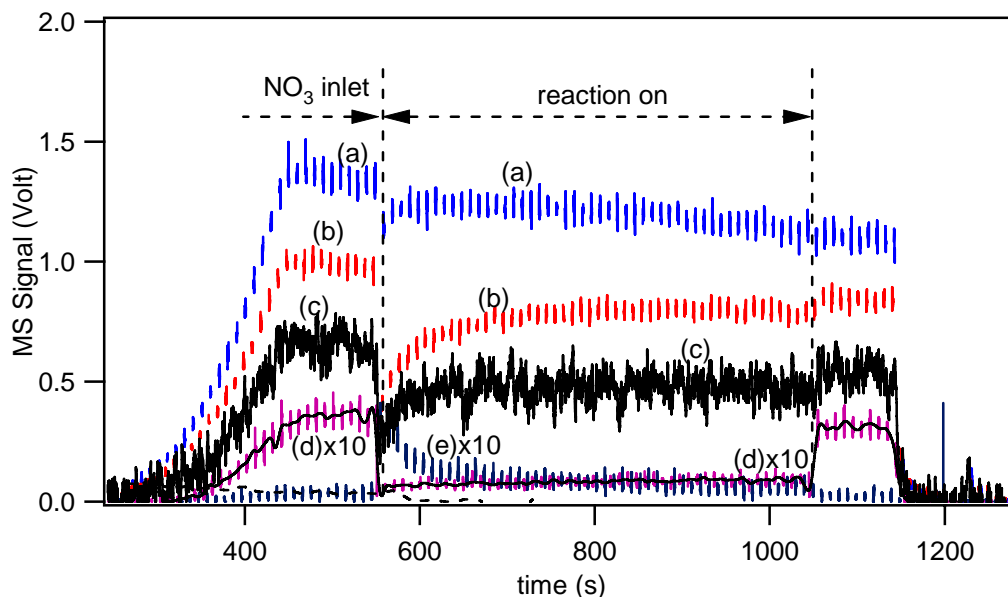
Figure 5.2. NO$_3$ uptake on a sample of 10 mg of grey soot at [NO$_3$] = (7.0 ± 1.0) x 10^{11} cm^{-3}. Curves (a), (b), (d), (e) and (f) correspond to the raw MS signals monitored at m/e 30, 46, 62, 47 and 63, respectively. Curve (c) corresponds to the raw REMPI signal for NO$_2$ detection at $\lambda_{NO_2} = 511$ nm converted to a MS signal at m/e 46.

5.3 Detection of products

The spectra of the species involved in the NO$_3$ source share common fragment peaks when using MS detection. NO$_3$ was monitored using mass spectrometry at m/e = 62 (NO$_3^+$). The main common fragment and molecular ion peaks for NO$_3$, N$_2$O$_5$, NO$_2$, NO and HNO$_3$ are m/e 46 and 30. The REMPI detection of NO$_2$ allowed us to subtract with great accuracy the contribution of NO$_2$ to the total MS signal I_0^{46} at m/e 46 that originated from the NO$_3$ source.

As indicated above, the NO_3 source contains HNO_3 as an impurity that contributes to the total MS signal at m/e 46. Fortunately, HNO_3 has a measurable, albeit low intensity, parent peak at m/e 63 at the present experimental conditions.

In order to evaluate the contribution of HNO_3 at m/e 46 and 30 based on the MS amplitude at m/e 63 we have analyzed the MS spectrum of pure HNO_3. The observable peaks of HNO_3 are at m/e 46 (NO_2^+), m/e 30 (NO^+) and m/e 63 (HNO_3^+). NO NO_2 impurity in HNO_3 was observed according to REMPI detection at λ_{NO_2} = 511 nm that is specific for NO_2. Using the detailed mass spectrum of pure HNO_3 we have accurately determined the effective contribution of HNO_3 at m/e 46 and 30 by using the fragmentation pattern expressed as the ratios $f_{46} = \dfrac{I_0^{46(HNO_3)}}{I_o^{63(HNO_3)}} = 52 \pm 8$ and $f_{30} = \dfrac{I_0^{30(HNO_3)}}{I_o^{63(HNO_3)}} = 33 \pm 4$.

We remind the reader that the absolute NO_2 concentration $\left[NO_2\right]_{0(REMPI)}$ originating from the NO_3 source has been determined by means of REMPI detection as explained in Chapter 2. We therefore calculated the corresponding MS signal contribution $I_{0(REMPI)}^{46(NO_2)}$ at m/e 46 originating from the NO_3 source according to equation (3.E3). In the following, the subscript 0 and r will refer to continuous gas uptake experiments in the absence and presence, respectively, of the sample.

In the absence of the soot substrate, $I_{0(REMPI)}^{46(NO_2)}$ and $f_{46} \cdot I_0^{63(HNO_3)}$ have been subtracted from the total MS signal I_0^{46} at m/e 46 in order to attribute the remaining signal to the NO_2^+ fragment of the electron-impact ionization of NO_3 once the absence of undissociated N_2O_5 from the NO_3 source was established. The resulting MS signal $I_0^{46(NO_3)}$ at m/e 46 is given by equation (3.E4).

When the sample is exposed to the gases from the NO_3 source, NO_3 is taken up and reacts on soot resulting in a decrease of $[NO_3]$ which leads to a concomitant decrease of the MS signal I_r^{46} at m/e 46. For the following series of experiments we have determined $r_{46} = \dfrac{I_0^{46(NO_3)}}{I_0^{62(NO_3)}} = 8.5 \pm 1.5$ as the ratio of the MS signal $I_0^{46(NO_3)}$ at m/e 46 (NO_2^+) and $I_0^{62(NO_3)}$, the molecular ion peak at m/e 62 (NO_3^+) for NO_3 free radical.

As a result of the exposure of the sample to NO_3 in the presence of NO_2, we expect four possible reaction products: HNO_3, N_2O_5, HONO and NO. Under our experimental conditions HNO_3 may possibly be formed at high densities by heterogeneous

recombination of NO$_2$ and NO$_3$ to N$_2$O$_5$ and subsequent heterogeneous hydrolysis. In order to find other possible reaction products contributing to excess I_{exc}^{46} MS signal intensity at m/e = 46 not due to HNO$_3$, we have subtracted the following known contributions from the total MS signal I_r^{46}: a) $I_{r(REMPI)}^{46(NO_2)}$ for NO$_2$, b) $r_{46} \cdot I_r^{62(NO_3)}$ for NO$_3$, c) $f \cdot I_r^{63(HNO_3)}$ for the possible HNO$_3$ formation during the reaction. The final residual amplitude I_{exc}^{46} was calculated according to equation (3.E5). It is reasonable to expect that N$_2$O$_5$ may be the only reaction product contributing to an excess at m/e 46, as will be discussed below. Therefore, in the following I_{exc}^{46} will be named $I_{exc}^{46(N_2O_5)}$.

It was not possible to quantify a possible formation of NO by REMPI detection at $\lambda_{NO} = 452.6$ nm because its concentration dropped below the detection limit given by the chosen experimental conditions. Therefore, in order to establish the amount of NO due to excess at I_{exc}^{30} MS signal intensity at m/e = 30 during the exposure of soot to NO$_3$, we have accurately determined all the possible contributions to the total MS signal I_r^{30} at m/e 30. The major contribution to I_r^{30} comes from the mixture of NO$_2$ and NO$_3$ originating from the hot NO$_3$ source given that the amount of HNO$_3$ and N$_2$O$_5$ in the presence of the sample are small. Using a reference mass spectrum of pure NO$_2$ we have calculated the effective contribution of NO$_2$ at m/e 30 by using the fragmentation pattern expressed as the ratio

$$z_1 = \frac{I_0^{NO_2(30)}}{I_0^{NO_2(46)}} = 2.0 \pm 0.2 .$$

The ratio of the MS signal $I_0^{30(NO_3)}$ at m/e 30 (NO^+) and $I_0^{62(NO_3)}$ at m/e 62 (NO_3^+) for NO$_3$ radical has been defined as follows:

$$r_{30} = \frac{I_0^{30(NO_3)}}{I_0^{62(NO_3)}} = \frac{I_0^{30} - z_1 \cdot I_0^{46(NO_2)} - f_{30} \cdot I_0^{63(HNO_3)}}{I_0^{62(NO_3)}} = 6.3 \pm 0.8 , \text{ where } I_0^{30} \text{ is the total MS signal}$$

at m/e 30, $z_1 \cdot I_0^{46(NO_2)}$ and $f_{30} \cdot I_0^{63(HNO_3)}$ are the contributions for NO$_2$ and HNO$_3$ both at m/e 30, respectively.

As explained above, it is reasonable to expect that N$_2$O$_5$ will be a reaction product of the reaction of NO$_3$ on soot. However, we have to consider that pure N$_2$O$_5$ has fragment peaks at m/e 46 and 30 which are correlated by the fragmentation pattern expressed as the ratio

$$r_{N_2O_5} = \frac{I_0^{46(N_2O_5)}}{I_0^{30(N_2O_5)}} = 1.36 \pm 0.3 .$$

As shown in previous studies on soot[15], HNO$_3$ reacts on the soot surface resulting in the formation of volatile products such as HONO and NO that contribute to the total MS signal I_r^{30} at m/e 30. At the present experimental conditions HONO has a measurable, albeit low intensity, parent peak at m/e 47 ($HONO^+$). Therefore, the effective contribution of HONO at m/e 30 has been determined by using its fragmentation pattern expressed as the ratio $h = \dfrac{I_0^{30(HONO)}}{I_o^{47(HONO)}} = 22 \pm 0.5$. As already explained above HNO$_3$ present in the hot NO$_3$ source also provides a contribution to the MS amplitude at m/e 30.

Finally, during the exposure of soot to NO$_3$ we have subtracted the following known contributions from the total MS signal I_r^{30}: a) $\dfrac{I_{exc}^{46(N_2O_5)}}{r_{N_2O_5}}$ for the contribution of generated N$_2$O$_5$, b) $z_1 \cdot I_{r(REMPI)}^{46(NO_2)}$ for the contribution of NO$_2$ present in the NO$_3$ source, c) $r_{30} \cdot I_r^{62(NO_3)}$ for the contribution of NO$_3$, d) $h \cdot I_r^{47(HONO)}$ for HONO, e) $f_{30} \cdot I_r^{63(HNO_3)}$ for HNO$_3$. The final expression for the residual amplitude I_{exc}^{30} resulted from the following equation:

$$I_{exc}^{30} = I_r^{30} - \frac{I_{exc}^{46(N_2O_5)}}{r_{N_2O_5}} - z_1 \cdot I_{r(REMPI)}^{(NO_2)46} - r_{30} \cdot I_r^{62(NO_3)} - h \cdot I_r^{47(HONO)} - f_{30} \cdot I_r^{63(HNO_3)} \qquad (5.E1)$$

The resulting residual MS signal from equations (3.E5) and (5.E1) is related to the reaction products owing to the heterogeneous interaction of NO$_3$ with the exposed surface of the sample. It is reasonable to expect that N$_2$O$_5$ and NO may be the only reaction product contributing to m/e 46 and 30, respectively, as will be discussed below.

5.4.1 NO$_3$ interaction with grey decane soot

The interaction of NO$_3$ and decane soot was investigated in a series of uptake experiments performed at different masses of soot and at different [NO$_3$]. Figure 5.2, shows a typical uptake experiment of NO$_3$ on 10 mg of grey soot at [NO$_3$] = (7.0 $\pm$ 1.0) x 10^{11} cm^{-3}. After a steady flow of NO$_3$ had been established, the isolation plunger was lifted at t = 550 s and the substrate exposed to the NO$_3$ flow. Because of the uptake of NO$_3$ on soot, the number of molecules effusing through the escape orifice into the MS immediately decreases.

At t = 1050 s the sample compartment is sealed by lowering the plunger and the MS signal at m/e 62 returns to its initial value. The slight decrease of $I_0^{62(NO_3)}$ over extended periods of time such as displayed if Figure 5.2 can be explained by a slight decrease of the corresponding flow rate into the reactor. In all of the performed experiments we obtained an uptake of NO$_2$ that stems from the thermal decomposition of N$_2$O$_5$ and NO$_3$ (reaction (3.1). This led to a net decrease of the REMPI signal for NO$_2$ at λ_{NO_2} = 511 nm (curve (c), Figure 5.2).

Reference uptake experiments with pure NO$_2$ in the presence of grey soot were performed at [NO$_2$] = (2.3 ± 0.5) x 10^{12} cm^{-3} (Figure 5.3). A large and instantaneous rate of uptake was observed and attained steady-state conditions after 3 minutes of interaction.

The initial and steady-state uptake coefficient resulted in γ_0 = (3.0 ± 0.6) x 10^{-2} and γ_{ss} = (1.3 ± 0.2) x 10^{-3}, respectively. Simultaneously to the uptake of NO$_2$ a large product peak of HONO appears which shows that the conversion of NO$_2$ into HONO is a fast process (curve (c), Figure 5.3). The observed HONO yields defined as the ratio of the amount of HONO released to the amount of NO$_2$ taken up during the reaction time tended towards 100 ± 10 % (Figure 5.3).
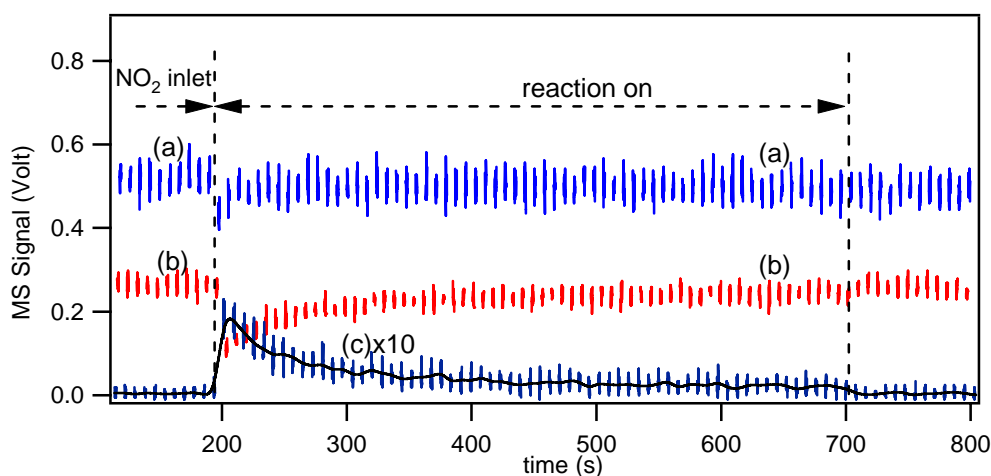
Figure 5.3. NO$_2$ uptake on a sample of 10 mg of grey soot at [NO$_2$] = (2.3 ± 0.5) x 10^{12} cm^{-3} (orifice diameter = 8 mm). Curves (a), (b) and (c) correspond to the raw MS signals monitored at m/e 30, 46 and 47, respectively. Curve (c) describes HONO production.

A similar behavior at low [NO$_2$] has been observed in recent work on the reactivity of NO$_2$ on flame soot[8]. The present reference experiments clearly showed that NO$_2$ adsorbs on

soot. This is in contrast with reference experiments with NO$_2$ on mineral dust which showed that NO$_2$ does not adsorb on dust substrate except on Saharan dust[16]. In that case NO$_2$ reacted only NO$_3$ adsorbed on the substrate via an Eley-Rideal mechanism.
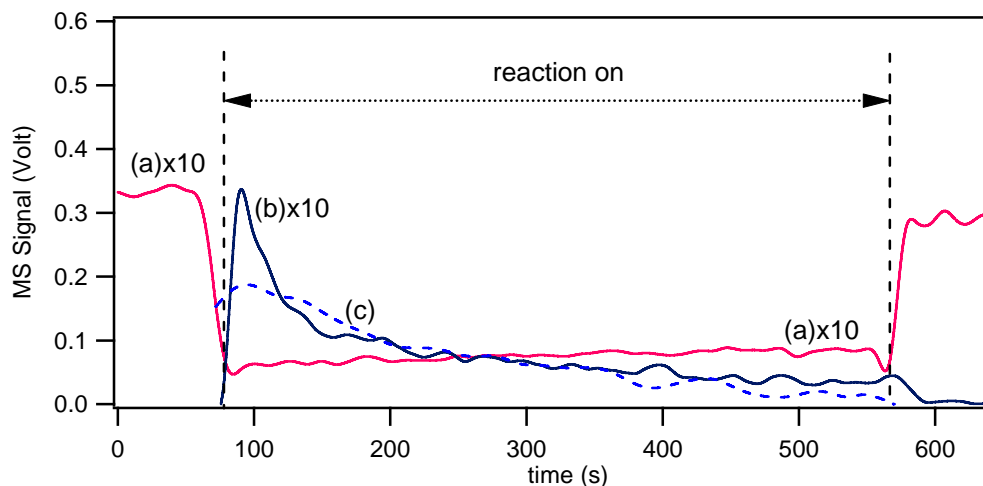
Figure 5.4a. Uptake of NO$_3$ on 10 mg of grey soot and resulting reaction products at $[NO_3] = (7.0 \pm 1.0) \times 10^{11}$ molecule cm^{-3} like in Figure 5.2 (orifice diameter = 8 mm). Curve (a) represents the raw MS signal at m/e 62 for the NO$_3$ uptake on the soot sample. Curve (b) represents the raw MS signal at m/e 47 related to the production of gas phase HONO. Curve (c) represents the corrected MS signal at m/e 30 corresponding to the production of gas phase NO.

During the uptake of NO$_3$ on grey soot the MS signal at m/e 62 (curve (a), Figure 5.4a) partially recovered as the exposure time increases, indicating a decrease in the rate of uptake of NO$_3$, presumably owing to a decrease of the net number of available surface sites for reaction. As a consequence we observed an apparent reduction of the uptake coefficient. As displayed in Figure 5.4a, a large burst of HONO at m/e 47 coincident with the uptake of NO$_3$ has been observed immediately after the exposure of the sample which reaches steady state after 500 s (curve (b), Figure 5.4a). Small amounts of NO have also been observed at the beginning of the reaction and tended to zero at steady-state conditions (curve (c), Figure 5.4a). A fast rate of initial formation of HONO and NO has been observed immediately after exposure of the sample to NO$_3$. The observed HONO formation results from the reduction of NO$_2$ by reducing H atoms in both $C - H$ bonds on the soot according to reactions (5.1a) and (5.1b) [17]:

$$NO_2 \rightarrow NO_{2(ads)} \qquad\qquad (5.1a)$$

$$NO_{2(ads)} \text{ or } NO_2 + \{C-H\}_{red} \rightarrow HONO + \{C\}_{ox} \qquad (5.1b)$$
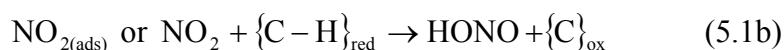
The species listed in curved brackets refer to surface adsorbates. $\{C-H\}_{red}$ represents a surface site that reduces NO$_2$ to HONO and $\{C\}_{ox}$ is the same site after surface oxidation by NO$_2$ on soot. The interaction of NO$_2$ with an adsorption site in reaction (5.1a) must be weak; otherwise NO$_2$ would not be sufficiently mobile to subsequently encounter other surface sites for reaction, (5.1b) in a Langmuir-Hinshelwood mechanism.
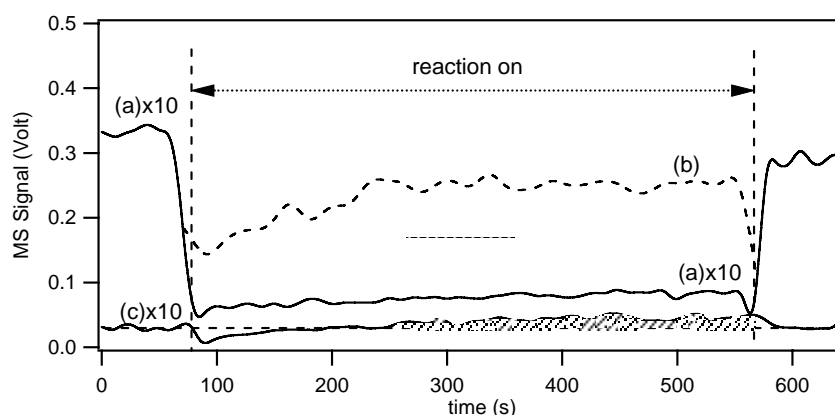
Figure 5.4b. Uptake of NO$_3$ on 10 mg of grey soot and resulting reaction products at [NO$_3$] = (7.0 ± 1.0) x 10^{11} molecule cm^{-3} (from experiment displayed in Figure 5.2, orifice diameter = 8 mm) Curve (a) represents the raw MS signal at m/e 62 for the NO$_3$ uptake on the soot sample. Curve (b) is the calculated MS signal at m/e 46, I_{exc}^{46}, corresponding to N$_2$O$_5$ formation. Curve (c) represents the raw MS signal at m/e 63 for the impurity HNO$_3$ uptake on soot. Positive flow MS signal at m/e 63 indicated by the hatched area under curve (c) represents the net amount of generated HNO$_3$.

For all grey and black soot samples we have observed the formation of small amounts of gas phase N$_2$O$_5$ which may be related to the uptake of NO$_2$ in the presence of adsorbed NO$_3$. It is important to note that NO$_2$ itself reacts both on grey and black decane soot[8]. Using relation (3.E5) we have calculated the yield of N$_2$O$_5$ from the increase of the MS signal at m/e 46, I_{exc}^{46}, displayed in Figure 5.4b (curve (b)). The yield of N$_2$O$_5$ following the

uptake of NO$_3$ continuously increases and reaches a steady-state after 500 s. The noise of curve (b) is the consequence of the large experimental uncertainty.

From the experiment displayed in Figure 5.4b we conclude that for an initial value of [NO$_3$] = (7.0 ± 1.0) x 10^{11} cm^{-3} and in the presence of [NO$_2$] = (1.0 ± 0.5) x 10^{12} cm^{-3}, (3.1 ± 0.3) x 10^{12} molecule cm^{-3} of N$_2$O$_5$ are produced at steady state conditions. Under our experimental conditions the formation of N$_2$O$_5$ may be related to the presence of NO$_2$ effusing from the NO$_3$ source via its reaction with adsorbed NO$_3$ on the soot substrate. The observed simultaneous uptake for both NO$_3$ and NO$_2$ suggests the formation of $N_2O_{5(ads)}$ through the heterogeneous recombination reaction (5.2a):

$$NO_{3(ads)} + NO_{2(ads)} \rightarrow N_2O_{5(ads)} \qquad (5.2a)$$
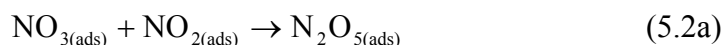
The conversion of NO_3 to N_2O_5 occurs via a Langmuir-Hinshelwood mechanism where NO_3 and NO$_2$ first adsorb onto the soot surface and subsequently react together forming N$_2$O$_5$ which in part leaves the surface. This reaction is the interfacial analogue of the well known gas-phase equilibrium (3.5b).

Once N$_2$O$_5$ has been formed in the adsorbed state, it may desorb into the gas phase.

$$N_2O_{5(ads)} \rightarrow N_2O_{5(g)} \qquad (5.2b)$$

HNO$_3$, present as an impurity, reacted on the soot substrate as well. This reaction has been studied in recent laboratory work using the same experimental apparatus[15]. As displayed in Figure 5.4b, a large initial uptake of HNO$_3$ was observed at m/e 63 (curve (c)). After a reaction time of 170 s, an excess in the MS signal at m/e 63 corresponding to formation rather than loss of HNO$_3$ was observed. The enhanced rate of formation of HNO$_3$ in the presence of soot means that part of $N_2O_{5(ads)}$ formed in reaction (5.2a) undergoes hydrolysis on the surface of soot. HNO$_3$ is then released back into the gas phase according to reaction (3.5d). At these experimental conditions we observe the production of (2.0 ± 0.5) x 10^{10} molecule cm^{-3} of HNO$_3$ at steady state. The yield of HNO$_3$ observed in uptake experiments performed at [NO$_3$] = (2.5 ± 0.5) x 10^{12} cm^{-3} on different amounts of grey and black soot was 1.5-2 % of the total number of NO$_3$ molecules taken up (see Table 5.2).

Grey soot	5 mg	10 mg	20 mg	average yield[(c)]
$NO_{3(lost)}$	$(3.2 \pm 0.7) \times 10^{18}$	$(3.3 \pm 0.7) \times 10^{18}$	$(3.3 \pm 0.7) \times 10^{18}$	$(3.3 \pm 0.7) \times 10^{18}$
$N_2O_{5(g)}$	[a]$(7.0 \pm 1.7) \times 10^{17}$ **22%**	[a]$(8.5 \pm 1.4) \times 10^{17}$ **25%**	[a]$(8.4 \pm 1.2) \times 10^{17}$ **22%**	$(8.5 \pm 1.4) \times 10^{17}$ **24%**
$NO_{2(lost)}$	$(2.4 \pm 0.6) \times 10^{18}$	$(2.5 \pm 0.5) \times 10^{18}$	$(3.7 \pm 0.7) \times 10^{18}$	$(3.1 \pm 0.6) \times 10^{18}$
$NO_{(g)}$	[a]$(3.2 \pm 0.5) \times 10^{17}$ **10%**	[a]$(3.3 \pm 0.7) \times 10^{17}$ **10%**	[a]$(4.6 \pm 1.0) \times 10^{17}$ **13%**	[a]$(4.0 \pm 0.9) \times 10^{17}$ **12%**
$HNO_{3(g)}$	[a]$(4.8 \pm 0.5) \times 10^{16}$ **1.5%**	[a]$(5.0 \pm 0.3) \times 10^{16}$ **1.5%**	[a]$(6.6 \pm 0.6) \times 10^{16}$ **2%**	[a]$(5.8 \pm 1.0) \times 10^{16}$ **1.5%**
$HONO_{(g)}$	[b]$(1.6 \pm 0.2) \times 10^{18}$ **94%**	[b]$(1.6 \pm 0.5) \times 10^{18}$ **98%**	[b]$(2.5 \pm 0.8) \times 10^{18}$ **87%**	[b]$(2.0 \pm 0.7) \times 10^{18}$ **92%**
Black soot	**5 mg**	**10 mg**	**20 mg**	**average yield[(c)]**
$NO_{3(lost)}$	$(3.2 \pm 0.5) \times 10^{18}$	$(3.4 \pm 0.8) \times 10^{18}$	$(3.5 \pm 0.5) \times 10^{18}$	$(3.5 \pm 0.5) \times 10^{18}$
$N_2O_{5(g)}$	[a]$(1.0 \pm 0.6) \times 10^{18}$ **31%**	[a]$(7.2 \pm 1.2) \times 10^{17}$ **20%**	[a]$(7.0 \pm 1.0) \times 10^{17}$ **20%**	[a]$(7.0 \pm 1.0) \times 10^{17}$ **20%**
$NO_{2(lost)}$	$(2.8 \pm 0.4) \times 10^{18}$	$(3.0 \pm 0.6) \times 10^{18}$	$(3.0 \pm 0.8) \times 10^{18}$	$(3.0 \pm 0.6) \times 10^{18}$
$NO_{(g)}$	[a]$(4.5 \pm 0.7) \times 10^{17}$ **14%**	[a]$(5.1 \pm 0.4) \times 10^{17}$ **15%**	[a]$(6.3 \pm 0.5) \times 10^{17}$ **18%**	[a]$(5.7 \pm 0.5) \times 10^{17}$ **16%**
$HNO_{3(g)}$	[a]$(4.8 \pm 0.5) \times 10^{16}$ **1.5%**	[a]$(6.8 \pm 0.7) \times 10^{16}$ **2%**	[a]$(5.2 \pm 0.5) \times 10^{16}$ **1.5%**	[a]$(6.0 \pm 0.7) \times 10^{16}$ **2%**
$HONO_{(g)}$	-	-	-	-

[a]Yield of N_2O_5, NO and HNO_3 given as percentage with respect to the total number of molecules of NO_3 taken up on grey and black soot during a reaction time of 500 s.

[b]Yield of HONO given as a percentage with respect to the total number of molecules of $NO_{2(lost)} - N_2O_{5(g)}$ taken up during a reaction time of 500 s.

Dash (-) indicates that no reaction product has been observed.

[c]The average yield is calculated on the basis of the results obtained for 10 and 20 mg of soot because there is no mass dependence as shown from Figures 5.11 and 5.12.

Table 5.2. Summary of the reaction products during the heterogeneous reaction of NO_3 on grey soot samples at $[NO_3]_0 = (2.3 \pm 0.5) \times 10^{12}$ cm^{-3} and $[NO_2]_0 = (6.0 \pm 1.0) \times 10^{12}$ cm^{-3} (orifice diameter = 8 mm).

An increase of gas phase HNO$_3$ formation in the presence of soot aerosol has been observed in recent experimental work at very low humidities in which NO$_2$, HNO$_3$, NO$_3$/N$_2$O$_5$ reacted on soot particles in a large aerosol chamber[18]. In the same study the reaction probability for reaction (3.5d) was assumed to be time independent and resulted in $\gamma = (4.0 \pm 2.0) \times 10^{-5}$.

In Table 5.2 we report the product yields for the NO$_3$ reaction on three different amounts of grey soot at [NO$_3$] = $(2.5 \pm 0.5) \times 10^{12}$ cm^{-3}. The mass balance reveals that 23-34 % of NO$_2$ taken up on grey soot has been converted into gas phase N_2O_5 according to reactions (5.2a) and (5.2b). The remaining 66-77 % of reacted NO$_2$ equals the yield of HONO produced according to reaction (5.1b) thereby satisfying the NO$_2$ mass balance for the number of molecules N of NO$_2$, namely $N(N_2O_5) + N(HONO) = N(NO_2)$. This condition summarizes that HONO is exclusively generated from the NO$_2$ precursor and that N$_2$O$_5$ contains one molecule of NO$_2$. Therefore, we may conclude that NO$_3$ reacting on grey soot does not generate HONO owing to the closed mass balance of NO$_2$. The fact that we observe a slow production of NO may not be attributable to the presence of NO$_2$. Previous work has already shown that HONO is the only gas phase product resulting from the reaction of pure NO$_2$ with grey soot[8,9]. Therefore, NO$_3$ may decompose into NO on the soot substrate according to the following decomposition reaction at the exclusion of NO$_2$ as a NO precursor:
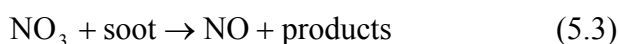
$$NO_3 + soot \rightarrow NO + products \qquad (5.3)$$

The amount of produced NO has been calculated from the excess MS signal at m/e 30, I_{exc}^{30} in according to equation (5.E1). The yield of NO did not show a significant variation with [NO$_3$] and the amount of soot. Table 5.2 displays the fact that NO corresponds to nearly 10-12% of NO$_3$ taken up on the substrate. In addition, NO is unreactive towards fresh unexposed soot samples[5,8], a result obtained in reference experiments for the present soot samples.

In order to explain the trend of the observed product yields in Figures 5.4a and 5.4b we need to analyse the reaction mechanism at the beginning (between t = 62 s and t = 210 s) and at t > 210 s of the uptake process, respectively. At the beginning the fast disappearance of gas phase NO$_2$ leads to fast HONO production (reaction (5.1b)). At the same time, the fast uptake of NO$_3$ enhances its decomposition on the substrate resulting in

a fast gas phase production of NO (reaction (5.3)). Consequently, only part of NO$_{3(ads)}$ reacts with NO$_2$ and recombines to N$_2$O$_5$ according to reaction (5.2a). At t > 210 s the number of adsorbed NO$_3$ molecules increases thereby inhibiting the turnover of available surface sites where NO$_3$ decomposition can take place. Therefore, reactions (5.2a) and (5.2b) become predominant with respect to reactions (5.1b) and (5.3) at later reaction time. On the other hand, HONO production is on-going in steady-state by continuous NO$_2$ reaction on grey soot.

We therefore conclude that according to Table 5.2 32 -35 % of NO$_3$ which reacted on grey soot has been converted into N$_2$O$_5$ and NO. The remaining amount of NO$_3$ is irreversibly taken up on the substrate, however no saturation for uptake of NO$_3$ has been observed.

5.4.2 NO$_3$ interaction with black decane soot

The reaction of NO$_3$ on black soot was examined in the same manner as for grey soot discussed above (Figure 5.5). A fast initial rate of uptake γ_0 has been observed for all experiments performed within a [NO$_3$] which ranged between $(2.7 \pm 0.5) \times 10^{11}$ cm^{-3} and $(2.3 \pm 0.5) \times 10^{12}$ cm^{-3} as reported in Table 5.2.
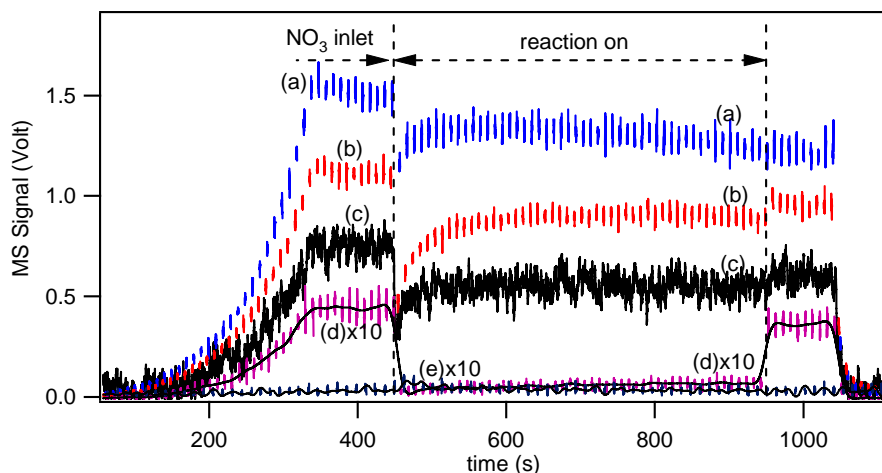
Figure 5.5. NO$_3$ uptake on a sample of 10 mg of black soot at [NO$_3$] = $(7.0 \pm 1.0) \times 10^{11}$ cm^{-3} (orifice diameter = 8 mm) Curves (a), (b), (d) and (e) correspond to the raw MS signals monitored at m/e 30, 46, 62 and 47, respectively. Curve (c) corresponds to the raw REMPI signal for NO$_2$ detection at λ_{NO_2} = 511 nm converted to a MS signal at m/e 46.

The amount of produced NO has been calculated from the excess MS signal at m/e 30, I_{exc}^{30} in according to equation (5.E1). This signal has been converted into a flow rate usnig a calibration factor for pure NO and subsequently integrated over the reaction time. From reference uptake experiments with pure NO_2 in the presence of black soot, we observed NO yields, defined as the ratio of the amount of NO released to the amount of NO_2 taken up during the reaction time, tended towards 40 ± 10 % (Figure 5.6). Similar behavior at low [NO_2] was observed in recent work on the reactivity of NO_2 on flame soot[8].
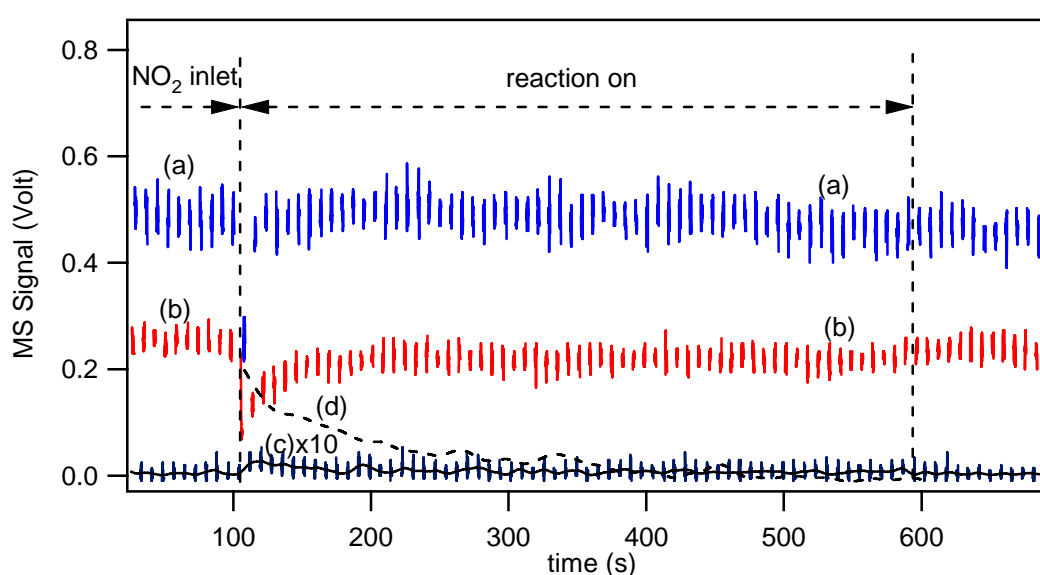
Figure 5.6. NO_2 uptake on a sample of 10 mg of black soot at [NO_2] = (2.3 ± 0.5) x 10^{12} cm^{-3} (orifice diameter = 8 mm). Curves (a), (b) and (c) correspond to the raw MS signals monitored at m/e 30, 46 and 47, respectively. Curve (d) (broken line) is related to NO production.

Figure 5.7 shows the uptake γ of NO_3 on 10 mg of black and grey soot at [NO_3] = (7.0 ± 1.0) x 10^{11} cm^{-3}. The value of γ_0 for black soot is twice that observed for grey soot. At steady state conditions the situation is reversed where γ_{ss} for black soot is smaller by a factor of two with respect to γ_{ss} for grey soot. However, the number on NO_3 molecules taken up on both substrates during the exposure time of 500 s is approximately the same.

As already observed for grey soot, simultaneous uptake of both NO$_3$ and NO$_2$ on black soot suggests the formation of small amounts of gas phase N$_2$O$_5$ according to reactions (5.2a) and (5.2b).
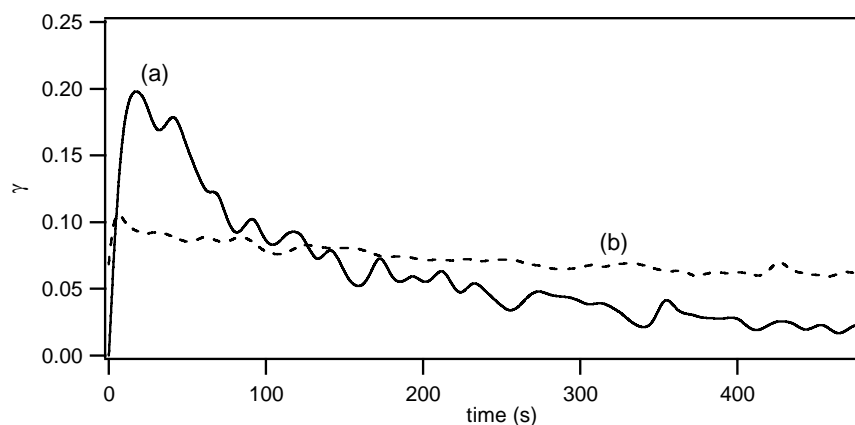
Figure 5.7. Uptake coefficient γ vs. time for NO$_3$ on 10 mg of black (a) and grey (b) soot. [NO$_3$] = (7.0 ± 1.0) x 10^{11} cm^{-3} (orifice diameter = 8 mm).

Figure 5.8 displays the NO product flow generated during uptake of NO$_3$ on 10 mg of black and grey soot at the same experimental conditions. As already discussed NO$_2$ present in the hot NO$_3$ source reacts with black soot to produce mainly NO as exemplified in the interaction with amorphous carbon[5]. NO$_2$ presumably interacts with black soot resulting in the formation of HONO akin to the reaction on grey soot which to a large extent decomposes into NO according to the following reaction mechanism proposed by Stadler[8]:

$$NO_2 + \{C-H\}_{red} \rightarrow HONO_{(ads)} + \{C\}_{ox} \qquad (5.4a)$$

$$2HONO_{(ads)} \rightarrow NO + NO_{2(ads)} + H_2O_{ads} \qquad (5.4b)$$
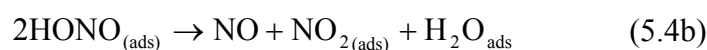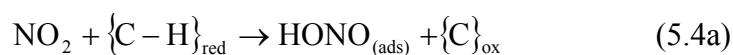
The difference in the NO yields between black and grey soot, curves (a) and (b) in Figure 5.8 is clearly related to NO formation according to the reaction mechanism (5.4a) and (5.4b) and may occur in addition to the NO yield originating from the heterogeneous decomposition of NO$_3$ on the substrate according to reaction (5.3) as was the case for grey

soot (Figure 5.8, Table 5.2). Therefore, the separation of NO formation owing to HONO and NO_3 decomposition is not possible for the black soot substrate.
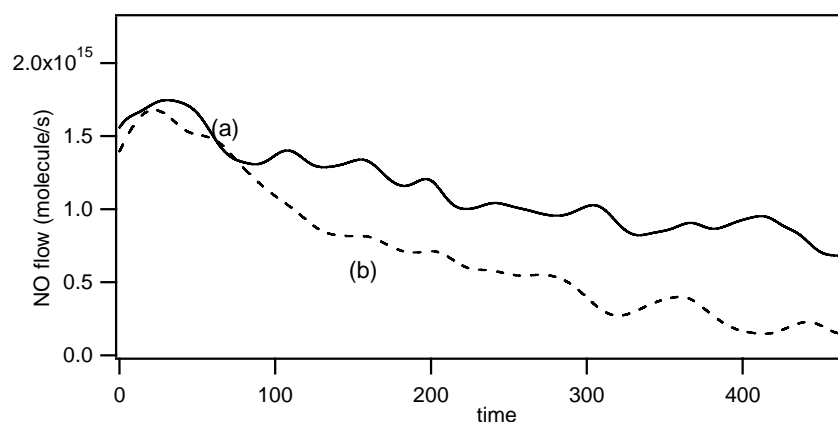
Figure 5.8. NO rate of formation vs. time for NO_3 on 10 mg of (a) black and (b) grey soot. $[NO_3] = (7.0 \pm 1.0)$ x 10^{11} cm^{-3} (orifice diameter = 8 mm).

In recent work performed by Stadler[8], black decane soot was exposed to a flow of pure HONO in order to decide whether or not HONO produced on black soot may irreversibly adsorb on the surface or decompose to NO. In that work fast uptake of HONO and production of NO was observed. The total NO product yield at limiting high concentration was 50% with respect to HONO taken up, whereas for $[HONO] = (3.7 \pm 0.4)$ x 10^{11} cm^{-3} the total product remaining yield consisted of a 40% NO and 10 % NO_2. The missing balance of nitrogen was attributed to a reservoir of HONO or reaction product adsorbed on the soot surface. We note that the NO rate of formation resulting from HONO decomposition on black soot is a slow process and is sustained at steady state conditions. On the other hand, the NO rate of formation resulting from NO_3 decomposition on grey soot rapidly tends to zero at steady state conditions as shown in Figure 5.8.

Table 5.3 reports the NO yield resulting from the uptake of NO_3 an 10 mg of grey and black soot at $[NO_3]$ between (2.7 ± 0.5) x 10^{11} cm^{-3} and (2.3 ± 0.5) x 10^{12} cm^{-3}. The yield of NO for black soot over an integration period of 500 s was 5 - 8 % larger than for grey soot. The calculated NO yield expressed as a percentage with respect to the total number of molecules of NO_3 taken up during the same reaction time resulted in a value of (13 ± 3.0) % for grey soot and (20 ± 5.0) % for black soot. The larger value of the NO

yield found for black soot is clearly attributable to HONO decomposition in the aftermath of the uptake of NO$_2$ on black soot. The small difference in the NO yields reported in Table 5.3 suggests that most of HONO remains adsorbed on black soot rather than decompose and form NO.

[NO$_3$]$_0$ cm^{-3}	^{a}NO (grey soot)	^{a}NO (black soot)
$(2.7 \pm 0.5) \times 10^{11}$	$(1.6 \pm 0.4) \times 10^{17}$ **13%**	$(2.0 \pm 0.5) \times 10^{17}$ **20%**
$(3.8 \pm 1.8) \times 10^{11}$	$(2.0 \pm 0.6) \times 10^{17}$ **11%**	$(2.6 \pm 0.7) \times 10^{17}$ **19%**
$(7.0 \pm 1.0) \times 10^{11}$	$(2.6 \pm 0.5) \times 10^{17}$ **9%**	$(4.3 \pm 0.4) \times 10^{17}$ **16%**
$(1.5 \pm 0.5) \times 10^{12}$	$(3.0 \pm 0.7) \times 10^{17}$ **8%**	$(5.8 \pm 0.8) \times 10^{17}$ **14%**
$(2.3 \pm 0.5) \times 10^{12}$	$(3.3 \pm 0.4) \times 10^{17}$ **10%**	$(5.1 \pm 0.7) \times 10^{17}$ **15%**

^{a}Yield of NO given as a percentage with respect to the total number of molecules of NO$_3$ taken up during the same reaction time.

Table 5.3. Summary of NO yield resulting from the uptake of NO$_3$ with 10 mg of grey and black soot at different [NO$_3$] (orifice diameter = 8 mm).

As reported in Table 5.3, the absolute yield of NO increases by almost a factor of 2 and 2.5 for grey and black soot, respectively at [NO$_3$] > $(7.0 \pm 1.0) \times 10^{11}$ cm^{-3}. This surprising result apparently depends on [NO$_3$], thus suggesting that the decomposition of NO$_3$ into NO involves a bimolecular or higher order process on black soot which becomes observable at high surface coverage of NO$_3$. We know from previous work[8] that NO cannot originate from NO$_2$ reacting on grey soot. The present work suggests that the calculated NO desorbing form black soot comes from decomposition of adsorbed HONO on the substrate.

5.5 Uptake kinetics of NO$_3$ on decane soot

The interaction of NO$_3$ with grey and black decane soot shows that after an initial fast uptake of NO$_3$ there is no saturation of the sample at steady state conditions. Figure 5.9 and Table 5.4 display the values of γ_{ss} as a function of [NO$_3$] for grey and black soot. The uncertainties for NO$_3$ uptake experiments were determined from the signal to noise ratio of the MS signal at m/e 62.

After extrapolation of the data we note that for a variation of [NO$_3$] between $(2.7 \pm 0.5) \times 10^{11}$ cm^{-3} and $(7.0 \pm 1.0) \times 10^{11}$ cm^{-3} γ_{ss} decreases from 0.2 ± 0.03 to 0.11 ± 0.01 for both types of soot. Variations of [NO$_3$] between $(7.0 \pm 1.0) \times 10^{11}$ cm^{-3} and $(2.3 \pm 0.5) \times 10^{12}$ cm^{-3} result in a constant value of $\gamma_{ss} = (6.5 \pm 1.5) \times 10^{-2}$, independent of [NO$_3$].
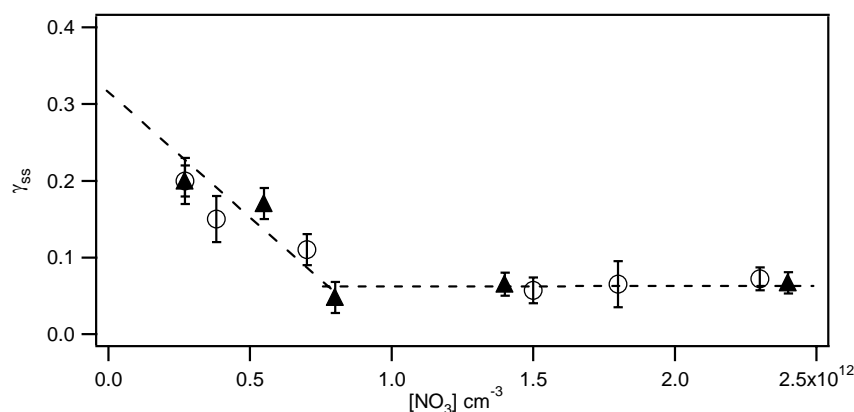
Figure 5.9. Uptake coefficient γ_{ss} of NO$_3$ as a function of [NO$_3$] (orifice diameter = 8 mm): NO$_3$ on black (triangles) and grey soot (open circles).

[NO$_3$]$_0$ cm^{-3}	γ_0 (grey soot)	γ_{ss} (grey soot)
$(2.7 \pm 0.5) \times 10^{11}$	0.44 ± 0.05	0.2 ± 0.02
$(3.8 \pm 1.8) \times 10^{11}$	0.35 ± 0.06	0.15 ± 0.03
$(7.0 \pm 1.0) \times 10^{11}$	0.15 ± 0.07	0.11 ± 0.02
$(1.5 \pm 0.5) \times 10^{12}$	0.12 ± 0.05	$(5.7 \pm 1.3) \times 10^{-2}$
$(1.8 \pm 0.5) \times 10^{12}$	0.12 ± 0.05	$(6.5 \pm 1.0) \times 10^{-2}$
$(2.3 \pm 0.5) \times 10^{12}$	0.12 ± 0.04	$(7.2 \pm 1.5) \times 10^{-2}$
[NO$_3$]$_0$ cm^{-3}	γ_0 (black soot)	γ_{ss} (black soot)
$(2.7 \pm 0.5) \times 10^{11}$	0.5 ± 0.07	0.2 ± 0.03
$(5.5 \pm 1.0) \times 10^{11}$	0.35 ± 0.08	0.17 ± 0.02
$(8.0 \pm 0.5) \times 10^{11}$	0.3 ± 0.04	$(6.7 \pm 1.4) \times 10^{-2}$
$(1.4 \pm 0.5) \times 10^{12}$	0.2 ± 0.05	$(6.5 \pm 1.5) \times 10^{-2}$
$(2.3 \pm 0.5) \times 10^{12}$	0.18 ± 0.03	$(4.8 \pm 1.0) \times 10^{-2}$

Table 5.4. Summary of uptake experiments of NO$_3$ on 10 mg grey and black decane soot: initial (γ_0) and steady state (γ_{ss}) uptake coefficients (orifice diameter = 8 mm).

From this series of measurements it is evident that γ_{ss} follows a rate law pseudo first order in NO$_3$ for [NO$_3$] > $(7.0 \pm 1.0) \times 10^{11}$ cm^{-3}. Conversely, for [NO$_3$] < $(7.0 \pm 1.0) \times 10^{11}$ cm^{-3}

the inverse dependence of γ_{ss} on [NO$_3$] suggests that the mechanism of NO$_3$ uptake is complex and does not correspond to a simple first-order uptake. A similar behavior has been observed for the interaction of NO$_3$ with mineral dust substrates such as Kaolinite[16] discussed in Chapter 3.
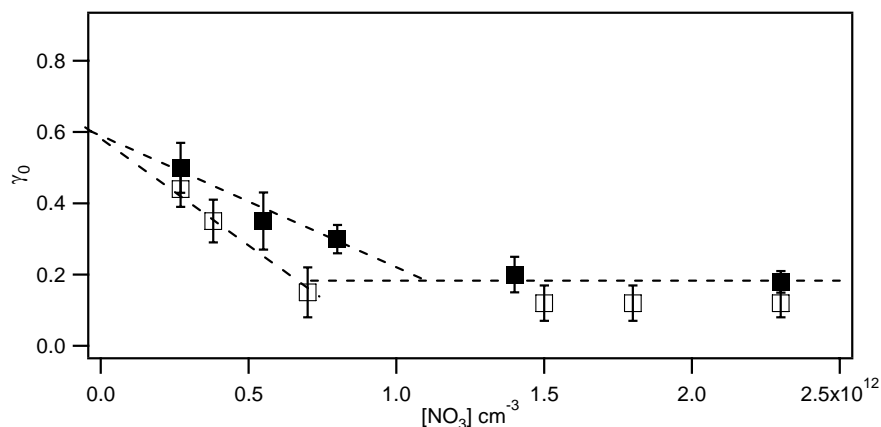
Figure 5.10. Uptake coefficient γ_0 of NO$_3$ as a function of [NO$_3$] (orifice diameter = 8 mm): NO$_3$ on black (full squares) and grey soot (open squares).

If γ_{ss} for black and grey soot seems to follow the same trend as a function of [NO$_3$], this is not the case for the value of the initial uptake coefficient γ_0. As shown in Figure 5.10 for [NO$_3$] > (7.0 ± 0.5) x 10^{11} cm^{-3} the γ_0 value of NO$_3$ corresponds to a pseudo-first order reaction and γ_0 for black and grey decane soot are almost identical. However, at [NO$_3$] < (1.0 ± 0.5) x 10^{11} cm^{-3} the reactivity as measured by γ_0 of NO$_3$ on black soot is larger with respect to grey soot.
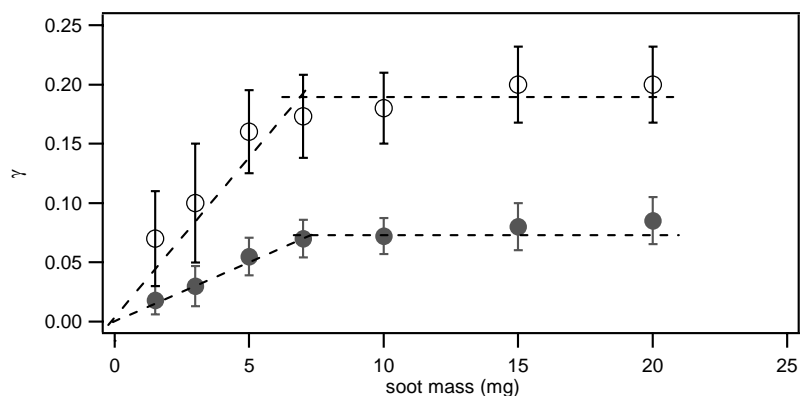
Figure 5.11. Uptake of NO$_3$ on grey soot: dependence of the initial (open circles) and steady state (full circles) uptake coefficient on sample mass at $[NO_3] = (2.3 \pm 0.5) \times 10^{12}$ cm^{-3} (orifice diameter = 8 mm).

Figures 5.11 and 5.12 display the steady state uptake γ_{ss} of NO$_3$ as a function of the mass of grey and black soot (Table 5.5). A linear dependence γ_{ss} as a function of the substrate mass is clearly visible for soot masses of up to 7 mg.
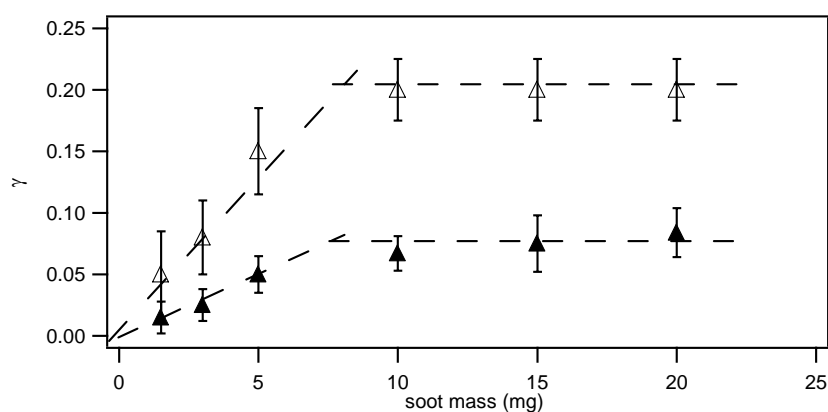
Figure 5.12. Uptake of NO$_3$ on black soot: dependence of the initial (open triangles) and steady state (full triangles) uptake coefficient on sample mass at $[NO_3] = (2.3 \pm 0.5) \times 10^{12}$ cm^{-3} (orifice diameter = 8mm).

We note that for the interaction NO$_3$-soot there is no mass dependence beyond the mass of 7 mg which we interpret as the minimum mass required to form a coherent monolayer of

soot. This value of 7 mg corresponds to a soot loading of $7/19.6 = 0.37$ mg/cm^2 and is identical for black soot. In earlier work[3] a value for the threshold loading of 0.41 ± 0.1 mg/cm^2 has been determined. Soot is a porous material and on the time scale of our experiment we do not expect NO$_3$ to explore the internal surface, of the pores as given for instance by the BET surface area as suggested by the present results.

Mass (mg)	γ_0 grey soot	γ_{ss} grey soot	γ_0 black soot	γ_{ss} black soot
1.5	$(7.0 \pm 4.0) \times 10^{-2}$	$(1.8 \pm 1.2) \times 10^{-2}$	$(5.0 \pm 3.5) \times 10^{-2}$	$(1.5 \pm 1.3) \times 10^{-2}$
3	0.1 ± 0.05	$(3.0 \pm 1.7) \times 10^{-2}$	$(8.0 \pm 3.0) \times 10^{-2}$	$(2.5 \pm 1.3) \times 10^{-2}$
5	0.16 ± 0.035	$(5.5 \pm 1.6) \times 10^{-2}$	0.15 ± 0.035	$(5.0 \pm 1.5) \times 10^{-2}$
7	0.17 ± 0.035	$(6.5 \pm 1.6) \times 10^{-2}$		
10	0.12 ± 0.030	$(7.2 \pm 1.2) \times 10^{-2}$	0.18 ± 0.03	$(6.7 \pm 1.4) \times 10^{-2}$
15	0.2 ± 0.032	$(8.0 \pm 2.0) \times 10^{-2}$	0.2 ± 0.03	$(7.5 \pm 2.3) \times 10^{-2}$
20	0.2 ± 0.032	$(8.5 \pm 2.0) \times 10^{-2}$	0.2 ± 0.03	$(8.4 \pm 2.0) \times 10^{-2}$

Table 5.5. Summary of uptake experiments with NO$_3$ on grey and black soot as a function of sample mass ([NO$_3$] = $(2.3 \pm 0.5) \times 10^{12}$ cm^{-3}, orifice diameter = 8mm).

We conclude that it is not necessary to apply the pore diffusion theory[19] in the case of NO$_3$ - soot in order to correct γ of NO$_3$ for the effect of the pore diffusion of soot. We take this result as justification to use the geometric surface area in evaluating the gas-surface collision frequency ω under the constraint of the present experimental conditions of low gas-phase residence times for NO$_3$, in part owing to the measured large values of the uptake coefficient γ_{ss}. The linear mass dependence of γ_0 and γ_{ss} observed below 7 mg for grey and black soot and displayed in Figures 5.11 and 5.12 means that we do not have formed a coherent layer of soot on the sample holder. Beyond 7 mg of soot the initial uptake coefficient γ_0 is very large and stayed constant, about 0.2, and the molecule of NO$_3$ does not have the time to explore the internal surface area of the substrate. Therefore, as already discussed for N$_2$O$_5$ on mineral dust substrates, we do not think that the application of the pore diffusion theory[19] may be applied for γ_0. At steady state conditions we observed that the uptake coefficient γ_{ss} follows the same trend as for γ_0. In that case the application of the pore diffusion theory may be only interpreted as a lower limit for γ whereas γ_{ss} based on the geometrical surface area may be regarded as an upper limit to the true value of γ.

The amount of adsorbed NO$_3$ for the uptake experiments on grey and black soot turned out to be the same. At [NO$_3$] = (2.3 ± 0.5) x 10^{12} cm^{-3} (3.3 ± 0.7) x 10^{18} molecules of NO$_3$ were adsorbed on 10 mg of soot during a reaction time of 500 s. During this time the samples did not saturate. As discussed in recent work on the interaction of NO$_3$ on mineral dust, NO$_3$ may be represented by a 4.5 Å diameter sphere with a projected surface area of 1.6 x 10^{-15} cm^2/molecule which leads to a full surface coverage of 6.3 x 10^{14} molecules cm^{-2}. The 10 mg sample of grey soot has a total surface area of 6.9 x 10^3 cm^2 based on a BET surface area of 69 m^2/g (see Table 5.1). This leads to 1.3x10^{16} and 4.3 x 10^{19} molecules NO$_3$ forming a monolayer on 10 mg of soot based on the geometric and BET surface area, respectively. Therefore, the total number of 3.3 x 10^{18} molecules of NO$_3$ taken up on the substrate led to a surface concentration of $\frac{3.3 \text{x} 10^{18}}{6.9 \text{x} 10^3} = 4.8 \text{x} 10^{14}$ molecule cm^{-2} which corresponds to a coverage (θ) of approximately 76 % based on the BET surface area.

5.6 Conclusions

Very recently, HONO formation was observed under laboratory conditions when NO$_2$ was adsorbed on soot particles in the presence of water vapour[8,17]. It was shown that NO$_2$ can be reduced on fresh soot particles involving reactive sites, possibly weakly bound hydrogen atoms or other reducing precursors. In addition, the maximum number of NO$_2$ molecules which can be reduced on the surface of soot particles is limited to less than a monolayer based on the total internal surface such as measured by BET. Therefore, soot cannot be the exclusive source of HONO in the polluted boundary layer[1]. However, from the present results it is clear that NO$_3$ decomposition on grey soot may lead to an additional source of NO at night.

From the present uptake experiments performed on grey and black soot we may extrapolate γ to vanishing NO$_3$ concentration as displayed in Figures 5.9 and 5.10 and obtain an estimation of γ_{ss} for [NO$_3$] < 7.0 x 10^{11} molecule cm^{-3}. With tropospheric [NO$_3$] at a typical value of 2.0 x 10^9 molecule cm^{-3}, γ_{ss} tends towards values larger than 0.3 according to the results displayed in Figure 5.9

The NO_3 loss rate constant (k_{het}) due to heterogeneous uptake onto aerosols is given by $k_{het} = \tau^{-1}(NO_3) = \gamma A\bar{c}/4$ where γ is the uptake coefficient of NO_3 and is a function of the mineral dust aerosol composition; A is the surface area density of the dust and $\bar{c}$ is the mean molecular speed of NO_3.

Urban air masses typically contain 10 μg m^{-3} black carbon aerosols[20], which corresponds to an aerosol surface area density of 7.0 x 10^{-6} cm^2 cm^{-3} and 2.2 x 10^{-5} cm^2 cm^{-3} for grey and black soot, respectively assuming the BET surface area reported in Table 5.1. Using these values and $\gamma = 0.3$ from our extrapolated value for NO_3 from figure 5.9 we evaluate a lifetime of 3 min and 1 min for NO_3 on grey and black soot, respectively. As already discussed in Chapter 3, this value has to be compared to the diurnal photolysis of NO_3 in fact during the day NO_3 has a short lifetime of about 5s due to its strong absorption in the visible region (662 nm). Since the photochemical gas-phase loss process of NO_3 only takes place during the day, NO_3 loss by reaction on soot and other aerosol surfaces such as mineral dust[21] is important only during the night.

In recent study on soot aerosol[18] the uptake of NO_3 on soot yielded an upper limit of $\gamma \leq 3.0$ x 10^{-4} at very low relative humidities ($H_2O < 10$ ppm), whereas at 50% rh it resulted in an upper limit of $\gamma \leq 1.0$ x 10^{-3}. These values are 2 (50% rh) and 3 order of magnitude lower than the γ value of 0.3 that results from the extrapolation for $[NO_3] < 7.0$ x 10^{11} molecule cm^{-3} in figure 5.9. In that same study[18] the impact of soot aerosol surface reactions on the formation of photochemical ozone was investigated in a box model calculation[18]. The results showed that soot has a minor impact on ozone formation at low $[NO_y]$, in contrast soot may cause ozone reduction of up to 10% at high $[NO_y]$. However, we must point out that the nature of the carbonaceous substrate, namely carbon from a spark ignition generator[18], is most probably significantly different from flame soot used in the present study.

5.7 Outlook

The large reactivity of NO_3 on grey and black soot and its subsequent reaction with adsorbed NO_2 coming from the hot NO_3 source resulted in rapid production of N_2O_5. As reported in Table 5.2, the yield of N_2O_5 approximately corresponds to 22-25 % of NO_3 taken up on grey and black soot. Reference experiments will be performed in the Knudsen flow reactor in order to measure the reactivity of pure N_2O_5 on soot. These measurements will allow us to determine the fraction of N_2O_5 generated as a primary product in reactions (5.2a) and (5.2b) and the fraction released into the gas phase upon uptake of NO_3. Particular attention will be paid to the detection of potential gas phase products such as NO, NO_2 and HNO_3. For this purpose we are looking at a new dye laser frequency in order to increase the sensitivity of REMPI detection of NO at $\lambda_{NO} = 452.6$ nm and possibly also of NO_2.

5.8 References

(1)   Schurath, U.; Naumann, K. H.: Heterogeneous processes involving atmospheric particulate matter, Pure and Applied Chemistry, 70, 1353-1361, (1998).

(2)   Kamm, S.; Möhler, O.; Naumann, K. H.; Saathoff, H.; Schurath, U.: The heterogeneous reaction of ozone with soot aerosol, Atmospheric Environment, 33, 4651-4661, (1999).

(3)   Salgado, M. S.; Rossi, M. J.: Flame soot generated under controlled combustion conditions: Heterogeneous reaction of NO_2 on hexane soot, International Journal of Chemical Kinetics, 34, 620-631, (2002).

(4)   Kleffmann, J.; Becker, K. H.; Lackhoff, M.; Wiesen, P.: Heterogeneous conversion of NO_2 on carbonaceous surfaces, Physical Chemistry Chemical Physics, 1, 5443-5450, (1999).

(5)   Tabor, K.; Gutzwiller, L.; Rossi, M. J.: Heterogeneous Chemical-Kinetics of NO_2 on Amorphous-Carbon at Ambient-Temperature, Journal of Physical Chemistry, 98, 6172-6186, (1994).

(6)   Rogaski, C. A.; Golden, D. M.; Williams, L. R.: Reactive uptake and hydration experiments on amorphous carbon treated with NO_2, SO_2, O_3, HNO_3, and H_2SO_4, Geophysical Research Letters, 24, 381-384, (1997).

(7)   Akhter, M. S.; Chughtai, A. R.; Smith, D. M.: The Structure of Hexane Soot-I - Spectroscopic Studies, Applied Spectroscopy, 39, 143-153, (1985).

(8)   Stadler, D.; Rossi, M. J.: The reactivity of NO_2 and HONO on flame soot at ambient temperature: The influence of combustion conditions, Physical Chemistry Chemical Physics, 2, 5420-5429, (2000).

(9)   Gerecke, A.; Thielmann, A.; Gutzwiller, L.; Rossi, M. J.: The chemical kinetics of HONO formation resulting from heterogeneous interaction of NO_2 with flame soot, Geophysical Research Letters, 25, 2453-2456, (1998).

(10)   Kalberer, M.; Ammann, M.; Arens, F.; Gäggeler, H. W.; Baltensperger, U.: Heterogeneous formation of nitrous acid (HONO) on soot aerosol particles, Journal of Geophysical Research-Atmospheres, 104, 13825-13832, (1999).

(11)   Finlayson-Pitts, B. J.; Pitts, J. N.: Tropospheric Air Pollution: Ozone, Airborne Toxics, Polycyclic Aromatic Hydrocarbons, and Particles, Science, 276, 1045-1052, (1997).

(12)   Staffelbach, T.; Neftel, A.; Blatter, A.; Gut, A.; Fahrni, M.; Stähelin, J.; Prevôt, A.; Hering, A.; Lehning, M.; Neininger, B.; Bäumle, M.; Kok, G. L.; Dommen, J.; Hutterli, M.; Anklin, M.: Photochemical oxidant formation over southern

Switzerland .1. Results from summer 1994, Journal of Geophysical Research-Atmospheres, 102, 23345-23362, (1997).

(13)   Kirchstetter, T. W.; Harley, R. A.; Littlejohn, D.: Measurement of nitrous acid in motor vehicle exhaust, Environmental Science & Technology, 30, 2843-2849, (1996).

(14)   Sakamaki, F.; Hatakeyama, S.; Akimoto, H.: Formation of Nitrous-Acid and Nitric-Oxide in the Heterogeneous Dark Reaction of Nitrogen-Dioxide and Water-Vapor in a Smog Chamber, International Journal of Chemical Kinetics, 15, 1013-1029, (1983).

(15)   Munoz, M. S. S.; Rossi, M. J.: Heterogeneous reactions of HNO_3 with flame soot generated under different combustion conditions. Reaction mechanism and kinetics, Physical Chemistry Chemical Physics, 4, 5110-5118, (2002).

(16)   Karagulian, F.; Rossi, M. J.: The heterogeneous chemical kinetics of NO_3 on atmospheric mineral dust surrogates, Physical Chemistry Chemical Physics, 7, 3150, (2005).

(17)   Ammann, M.; Kalberer, M.; Jost, D. T.; Tobler, L.; Rössler, E.; Piguet, D.; Gäggeler, H. W.; Baltensperger, U.: Heterogeneous production of nitrous acid on soot in polluted air masses, Nature, 395, 157-160, (1998).

(18)   Saathoff, H.; Naumann, K. H.; Riemer, N.; Kamm, S.; Möhler, O.; Schurath, U.; Vogel, H.; Vogel, B.: The loss of NO_2, HNO_3, NO_3/N_2O_5, and $HO_2/HOONO_2$ on soot aerosol: A chamber and modeling study, Geophysical Research Letters, 28, 1957-1960, (2001).

(19)   Keyser, L. F.; Moore, S. B.; Leu, M. T.: Surface-Reaction and Pore Diffusion in Flow-Tube Reactors, Journal of Physical Chemistry, 95, 5496-5502, (1991).

(20)   Berner, A.; Sidla, S.; Galambos, Z.; Kruisz, C.; Hitzenberger, R.; tenBrink, H. M.; Kos, G. P. A.: Modal character of atmospheric black carbon size distributions, Journal of Geophysical Research-Atmospheres, 101, 19559-19565, (1996).

(21)   Martinez, M.; Perner, D.; Hackenthal, E. M.; Kulzer, S.; Schütz, L.: NO_3 at Helgoland during the NORDEX campaign in October 1996, Journal of Geophysical Research-Atmospheres, 105, 22685-22695, (2000).

CHAPTER 6

THE HETEROGENEOUS DECOMPOSITION OF OZONE ON ATMOSPHERIC MINERAL DUST SURROGATES AT AMBIENT TEMPERATURE

6.1 Introduction

Ozone decomposition on mineral dust is a reaction of atmospheric significance that has attracted considerable attention[1-6]. So far, the mechanism for O_3 destruction on mineral dust is unclear. Recent work has shown that ozone loss can be due to decomposition, catalytic destruction or absorption on mineral oxides[7].

Dentener and co-workers suggested[2] in their modelling studies, that the ozone destruction on mineral aerosol surfaces could lead to a 10% reduction of O_3 concentration in the dust source areas. This study assumed a reaction probability $\gamma = 5.0 \times 10^{-5}$ for O_3 on mineral dust surfaces. Recently, Bauer and co-workers[8] have found a decrease of 5% of the global tropospheric ozone mass in a global modelling study employing an uptake coefficient $\gamma_{O_3} = 1.0 \times 10^{-5}$ as a best guess. On the other hand, another modelling study which considered the coupling of the photochemical and heterogeneous effects of dust[9], led to a global ozone decrease of 0.7% assuming $\gamma_{O_3} = 5.0 \times 10^{-5}$. These significant differences may be caused by differences in the model formulations.

The present chapter reports a kinetic study of the heterogeneous reaction of O_3 on mineral dust surrogates presented as powders; its objective is to investigate the mechanism of adsorption of ozone on surrogates of mineral dust as well as the kinetics of the heterogeneous reaction including reaction products that are released into the gas phase.

6.2 Experimental setup

All experiments were performed in the Knudsen flow reactor operating in the molecular flow regime. The characteristic parameters and relevant kinetics expressions for steady state and pulsed valve experiments are reported in Chapter 2 as well the production of O_3. The mineral dust composition used in this study is reported in Table 3.1. The two kinds of sample holders, TEFLON® coated Pyrex of 19.6 cm^2 of available sample surface and an internal reduction piece made out of DELRIN® of available surface area of 4.9 cm^2, did not show any reactivity with O_3 under the present experimental conditions.

According to the UV absorption we estimated that the O_2 impurity in the O_3 sample amounted to 15-28% of the total pressure. Mass m/e 32 was both a marker for the potential reaction product O_2 as well as an important fragment of O_3. In addition, one has to consider that the MS signal $S_{32}(t)$ at m/e 32 will contain the contributions due to the O_2 impurity present in the O_3 sample that amounts to 15-28% of the total pressure according to UV absorption, and due to the small O_2 background already present in the flow reactor.

Ozone has a measurable fragment and a parent peak at m/e 32 (O_2^+) and m/e 48 (O_3^+), respectively. In the absence of the sample, one has to consider the contributions to the MS signal S_{32}^0 at m/e 32 due to the O_2 impurity S_{32}^{imp} in the O_3 sample and to the O_2 background S_{32}^{back} in the flow reactor. We define $S_{32}^{imp} = \dfrac{F_{O_2}^{imp}}{C_{O_2}}$ where $F_{O_2}^{imp}$ is the O_2 flow relative to the total measured flow $F_{O_2+O_3}^{tot}$ and is expressed as $F_{O_2}^{imp} = F_{O_2+O_3}^{tot} \cdot \dfrac{x}{100}$ with x(%) being the percentage O_2 impurity in the total measured flow $F_{O_2+O_3}^{tot}$. The calibration factor C_{O_2} has been determined in separate experiments where the MS signal intensity at m/e 32 was measured as a function of the injected pure O_2 flow. The percentage of O_2 in O_3 is measured in separate calibration experiments using UV absorption as discussed above.

Before exposing the substrate to ozone the corrected MS signal at m/e 32, $\overline{S}_{32}^0$, is given by equation (6.E1):

$$\overline{S}_{32}^{0} = S_{32}^{0} - S_{32}^{back} - S_{32}^{imp} \qquad (6.E1)$$

Upon lifting the plunger the flow $F_{O_2}(t)$ of oxygen produced by ozone decomposition on the examined substrate has been calculated using the following equation (6.E2):

$$F_{O_2}(t) = \left(S_{32}^{r}(t) - S_{32}^{back} - S_{32}^{imp} - R^{\frac{32}{48}} S_{48}(t) \right) \cdot C_{O_2} \qquad (6.E2)$$

where $S_{32}^{r}(t)$ is the raw MS signal at m/e 32 during O_3 uptake, $R^{\frac{32}{48}} = \overline{S}_{32}^{0}/S_{48}^{0} = 1.7 \pm 0.5$ represents the ratio between the corrected MS signal at m/e 32 and 48 before the exposure of the sample to ozone, $S_{48}(t)$ is the MS signal at m/e 48 during the uptake experiment and C_{O_2} is the calibration factor for oxygen. Equation (6.E2) assumes that molecular oxygen does not react with the sample; a fact that has been established is separate reference experiments. Therefore, $\Delta F_{O_3}(t) = F_{O_3}^{in}(t) - F_{O_3}^{out}(t)$ represents the flow or the rate of O_3 lost during the uptake experiment that was calculated by calibrating the resulting MS signal at m/e 48.

The parameter of main interest is given by the ratio $r(t) = F_{O_2}(t)/\Delta F_{O_3}(t)$ as a function of time during which the surface is exposed to O_3. It is the relative yield of O_2 generated per O_3 molecule destroyed on the substrate.

6.3.1 O_3 reaction on poorly ordered Kaolinite

The uptake of ozone on Kaolinite samples taken as a surrogate for mineral dust monitored at m/e 48 was measured at room temperature (RT) with the goal to obtain a quantitative measure of the reaction kinetics as well as the reaction products. The measurements were performed at ozone concentrations in the range 4.0×10^{11} to 2.4×10^{12} cm^{-3}. In the present data analysis, the observed uptake coefficient γ_{obs} (equation 2.8) was calculated using the geometric surface area A_s of the sample holder. The observed uptake coefficient γ_{obs} became γ_{ss}, the steady state uptake coefficient, once steady state conditions were achieved after an exposure time of 600 s or so; γ_0 is γ_{obs} at t = 0 s, that is immediately after lifting

the plunger. Figure 6.1 shows a representative uptake experiment of ozone on 0.2 g of Kaolinite spread out on a surface A_s of 4.9 cm^2. Curves (a) and (b) correspond to the raw MS signal monitored at 32 (O_2^+) and m/e 48 (O_3^+), respectively. A constant flow of O_3 that was isolated from the sample by the isolation plunger was initially established. When the flow of O_3 reached a constant level, the isolation plunger was lifted and the initial uptake coefficient γ_0 of ozone on the substrate was obtained. A decrease of the uptake of ozone with exposure time was observed until steady state uptake is reached at $t \geq 800$ s. This steady state level is presumably controlled by the competition between the rate of adsorption, heterogeneous reaction and desorption of ozone or its decomposition products.
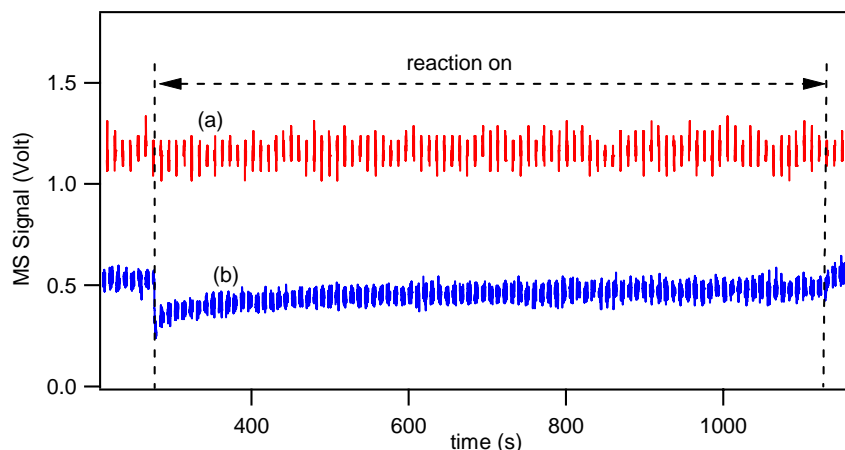
Figure 6.1. Representative Knudsen-Cell experiment for O_3 uptake on 0.2 g sample of Kaolinite. Curves (a) and (b) correspond to raw MS signals monitored at m/e 32 and 48, respectively ([O_3] = (2.7 ± 0.7) x 10^{12} cm^{-3}; 14 mm orifice; surface sample area A_s = 4.9 cm^2).

Uptake experiments of O_3 on Kaolinite powder were systematically carried out by varying the initial concentration of O_3 and its residence time τ_g. For a given orifice size and thus τ_g we observed that k_{ss} was independent of [O_3] within experimental uncertainty. As a case in point we present data for the 14 mm orifice ($\tau_g = 0.2$ s) and for [O_3] ranging between (4.0 ± 0.5) x 10^{11} and (2.4 ± 0.7) x 10^{12} cm^{-3}, leading to k_{ss} = (0.203 ± 0.033) s^{-1}, and a steady state uptake coefficient γ_{ss} = (9.0 ± 1.5) x 10^{-3} (dashed line in Figure 6.2, Table 6.1) based on the geometric surface area of the sample support.

From this series of measurements it is evident that the decomposition reaction of ozone on Kaolinite corresponds to a pseudo first-order rate constant k_{ss}. However, if we decrease the orifice size, thus increase τ_g at constant $[O_3] = (2.4 \pm 0.7) \times 10^{12}$ cm^{-3} the values of k_{ss} decrease as displayed in Figure 6.3 and Table 6.2. The strong dependence of k_{ss} on τ_g at a given $[O_3]$ suggests that the mechanism of ozone uptake is complex and does not correspond to a simple first-order rate law for uptake.
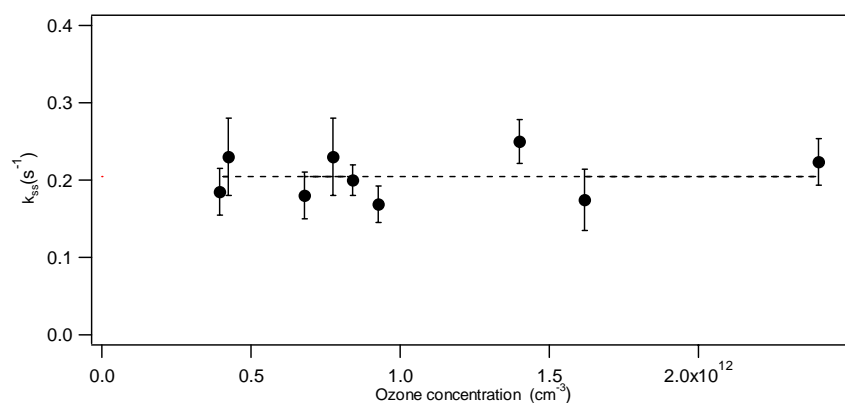
Figure 6.2. Plot of the pseudo-first order rate constant k_{ss} for steady state uptake of O_3 on 0.2 g of Kaolinite versus O_3 concentration at ambient temperature (14 mm orifice; surface sample area $A_s = 4.9$ cm^2).

$[O_3]$ (cm^{-3})	k_{ss} (s^{-1})	γ_{ss}
$(4.0 \pm 0.5) \times 10^{11}$	0.18 ± 0.035	$(8.3 \pm 1.6) \times 10^{-3}$
$(4.2 \pm 0.8) \times 10^{11}$	0.23 ± 0.027	$(1.0 \pm 0.12) \times 10^{-2}$
$(6.8 \pm 0.7) \times 10^{11}$	0.18 ± 0.035	$(8.3 \pm 1.6) \times 10^{-3}$
$(7.7 \pm 1.0) \times 10^{11}$	0.23 ± 0.027	$(1.0 \pm 0.12) \times 10^{-2}$
$(8.4 \pm 1.1) \times 10^{11}$	0.20 ± 0.022	$(9.0 \pm 1.0) \times 10^{-3}$
$(9.3 \pm 1.3) \times 10^{11}$	0.17 ± 0.040	$(7.7 \pm 1.8) \times 10^{-3}$
$(1.4 \pm 0.3) \times 10^{12}$	0.25 ± 0.037	$(1.1 \pm 0.17) \times 10^{-2}$
$(1.6 \pm 0.5) \times 10^{12}$	0.17 ± 0.040	$(7.7 \pm 1.8) \times 10^{-3}$
$(2.4 \pm 0.7) \times 10^{12}$	0.22 ± 0.036	$(1.0 \pm 0.16) \times 10^{-2}$

Table 6.1. Results of uptake experiments of O_3 on 0.2 g (40.8 mg/cm^2) of Kaolinite at different concentrations and ambient temperature (14 mm orifice; surface sample area $A_s = 4.9$ cm^2).

These observations indicate that the reactivity of O_3 on Kaolinite decreases for long residence times τ_g as the heterogeneous reaction rate not only depends on the gas phase concentration but apparently also on intermediates whose surface concentration depend on the extent of reaction that scales with τ_g. Therefore, the conclusion that the rate law is first order in O_3 based on the results of Figure 6.2 may be erroneous because of the apparent independence of k_{ss} on $[O_3]$ over a narrow concentration range.
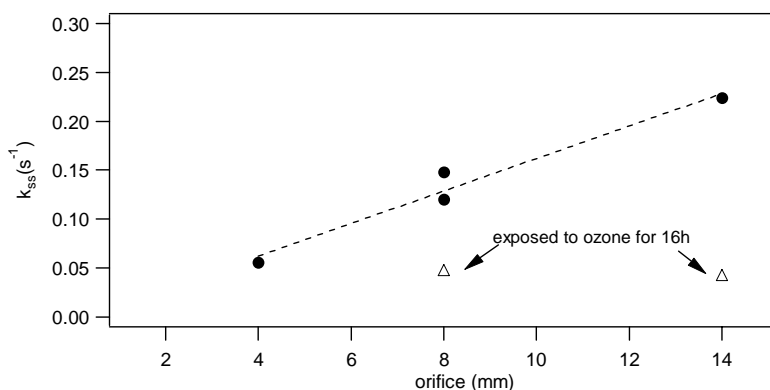
Figure 6.3. Plot of k_{ss} of O_3 on 0.2 g of Kaolinite versus orifice size (full circles) at surface sample area A_s = 4.9 cm^2; ($[O_3]$ = (2.0 ± 0.5) x 10^{12} cm^{-3}). Open triangles correspond to samples that have been exposed to 4 mbar of O_3 for 16 h off-line.

k_{ss} (s^{-1})	γ_{ss}	Orifice (mm)	τ_g (s)	#$_{O3}$ reacted ($\Delta t \sim 800$ s)
(2.2 ± 0.27) x 10^{-1}	(1.0 ± 0.12) x 10^{-2}	14	0.2	7.4 x 10^{17}
[a](4.8 ± 3.2) x 10^{-2}	(2.2 ± 1.4) x 10^{-3}	14	0.2	-
(1.5 ± 0.3) x 10^{-1}	(6.7 ± 1.4) x 10^{-3}	8	0.5	3.9 x 10^{17}
(1.2 ± 0.35) x 10^{-1}	(5.5 ± 1.6) x 10^{-3}	8	0.5	3.2 x 10^{17}
[a](4.3 ± 3.5) x 10^{-2}	(2.0 ± 1.6) x 10^{-3}	8	0.5	-
(5.6 ± 3.0) x 10^{-2}	(2.5 ± 1.4) x 10^{-3}	4	2.0	3.0 x 10^{17}

[a] after O_3 exposure (16h)

Table 6.2. Uptake experiments of O_3 on 0.2 g of Kaolinite for different orifices (A_s = 4.9 cm^2; $[O_3]$ = (2.0 ± 0.5) x 10^{12} cm^{-3}; integration time $\Delta t \sim 800$ s).

In order to confirm this hypothesis, further experiments were carried out on samples of Kaolinite by exposing them to a partial pressure of 4 Torr of O_3 during 16h in a separate static vessel. In the following we used the 8 and 14 mm orifices in order to probe the heterogeneous uptake of O_3 and obtained $k_{ss} = (4.3 \pm 3.5)$ x 10^{-2} and (4.8 ± 3.2) x 10^{-2} s^{-1} for the 8 and 14 mm orifices, respectively. A similar value, namely $k_{ss} = (5.6 \pm 3.0)$ x 10^{-2} s^{-1}, was already found for the 4 mm orifice without preliminary exposure to O_3 as shown in Figure 6.3. It seems that a long exposure of the sample to O_3 deactivates a large fraction of reactive surface sites and leads to values of γ that are up to a factor of five smaller than γ_{ss} measured at low τ_g (Figure 6.3). However, a constant "baseline" reactivity persists at steady-state independent of τ_g, after O_3 pre-treatment. Therefore, this "baseline" or residual rate constant for O_3 decomposition is independent of $[O_3]$ following the results displayed in Figure 6.3 as well as of τ_g used to probe the O_3/Kaolinite interaction (open triangles in Figure 6.3, Table 6.2). Theoretically, the value of r(t) should tend towards 1.5 for the decomposition of O_3 according to the following pseudo-elementary reactions:

$$O_3 + SS \rightarrow O(SS) + O_2 \qquad\qquad (6.1)$$

$$O_3 + O(SS) \rightarrow O_2 + O_2(SS) \qquad\qquad (6.2)$$
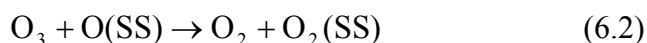
where SS and O(SS) are reactive surface sites for O_3 and the atomic oxygen intermediate after O_3 decomposition, respectively. $O_2(SS)$ indicates an adsorbed peroxy species formed in reaction (6.2) through oxidation of the atomic oxygen intermediate O(SS) by O_3. The present measurements do not allow the positive identification of the formation of O(SS) or O_2(SS). However, spectroscopic studies on the decay of O_3 on a manganese oxide substrate by Li and Oyama[10,11] showed evidence of the formation of a peroxy species akin to $O_2(SS)$ on the substrate surface. The final step in the ozone decomposition reaction may be the thermal decomposition of the peroxide species to form gaseous O_2 according to:

$$O_2(SS) \rightarrow O_2 + SS \qquad\qquad (6.3)$$

Reaction (6.1) is much faster than reactions (6.2) and (6.3), and does not involve the most-abundant reaction intermediate, the peroxide species $O_2(SS)$. Therefore, reactions (6.2) and (6.3) will be rate-limiting and thus measurable. Reactions (6.1) and (6.2) are presumed to be irreversible because we have never detected O_3 in desorption using mass spectrometry.

The net is the sum of reactions (6.1), (6.2), and (6.3) and describes the catalytic decomposition of O_3 on mineral dust:

$$2O_3 \rightarrow 3O_2 \qquad\qquad (6.4)$$

This mechanism may explain why transition metal oxides such as manganese oxide, are good catalysts for ozone decomposition.

In the O_3 uptake experiment reported in Figure 6.4 r(t) was always less than 1.5 so that catalytic decomposition of O_3 may be ruled out.
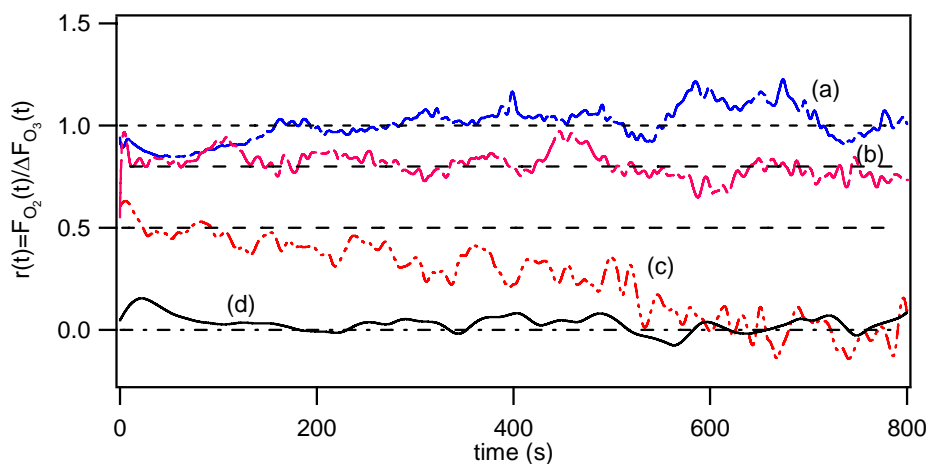
Figure 6.4. The relative yield r(t) during the uptake experiment of O_3 on 0.2 g of Kaolinite. Curves (a), (b) and (c) represent plots of r(t) at 14 mm (τ_g = 0.2 s), 8 mm (τ_g = 0.5 s) and 4 mm (τ_g = 2.0 s) orifices, respectively. Curve (d) represents a plot of r(t) at 1 mm for a saturated sample exposed to 4 Torr of O_3 during 16 h. ([O_3] = (2.0 ± 0.5) x 10^{12} cm^{-3}, A_s = 4.9 cm^2).

At steady state r(t) ranges from 1.0 for a short residence time τ_g = 0.2 s for O_3 (curve (a), Figure 6.4), to essentially 0.2 for large residence time τ_g = 2.0 s (curve (c), Figure 6.4).

For the O_3-pretreated Kaolinite discussed above, the ratio r(t) hovers at small values so that r(t) < 0.5 during the whole duration of the uptake (curve (d), Figure 6.4).

The full mechanism is not as simple as just shown in reactions (6.1), (6.2), (6.3) and (6.4). There is evidence from the inverse dependence of the kinetics on the residence time τ_g (displayed in Figure 6.3) that suggests that O_3 may also bind to the substrate without O_2 release. In order to be able to describe this large variation in r(t) the present results suggest a mechanism consisting of four pseudo-elementary reactions for the heterogeneous interaction of O_3 with Kaolinite. Initially, O_3 collides with a reactive surface site SS on the surface and deposits an O atom (reaction (6.1)). This reaction initiates the heterogeneous decomposition of O_3 on chemically reactive surface sites (SS) on the substrate and plays an important role at short residence time τ_g of O_3 leading to r(t) = 1.0 (curve (a), Figure 6.4). Two other types of reactions may be proposed where O_3 directly reacts with the surface to form a complex without O_2 formation according to reactions (6.5) and (6.6):

$$O_3 + SS \rightarrow adduct \tag{6.5}$$

$$O_3 + O(SS) \rightarrow adduct \tag{6.6}$$

These reactions are introduced in order to explain the disappearance of O_3 without the formation of gas phase O_2. Without any detailed knowledge of the surface, the nature and molecular structure of the complex resulting from reaction (6.5) remains obscure.

Without any detailed knowledge of the surface, the nature and molecular structure of the complex resulting from reaction (6.5) remains obscure. However, for the adduct resulting from reaction (6.6) a structure may be proposed under the assumption that the solid state reactant resulting from reaction (6.1) is $SS^{\delta^+} - O^{\delta^-}$:
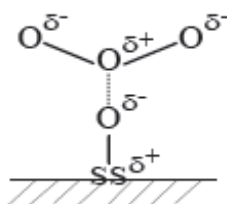
The larger rate of O_3 disappearance compared to O_2 formation is expected to hold for short residence times of O_3 at the beginning of the interaction between O_3 and the Kaolinite powder substrate just after having lifted the plunger and leads to $r(t) = 1.0$. The combination of reactions (6.1) and (6.5) or (6.6) enables values of $r \leq 1.0$ because all the measured values of $r(t)$ decrease from 1.0 to a low value of $r(t) \sim 0.2$ at large values of τ_g and large extents of reaction as shown in Figure 6.4. Considering the data displayed in Figure 6.4 it appears in conclusion that adduct formation, reaction (6.5) or (6.6), is favoured over reaction (6.1) at increasing extents of reaction at constant $[O_3]$. At the beginning of reaction $r(t)$ is close to one and drops to 0.5 at longer reaction times which corresponds to the increasing importance of reaction (6.6) compared to reaction (6.1) (curve (a), Figure 6.4). However, the fact that $r(t)$ drops below 0.5 as displayed in Figure 6.4 (curves (c) and (d)) points to the fact that reaction (6.5) is also occurring at the beginning of the O_3 uptake experiment. If reaction (6.5) would exclusively be occurring, $r(t) = 0$ would be obtained.
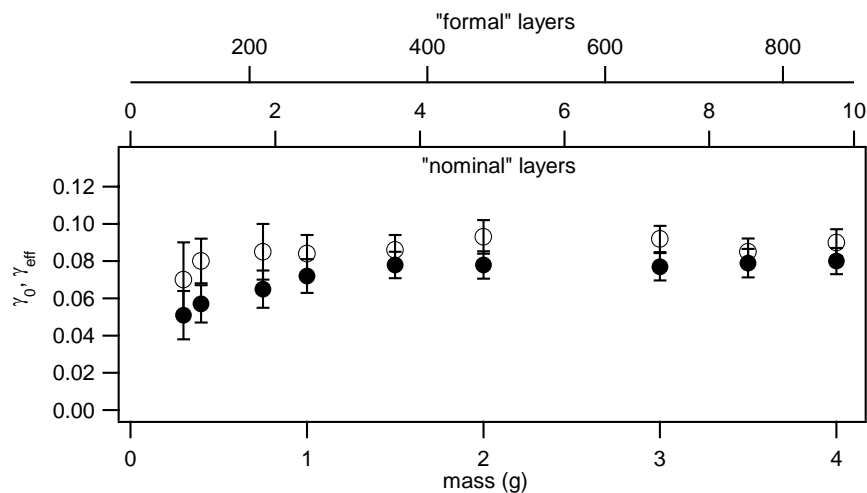
Figure 6.5. Dependence of the uptake coefficient γ_0 (open circles) on sample mass at $[O_3] = (4.5 \pm 1.0) \times 10^{11}$ cm^{-3} at an orifice diameter of 14 mm for the uptake of O_3 on Kaolinite powder ($A_s = 19.6$ cm^2). Full circles display γ_{eff} obtained in pulsed valve experiments carried out under the same experimental conditions.

In order to establish whether or not the effective available surface area is influenced by the internal surface area formed by interstitial voids between individual dust particles, the

mass dependence of the O_3 uptake on Kaolinite was measured in the Knudsen flow reactor at ambient temperature and at $[O_3] = (4.5 \pm 1.0) \times 10^{11}$ cm^{-3}. The mass of Kaolinite ranged from 0.3 to 4 g and the results are shown in Figures 6.5 and 6.6.

The steady state and initial uptake coefficient γ_{ss} and γ_0, respectively, of O_3 were found to linearly increase at low masses of Kaolinite as displayed in Figures 6.5 and 6.6 for γ_0 (see Table 6.3). Samples below 0.4 g may be considered to be part of this linear mass-dependent regime. Increasing the sample mass further had a negligible effect on the amount of O_3 adsorbed because not the entire sample surface is apparently available for O_3 adsorption. This maximum value is attributed to the inability of O_3 to penetrate through several layers of the sample during the residence time of O_3 in the gas phase, thus resulting in a constant number of molecules taken up despite the increasing sample mass. The fact that we observe an 'apparent' mass dependence of γ_0 from 0 to 0.4 g is interpreted by the fact that we are 'filling' a coherent sample layer.

Mass (g)	γ_0	γ_{eff}	γ_{ss}
0.3	$(7.0 \pm 2.0) \times 10^{-2}$	$(5.2 \pm 1.3) \times 10^{-2}$	$(8.9 \pm 2.7) \times 10^{-3}$
0.4	$(8.0 \pm 1.2) \times 10^{-2}$	$(5.7 \pm 1.0) \times 10^{-2}$	$(9.5 \pm 2.2) \times 10^{-3}$
0.75	$(8.5 \pm 1.5) \times 10^{-2}$	$(6.5 \pm 1.0) \times 10^{-2}$	$(1.44 \pm 0.27) \times 10^{-2}$
1.0	$8.4 \pm 1.0) \times 10^{-2}$	$(7.2 \pm 0.9) \times 10^{-2}$	$(1.27 \pm 0.3) \times 10^{-2}$
1.5	$(8.6 \pm 0.8) \times 10^{-2}$	$(7.8 \pm 0.74) \times 10^{-2}$	$(1.62 \pm 0.18) \times 10^{-2}$
2.0	$(9.3 \pm 0.9) \times 10^{-2}$	$(7.8 \pm 0.73) \times 10^{-2}$	$(1.7 \pm 0.20) \times 10^{-2}$
3.0	$(9.2 \pm 0.7) \times 10^{-2}$	$(7.7 \pm 0.73) \times 10^{-2}$	$(1.64 \pm 0.22) \times 10^{-2}$
3.5	$(8.5 \pm 0.7) \times 10^{-2}$	$(7.9 \pm 0.76) \times 10^{-2}$	$(1.67 \pm 0.13) \times 10^{-2}$
4.0	$(9.0 \pm 0.7) \times 10^{-2}$	$(8.0 \pm 0.7) \times 10^{-2}$	$(1.74 \pm 0.13) \times 10^{-2}$

Table 6.3. Measured uptake coefficients γ_{ss} of O_3 on Kaolinite by using the geometric surface area of the substrate ($A_s = 19.6$ cm^2, 14 mm orifice) at $[O_3] = (4.5 \pm 1.0) \times 10^{11}$ cm^{-3}.
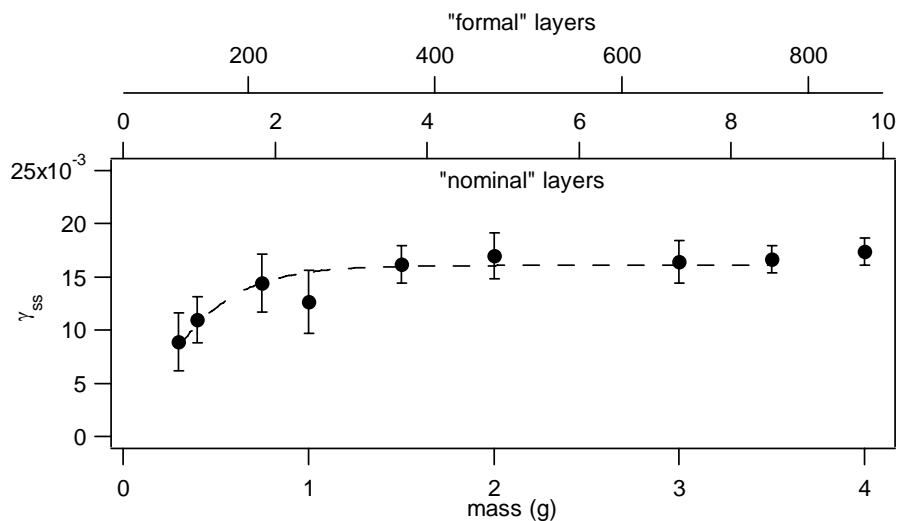
Figure 6.6. Dependence of the steady state uptake coefficient γ_{ss} on sample mass at $[O_3] = (4.5 \pm 1.0) \times 10^{11}$ cm^{-3} at an orifice diameter of 14 mm for the uptake of O_3 on Kaolinite powder ($A_s = 19.6$ cm^2). The numerical fit of the data using the pore diffusion model is represented by dashed lines.

In order to better define the saturation behaviour of O_3 on the substrate a series of uptake experiments were performed employing a pulsed valve to admit O_3 into the reactor. The increase of γ_{eff} with the sample saturates at large sample mass and stays constant at $(8.0 \pm 0.7) \times 10^{-2}$ as displayed by the full circles in Figure 6.5. The same behaviour is observed for γ_0 which stays constant at $(9.0 \pm 0.7) \times 10^{-2}$ at large sample masses. As shown in Figure 6.5, γ_{eff} and γ_0 are identical within experimental uncertainty for all performed experiments.

The results displayed in Figures 6.5 and 6.6 have been plotted as a function of the mass and of the number of layers of Kaolinite. In order to determine the number of layers the total volume of Kaolinite powder was calculated from its true density $\rho_t = 2.3$ g/cm^3 and the mass of the sample spread out across the geometric area of the sample holder. From the average particle size and the thickness of the sample we obtain the number of layers. A typical grain diameter of 1.0 μm has been obtained from the manufacturer's undocumented specifications of the used Kaolinite powder (Table 3.1). However, most mineral dust powders are porous materials and the microstructure of the dust substrate is composed of clusters of random distribution with interstitial voids between them.

Therefore it is more reasonable to take into account a grain size diameter that is much larger than 1.0 μm as suggested by electron microscopy (SEM) of similar material where characteristic grain diameters are in the tens of μm (© OMNI Laboratories, Inc, http://www.omnilabs.com/).

The plot in Figure 6.5 shows that a mass of 0.4 g corresponds to one nominal layer of ca. 90 μm average diameter particles of Kaolinite spread out over the geometric surface of the sample holder (19.6 cm^2). Thus, one nominal layer of Kaolinite will contain closely packed spheres of "effective" grain diameter of 90 μm. Therefore, the linear mass-dependent portion of γ_{ss} vs. mass in the 0 to 0.4 g range corresponds to a sample holder partially covered with 90 μm diameter Kaolinite particles which is the structural model we adopt in this work. In a recent study on NO_3 reaction on mineral dust[12] we have obtained similar results for the mass dependence of γ including an "effective" grain diameter of 50 μm for Kaolinite powder.

Figure 6.6 displays steady state uptake experiments performed on the same amount of Kaolinite as in the experiments reported in Figure 6.5. The trend of these measurements is identical to that observed in pulsed valve experiments. Beyond a mass of 0.4 g the steady state value of γ_{ss} stabilizes at $(1.6 \pm 0.3) \times 10^{-2}$, a factor at 5 less that γ_0. The use of the BET surface area and the application of the pore diffusion (KLM) theory[13] yields $\gamma_{pd,ss} = (2.7 \pm 0.3) \times 10^{-6}$. The BET surface area for Kaolinite and other dust samples used in this work is reported in Table 3.1. The theoretical curve in Figure 6.6 has been fitted to the observed steady state uptake coefficient γ_{ss} as a function of sample mass using a grain diameter for Kaolinite of 1 μm, a surface sample area $A_s = 19.6$ cm^2, as fitting parameters at a fixed orifice diameter of 14 mm and $[O_3] = (4.5 \pm 1.0) \times 10^{11}$ cm^{-3}.

The use of the BET surface area and the Pore Diffusion Theory substantially underestimate the true uptake coefficient for Kaolinite approximately by a factor of 50 - 100 as well discussed below. The discrepancy to γ based on the geometric surface area A_s is more than a factor of 10^3. Therefore, we propose to regard $\gamma_{pd,ss}$ as a lower limit to the true value of γ_{ss}. We want to point out that the results obtained from the pulsed valve experiments (γ_{eff}) are virtually identical to the results at "zero" time (γ_0) after the start of the uptake reaction as displayed in Figure 6.1. These results reflect the fact that O_3 explores the external surface of the Kaolinite sample at t = 0 and that it is improbable

for the gas to explore the BET surface area of the sample within a time representative of a pulse decay.

An additional series of experiments concerns the thermal cycling behaviour of Kaolinite that had previously been exposed to several Torr of O_3 in order to discover stable reaction products that desorb upon heating of the poisoned substrate. For a 1.5 g Kaolinite sample $k_{ss} = 6.3$ x 10^{-2} s^{-1} corresponding to $\gamma_{ss} = 1.4$ x 10^{-2} was measured in the 4 mm diameter flow reactor after pumping the sample for 30 minutes. After exposing Kaolinite to 8 Torr of O_3 for 12 h γ_{ss} decreased to 9.4 x 10^{-4} in agreement with trends discussed in Figure 6.3. After heating the exposed sample to 80°C and letting it cool down to ambient temperature γ_{ss} increased by roughly an order of magnitude to 8.8 x10^{-3}. During the thermal treatment only desorption of H_2O but no O_2 was observed. This rejuvenation of the Kaolinite sample is consistent with the thermal decomposition of the surface peroxide species observed by Li and Oyama[17,18] according to reaction (6.3) which implies an increase of the number of surface sites SS for adsorption of O_3 upon thermal decomposition of O_2(SS). However, this regeneration of SS only affects the value of γ_{ss} and leaves γ_0 unchanged in contrast to the O_3 exposure which also decreases γ_0 for O_3 uptake. We certainly expected to find O_2 among the desorbing products but did not observe significant amounts, probably owing to the relatively large background of O_2 in the flow reactor. This type of desorption experiments will be performed in the future in a suitably modified Knudsen flow reactor in conjunction with surface-sensitive spectroscopic methods that will contribute towards the understanding of the underlying molecular mechanisms.

6.3.2 Reaction of O_3 on $CaCO_3$ and natural limestone

We have performed uptake experiments of O_3 on $CaCO_3$ using a sample of 1 g spread out on a surface area A_s of 4.9 cm^2 and a residence time $\tau_g = 0.2$ s corresponding to an orifice of 14 mm. At $[O_3] = (5.3 \pm 0.5)$ x 10^{12} cm^{-3} the ratio between the O_2 product yield and the total O_3 loss results in r(t) = 1.4 and in a measured value of $\gamma_{ss} = (3.6 \pm 1.8)$ x 10^{-3} and $\gamma_0 = (1.2 \pm 0.3)$ x 10^{-2} (Table 6.4 and Figure 6.7, curve (a)). At the beginning of the reaction we have obtained r(t) ≤ 1.0 and at steady state conditions r(t) tends towards 1.5

which corresponds to heterogeneous decomposition using the substrate as a catalyst. An important remark is the "inverse" behavior of r(t) of O_3 on $CaCO_3$ with the extent of reaction (curve (a), Figure 6.7) as opposed to the decrease of r(t) with reaction time for O_3 on Kaolinite (curve (a)-(c), Figure 6.4).
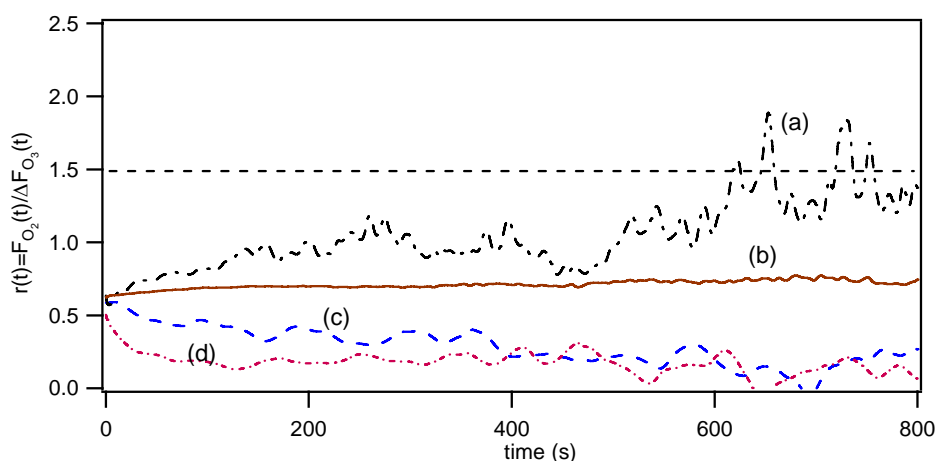
Figure 6.7. The relative yield r(t) during the uptake experiment of O_3 on 1 g of $CaCO_3$ (curve (a) , orifice = 14 mm), 0.3 g of Saharan Dust (curve (b)), 1 g of natural limestone (curve (c)), and 0.3 g of Arizona Medium Test Dust (curve (d)) ($[O_3] = (3.5 \pm 0.5)$ x 10^{12} cm^{-3}, $A_s = 4.9$ cm^2 and 4 mm orifice ($\tau_g = 2.0$ s)).

For comparison purposes we have carried out a systematic study of γ_{ss} as a function of sample mass in order to determine a corrected uptake coefficient γ_{pd} of O_3 on $CaCO_3$ powder using the pore diffusion model[13]. We have used a large sample surface area of $A_s = 19.6$ cm^2 and an expanded range of sample masses. At steady state $\gamma_{ss,pd} = (7.8 \pm 0.7)$ x 10^{-7} with a tortuosity factor $\tau = 2.0$ was found for $[O_3] = (5.3 \pm 0.7)$ x 10^{12} cm^{-3}. The fit to the measured values of γ_{ss} resulted in a value of the γ_{pd} that is smaller by a factor of 4.6 x 10^3 with respect to the measured value γ_{ss} reported above.
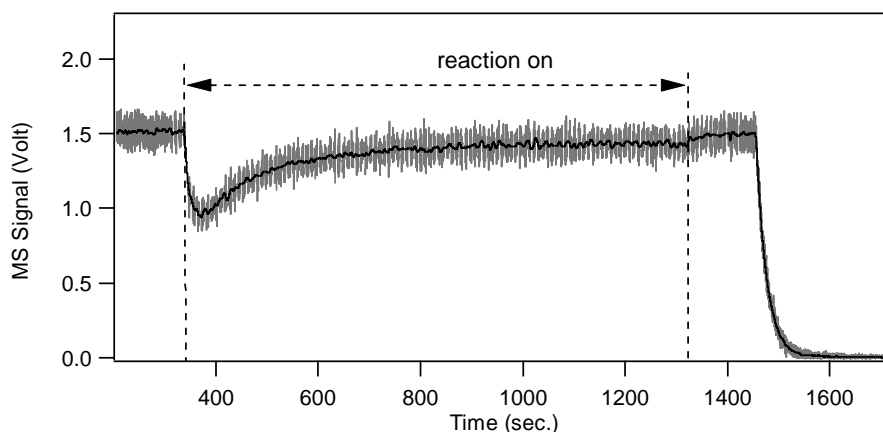
Figure 6.8. Knudsen-Cell experiment for O_3 uptake on a 2g marble sample of $CaCO_3$. The curve correspond to raw MS signals monitored at m/e 48 ($[O_3]$ = (2.0 ± 1.2) x 10^{12} cm^{-3}; 1 mm orifice; surface sample area A_s = 19.6 cm^2).

In order to assess whether or not the pore diffusion model may yield a lower limit for γ, we have performed a few uptake experiments on a cut marble sample from Carrara (Italy, solid crystalline $CaCO_3$). In this case we do not expect interstitial diffusion to occur and the projected surface area of the sample that is relevant for uptake is the geometric surface area A_s of 19.6 cm^2. For $[O_3]$ = (2.0 ± 1.2) x 10^{12} cm^{-3} and a residence time τ_g = 28 s (orifice diameter of 1mm) we found $\gamma_{0,marble}$ = (2.3 ± 0.4) x 10^{-4} and $\gamma_{ss,marble}$ = (3.5 ± 1.6) x 10^{-5} as displayed in Figure 6.8. As displayed in Table 6.4 the uptake values γ_0 and γ_{ss} calculated on the basis of the geometric surface area A_s of the powder sample are overestimated by a factor of 50 and 100, respectively, compared to the uptake values calculated form the reaction of O_3 on marble. On the other hand, the uptake value $\gamma_{ss,pd}$ calculated by applying the pore diffusion theory (KLM) is underestimated by a factor of 50 or so compared to γ_0 and γ_{ss} calculated on the basis of the geometric surface area. We therefore take this factor of 50 to 100 which we extend to the remaining mineral dust surrogates as a rough guide as to the estimate the true uptake coefficient for $CaCO_3$ using the γ values based on A_s as a starting point. We stress that $\gamma_{ss,pd}$ and γ_0, γ_{ss} based on A_s are lower and higher limits to the true values of γ.

Two series of experiments were performed on 1g of natural limestone composed of $CaCO_3$ (97 %) that contained a small percentage of metal oxides, especially iron and

aluminium oxides (see Table 3.1). As reported in Table 6.4, the values of γ_0 and γ_{ss} measured at low [O_3] were larger by a factor of 6 with respect to those high [O_3] which is a general trend observed for many mineral dust materials (see Table 6.4). From these measurements it is evident that both γ_0 and γ_{ss} do not follow a rate law pseudo first order in O_3 and suggests that the mechanism of O_3 uptake is complex.

Sample	Orifice (mm)	[O_3] (cm^{-3})	γ_0	γ_{ss}
Kaolinite	14	$(2.4 \pm 0.7) \times 10^{12}$	$(6.3 \pm 0.2) \times 10^{-2}$	$(1.0 \pm 0.2) \times 10^{-2}$
CaCO$_3$	14	$(5.3 \pm 0.7) \times 10^{12}$	$(1.2 \pm 0.3) \times 10^{-2}$	$(3.6 \pm 0.2) \times 10^{-3}$
Natural Limestone	4	$(3.0 \pm 0.7) \times 10^{12}$	$(1.3 \pm 0.2) \times 10^{-2}$	$(1.6 \pm 0.5) \times 10^{-3}$
Saharan Dust	4	$(3.5 \pm 0.7) \times 10^{12}$	$(9.3 \pm 2.6) \times 10^{-2}$	$(6.7 \pm 1.3) \times 10^{-3}$
Arizona Test Dust	4	$(3.3 \pm 0.7) \times 10^{12}$	$(1.3 \pm 0.6) \times 10^{-2}$	$(2.2 \pm 1.2) \times 10^{-3}$
Natural Limestone	4	$(2.0 \pm 1.0) \times 10^{13}$	$(2.1 \pm 0.3) \times 10^{-3}$	$(2.4 \pm 0.7) \times 10^{-4}$
Saharan Dust	4	$(1.0 \pm 0.4) \times 10^{13}$	$(3.7 \pm 1.8) \times 10^{-2}$	$(3.3 \pm 2.5) \times 10^{-3}$
Arizona Test Dust	4	$(8.0 \pm 1.5) \times 10^{12}$	$(1.3 \pm 0.7) \times 10^{-2}$	$(2.5 \pm 1.2) \times 10^{-3}$

Table 6.4. Summary of the reactive uptake coefficients for various mineral dust surrogates obtained in the present work based on the geometric surface area.

Interestingly, on this substrate the ratio r(t) for ozone uptake and decomposition remains below 0.5 even at a high concentration of ozone and long residence time (Figure 6.7, curve (c)). This kind of sample seems to be an excellent absorber of O_3 without extensive decomposition at ambient temperature. Despite the high percentage of CaCO$_3$ in natural limestone the presence of small amounts of metal oxides such as Fe$_2$O$_3$ in excess CaCO$_3$ could be responsible for the suppression of O_2 formation.

When we compare γ for CaCO$_3$ and natural limestone at roughly the same ozone concentration ([O_3] = $(4.0 \pm 1.0) \times 10^{12}$ cm^{-3}) we find that the values for γ_0 are the same

whereas γ_{ss} is a factor of 2.5 larger for $CaCO_3$ according to Table 6.4, presumably because of a faster saturation process in natural limestone compared to pure $CaCO_3$.

6.4 Reaction of O_3 on Saharan Dust and Arizona Medium Test Dust

Two series of experiments were performed on 0.3 g of Saharan Dust using two different ozone concentrations. As reported in Table 6.4, γ_0 and γ_{ss} measured at low $[O_3]$ were larger by a factor of 2.5 and 2, respectively, compared to the values at high $[O_3]$.

As already observed for natural limestone, γ_0 and γ_{ss} do not follow a rate law pseudo first order in O_3 and suggests that the mechanism of O_3 uptake is complex. A similar dependence has been observed before by Hanisch and Crowley[7] in their work on ozone decomposition on Saharan dust and by Sullivan and coworkers[14] in their study of ozone decomposition on fresh alumina films. The reason for this behaviour may be related to the finite number of available surface sites of the substrate that are not completely saturated at low $[O_3]$ resulting therefore in a larger value of γ compared to high $[O_3]$.

For steady state uptake performed at $[O_3] = (3.5 \pm 0.5)$ x 10^{12} cm^{-3} the ratio r(t) has been found to be approximately 0.8 (Figure 6.7, curve (b)), whereas for $[O_3] = (1.0 \pm 0.4)$ x 10^{13} cm^{-3} it stabilizes around 1.0.

On 0.3 g Arizona Medium Test Dust, we found identical values of γ_0 and γ_{ss} for both values of $[O_3]$ as reported in Table 6.4. The ratio r(t) at steady state conditions tends towards a value of approximately 0.4 for both ozone concentrations (Figure 6.7, curve (d)) indicating a significant reactivity for O_3 uptake on this substrate and lack of ozone decomposition leading to O_2 formation. Both Arizona Test Dust and natural limestone result in a similar r(t) dependence for ozone decomposition, distinctly different from results for Saharan Dust. Saharan Dust contains a significant percentage of metal oxides, with r(t) tending towards values between 0.8 and 1.0 at steady state conditions. If we analyse the chemical composition of the mineral dust examined in this work more carefully, we note that iron oxides such as Fe_2O_3, FeO and Fe_3O_4 are present in different percentages: Saharan Dust contains more iron than Natural limestone and Arizona Test

Dust a fact that may be responsible for the difference in γ and r(t) on the different substrates. Specifically, we note that r(t) increases with the amount of iron oxides in the sample which leads to dominant O_3 decomposition resulting in O_2 in contrast to O_3 uptake. This aspect is supported by recent work of Michel et al. who found that the initial reactivity of oxide powders towards ozone followed the order α-Fe_2O_3>α-Al_2O_3>SiO_2>Kaolinite with the Saharan sand and China loess having lower reactivities more in line with SiO_2 and Kaolinite[15]. In this investigation, the initial reactive uptake coefficient γ_0 of O_3 on several mineral oxide powders was measured using a Knudsen reactor leading to γ_0 = (2.0 ± 0.3) x 10^{-4} for α-Fe_2O_3, (1.2 ± 0.4) x 10^{-4} for α-Al_2O_3, (6.3 ± 0.9) x 10^{-5} for SiO_2 and (3 ± 1) x 10^{-5} for Kaolinite. The greater reactivity of the iron oxides is also in agreement with the observations by Suzuki who carried out a laboratory study of O_3 reactivity on various mineral oxides[6]. Using a UV absorption monitor, the authors report the relative O_3 reactivity of silica, α-Fe_2O_3, Fe_3O_4, and α-Al_2O_3 in comparison with natural sea sand collected in Japan, which was further separated into an "iron sand" and a "remainder sand" component. The "iron sand" component had a reactivity similar to Fe_3O_4, a major component in the "iron sand", that decomposed O_3 at a faster rate than the natural sand and the "remainder sand". This suggests that iron oxide such as Fe_3O_4 more effectively destroys ozone than the other solid phases present in the sand. It was concluded that iron-containing compounds had a superior ozone decomposition rate than alumina and silica model compounds in agreement with the present kinetic results.

6.5 Comparison with literature values

Previous results on the uptake coefficients for O_3 uptake on mineral dust obtained by other authors are displayed in Table 6.5 for comparison purposes. O_3 uptake on Saharan sand and calcite has been investigated using a fluidized-bed reactor[16]. Although uptake coefficients have not been derived they may be estimated from the data presented employing the BET surface area of the substrate which will lead to a lower limiting value. For Saharan sand the signal reduction obtained in that work corresponds to an initial

uptake coefficient of $\gamma_{0,\,BET}$ = 2.3 x 10^{-7} at $[O_3]$ = 2.5 x 10^{12} cm^{-3}. In a similar manner, the initial uptake coefficient for calcite resulted in a value of $\gamma_{0,\,BET}$ = 4.3 x 10^{-7}.

Sample	$\gamma_{0,BET}$	$\gamma_{ss,BET}$	$\gamma_{pd,ss}$	$\gamma_{pd,ss}$ (this work)
Kaolinite	(3.0 ± 1.0) x 10^{-5} (Michel et al.)[15]	–	–	(2.7 ± 0.3) x 10^{-6}
Saharan sand	(6 ± 2.0) x 10^{-5} (Michel et al.)[15]	6.0 x 10^{-6} (Michel et al.)[15]		
Saharan Dust	2.3 x 10^{-7} (Alebic-Juretic et al.)[16] –	–	– (2.2$^{+1.4}_{-1.2}$) x 10^{-6} (Hanisch and Crowley)[7]	
CaCO$_3$	4.3 x 10^{-7} (Alebic –Juretic et al.)[16]	–	–	(7.8 ± 0.7) x 10^{-7}

Table 6.5. Typical initial and steady-state reactive uptake coefficients for various mineral dust surrogates obtained in previous work.

In recent work performed by Hanisch and Crowley[7] the heterogeneous reaction of O_3 on Saharan Dust has been investigated at ambient temperature (296 K). The conversion efficiencies r for O_2 formed presented in that work were 1.0 and 1.3 mole of O_2 per O_3 destroyed for unheated and heated samples (T = 450 K), respectively. In the same work[7] it was shown that γ for the irreversible destruction of O_3 on Saharan dust surfaces depended on the O_3 concentration leading to $\gamma_0^{pd} = (5.5^{+4.0}_{-3.0})$ x 10^{-5} and $\gamma_{ss}^{pd} = (2.2^{+1.4}_{-1.2})$ x 10^{-6} using the pore-diffusion (KLM) model at $[O_3]$ = (8.4 ± 3.4) x 10^{12} cm^{-3}. Experiments at $[O_3]$ = 6.0 x 10^{12} cm^{-3} using Arizona Test Dust and Kaolinite[17] were performed as well. Only measured values of γ_0 were reported; for unheated Kaolinite γ_0 = 1.0 x 10^{-4} was close to or below the detection limit whereas γ_0 = 2.0 x 10^{-3} was found for Arizona Test Dust.

In two other recent studies that employed a Knudsen reactor the mass-independent uptake coefficient, γ_{BET}, was determined from the observed γ_{obs} values obtained from the linear mass-dependent portion of the plots γ_{obs} versus sample mass according to equation (6.E3):

$$\gamma_{obs} = \gamma_{BET} \left(\frac{S_{BET} m_S}{A_S} \right) \qquad (6.E3)$$

where m_s is the sample mass, S_{BET} and A_s are the specific BET and geometric surface areas, respectively. For O_3 uptake on ground Saharan sand at $[O_3] = 1.9 \times 10^{11}$ cm^{-3} Michel and co-workers[15,18] obtained $\gamma_{0,BET} = (6.0 \pm 2.0) \times 10^{-5}$ whereas at steady state conditions $\gamma_{ss,BET} = 6.0 \times 10^{-6}$ was found. In comparison, we have found $\gamma_{pd,ss} = 2.4 \times 10^{-6}$, a value lower by a factor of 2.5 (Table 6.5).

The uptake coefficient, γ_{BET}, calculated from the present values of γ_{ss} using the BET surface area resulted in $\gamma_{ss,BET} = (2.0 \pm 0.6) \times 10^{-6}$ for Kaolinite at $[O_3] = (4.5 \pm 1.0) \times 10^{11}$ cm^{-3}, whereas $\gamma_{ss,BET} = (8.3 \pm 0.4) \times 10^{-7}$ for $CaCO_3$ at $[O_3] = (5.3 \pm 0.7) \times 10^{12}$ cm^{-3}. These values are identical to those found from the pore diffusion model within experimental uncertainty. However, we would like to reiterate, that these γ values are likely lower limits to the true values.

Finally, measurements of O_3 deposition velocities (v_{dep}) have been performed on various substrates including Kaolinite sand and $CaCO_3$ [19]. Using these data and the expression $\gamma = 4v_{dep} / \overline{c}$, Dentener et al.[2] estimated γ values for O_3 in the range 10^{-4} to 10^{-5}. This estimate falls far short of the range of the present results for $[O_3] = (2.0 \pm 0.5) \times 10^{12}$ cm^{-3} if the corresponding steady-state uptake coefficients based on the geometric surface area are used.

6.6 Conclusions

The present data indicate that the reactivity of O_3 on Kaolinite decreases with residence time τ_g and that the heterogeneous reaction rate not only depends on the gas phase concentration of ozone but apparently also on intermediates whose surface concentration depends on the extent of reaction, that is on τ_g.

Despite the difficulty to detect O_2 as a product species from O_3 decomposition we report the relative product formation rate as a function of time resulting from the decomposition of O_3 on the different substrates by monitoring the ratio $r(t) = F_{O_2}(t)/\Delta F_{O_3}(t)$. There is no simple common mechanism that may explain ozone decomposition on each type of mineral dust substrate which means that no single surrogate material cited above can be representative of "mineral dust" as far as the heterogeneous reaction with ozone is concerned.

We claim that neither γ_0 nor γ_{ss} is a good indicator for O_3 reactivity that is able to distinguish between the different substrates because the resulting γ values are all very similar for all the examined substrates within a range of $(1.2 \pm 0.3) \times 10^{-2}$ to $(9.3 \pm 2.6) \times 10^{-2}$ for γ_0 and $(1.6 \pm 0.5) \times 10^{-3}$ to $(1.0 \pm 0.2) \times 10^{-2}$ for γ_{ss}. The use of values derived from the pore diffusion (KLM) theory[13] and from the BET surface area leads to a lower limit for O_3 uptake that underestimates the kinetics of O_3 with mineral dust.

The uptake values derived from the pore diffusion theory found for Kaolinite and $CaCO_3$ are lower by a factor 3.0×10^3 with respect to those calculated using the geometric surface area A_s of the sample. We assume that Arizona Test Dust, Saharan Dust and natural limestone will follow the same trend. The uptake experiment performed on crystalline $CaCO_3$ (marble) suggests that the pore diffusion correction of the measured γ value will lead to an underestimation of the true value by a factor of 50 -100. Therefore, we may conclude that for all mineral dust samples used in this work the uptake value γ is of the order of 10^{-5}. On the other hand, r(t) seems to be a better indicator for the reaction of these surrogates with O_3 because it discriminates the different samples to a larger extent compared to the absolute values of γ_0 or γ_{ss} of the various types of substrates.

In order to estimate the effect of ozone uptake on mineral dust we used field measurements of a dust event reported in recent work[20]. At an altitude of 4 km the total aerosol surface area was 1.5×10^{-6} cm^2 cm^{-3} and $[O_3]$ was 31 ppb (5.0×10^{11} cm^{-3}) at 279 K. If we take a γ value of 3.5×10^{-5} as a lower limit for the uptake of O_3 on mineral dust, the lifetime of O_3 is 10 days. This lifetime comes quite close to that found in the recent work of Hanisch and Crowley[7] and Sullivan et al.[14] who used a lower limit for γ of about 10^{-5} and estimated a lifetime ranging between 33 and 55 days for the same aerosol surface area.

In conclusion, the present results show a low reactivity of O_3 on mineral dust surrogates as exemplified by experiments on crystalline $CaCO_3$ resulting in $\gamma = 10^{-5}$. This value is larger by a factor of 10 compared to Hanisch and Crowley[7] and Michel and co-workers[15] who report γ values of the order of 10^{-6} using pore diffusion (KLM) theory[13].

6.7 General conclusions and outlook

Recent modelling studies have been carried out in order to estimate the total decrease of tropospheric trace gases such as HNO_3, N_2O_5, NO_3 and O_3 in the presence of mineral dust[8,9]. However, these studies reveal significant differences in model formulation such as dust surface areas, chemistry schemes, trace gas concentrations, and differences in the computation of the heterogeneous removal rates. The present thesis intends to reduce the uncertainties regarding the value of the uptake coefficient γ of gas phase species that undergo irreversible reactions on mineral dust surfaces and may play a decisive role in controlling the outcome of these model simulations. Table 6.6 reports the g values used in the work of Bauer et al.[8] and Bian and Zender[9]. The last column reports the steady state values γ_{ss} that were found from the present experiments on mineral dust surrogates. We propose that these values may be used in future modelling studies for trace gas concentrations lower than 5.0×10^{11} cm^{-3}. We see from Table 6.6 that the γ values found from the present laboratory work are larger by at least two orders of magnitude compared to the estimated values used in the modelling studies[8,9]. Previous and recent laboratory work has mainly been oriented towards the reactivity of HNO_3 and O_3 on mineral dust substrates. As reported in Table 6.6, only a single recent study has been performed on the reactivity of N_2O_5 in a Knudsen flow reactor[21]. The uptake coefficients found in that work are quite close to those obtained in the present thesis work. However, we think that at tropospheric concentrations of N_2O_5 γ will be much larger than previously believed, especially for the case of Saharan Dust. Such large values for γ may have important consequences for the decrease of ozone because NO_3 and N_2O_5 are precursors for HNO_3 formation which itself is an important precursor for O_3.

The goal of the present laboratory study has been to understand as well as possible a few isolated heterogeneous reactions of a trace gas interacting with mineral dust. However, we have to consider that real atmospheric conditions at which these heterogeneous reactions take place in the troposphere are different from the used experimental conditions. There are mainly two aspects that may influence the measurement of the "true" (= environmental) value of γ at the experimental conditions used in this work:

(a) The choice of the appropriate surface area for mineral dust samples;

(b) The relative humidity at which the present experiments were carried out.

It has already been shown by previous studies that points (a) and (b) presented above may strongly affect the final result. We think that the Knudsen flow reactor is very useful for the understanding of the kinetics of heterogeneous reactions, especially for the determination of the reaction products. However, in order to "reproduce" or simulate real atmospheric conditions it would be preferable to work with aerosols of mineral dust samples generated by dry dispersion. This method has already been employed in recent work performed by Vlasenko et al.[23] for the investigation of the heterogeneous reaction of HNO_3 on Arizona Test Dust[22,23]. In that study, a dry dispersion generation method was used to produce submicron size dust aerosol in a flow tube which was used to measure the kinetics of the heterogeneous reaction of HNO_3 with aerosol particles at different values of relative humidity (12% <rh<73%). This is the first study that applies such a method for the generation of atmospheric mineral dust using a kinetic flow-tube technique. In addition, the reactive surface area of the suspended aerosol particles has been estimated from the measurement of the mobility diameter (SMPS). The results obtained from this experimental work were in agreement with those obtained by Hanisch and Crowley[24] at very dry conditions typical of the Knudsen reactor (rh < 1%). We think that this is a good starting point for the confirmation of laboratory experiment carried out in a Knudsen flow reactor.

A further potential improvement of the present method may be the probing of aerosol particles by monitoring scattered visible light. This is a simple direct non-invasive experimental method that keeps the probe particles intact and may be complementary to the use of UV light and soft x-ray radiation for the study of aerosol chemistry and physics.

	γ(Bauer et al.[8])	γ(Bian and Zender[9])	γ_{ss}(present work)	γ_{ss}(recent laboratory work)
HNO₃	0.1	1.1×10^{-3}	-	0.11 [24]
				0.11 [23]
				5.4×10^{-2} [25]
NO₃	3.0×10^{-3}	0.1	0.2	-
N₂O₅	3.0×10^{-3} (rh = 30 %)	1.0×10^{-3}	0.2	1.3×10^{-2} [21]
	3.0×10^{-3} (rh = 70 %)			
O₃	1.0×10^{-5}	5.0×10^{-5}	1.0×10^{-5}	7.0×10^{-6} [7]
				6.0×10^{-6} [26]

Table 6.6. Typical uptake coefficients on mineral dust of various trace gases used in modeling studies resulting from laboratory studies.

6.8 References

(1)   Bonasoni, P.; Cristofanelli, P.; Calzolari, F.; Bonafé, U.; Evangelisti, F.; Stohl, A.; Sajani, S. Z.; van Dingenen, R.; Colombo, T.; Balkanski, Y.: Aerosol-ozone correlations during dust transport episodes, Atmospheric Chemistry and Physics, 4, 1201-1215, (2004).

(2)   Dentener, F. J.; Carmichael, G. R.; Zhang, Y.; Lelieveld, J.; Crutzen, P. J.: Role of mineral aerosol as a reactive surface in the global troposphere, Journal of Geophysical Research-Atmospheres, 101, 22869-22889, 10.1029/96JD01818., (1996).

(3)   Horvarth, M.; Bilitzky, L.; Huttner, J.: Ozone, Elsevier, New York, 26-29, (1985).

(4)   Jacob, D. J.: Heterogeneous chemistry and tropospheric ozone, Atmospheric Environment, 34, 2131-2159, (2000).

(5)   Kamm, S.; Möhler, O.; Naumann, K. H.; Saathoff, H.; Schurath, U.: The heterogeneous reaction of ozone with soot aerosol, Atmospheric Environment, 33, 4651-4661, (1999).

(6)   Suzuki, S.; Hori, Y.; Koga, O.: Decomposition of Ozone on Natural Sand, Bulletin of the Chemical Society of Japan, 52, 3103-3104, (1979).

(7)   Hanisch, F.; Crowley, J. N.: Ozone decomposition on Saharan dust: an experimental investigation, Atmospheric Chemistry and Physics, 3, 119-130, (2003 d).

(8)   Bauer, S. E.; Balkanski, Y.; Schulz, M.; Hauglustaine, D. A.; Dentener, F.: Global modeling of heterogeneous chemistry on mineral aerosol surfaces: Influence on tropospheric ozone chemistry and comparison to observations, Journal of Geophysical Research-Atmospheres, 109, art. no.-D02304, doi:10.1029/2003JD003868., (2004).

(9)   Bian, H. S.; Zender, C. S.: Mineral dust and global tropospheric chemistry: Relative roles of photolysis and heterogeneous uptake, Journal of Geophysical Research-Atmospheres, 108, 4672, doi:10.1029/2002JD003143., (2003).

(10)   Li, W.; Gibbs, G. V.; Oyama, S. T.: Mechanism of ozone decomposition on a manganese oxide catalyst. I. In situ Raman spectroscopy and ab initio molecular orbital calculations, Journal of the American Chemical Society, 120, 9041-9046, (1998).

(11)   Li, W.; Oyama, S. T.: Mechanism of ozone decomposition on a manganese oxide catalyst. 2. Steady-state and transient kinetic studies, Journal of the American Chemical Society, 120, 9047-9052, (1998).

(12)   Karagulian, F.; Rossi, M. J.: The heterogeneous chemical kinetics of NO$_3$ on atmospheric mineral dust surrogates, Physical Chemistry Chemical Physics, 7, 3150, (2005).

(13)   Keyser, L. F.; Moore, S. B.; Leu, M. T.: Surface-Reaction and Pore Diffusion in Flow-Tube Reactors, Journal of Physical Chemistry, 95, 5496-5502, (1991).

(14)   Sullivan, R. C.; Thornberry, T.; Abbatt, J. P. D.: Ozone decomposition kinetics on alumina: effects of ozone partial pressure, relative humidity and repeated oxidation cycles, Atmospheric Chemistry and Physics, 4, 1301-1310, (2004).

(15)   Michel, A. E.; Usher, C. R.; Grassian, V. H.: Reactive uptake of ozone on mineral oxides and mineral dusts, Atmospheric Environment, 37, 3201-3211, (2003).

(16)   Alebic-Juretic, A.; Cvitas, T.; Klasinc, L.: Ozone destruction on powders, Ber. Bunsen Ges. Phys. Chem.,, 96, 493-495, (1992).

(17)   Hanisch, F.; Crowley, J. N.: Ozone decomposition on Saharan dust: an experimental investigation, Atmospheric Chemistry and Physics, 3, 119-130, (2003).

(18)   Michel, A. E.; Usher, C. R.; Grassian, V. H.: Heterogeneous and catalytic uptake of ozone on mineral oxides and dusts: A Knudsen cell investigation, Geophysical Research Letters, 29, art. no.-1665, (2002).

(19)   Garland, J. A.: Dry deposition of SO$_2$ on other gases, in Atmospheric surface exchange of particulate and gaseous pollutants, US ERDA symposium series, Richland, Washington, USA, (1974).

(20)   de Reus, M.; Dentener, F.; Thomas, A.; Borrmann, S.; Strom, J.; Lelieveld, J.: Airborne observations of dust aerosol over the North Atlantic Ocean during ACE 2: Indications for heterogeneous ozone destruction, Journal of Geophysical Research-Atmospheres, 105, 15263-15275, (2000).

(21)   Seisel, S.; Börensen, C.; Zellner, R.: Kinetics and mechanism of the uptake of N$_2$O$_5$ on mineral dust at 298 K, Atmospheric Chemistry and Physics Discussions, 5, 5645-5667, (2005).

(22)   Vlasenko, A.; Sjogren, S.; Weingartner, E.; Gaggeler, H. W.; Ammann, M.: Generation of submicron Arizona test dust aerosol: Chemical and hygroscopic properties, Aerosol Science and Technology, 39, 452-460, (2005).

(23)   Vlasenko, A.; Sjogren, S.; Weingartner, E.; Stemmler, K.; Gäggeler, H. W.; Ammann, M.: Effect of humidity of nitric acid uptake to mineral dust aerosol particles, Atmospheric Chemistry and Physics Discussions, 5, 11821-11860, (2005).

(24)   Hanisch, F.; Crowley, J. N.: The heterogeneous reactivity of gaseous nitric acid on authentic mineral dust samples, and on individual mineral and clay mineral components, Physical Chemistry Chemical Physics, 3, 2474-2482, (2001 b).

(25)   Seisel, S.; Börensen, C.; Vogt, R.; Zellner, R.: The heterogeneous reaction of HNO$_3$ on mineral dust and gamma-alumina surfaces: a combined Knudsen cell and DRIFTS study, Physical Chemistry Chemical Physics, 6, 5498-5508, (2004).

(26)   Chang, R. Y. W.; Sullivan, R. C.; Abbatt, J. P. D.: Initial uptake of ozone on Saharan dust at atmospheric relative humidities, Geophysical Research Letters, 32, (2005).

Chapter 7

# REACTION OF F(^{2}P) WITH HNO$_3$ AS A NITRATE RADICAL SOURCE

## 7.1 Microwave discharge of F$_2$ for NO$_3$ generation

The uptake experiments performed with NO$_3$ on mineral dust surrogates and laboratory flame soot were carried out using the thermal decomposition of N$_2$O$_5$ as a source for NO$_3$ which was always accompanied by NO$_2$. In the present chapter we want to present an experimental set up to operate a source of NO$_3$ in the absence of NO$_2$. For this purpose we used the reaction of F atoms with HNO$_3$ according to equation (7.1):

$$F(^2P) + HNO_3 \rightarrow HF + NO_3 \qquad (7.1)$$

Despite its widespread use as a NO$_3$ source, the first room temperature measurement of the rate constant k_{II} for reaction (7.1) has only recently been reported[1] and resulted in a value of (2.7 ± 0.5) x 10^{-11} cm^3 molecule^{-1} s^{-1} at 298 K.

In order to run reaction (7.1) a discharge flow reactor was coupled to the Knudsen flow reactor. The system is schematically described in Figure 7.1. A microwave discharge cavity (2460 MHz, 20 W) produced F atoms in a sapphire (crystalline Al$_2$O$_3$) tube from a flow of F$_2$ diluted at 4.6 % in helium (MESSER) according to reaction (7.2):

$$F_2 + \text{energetic radiation} \rightarrow F(^2P) \qquad (7.2)$$
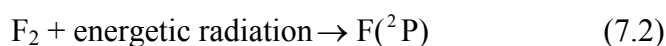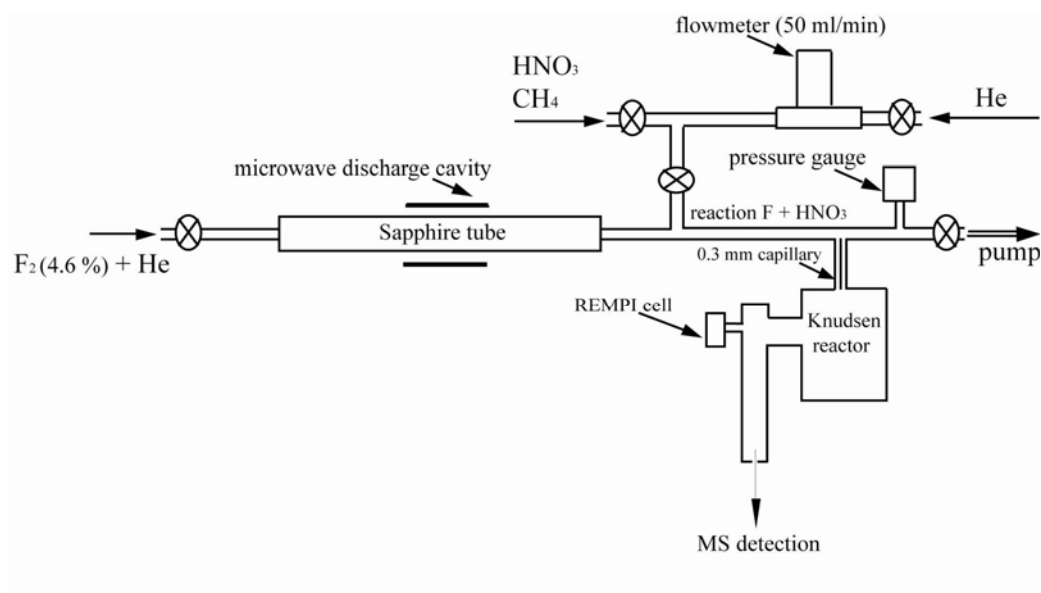
Figure 7.1. Experimental set up of the microwave flow discharge fitted to the Knudsen flow reactor.

Figure 7.2. Picture of the experimental set up sketched schematically in Figure 7.1.

The sapphire tube was connected to the Knudsen flow reactor by a capillary made of TEFLON of internal diameter 0.3 mm. The sapphire tube where the microwave discharge took place had a total length of 20 cm and an internal diameter of 0.8 cm. F atoms produced in the discharge

reacted with excess HNO$_3$ which was introduced 5 cm downstream of the microwave cavity. A flow of pure helium diluted and admitted HNO$_3$ in the discharge flow reactor. The flow of helium was controlled by a digital flowmeter (BRONKHORST) with a maximum range of 50 ml/min. A distance of 12 cm was allowed for the NO$_3$ production through reaction (7.1) which was to be completed before sampling of NO$_3$ across a TEFLON capillary connected to the Knudsen reactor. The pumping rate for helium in the discharge flow reactor has been determined according to expression (7.E1):

$$S = F_{He} / [He] \qquad\qquad (7.E1)$$

A volumetric pumping rate $S = 56$ cm^3 s^{-1} was measured. The helium concentration [He] was calculated from the measured pressure of helium P_{He} in the discharge flow reactor according to expression (7.E2):

$$[He] = \frac{P_{He} N_A}{RT} \qquad\qquad (7.E2)$$

where R is the ideal gas constant, T the temperature in Kelvin and N_A Avogadro's number.

In order to calculate the concentration of F$_2$ diluted in helium in the discharge flow reactor, we used a gas sample of F$_2$ diluted in helium and calculated [F$_2$] using expression (7.E1) by considering that F$_2$ was 4.6 % by volume of the total measured [He]. For HNO$_3$ we proceeded in similar manner by controlling the percentage of its dilution with helium when we adjusted the setting of the digital flowmeter.

As will be explained below, the rate $k_I = [F(^2P)]k_{II}$ of reaction (7.1), resulted in 4.6×10^2 s^{-1}, for a typical $[F(^2P)] = 1.7 \times 10^{13}$ molecule cm^{-3}. Therefore, the lifetime τ_I for reaction (7.1) is $1/k_I = 2.2$ ms. The reacto-diffusive length, $l(\tau_I) = \sqrt{3D_{He}\tau_I}$, is a measure of the mean distance across which mixing and reaction (7.1) of the F/HNO$_3$ mixture takes place. As an approximation of D_{He} we chosen the diffusion coefficient of ground state Mg in He, $D = 340 \pm 27$ cm^2 s^{-1} for 1 Torr [2]. Therefore, $l(\tau_I)$ has been estimated at 1.5 cm. From the dimensions of the microwave discharge flow reactor we may estimate the reacto-diffusive length $l(t_D) = \sqrt{3D_{He}t_D}$ using the chosen flow F_{He} of helium. For a helium flow $F_{He} = 1.4 \times 10^{18}$ molecule s^{-1} we calculate $[He] = 1.3 \times 10^{16}$ molecule cm^{-3} for a pumping rate of helium of $S = 56$ cm^3 s^{-1}. The relation

between F_{He} and [He] in the discharge flow reactor is simply given by the following expression (7.E3):

$$F_{He} = [He] \cdot A \cdot v \qquad (7.E3)$$

where A is the cross section expressed in cm^2 of the flow tube in which reaction (7.1) takes place and v is the helium flow speed, expressed in cm s^{-1}, that we used in order to calculate the diffusion time t_D of helium in the discharge flow reactor. From expression (7.E3) we found a diffusion time of t_D = 40 ms. Therefore, the reacto-diffusive length $l(t_D)$ is calculated as 6.4 cm which is larger that $l(\tau_I)$ by a factor of four. This means that we have available a long distance (12 cm) over which to allow complete abstraction of H from HNO$_3$ in view of NO$_3$ production. The gas concentrations in the Knudsen reactor were calculated as explained in Chapter 2.

A first experiment consisted of the measurement of the flow of F$_2$ following the discharge. The raw MS signal at m/e 38 displayed in Figure 7.3 (curve (a)) corresponds to the F$_2$ flow into the Knudsen reactor across the inlet capillary. After the flow was established the microwave discharge has been switched on, the inlet flow of F$_2$ decreased by more than 95 % producing a large amount of HF (curve (b), Figure 7.3).
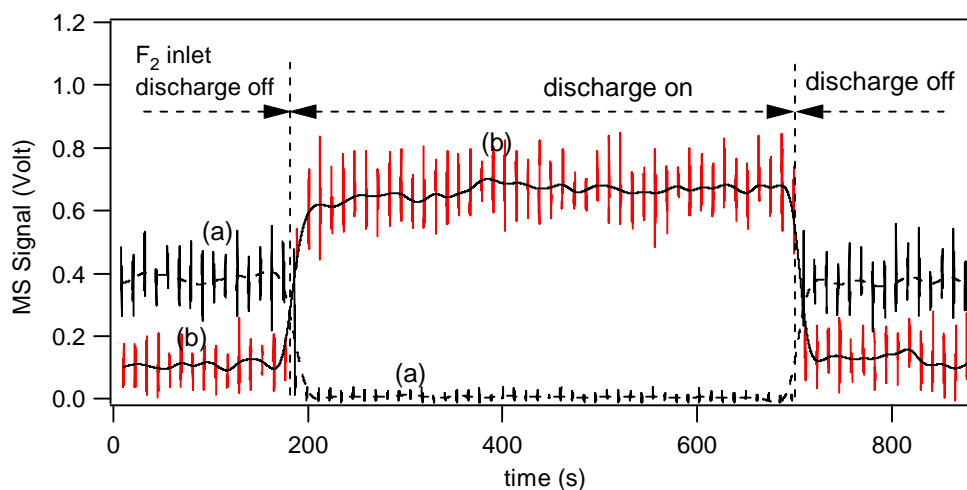

Figure 7.3. MS signals at m/e 38 (curve (a)) and 20 ((curve (b) corresponding to F$_2$ and HF, respectively. The decrease of the MS signal at m/e 38 indicates that the microwave discharge has been switched on. The discharge of F$_2$ takes place in the discharge flow reactor upstream of the inlet capillary to Knudsen flow reactor as illustrated in Figure 7.1.

7.2 The F + CH$_4$ Reaction

In order to characterize the source of F atoms and to verify if any important heterogeneous loss of F atoms occurred, preliminary experiments were performed employing methane CH$_4$ according to reaction (7.3):

$$CH_4 + F(^2P) \rightarrow CH_3 + HF \qquad\qquad (7.3)$$

The rate constant k for reaction (7.1) is $(4.7 \pm 0.5) \times 10^{-11}$ cm^3 molecule^{-1} s^{-1} at 298 K [3]. Methane has a fragment at m/e 15 and its molecular ion peak at m/e 16, F(^{2}P) is monitored at m/e 19, and HF at m/e 20. These masses have been detected by using the mass spectrometer that sampled the Knudsen flow reactor.
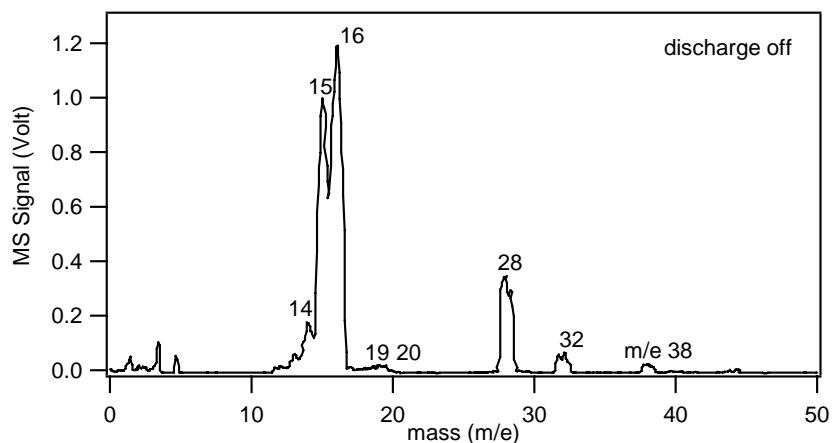
Figure 7.4. Typical mass spectrum for a mixture of F$_2$ and CH$_4$ flowing form the discharge flow reactor into the Knudsen flow reactor when the microwave discharge was switched off. The peaks at m/e 38 and 15 correspond to the presence of F$_2$ and CH$_4$ respectively.
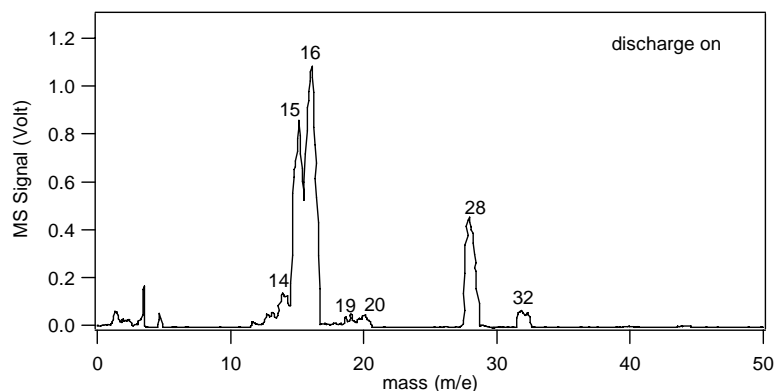
Figure 7.5. Typical mass spectrum for a mixture of F$_2$ and CH$_4$ flowing from the discharge flow reactor into the Knudsen flow reactor when the microwave discharge was switched on. The peak at m/e 38 has disappeared and we note the small increase of peaks at m/e 19 and 20 corresponding to F atoms and HF formation. The decrease of the CH$_4$ signal and the increase of the C$_2$H$_4$ signal indicates a reaction of F atoms with CH$_4$.

Figures (7.4) and (7.5) display the two mass spectra of methane before and after the reaction with F atoms in the microwave flow discharge system located upstream of the Knudsen flow reactor. Figure 7.5 displays a decrease in the MS signals at m/e 15 and 16 indicating a decrease in methane concentration. Methyl radical, CH$_3$, resulting from reaction (7.3) is expected to undergo a homogeneous recombination reaction to ethane, C$_2$H$_6$, according to reaction (7.4):

$$CH_3 + CH_3 \rightarrow C_2H_6 \qquad\qquad (7.4)$$

In addition, C$_2$H$_6$ (monitored at m/e 30 and 29) may be chemically activated resulting in the formation of C$_2$H$_4$ which has mass fragments at m/e 26, 27 and its molecular ion at m/e 28. As displayed in Figure (7.5), the fact that we observe an increase in the MS signal at m/e 28 may be attribute to formation of CO. When we coupled the discharge flow reactor using to the Knudsen flow reactor we measured an increase in the oxygen concentration from 4.2 x 10^9 to 7.8 x 10^9 cm^{-3}. Therefore, possible leaks in the discharge flow reactor may be responsible for secondary reactions of F atoms with O$_2$ such as $F + O_2 \rightarrow FO + O$.

Table 7.1 reports the concentrations of all reactants in the discharge flow and in the Knudsen reactor for the experiment displayed in Figure 7.5. In Figure 7.5 a slight increase of the MS signals at m/e 19 and 20 corresponding to the production of F atoms and HF, respectively, is

noted. From an initial concentration of F$_2$ 1.0 x 10^{15} cm^{-3} and considering that the initial flow of F$_2$ decreases more that 95 % we should expect a concentration of 2.0 x 10^{15} F atoms cm^{-3} once that the microwave discharge has been switched on. On the other hand, from the decrease of the MS signal at m/e 16, we measured a decrease of only 13 % of [CH$_4$]$_0$ in the discharge flow reactor. If we attribute the decrease of [CH$_4$]$_0$ to the reaction with F atoms, according to equation (7.3), then only 1.2 x 10^{15} F atoms cm^{-3} effectively reacted with CH$_4$. Therefore, it is reasonable to suppose that 60 % of the original production of F atoms reacted with CH$_4$ whereas the other 40 % reacted by forming HF or other reaction products.

|	Discharge flow reactor cm^{-3}	Knudsen reactor cm^{-3}
[He]	2.0 x 10^{16}	1.2 x 10^{13}
[CH$_4$]$_0$	9.5 x 10^{15}	6.8 x 10^{11}
Δ[CH$_4$]$_0$	1.2 x 10^{15}	8.8 x 10^{10}
[F$_2$]	1.0 x 10^{15}	1.6 x 10^{12}
[F(^{2}P)]	2.0 x 10^{15}	-
[O$_2$]	5.5 x 10^{12}	7.8 x 10^{9}

Table 7.1. Typical concentrations for CH$_4$ and F$_2$ used in the discharge flow reactor and measured using the Knudsen flow reactor a sampling device.

7.3 The F + HNO$_3$ Reaction

A large number of experiments were carried out at 298 K in order to use reaction (7.1) for the generation of NO$_3$ radicals. For the performed experiments we used the following ranges of experimental parameters: total pressure in the discharge flow reactor, 750 – 800 mTorr (mainly helium); [F(^{2}P)], (0.5 – 2.0) x 10^{13} cm^{-3} and [HNO$_3$], (1.2 – 6.5) x 10^{13} cm^{-3}, with initial ratios [HNO$_3$] / [F] ranging from 2 to 8.

Figure 7.6 displays a typical experiment where a steady state flow of HNO$_3$ is mixed with F atoms produced after the microwave discharge has been switched on. The raw MS signal at m/e 63 displayed in Figure 7.6 is proportional to the flow of HNO$_3$ and its decrease when the microwave discharge is switched on. Together with MS detection we use REMPI detection of NO$_2$ at λ = 511 nm in order to determine the nature of a possible secondary reaction product

occurring during NO$_3$ formation. From the decrease of the MS signal at m/e 63 we measure a decrease of 65 % of the flow of HNO$_3$ when the microwave discharge is switched on as displayed in Figure 7.6. We attribute this decrease to the reaction of HNO$_3$ with F atoms according to reaction (7.1). As already stated for the reaction of CH$_4$ with F atoms, we should expect a concentration of 1.3 x 10^{15} cm^{-3} F atoms after that the microwave discharge has been switched on based on an initial concentration of F$_2$ 6.5 x 10^{14} cm^{-3} (Table 7.2) and considering that the initial flow of F$_2$ decreased by more than 95 %. Therefore, 35 % of the initially generated F atoms reacted by forming HF or other reaction products.
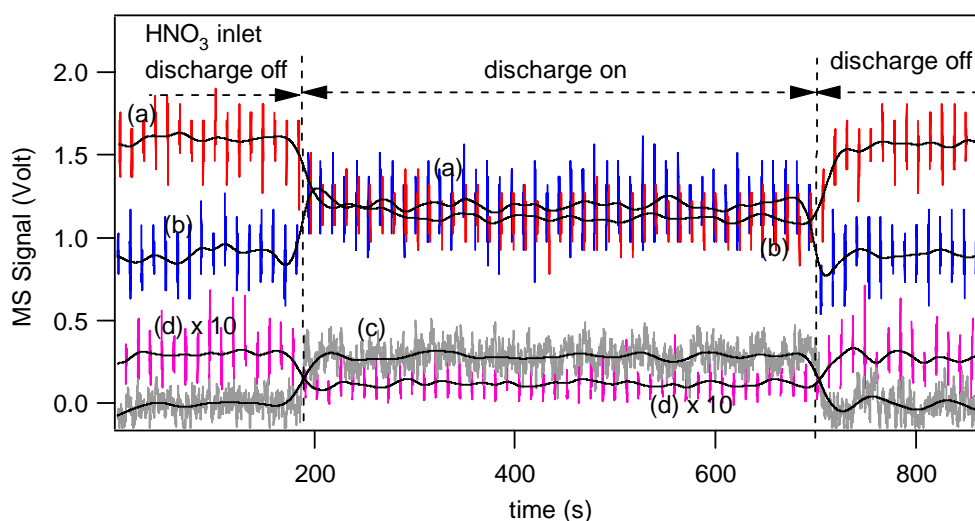
Figure 7.6. Typical experiment used to produce NO$_3$ by reaction of HNO$_3$ with F atoms. For t between 0 and 200 s the MS signals at m/e 46 (curve (a)), 30 (curve (b)) and 63 (curve (d)) correspond to HNO$_3$ prior to reacting with F atoms. At t = 200 s the microwave discharge is switched on and the MS signal at m/e 63 decrease. At the same time we can record an increase of the REMPI signal (curve (c)) at λ = 511 mn corresponding to a formation of NO$_2$.

It is reasonable to suppose that the decrease of HNO$_3$ is directly related to the production of F atoms. As the microwave discharge is switched on, an important quantity of NO$_2$ is observed simultaneously with the decrease of the HNO$_3$ flow (Table 7.2). The amount of NO$_2$ has been measured by REMPI detection of NO$_2$ in the Knudsen flow reactor (Chapter 2).

	Discharge flow reactor cm^{-3}	Knudsen reactor cm^{-3}
[He]	1.3×10^{16}	4.5×10^{13}
[HNO$_3$]$_0$	2.6×10^{13}	1.4×10^{11}
Δ[HNO$_3$]$_0$	1.7×10^{13}	9.1×10^{10}
[F$_2$]	6.5×10^{14}	2.2×10^{12}
[F(^{2}P)]	1.3×10^{15}	-
[NO$_2$]	Not measured	2.1×10^{11}

Table 7.2. Typical concentrations for HNO$_3$ and F$_2$ used in the discharge flow and in the Knudsen flow reactor in order to produce NO$_3$.

7.4 Conclusions

Following these measurements we did not observe a measurable gas phase production of NO$_3$ that we could detect in the Knudsen flow reactor despite our numerous efforts by changing all the degrees of freedom. The reasons for this unsuccessful attempt at generating NO$_3$ in the absence of NO$_2$ result may be:

- The amount of NO$_3$ is smaller than the detection limit of the MS detection system.
- The number of F atoms may be larger than measured by the decrease of HNO$_3$ as reported in Table 7.2. We therefore assume that NO$_3$ formed following reaction (7.1) may react with an excess of F atoms according to equation (7.5):

$$F(^2P) + NO_3 \rightarrow FO + NO_2 \qquad\qquad (7.5)$$
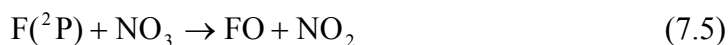
The secondary reaction (7.5) was observed to be very fast by Ravishankara and Wine[4], who used reaction (7.1) as a source of NO$_3$. They proposed a lower limit of 5.0×10^{-11} cm^3 molecule^{-1} s^{-1} for the rate constant of reaction (7.5) at room temperature. This could explain the possible formation of NO$_2$ in the experiment displayed in Figure 7.6.

- An additional explanation for the formation of NO$_2$ may be the secondary thermal decomposition of NO$_3$ in the discharge flow reactor according to reaction (7.6):

$$NO_3 \rightarrow NO_2 + \tfrac{1}{2}O_2 \tag{7.6}$$

The residence time of NO$_3$ in the discharge flow reactor has been estimated from expression (7.E3) and resulted in 40 ms. This time is much lower than the lifetime $\tau = 5$ s for NO$_3$ [5], therefore, we do not think that NO$_3$ decomposes before reaction with F atoms.

Owing to the fact that the Knudsen flow reactor operates at pressures of almost 100 times lower than the discharge flow reactor we think that the combination of a Knudsen flow and a discharge flow reactor is a suboptimal experimental means for the production and detection of NO$_3$ following reaction (7.1).

7.5 References

(1)   Mellouki, A.; Lebras, G.; Poulet, G.: Discharge Flow Kinetic-Study of NO$_3$ Reactions with Free- Radicals - the Reaction of NO$_3$ with Cl, Journal of Physical Chemistry, 91, 5760-5764, (1987).

(2)   Redko, T. P.; Rusinov, I. M.; Blagoev, A. B.: Diffusion of Ground-State (3s^2 ^{1}S$_0$) and Metastable (3s3p ^{3}P$_{0,1,2}$) Magnesium Atoms in He and Ne, Journal of Physics B-Atomic Molecular and Optical Physics, 26, 107-111, (1993).

(3)   Moore, C.; Smith, I. W. M.: Rate Constants for the Reactions of Fluorine-Atoms with Alkanes and Hydrofluorocarbons at Room-Temperature, Journal of the Chemical Society-Faraday Transactions, 91, 3041-3044, (1995).

(4)   Ravishankara, A. R.; Wine, P. H.: Absorption Cross-Sections for NO$_3$ between 565 and 673 nm, Chemical Physics Letters, 101, 73-78, (1983).

(5)   Jacob, D. J.: Heterogeneous chemistry and tropospheric ozone, Atmospheric Environment, 34, 2131-2159, (2000).

Appendix

THE PORE DIFFUSION MODEL

When a sample has a non-negligible internal surface such as a porous surface or internal void, we tend to overestimate the uptake coefficient because, in fact, ω is larger than calculated on the basis of the geometrical surface area. Keyser and co-workers [1] have applied the well known pore diffusion model to heterogeneous reactions of atmospheric relevance by attempting to correct measured uptake coefficients on solid powders. The uptake coefficient γ_{pd} resulting from the application of the pore diffusion model is related to the observed uptake coefficient γ_{ss} in equation (A.1):

$$\gamma_{SS} = \gamma_{pd}\rho_b S_{BET}(h_e + \eta h_i) \qquad (A.1)$$

where S_{BET} is the specific BET surface area, h_e the height of the first layer, h_i the height of all the internal layers calculated from the total mass m of the sample ($h_i = m/A_s\rho_b - h_e$) and ρ_b is the bulk density of the sample. The total number of layers of the sample, N_{Layers}, is given by $N_{Layers} = m/A_s\rho_b d$ where d is the average size of the particle. The effectiveness factor is given by $\eta = \dfrac{\tanh\Phi}{\Phi}$ with Φ being the Thiele modulus defined in equation (A.2):

$$\Phi = \frac{m}{\rho_b A_s d}\left(\frac{3\rho_b}{2(\rho_t - \rho_b)}\right)\sqrt{3\tau\gamma_{pd}} \qquad (A.2)$$

The effectiveness factor of a porous solid primarily depends on the relative rates of surface reaction and gas-phase diffusion; it is defined as the ratio of the observed

diffusion-limited reaction rate to the rate that would be observed if diffusion into the bulk of the powder were extremely fast. The effectiveness may also be thought of as the fraction of the internal surface which partakes in the heterogeneous reaction. In porous solids actual diffusive mass transfer can be slower than predicted because within these materials diffusion does neither occur in straight-line paths nor in pores of uniform cross section. To account for this the tortuosity factor τ is introduced. Although it has its basis in theory, the tortuosity factor remains a fitting parameter in practice because most porous solids are not characterized well enough. For any regular lattice consisting of identical pores $\tau = 3$ [2]. This result is also obtained for a network of randomly oriented cylindrical pores[3]. If the pore size is distributed, τ may exceed 3 a little. On the other hand, measurements of the tortuosity factor in a pack of spheres with a narrow particle size distribution gives $\tau < 3$ [4]. This discrepancy stems, in part, from the assumption that the pores can be regarded as infinitesimally wide in comparison to their length, and therefore leads to the conclusion that molecular diffusion in each pore is unidimensional in a direction parallel to the pore axis. In a short communication Friedman and Seaton (1995) proposed an approximate correction to take into account the finite aspect ratio of the pores. The corrected tortuosity factor became significantly different from $\tau = 3$ except for what are unrealistically low porosities, at least for most porous materials of practical interest. The corrected τ value should be unity for a medium of very high porosity and should approach the value of 3 for a medium with low porosity[5].

The analysed powder is characterised by a large distribution of grain diameters, so that the correction factor calculation for this substrate can be carried out only qualitatively. This complication is somewhat avoided because enough powder is present in these experiments so that the correction is calculated for the limit of many grain layers. When N_{Layers} is large, the correction factor is far more sensitive to the bulk density of the powder than the diameter of the grains. In addition, the value of the correction factor becomes independent of the grain diameter in the limit of large N_{Layers}.

References

(1)   Keyser, L. F.; Moore, S. B.; Leu, M. T.: Surface-Reaction and Pore Diffusion in
        Flow-Tube Reactors, Journal of Physical Chemistry, 95, 5496-5502, (1991).

(2)   Sahimi, M.; Gavalas, G. R.; Tsotsis, T. T.: Statistical and Continuum Models of
        Fluid Solid Reactions in Porous-Media, Chemical Engineering Science, 45, 1443-
        1502, (1990).

(3)   Johnson, M. F. L.; Stewart, W. E.: Pore Structure and Gaseous Diffusion in Solid
        Catalysts, Journal of Catalysis, 4, 248-&, (1965).

(4)   Kim, J. H.; Ochoa, J. A.; Whitaker, S.: Diffusion in Anisotropic Porous-Media,
        Transport in Porous Media, 2, 327-356, (1987).

(5)   Friedman, S. P.; Seaton, N. A.: A Corrected Tortuosity Factor for the Network
        Calculation of Diffusion-Coefficients, Chemical Engineering Science, 50, 897-
        900, (1995).

CURRICULUM VITAE

FEDERICO KARAGULIAN

Date of birth: 22nd September 1975
Place of birth: Milan, Italy
Nationality: Italian
Marital Status: Single
Address: Ch. de la Foret 18, 1024 Ecublens (VD) Switzerland
                        Via Caravaggio 16, 28922 Verbania (VB) ITALIA

Education

1994-2000   Physics Graduate at the Universita' degli Studi di Milano with final vote obtained in May 2000 of 104/110. Address: Physics of Matter (Solid State Physics). Subject of diploma work: Study of traps and recombination centers in scintillator glasses doped with rare earths: Tb^{3+} and Gd^{3+}.

2000-2001   Centro Tecnico Chimico Fisico Biologico (CENTECHIFIS), Civitavecchia (ROME). Lieutenant of the Italian Army Engineers.

2002-2005   Ph.D. student in the Laboratoire de Pollution Atmospherique (LPAS), under the supervision of Dr. M.J. Rossi, at the Swiss Federal Institute of Technology in Lausanne (EPFL), Switzerland. Subject of the thesis: Heterogeneous reactions of atmospheric trace gases on solid substrates. Chemical kinetics, global change, atmospheric chemistry, aerosol particles.

Languages

Italian mother tongue
Knowledge of English language both spoken and written
Knowledge of French language both spoken and written.

Pubblications

- Optical absorption and thermoluminescence of Tb^{3+}-doped phosphate scintillating glasses, Vedda A, Martini M, Nikl M, Mihokova E, Nitsch K, Solovieva N, Karagulian F *Journal of Physics Condensed-Matter* 14 (32): 7417-7426 AUG 19 2002.

- The heterogeneous chemical kinetics of NO_3 on atmospheric mineral dust surrogates, F. Karagulian and M.J. Rossi. *Physical Chemistry Chemical Physics,* 2005, **7**(17), 3150.

- The heterogeneous chemical kinetics of N_2O_5 on $CaCO_3$ and other atmospheric mineral dust surrogates, F. Karagulian and M.J. Rossi *Atmospheric Chemistry and Physics Discussion*, 5, 10369-10408, 2005).

- The heterogeneous ozone decomposition on mineral dusts, F. Karagulian and M.J. Rossi accepted for publication to *International Journal of Chemical Kinetics*, KIN-05-0136.R1, 2005.

- High reactivity and chemical kinetics of NO_3 on laboratory flame soot, F. Karagulian and M.J. Rossi (in preparation).